

OBSERVATIONAL AND MODELLING STUDIES OF THE FRASER RIVER PLUME

by

JAMES ALEXANDER STRONACH

M.Sc., University of Saskatchewan, 1972

A THESIS SUBMITTED IN PARTIAL FULFILLMENT OF
THE REQUIREMENTS FOR THE DEGREE OF
DOCTOR OF PHILOSOPHY

in

THE FACULTY OF GRADUATE STUDIES

DEPARTMENT OF PHYSICS

INSTITUTE OF OCEANOGRAPHY

We accept this thesis as conforming
to the required standard

THE UNIVERSITY OF BRITISH COLUMBIA
December, 1977

copyright James Alexander Stronach, 1977

In presenting this thesis in partial fulfilment of the requirements for an advanced degree at the University of British Columbia, I agree that the Library shall make it freely available for reference and study.

I further agree that permission for extensive copying of this thesis for scholarly purposes may be granted by the Head of my Department or by his representatives. It is understood that copying or publication of this thesis for financial gain shall not be allowed without my written permission.

James Stronach

Department of Physics

The University of British Columbia
2075 Wesbrook Place
Vancouver, Canada
V6T 1W5

Date

Dec. 7 / 77

ABSTRACT

The Fraser River plume is the brackish surface layer formed when the Fraser River discharges into the Strait of Georgia. Two approaches to understanding the dynamics of the plume are discussed. Initially, a series of field observations was carried out in the plume. These consisted mainly of CSTD profiles and current profiles in the upper 10-20 meters of the water column. Also, a surface current meter was installed for 34 days at the mouth of the Fraser River. The principal conclusions of the field observations are: the plume is strongly sheared in the vertical and strongly stratified; this vertical structure is most apparent in the vicinity of the river mouth, and around the time of maximum river discharge (near low water in the Strait); and that the water moving outward from the river mouth subsequently acquires velocities and salinities appropriate to the water beneath it with length and time scales for this change of order 50 km and 8 hours. The plume thickness varies between 0 and 10 meters; the salinity varies from 0 to that of the water beneath it (approx. 25 ‰); and the difference between the plume velocity and that of the water beneath it varies from up to 3.5 m/sec to 0 m/sec, and is typically of order 0.5 m/sec over much of the plume area.

Inspired by the field data, a model of the thin upper layer was developed. The independent variables are the two components of transport in the upper layer, the thickness of the layer, and the integrated salinity in the upper layer. The bottom of the upper layer has been tentatively defined by an isopycnal surface. The mixing across this interface is modelled by an

upward flux of salt water (entrainment), and a downward flux of brackish water (termed depletion in this work). The dynamical effects included in this model are: the local time derivative; the field accelerations; the buoyant spreading pressure gradient (including the effects of salinity on the density field); the entrainment of tidally moving water and the loss by the depletion mechanism of water with the plume momentum; the frictional stress between the plume and the water beneath it; the forcing due to the baroclinic tidal slopes; and the Coriolis force. Subsets of the full model equations are examined, to clarify certain aspects of the plume dynamics. Preliminary results from the numerical solution of the full model equations are presented, and a comparison is made between the paths of lagrangian trackers produced by the model and drogue tracks observed in the plume. Future improvements to the model are discussed.

TABLE OF CONTENTS

ABSTRACT	ii
LIST OF TABLES	v
LIST OF FIGURES	vi
ACKNOWLEDGEMENTS	xiv
1. INTRODUCTION	1
2. FIELD OBSERVATIONS OF THE PLUME	9
3. A MODEL OF THE FRASER RIVER PLUME	26
4. AIDS TO INTUITION ABOUT THE PLUME	43
5. NUMERICAL MODELING OF THE FRASER RIVER PLUME	71
6. CONCLUDING DISCUSSION	93
REFERENCES CITED	97
APPENDIX	103
TABLES	114
FIGURES	117

LIST OF TABLES-

TABLE I. HARMONIC ANALYSIS OF RIVER SPEEDS	114
TABLE II. HARMONIC ANALYSIS OF POINT ATKINSON ELEVATIONS.	115
TABLE III. SCALE ANALYSIS OF TERMS IN THE EQUATION OF MOTION.	116

LIST OF FIGURES

Figure 1. Chart showing the Straits of Georgia and Juan de Fuca	117
Figure 2. Salinity distribution in the Strait of Georgia and Juan de Fuca Strait, 1-6 July 1968	118
Figure 3. Salinity distribution in the Strait of Georgia and Juan de Fuca Strait, 4-8 Dec. 1967	119
Figure 4. Chart showing the Fraser River delta, and central Strait of Georgia	120
Figure 5. The daily Fraser River discharge for 1976, measured at Hope.	121
Figure 6. Chart of the river mouth area, showing the location of the current meter mooring	122
Figure 7. Smoothed current meter record	123
Figure 8. the low frequency component of the current meter record	124
Figure 9. The tidal part of the current meter record	125
Figure 10. Tidal elevations at Point Atkinson during the time the current meter was in operation	126
Figure 11. A reconstruction of the tidal signal from constituents obtained by harmonic analysis	127
Figure 12. Profiles of S, T, sigma T and current speed for 1330 PST, May 8, 1976, at the current meter mooring	128
Figure 13. The salinity distribution as a function of time at the river mouth, January 21, 1975	129
Figure 14. Station positions and times, wind and tide for April 6, 1976	130
Figure 15. Salinity section along line h-r for April 6 1976	131
Figure 16. S, T, sigma T profiles at station j, 1744 PST, April 6, 1976	132
Figure 17. S, T, sigma T profiles at station k, 1750 PST, April 6, 1976	133
Figure 18. S, T, sigma T profiles at station l, 1758 PST, April 6, 1976	134

Figure 19. Station positions and times, wind and tide for April 15, 1976	135
Figure 20. Salinity distribution along line e-m and along line m-r for April 15, 1976	136
Figure 21a. S, T, sigma T profiles at station k, 1710 PST, April 15, 1976	137
Figure 21b. S, T, sigma T profile at station l, 1713 PST, April 15, 1976	137
Figure 22. Station positions and times, wind and tide for April 28, 1976	138
Figure 23. Salinity section for April 28 1976, along a line from a front at station g to station h	139
Figure 24. Station positions and times, wind and tide for June 4, 1976	140
Figure 25a. Salinity section along line o-s, June 4, 1976	141
Figure 25b. Salinity section along line x-t, June 4, 1976	141
Figure 26. Station positions and times, wind and tide for July 3, 1975	142
Figure 27a. Salinity section along line a-l, July 3, 1975	143
Figure 27b. Salinity section along line p-s, July 3, 1975	143
Figure 28. S, T, sigma T profiles at station a, 0642 PST, July 3, 1975	144
Figure 29. S, T, sigma T profiles at station e, 0733 PST, July 3, 1975	145
Figure 30. S, T, sigma T profiles at station j, 1106 PST, July 3, 1975	146
Figure 31. Sketch of the plume observed by aerial survey, 0900 PST, July 2, 1975	147
Figure 32. S T, sigma T profiles on the silty side of the front, 1250 PST, July 2, 1975	148
Figure 33. S, T, sigma T profiles on deep blue side of front, 1325 PST, July 2, 1975	149
Figure 34. S, T, sigma T profiles on silty side of front, 0849 PST, July 4, 1975	150

Figure 35. S, T, sigma T profiles on deep blue side of front, 0853 PST, July 4, 1975	151
Figure 36. The evolution of a front, January 18, 1976	152
Figure 37. Station positions and times, wind and tide for July 23, 1975	153
Figure 38a. Paths of drogues released in region A, July 23, 1975	154
Figure 38b. Paths of drogues released in region B, July 23, 1965	154
Figure 39. S, T, sigma T profiles in region A, 1025 PST, July 23, 1975	155
Figure 40. Speed profile in region A, 1015 PST to 1045 PST, July 23, 1975	156
Figure 41. Station positions and times, wind and tide for July 13, 1976	157
Figure 42. S, T, sigma T profiles at station g, 1304 PST, July 13, 1976	158
Figure 43. Speed profile at station g, 1317 PST, July 13, 1976	159
Figure 44. Polar plot of velocity vectors, station g, 1317 PST, July 13, 1976	160
Figure 45. Station positions and times, wind and tide for Sept. 17, 1976	161
Figure 46. S, T, sigma T profiles at station a, 0646 PST, Sept. 17 1976	162
Figure 47. Speed profile at station a 0655 PST, Sept. 17, 1976	163
Figure 48. Polar plot of velocity vectors, station a, 0655 PST, Sept. 17, 1976	164
Figure 49. S, T, sigma T profiles at station j, 1512 PST, Sept. 17, 1976	165
Figure 50. Speed profile at station j, 1458 PST, Sept. 17, 1976	166
Figure 51. Polar plot of velocity vectors, station j, 1458 PST, Sept. 17, 1976	167
Figure 52. An idealized Strait of Georgia, showing contours of surface salinity	168

Figure 53. A salinity section along AA', Fig. 52, and salinity profiles at three stations	168
Figure 54. The control volume, indicated by dashed lines, surrounding the plume defined by the $S=25\text{‰}$ contour	169
Figure 55. Definition sketch for the equations derived in Chapter 3	169
Figure 56a. The orientation of the two characteristics C_+ and C_- with respect to the streamline direction	170
Figure 56b. The region of solution, filled up with intersecting characteristics	170
Figure 57. Streamlines and lines of equal thickness, from Rouse et al, 1951	171
Figure 58a. Schematic diagram for the model of surfacing isopycnals	172
Figure 58b. The thickness of the upper layer predicted by Egn. 4.13	172
Figure 59a. The control volume used to obtain conditions at a strong discontinuity	173
Figure 59b. Sketch of upper layer conditions used to obtain the integrated pressure term	173
Figure 60a. An element of the implicit characteristic solution, Egn. 4.26	174
Figure 60b. A characteristic intersecting the front at (S, t)	174
Figure 60c. Two characteristics intersecting at a hydraulic jump	174
Figure 61. The characteristic diagram for the kinematic wave solution	175
Figure 62. The distribution of u at $t=14$, from the kinematic wave solution	176
Figure 63a. The vertical distribution of salinity for $K=Z^2/(0.2^2)$	177
Figure 63b. The vertical distribution of salinity for $K=1$	177
Figure 64a. Depth of the upper layer as a function of time	178
Figure 64b. Total salt content of the upper layer as a function of time	178

Figure 65. An isoconcentration curve and velocity vectors for a turbulent plane jet	179
Figure 66a. Schematic diagram of a turbulent jet	180
Figure 66b. A section through the plume, showing the effect the choice of bottom salinity has on flow through an open boundary	180
Figure 67. A typical computational element of the numerical grid used in this research	181
Figure 68. The complete grid used for the square box model ..	182
Figure 69. Flux out of the open ends of the linear model	183
Figure 71. Velocity vectors after 100 timesteps of the square box model with non-linear terms	184
Figure 71. The same as Fig. 70, but at timestep 500	185
Figure 72. The same as Fig. 70, but at timestep 1000	186
Figure 73a. Influx and efflux for the model of Figs. 70, 71, 72	187
Figure 73b. Influx and efflux for the model of Figs. 74, 75	187
Figure 74. Flow field calculated in the same way as for Fig. 70, with the addition of horizontal eddy viscosity	188
Figure 75. Flow field calculated in the same way as for Fig. 71, with the addition of horizontal eddy viscosity	189
Figure 76. The propogation of a hump of water out of the system	190
Figure 77. The distribution of velocity and elevation for Fig. 74, along the line from the river mouth the opposite solid boundary	191
Figure 78a,b. Comparison of elevation fields from a 0.33 km grid size model and a 1 km grid size model	192
Figure 79a,b. Comparison of entrainment velocity from a 0.33 km mesh model and a 1 km mesh model	192
Figure 80a,b. Comparison of u-velocity fields from a 0.33 km mesh model and a 1 km mesh model	193
Figure 81a,b. Comparison of v-velocity fields from a 0.33 km mesh model and a 1 km mesh model	193

Figure 82. Flow field produced by a model with variable river flow, tidal streams and elevations, Coriolis force, and a constant Proudman number boundary condition	194
Figure 83. Flow field produced by a model with constant river flow, tidal elevations, Coriolis force, friction constant of 0.005, and using $\partial^2 F^2 / \partial n^2 = 0$ as a boundary condition	195
Figure 84. Flow field produced by a model identical to that of Fig. 83, but with a friction coefficient of .001	196
Figure 85. Velocity vectors for a model with density effects, tidal elevations, no Coriolis force, and constant river flow	197
Figure 86. The model of Fig. 85, 2 hours later	198
Figure 87. The model of Figure 85, 4 hours later	199
Figure 88. The model of Fig. 85, 6 hours later	200
Figure 89. The model of Fig. 85, 8 hours later	201
Figure 90. The model of Fig. 85, 10 hours later	202
Figure 91. The model of Fig. 85, 12 hours later	203
Figure 92. Salinity distribution at hour 186, corresponding to the flow field of Fig. 88	204
Figure 93. The salinity distribution at hour 192, corresponding to Fig. 91	205
Figure 94. The distribution of upper layer thickness at hour 186, corresponding to Fig. 88	206
Figure 95. The distribution of upper layer thickness at hour 192, corresponding to Fig. 91	207
Figure 96. Droque tracks produced over a 24 hour period by the flow field of Figs. 85, 91	208
Figure 97. Droque tracks produced over 24 hours by the flow field of Fig. 98, using an augmented flow at the boundaries during outflow	209
Figure 98. A typical velocity field produced by a model with augmented flow at the open boundaries during outflow	210
Figure 99. Droque tracks for drogues released shortly before low water. (from Cordes, 1977)	211

Figure 100. The discharge out of the open boundaries of a model with tidal elevations, variable density, constant river flow, and no Coriolis force	212
Figure 101. Drogue tracks produced when drogues were released at zero river flow, approaching high water	213
Figure 102. Drogue tracks produced when drogues were released at half maximum river flow, during the ebb, when river flow is increasing	213
Figure 103. Drogue tracks produced when drogues were released at maximum river flow, near the end of the ebb	214
Figure 104. Drogue tracks produced when drogues were released at half maximum river flow during the flood stage of the tide	214
Figure 105. Velocity field produced by a model with depletion	215
Figure 106. Drogue tracks produced over 12 hours by the model which produced the flow field of Fig. 105	216
Figure 107. Elevation field produced by the model with depletion	217
Figure 108. Elevation field at 72 hours, produced by the model with depletion	218
Figure 109. Velocity field produced by the first real geometry model, at time of maximum river flow	219
Figure 110. Distribution of upper layer thickness at the end of the ebb	220
Figure 111. Distribution of upper layer thickness at the end of the flood	221
Figure 112. Drogue tracks produced over 12 hours by drogues released at maximum river flow	222
Figure 113. Normalized elevations, currents, and river discharge used in the second version of the real geometry model	223
Figure 114. Distribution of velocities and surface slopes used in the second version of the real geometry model	224
Figure 115. Velocity field of the model with more realistic tidal forcing, at 8 hours	225
Figure 116. Velocity field produced by the model of Fig. 115, 4 hours later	226

Figure 117. Velocity field produced by the model of Fig. 115, 8 hours later	227
Figure 118. Velocity field produced by the model of Fig. 115, 12 hours later	228
Figure 119. Velocity field produced by the model of Fig. 115, 16 hours later	229
Figure 120. Tracks produced by drogues released at hour 6, approximately high low water	230
Figure 121. Tracks produced by drogues released at hour 12, low high water	231
Figure 122. Tracks produced by drogues released at 18 hours, at maximum river discharge, near low low water	232
Figure 123. Tracks produced by drogues travelling in the same flow field as those in Fig. 122, but with a correction for vertical shear in calculating the drogue velocity	233
Figure 124. A comparison of drogue tracks from Cordes(1977) and this model	234
Figure 125. Distribution of upper layer thickness at hour 8	235
Figure 126. Distribution of upper layer thickness at hour 12	236
Figure 127. Distribution of upper layer thickness at hour 16	237
Figure 128. Distribution of upper layer thickness at hour 20	238
@ figure 129. Distribution of upper layer thickness at hour 24	239
Figure 130. Schematic diagram of a possible extension of the upper layer model to 2 layers	240
Figure 131. The distribution of salt as calculated by a first order scheme	241
Figure 132. The distribution of salt as calculated by a second order scheme	242

ACKNOWLEDGEMENT

Although many people help in carrying through a thesis project, I would like in particular to acknowledge the assistance of Dr. P. B. Crean, and Dr. P. H. Leblond. Dr. Crean, of Environment Canada, was particularly helpful in guiding much of the research, both the field work and in developing the numerical model. Dr. Leblond, my thesis supervisor, always offered a positive approach to the work, particularly in the writing of the thesis. I would also like to thank A. B. Ages (OAS) for the use of the CSTD probe; and Dr. M. Miyake (OAS) for the use of the sonic current meter.

The financial support of the National Research Council and the University of British Columbia, through a Macmillan family scholarship is gratefully acknowledged.

CHAPTER 1

INTRODUCTION

One of the most striking oceanographic features of the Strait of Georgia is the Fraser River plume. Referring to Fig. 1, the Strait of Georgia is the body of water separating Vancouver Island from the British Columbia mainland. The Fraser River, located south of Vancouver, discharges into the eastern side of the Strait of Georgia. Particularly during the late spring and early summer, in times of large river runoff, the Fraser River plume appears to be a layer of muddy brown water floating on the dark blue Strait of Georgia water; the plume is frequently bounded by a sharp colour discontinuity. The boundary between the two water masses may also be diffuse, and there are sometimes weaker colour discontinuities within the body of the plume. Colour is, however, a misleading indicator of the plume, because sediment does not necessarily sink at the same rate at which the salinity and momentum differences between the plume and the ambient water decrease. For purposes of this thesis, the following two-part definition of the plume will be used:

1) the plume is the mixed water formed when the Fraser River discharges into, and mixes with, the ambient Strait of Georgia water;

2) in order to be associated with the plume, this mixed water must retain a significant identity as river water, for example it must be fresher than some arbitrary maximum salinity, for example 25‰ (parts per thousand). The value of this arbitrary salinity is subject to variation, depending on the season, and on what properties of the plume one wants to

describe.

Because it is less dense than the ambient water, the plume is a relatively thin layer, floating on and interacting with the denser Strait of Georgia water.

There are two main reasons for studying the Fraser River plume. As mentioned above, it is a striking feature of the Strait of Georgia, and for that reason alone warrants attention. The other, more practical, reason is that the plume plays a very important role in the flushing and general circulation of the Strait of Georgia, which in turn influence the biological environment of the Strait. Biological properties of the Strait influenced by the Fraser River induced circulation include the supply of upwelled nutrients to the surface layers; the attenuation of sunlight by suspended sediment; and the horizontal advection and vertical migration of planktonic organisms.

REVIEW OF THE OCEANOGRAPHY OF THE STRAIT OF GEORGIA

At this point we will consider briefly the oceanography of the Strait of Georgia (Fig. 1). Waldichuk (1957) carried out an extensive study of the Strait of Georgia. Most of the circulation theory discussed below appeared in this paper. Further information comes from Crean and Ages (1971), who carried out a series of hydrographic cruises over a period of one year, occupying stations in the entire Juan de Fuca - Georgia system.

The Strait of Georgia is a fjord-type estuary - it is deep, has a freshwater source, is connected to the sea, and is

strongly stratified. The average depth is about 150 meters, but considerable areas are deeper than 200 meters. The Strait differs from simpler types of fjords in that it is very wide (on the average about 30 km.), and the major source of fresh water, the Fraser River, is near the main outlet of the system, where strong tidal mixing occurs. Further, there are two connections with the sea. At the northern end is found a complicated set of narrow channels, through which tidal currents reach 6 m/s. At the south, the Strait of Georgia is connected to Juan de Fuca Strait by another system of passes and sills, where tidal currents reach 1.5 m/s; Juan de Fuca Strait in turn has a free connection to the Pacific Ocean. Figures 2 and 3, from Crean and Ages (1971) show salinity sections along the centreline of the Strait of Georgia for the months of July and December. The Fraser River is seen to be a strong source of stratification in the summer, and a weaker source in the winter. One also sees the evidence for strong mixing in the region of Haro Strait in the south, and Cape Mudge in the north. With reference to Figures 2 and 3, one wonders what proportion of the Fraser River water flows north and is mixed there; what proportion flows south and is mixed there; and what proportion, while flowing north and south, is mixed in the middle of the Strait?

The prevailing winds are in general along the axis of the Strait - northwest and southeast (Waldichuk, 1957). However, there are frequent storms with variable wind direction, and the Fraser valley in particular modifies the direction of winds in the southern Strait.

More than 70% of the fresh water input to the Straits of Georgia and Juan de Fuca comes from the Fraser (Herlinveaux and Tully, 1961). The river discharges through a complicated system of channels in its delta, Fig. 4, but 80% of the flow passes through the Main Arm which is dredged to be about 400 meters wide and 10 meters deep. Flow velocities at the river mouth are tidally modulated, varying between about 0 m/s and 3.5 m/s over a tidal cycle. Further, the river discharge is very seasonal, Fig. 5, changing by an order of magnitude from about 1000 m³/sec during winter to about 10,000 m³/s during the spring-early summer freshet. If one defines the plume to be water which is fresher than, for example, 28 ‰, then from Fig. 2 and Fig. 3, its thickness is about 10 meters, and it covers most of the central Strait of Georgia during summer, and a considerably smaller area during winter. During summer, the fresh water fraction in this plume volume is much greater than during winter. Also, because of the lower stability of the plume in winter, it is more liable to be mixed away by storms, which are stronger in the winter.

There are very strong tides in the Strait of Georgia (Crean, 1976), and they exert considerable influence on the plume. First, the tide modulates the river flow, so that maximum river discharge occurs near low water, and the river is effectively shut off at high water. The river water, as it replenishes the plume already existing, is then acted on by the tides in the Strait. Frictional interaction with the tidal currents in the underlying water will drag the plume to the south during an ebb, and to the north during a flood. Velocity

differences between the plume and the water underneath give rise to vertical mixing, partially inhibited by the vertical density gradient. The barotropic surface slope will not only tend to move the plume up and down the Strait, but also gives a considerable cross channel forcing (due to the Coriolis force in the barotropic equations). Consequently, the plume moves about in a complicated manner, losing fresh water by mixing at about the same rate (tidally averaged) that it gains it from the river discharge. Near the river mouth, where there is the most available kinetic energy, there is intense mixing, but the resulting mixed water is fresh enough, and has the necessary river-directed momentum, to form an outgoing plume. This mixing produces an upwelling of nutrient rich salt water, which is very important from a biological point of view (de Lange Boom, 1976). As the river water proceeds outwards and mixes, the stability of the plume decreases, so that near the tidal mixing passes, mixing is almost complete. The seaward transport of salt water in the plume is compensated by a return flow of salt water beneath the plume, as in all estuarine circulations. Thus, studying the plume will aid in explaining the movements of deep water in the Strait of Georgia.

PREVIOUS STUDIES OF THE PLUME

Because of its interaction with the general circulation of the Strait, the plume has recieved considerable study.

Giovanda and Tabata (1970) presented the results of tracking drogues which were released near the Fraser River mouth, and followed for periods ranging from 2 to 33 hours.

Tabata (1972) attempted to identify the different types of water in the plume from aerial photographs.

DE Lange Boom (1976) described a mathematical model of chlorophyll distribution in the plume, with the hydrodynamic flow pattern being somewhat arbitrarily prescribed.

Cordes (1977) described the results of a rather sophisticated drogue tracking procedure in the plume.

STUDIES OF SIMILAR SYSTEMS

Recently Long (1975b), and Winter et al (1977), have discussed one layer models of fjords, similar in many respects to the model discussed in this thesis.

There also exists a considerable body of literature on thermal plumes due to cooling-water discharge from power plants (Koh and Fan, 1970; Stolzenbach and Harleman, 1971). Numerical and physical models exist for these plumes, but they are not applicable to the Fraser River plume. Usually there is only one independent variable, the distance along the plume axis; the other horizontal dimension being taken care of by empirical spreading coefficients and profiles of properties. The models are time-independent, and not adaptable to time-dependent situations; they are not adaptable to a system with partially enclosing solid boundaries.

Takano (1954a, 1954b, 1955), in a series of papers, discussed the spreading of a river plume issuing into an unbounded ocean. His model was time-independent, and involved a balance of Coriolis force, hydrostatic pressure gradient, and horizontal eddy viscosity; it predicted a bending to the right

of the plume, although the discharge remained symmetric about the entrant direction of the river. The choice of horizontal eddy viscosity was probably inappropriate because the most important friction is likely the interaction of the plume with the underlying water, and not with itself and water to the sides as in the case of horizontal eddy viscosity.

Wright and Coleman (1971) discussed the Mississippi River plume, which is in some ways similar to the Fraser River plume, the principal difference being that tides are about 1/10 as strong in the Gulf of Mexico as in the Strait of Georgia. They fit a model developed by Bondar (1970), similar to cooling-water plume models, to some field data. One would conclude from their work that buoyant spreading and entrainment are the two most important forces governing a plume.

Garvine (Garvine and Monk, 1974, Garvine, 1974, Garvine, 1977) has described field work done in the Connecticut River plume, and has developed a model to explain the propagation of the leading edge of a plume. The Connecticut River is much smaller than the Fraser in terms of discharge, but the plumes have many similarities - strong tidal currents act on them, and they both form distinct fronts. In the Garvine model frontal dynamics are controlled by the salinity and density profiles behind the front.

THIS RESEARCH

Although Garvine lays great stress on fronts as controlling the dynamics of plumes, the approach taken in this thesis is that before one can develop a model which includes fronts, one has to have a good model to describe the flow between the river mouth and the front, i.e. a time-dependent model of a thin continuous upper layer. In this thesis, two complementary methods to increase our understanding of the plume have been used. A fairly extensive, but exploratory, set of field measurements was carried out, using mainly a CSTD, and on a few occasions a profiling current meter. Based on the field work, a two dimensional, vertically integrated (over the plume thickness), time-dependent numerical model was developed. The model includes: the effects of barotropic tidal slopes and streams; the effects of vertical mixing on the distribution of salt and momentum; the Coriolis force; the stress between the upper and lower layers; and the buoyant spreading and inertial effects in the plume. This model is exploratory, in that it cannot predict nature very accurately, but allows us to check the effects and importance of various forces acting on the plume. Further field work will allow a better adjustment of the mixing and stress in the model.

CHAPTER 2

FIELD OBSERVATIONS OF THE PLUME

As mentioned in Chapter 1, various people have already made measurements of the Fraser River plume. There are a few salinity profiles available (Waldichuk, 1957; de Lange Boom, 1976), obtained by discrete sampling. There are also extensive drogue tracks available (Giovando and Tabata, 1972; Cordes, 1977), but they lack information about the vertical structure of velocity and salinity in the plume. In developing the observational aspects of this research, it was felt that a useful contribution to knowledge of the plume would be to investigate the vertical structure of velocity and salinity in the plume, with particular reference to location in the Strait of Georgia and stage of tide. In this chapter are described some of the field observations obtained using a continuous recording CSTD probe, (conductivity, salinity, temperature, and depth), and a profiling current meter. The observations were carried out in cooperation with P.B. Crean (Ocean and Aquatic Sciences, Environment Canada) at various times between January 1975 and September 1976. Two boats were used in this field work. In 1975 the CSV Richardson, a 20 meter vessel, was used to obtain CSTD profiles. In 1976 the Brisk, an 8 meter launch was used. As the Brisk required no operating crew other than the two scientists, (P.B. Crean and myself), and was always available, its operation allowed considerable flexibility. Using this boat, which was equipped with radar for accurate positioning, we did CSTD profiles, velocity profiles, and measured positions of the colour front associated with the plume.

All of the salinity and sigma-T profiles presented here were calculated from conductivity, temperature and depth data obtained with an Interocean model 513 CSTD probe and a chart recorder. The conductivity and temperature traces were digitized on the Mechanical Engineering digitizer at U.B.C., and salinity and sigma-T profiles calculated from them. The CSTD was designed to operate from 0 to 30 meters, so was ideal for our purposes. However, for a variety of reasons, the accuracy of the probe and chart recorder system is not reliable. The accuracy varied with time, depending on such factors as which boat was being used, the ambient temperature, and how long the chart recorder had been operating that particular day. For these reasons, the salinity profiles can only be considered to be accurate to about 0.5 ‰ unless one is comparing a series of successive casts. Fortunately, the error is not random, but systematic (e.g., the zero might be offset on the chart recorder), and the size of the salinity error is much smaller than the size of salinity variation in the plume, so that these low accuracy salinity profiles reveal almost all the pertinent salinity structure of the plume.

1. CONDITIONS AT THE RIVER MOUTH

A. Currents at the river mouth

Before proceeding to a discussion of the salinity and velocity structure of the plume, let us first look at conditions at the river mouth. It is easier to interpret the salinity measurements in the plume when we know the temporal relationship between the river discharge and the barotropic tide in the

Strait. As a preliminary stage in acquiring this information in full, the Canadian Hydrographic Service installed a bottom-moored surface current meter (Neyrpic design) at the mouth of the Fraser River, Figure 6. The installation position chosen is a compromise between putting the current meter in an out-of-the-way location safe from shipping, and putting it in the main channel, subject to the full river flow. The current meter was in place for 34 days, from April 6 to May 11, 1976. During this time, the river discharge increased from 1100 m³/sec to 7700 m³/sec, (Fig. 5), a typical variation during the onset of the spring freshet. At the end of each 10 minute interval the meter recorded the number of revolutions of its propellor (which converts to a speed), and the instantaneous magnetic heading at the end of the 10 minute interval. Because of the large mass of steel in the current meter mooring, the magnetic direction has to be used with caution. During times of significant outflow velocity, when the flow was presumably along the line of the Sand Heads jetty, (215° magnetic), the current meter indicated a direction of 306° magnetic, approximately perpendicular to the actual flow. During the high water part of the tidal cycle, when the actual surface velocity approaches zero, and sometimes assumes a direction toward the jetty, (a change of 90°), the magnetically determined direction changed by only 35°, to about 270°. In order to convert the speed signal into a velocity signal, the current meter record was treated as follows. For magnetic directions greater than 300°, corresponding to outflow conditions, the velocity was assumed to be entirely parallel to the channel, and directed downstream. For directions less than

300°, the velocities were very small, and it was decided to scale the magnetic variation of 30° (300° to 270°) into a variation of 180°, so that most of these low velocity periods were treated as flows up the channel. Because the velocity signal is sampled at 1 hour intervals in the subsequent harmonic analysis, it is impossible to reproduce the shape of the speed record very well, and the above treatment gives a smoother velocity record than if the small flows at high water were taken to have zero component in the direction of the river channel. Assuming the above conversion from speed to velocity, the record was prepared for harmonic analysis, in order to determine the relation between the river flow and the tides in the Strait. The signal was first band pass filtered by attenuating components with frequencies higher than one cycle per hour, and lower than one cycle per day. The signal resulting from removal of high frequency (periods less than one hour) components is shown in figure 7. The A6A6A7/6•6•7, $\Delta t=10$ min, filter of Godin (1970) was used to remove the high frequency components. The operator A6, for example, is a running mean of length 6 applied to the time series, and Δt is the spacing of sampled points. The low frequency component of the signal was obtained with the A24A24A25/24•24•25, $\Delta t=1$ hour filter, (Godin 1970), and is shown in Figure 8. The tidal band of frequencies was obtained by subtracting the low frequency signal, Figure 8, from the smoothed signal, Fig. 7, and is shown in Figure 9. This tidal record was then harmonically analysed. Because the record was not long enough, it was impossible to separate some constituents, for example the group K1, P1, S1. It was assumed

that the relations between the amplitudes and phases of these constituents in the river speed record were the same as for the same constituents obtained from an analysis of one year of observations of the elevation at Point Atkinson, a nearby permanent tide gauge. The results are shown in Table 1, and the results of harmonically analysing the observed Point Atkinson elevations for the same period of time, (Figure 10), are shown in Table 2. Note that the Point Atkinson elevations did not have the low frequencies filtered out, so have a significant mean as well as MM and MSf constituents. Finally, the velocity record was reconstructed from the harmonic analysis, and is shown in Figure 11. If the surface current consisted only of tidal and shallow water constituents, Fig. 9 and Fig. 11 should be identical. That they are not indicates a more complicated situation.

The following observations about the harmonic analysis should be made.

1). We would like to know when the maximum discharge occurs, relative to the water levels in the Strait. Comparing the records of surface current with the sea levels at Point Atkinson, maximum current occurs about 0.7 hours before low water at Pt. Atkinson. Using the phases from tables 1 and 2, for the M2 tidal constituent, low water occurs at $\omega t = 340^\circ$ (180° after maximum). Maximum current occurs at $\omega t = 312^\circ$. The difference, 28° , corresponds to 1 hour. For the S2 constituent, low water occurs at $\omega t = 358^\circ$, and maximum current at $\omega t = 337^\circ$, for a difference of 0.7 hour.

2). I didn't consider the L2 constituent in the above

calculation of the time of maximum river flow, even though it is the second strongest diurnal constituent, because its amplitude and phase are subject to some doubt. The L2 probably comes from the interaction $2M2-N2$, a diurnal shallow water constituent identical in frequency to L2 (Godin, 1970). There is a significant change in the L2 amplitude over the 18.6 year nodal period. The harmonic analysis program corrected the apparent L2 amplitude using this factor, whereas it should probably have applied the correction for $2M2-N2$, a much smaller correction.

3) Although there was a seven-fold increase of river discharge while the meter was in operation, the mean current, Fig. 8, showed only a slight increase. One must conclude that the thickness of the outflowing layer increased over the 34 days the meter was installed.

4). There were two events during which the measured water velocity was abnormally low for a day or two (Fig. 7). One occurred about day 106, the other day 129. Two possible explanations suggest themselves; one is meteorological forcing, the other is the presence of debris caught in the current meter propellor. On day 105-106, there was a storm, with NW winds of up to 52 mph. This would certainly affect the surface flow, and probably the measurement of it. However, day 129 (May 8) was calm. By fortunate coincidence, Dr. P. Crean happened to be doing current profiles while tied up to the current meter bouy. The measured surface current, 50 cm/sec around noon and early afternoon, agrees with that measured by the moored meter. Thus, for this period, there appears no ready explanation in terms of meteorological forcing, or meter malfunction.

B. VERTICAL CURRENT AND SALINITY STRUCTURE

Weather and other work never seemed to permit a very good measurement of the profiles of current at the river mouth during the time the surface current meter was in place. Figure 12 indicates the salinity and current structure present at the current meter mooring, Fig. 6, on May 8, 1976 (Julian day 129), at 1330 PST. Positive speeds refer to an outflow, and since only speed was measured by the current meter (a propellor-type General Oceanics model 2031, rigidly attached to a lead "fish" with large orienting fins and vanes), the zero crossing at 5 meters is only inferred from the minimum in speed at that depth.

Figure 13 indicates the evolution of the salinity structure over 10 hours at Sand Heads on January 21, 1975. The dashed line in the inset diagram indicates, as a function of time, the fraction of fresh water in the water column, considering pure salt water to have the salinity of the deepest water in each cast. Like the surface current, the fraction of fresh water reaches a maximum shortly before (about 2 hours before) low water.

2. SALINITY AND DENSITY STRUCTURE OF THE PLUME

The salinity information obtained in this research is in general agreement with that reported by Waldichuk (1957) and de Lange Boom (1976). It was however obtained with a continuously recording CSTD as opposed to discrete bottle casts. As will be apparent from the profiles in this section, the density structure very closely follows the salinity structure, the temperature structure having a relatively minor effect on the

density in the upper layer.

April 6, 1976

This is the first day the current meter was in position. The Fraser discharge at Hope was $1100 \text{ m}^3/\text{sec}$, and winds were light. Figure 14 indicates the positions of stations, labelled by letters. Figure 15 is a plot of salinity contours along the line h-r. The tidal curve (inset, Fig. 14), shows that these stations were done on a rising tide after a large fall. It is interesting to note that we passed a very weak colour front (slight colour change in the water) in the vicinity of station k, station k being on the fresh or eastern side of the front. Figures 16, 17, and 18 show the S, T, sigma-T profiles for stations j, k, l. There is a slight indication of fresher water at the surface at station k, Fig. 17, and a definite freshening of the surface layer at station l, Fig. 18. This surface layer becomes thicker and fresher as one proceeds from station l towards the river mouth at Sand Heads. In all three salinity curves, Figs. 16, 17, and 18, the pycnocline is found at about $S=25 \text{ ‰}$. We should also notice that as one proceeds outward from Sand Heads, the isopycnals gradually rise to the surface.

April 15, 1976

This series of CSTD's was taken along a rather complicated path, Fig. 19. The line g-h-i-j-k-l-m-n represents the boundary of a colour front. The lines f-g and n-o-p-q represent paths through the plume. Stations g, j, l, and m are on the plume side of the front, and stations h, i, k, and n are on the salt water side of the front. The salinity along line e-f-g-j-l-m is plotted in Figure 20, along with a continuation along m-o-p-q.

We note that these profiles were done on a rising tide, and that there had been a 10 hour period of strong northwest winds prior to the measurements. One notes that the profiles along the front (g,j,l,m) are fairly similar, and that comparing them to those along line m-o-p-q-r, the plume is considerably fresher and thicker in the inner regions than around the edges.

Figures 21a and 21b illustrate the salinity profiles at stations k and l respectively, k being outside the plume, and l being adjacent to k (about 50 m away), but on the plume side of the front. We note that for the profile in the plume, Fig. 21b, there appears to be a three layered structure to the profile - a surface brackish layer about 0.7 meters thick, lying on top of a layer of intermediate salinity about 2.5 meter thick, lying on top of the almost homogeneous lower water.

April 28, 1976

Referring to Fig. 22 for position information, Figure 23 shows a salinity section taken from a front at station g back toward Sand Heads, along a line g-h. It is interesting to note how nearly horizontal the isohalines are, and how the salinity varies continuously in the vertical through the plume.

June 4, 1976

The profile of salinity along line o-p-q-t-s (Fig 24) is shown in fig. 25a. The winds were light and the profiles were done about an hour after low water, at which time the river flow is quite strong. The daily discharge at Hope was $6,200 \text{ m}^3/\text{sec}$, a fairly high value. We see that near Sand Heads (station t, located 0.5 nautical miles from Sand Heads into the Strait), the water is almost entirely fresh and at station g, located 1

nautical mile from Sand Heads, the salinity varies from near zero at the surface to 27 ‰ at 7 meters.

Three possibilities suggest themselves as causes for the rise of isohalines as one proceeds downstream. One is that there is extensive lateral spreading of the flow near the river mouth. However, the drogue tracks of Cordes (1977) suggest that there is very little lateral spread of flow at times of high discharge. A second reason would be that there is extensive mixing at the river mouth. While doing the profiles at the river mouth on June 4 the water surface indicated considerable mixing activity- large diameter upwelling regions, and considerable patchiness in colour. The third possible reason is that the salt wedge (Hodgins, 1974) has been flushed out, and we are seeing the toe of the wedge outside the river mouth. However, the flushing out of the wedge is intimately connected with mixing, so the second and third reasons mentioned above are related.

In order to draw more detailed isopycnals near the river mouth, we did a series of CSTD casts while drifting out from Sand Heads, as shown in Fig 25b. Note that the horizontal scale is expanded in Fig. 25b. Station g of Fig. 25a is at the same location as station x of Fig. 25b. Stations x and t are separated by 0.5 nautical miles, or about 1 km. The isopycnals in Fig. 25b all rise uniformly as one proceeds outward.

July 3, 1976

Referring to Figure 26 for geographical locations, figure 27a shows a plot of salinity along line a-b-c-d-j-l, and figure 27b is a plot of salinity along s-q-m-o-p. July 1975 was a time of high runoff, (6,800 m³/sec on July 1), and one observes a

considerable amount of fresh water in these profiles. It is interesting to observe the changes in the actual profiles as one proceeds downstream. Figure 28, 29, and 30 show three of the profiles used to draw Fig. 27a (stations a, c, and j). Going from station a to station c, the upper layer does not thicken very much, but becomes approximately 5 ‰ saltier. Going from station c to station j, the upper layer almost entirely disappears, and becomes almost as salty as the lower layer. This erosion of the upper layer shows up in the salinity sections Fig. 27a, and 27b. As on April 6 1976, Fig. 15, as one proceeds away from the river mouth, one observes the fresh water layer getting thinner. More important, perhaps, one notices that the surface salinity increases, and generally all isopycnals rise toward the surface. This significant feature of the plume will play an important role in subsequent chapters.

3. FRONTS AND THE PLUME

A feature of the plume frequently commented upon is the sharp colour front, usually found on the northern boundary of the plume. Because of its possible dynamical significance, some effort was made to understand the nature of this front.

On July 2, 1975, a strong colour front was found by aerial survey, and Figure 31 indicates the main features of the plume at about 0900 PST. Figures 32 and 33 show profiles of S, T, and sigma-T on either side of this front, close to Porlier Pass. The plume appears to be a layer of relatively fresh water about 1 meter thick advancing onto the stratified ambient water. Along the front there is a very strong convergence as the rapidly

moving silty water approaches the clear, dark blue salty water. Consequently, the front is a very good collector of debris of varying size, ranging from air bubbles and foam to large logs. There is also considerable lateral shear at these fronts, and large scale eddies capable of turning the 8 meter Brisk in a complete circle in less than 5 minutes.

The apparently strong vertical circulation at the front suggested using dye as a tracer. We tried to obtain quantitative results using a fluorimeter, but were unsuccessful. However, on July 3, 1975 (Fig. 26) we were able to set up a very interesting experiment at stations q and r. A rather intense front (in terms of vertical circulation , though not in terms of colour) was found at stations q and r, heading south. Red rhodamine dye was released on the water surface, about 100 m upstream of the front. This dye advanced along the surface to the front, and then disappeared by downwelling. There was no evidence of it recirculating up into the surface waters, as it completely vanished at the front. However, when the CSV Richardson, of 2 meter draft, was manoeuvring about 100 meters upstream of the front, dye was stirred up to the surface by the ship's screw, indicating the dye was being left behind by the front.

Figures 34 and 35 show two sets of profiles for July 4, 1975, taken in about the same location as those of Figs. 32 and 33. They again represent conditions on either side of a colour front, Fig. 34 representing conditions on the fresher, siltier side of the front. There was a fairly strong Northwest wind (20 mph) blowing July 4, and we see that one result is to

homogenise the upper 2 to 3 meters on either side of the front. Interestingly, there was still a quite strong colour contrast across the front, in spite of wind mixing.

Figure 36 is an attempt to depict the evolution of a front in the winter, when, because of low river flow, the front does not extend over as large a region as during the summer. The front was readily identified, despite the low discharge of $1100 \text{ m}^3/\text{sec}$, because of a good colour contrast and a large amount of debris along it. We travelled along the front as it spread outward, obtaining the ship's position and hence the front position by radar, and the approximate orientation of the front by compass. The curves of Fig. 36, indicating successive assumed positions of the front, were drawn using the numbered points where position and orientation of the front were known. The tidal currents indicated in Fig. 36 were roughly inferred from point Atkinson elevations. One sees the front, initially inclined toward the south, gradually curving outward and northward as the river flow builds up and the tidal currents turn from ebb to flood.

4. CURRENTS IN THE PLUME

A predominant feature of currents in the plume is their very strong vertical shear. One method of determining the current structure is by use of Lagrangian trackers, or drogues. Drogues of three depths were used : a surface drogue (S), with drag element about 0.5 m in depth ; a medium drogue, (M), with drag element suspended from 0 to 2 meters ; and a deep drogue, (D), with drag element suspended from 2 to 4 meters. Figure 37

shows the wind and tide for July 23, 1975, and the location of two drogue tracking experiments. In Fig. 38a are shown the paths of the above described drogues, released simultaneously at the front on an ebbing tide in region A, Fig. 37. The deep drogue travelled southward the fastest, and the shallow drogue stayed with the front. The drogues were picked up and re-installed in region B, considerably behind the front, on the following flood; their paths are shown in figure 38b. Now, the shallow drogue travels northward the fastest. Figure 39 is a salinity profile corresponding to the ebbing conditions, and one certainly notices that, as in velocity, there is a great change in salinity as one descends from 0 to 4 meters.

Figure 40 shows a relative speed profile obtained with an Ott propellor-type current meter, on the morning of July 23, 1975, in region A of figure 37. The profile was obtained from a very shallow draft (approx. 0.2 meter) boat tied to a drogue similar to the deep one described above. The zero crossing is only inferred from the observed minimum in the speed. One has considerable confidence in the relative surface speeds measured, because the boat had such a shallow draft that it probably did not interfere with the flow. The salinity structure at the time of the speed profile is that shown in figure 39.

5. SONIC CURRENT METER MEASUREMENTS

For two weeks, in July and September of 1976, we borrowed a sonic current meter from M. Miyake (then of UBC, now of OAS). This meter measures the two horizontal components of flow relative to the meter, and the magnetic heading of the meter,

with a sampling frequency of 1 hz. Current profiles were obtained from the Brisk in the following way. To eliminate the large wire angles which result when the boat drifts with the surface current and one is measuring the deep (5-10 meter) currents, the boat was restrained by a sea anchor (a conical drag element, suspended at about 8 meters). Consequently, the ship drift was intermediate between the surface and deep velocities, and the relative speeds were such that the wire angle was always less than 20° , and usually considerably less. Ship drift was monitored by radar, and added to the measured currents, giving currents relative to a fixed coordinate system. The analog output of the current meter was recorded on magnetic tape, electronically digitized, and vector averages were calculated over the 2 to 5 minute period the current meter was held at each depth. The measurements on July 13, 1976 and Sept. 17, 1976 are particularly interesting.

July 13, 1976

Figure 41 shows the drift path of the ship, from station b to station i inclusive. The Hope discharge on July 11 was $8,600 \text{ m}^3/\text{sec}$, a high value for July. A front heading westward passed the ship at about 1225 PST, and figure 42 shows a profile of salinity at 1304 PST, station g, after the front had passed, and on the freshwater side of the front. Figure 43 shows the water speed at various depths at station g. The vertical structure of salinity and water current are remarkably similar. Figure 44 shows the result of plotting the currents at successive 1 meter depths on a polar co-ordinate system, with the dots representing the tips of the current vectors. There is a strong westward flow

at the surface, and a relatively weak flow to the southwest in the deeper water.

September 17 1976

Figure 45 shows the ship drift on this day. There are two sets of observations presented, identical in format to those of July 13. Thus, figures 46, 47, and 48 refer to conditions at 0646 PST, station a, and figures 49, 50, and 51 refer to conditions at 1512 PST, station j. We note that over this 8.5 hour period, the surface salinity has increased markedly, the thickness of the upper layer decreased, and the strong velocity shear present in the morning has disappeared. Some of the decrease in thickness is due to horizontal spreading and advection, but some is due to mixing, as indicated by the increased surface salinity. All of these attenuations in plume properties (vertical shear, thickness, salinity difference) occurred in the absence of significant winds.

6. A SHORT SUMMARY OF THE OBSERVATIONS

The plume is a brackish layer of thickness ranging from less than 1 to 10 meters. This layer is freshest and thickest near Sand Heads, and becomes thinner and saltier as one proceeds away from Sand Heads. At the river mouth, the momentum of the river water is directed in the direction of the jetty, except at high water, when the river flow is shut off. As one proceeds outward, this river momentum is lost, and the plume acquires the velocity of the tidal streams. The vertical structure of the plume is quite complicated. The bottom part undergoes extensive mixing with the deeper water, while, near the river mouth at

least, the top part is fed with relatively unmixed river water. (Because of the velocity shear and vertical salinity gradient, the transport of fresh water is much greater in the upper part of the plume than the lower.) Because the river flow is tidally modulated, the plume is fed with pulses of fresh water at tidal frequencies. These bursts of fresh water advance onto, and incorporate themselves into, the existing plume. If, because of strong wind mixing, there is no distinct plume in the Strait, then a front forms between the new discharge of river water and the ambient Strait water, the front being characterized by a significant colour change across it, and a strong convergence along it. If silty water already exists in the Strait, a somewhat weaker front forms, still being characterized by a vertical circulation.

CHAPTER 3

A MODEL OF THE FRASER RIVER PLUME

The field data described in Chapter 2 may be combined with basic hydrodynamic principles to construct a theoretical model of the plume. Such a model will be successful if it can tell us about the horizontal circulation patterns around the river mouth, and the amount and distribution of salt water entrainment into the plume. The results of the model may also be useful in resolving questions bearing on the nature of the mixing of fresh and salt water over large parts of the Strait and in particular the mechanism by which fresh water leaves the Strait.

The above points that our model must deal with are of ultimate concern in studies of the Fraser River Plume. However, a model may also be useful if it only points up where there are gaps in our understanding of the physical system. When the model fails to describe reality, and the failure is not due to the inadequacy of the mathematics, then we know that we must improve the model, usually by extension and generalization of the physics, inspired by field measurements. The numerical solutions of our model described below agree with field measurements to within an order of magnitude, and usually within a factor of 2; and indicate what should be measured in future field trips.

In this chapter, I will discuss the physical concepts that are to be incorporated in the model, and develop the mathematical equations that incorporate these physical principles. In Chapter 4 are presented some simple solutions of subsets of the full equations; in Chapter 5 the solution of the model equations by numerical means is discussed.

A CONTROL VOLUME DESCRIPTION OF THE PLUME

In order to initiate discussion of the plume, consider an idealized Strait of Georgia, with mean contours of surface salinity schematized in the plan view of Figure 52. Figure 53 shows a salinity section along line AA' of Figure 52, and the associated salinity profiles at the indicated locations. The usual procedure in developing a 2-layer model of a strongly stratified fluid is to consider the interface between the two layers to be associated with the pycnocline (Long, 1975b), or with a particular density interface (Charney, 1955). In order to be specific, I chose to define the base of the upper layer in terms of an isohaline surface which (as seen in the previous chapter) is equivalent to using a density surface. The explicit specification of an upper layer depth is important for two reasons. One is that the degree of turbulent interaction between the two layers depends on where the interface is chosen. The other reason is that one has to know how to compare computed and observed quantities, such as layer depth, and fluxes of salt, mass, and momentum. In the case of the Fraser River plume, the isopycnal chosen corresponds approximately to the base of the pycnocline, so in a sense this model is compatible with both definitions of upper layer thickness.

Choosing the $S=25\text{‰}$ contour as the plume lower boundary, let us first treat the plume in the control volume approach (Figure 54). The control volume is bounded by the $S=25\text{‰}$ contour, and receives fresh water from the river at a tidally modulated rate. It also receives salt water from below, as indicated by the increase of salinity downstream. Averaged over

a few tidal cycles, the volume of the control volume is constant, so these two inflows must be matched by an outflow. This outflow presumably occurs mainly at the downstream extremity of the plume. As one follows a streamline near the outer edge of the plume, the salinity along this streamline increases, by means of small scale mixing, until it exceeds our agreed upon limit for the boundary of the plume, and passes out of the control volume. The inflow of salt water into the plume has been called entrainment (Turner, 1974), and it appears that a name has to be invented for flow out of the control volume. Perhaps depletion is the most evocative term for this phenomenon. Thus, when the river flow is strong and there is vigorous entrainment, the control volume expands somewhat, and spreads outward. The outer edges are then eroded by gentler mixing, expressed mathematically as the sum of entrainment and relatively stronger depletion. (Both terms are needed, entrainment to increase the salinity of the layer, and depletion to balance the volume added by entrainment.)

Considering now the momentum balance, the water in the control volume, as well as the boundary of that volume, moves back and forth in the Strait for a variety of reasons. These reasons fall into 3 categories:

- 1) bodily fluxes of momentum - the river momentum, the momentum of the entrained water, and the momentum removed by depletion, i.e., when the water leaves the control volume, it takes its momentum with it;
- 2) contact forces - the effects of wind stress are omitted in the model developed here, so the only contact force is the stress at

the interface between two countermoving fluids, friction and form drag;

3) body forces - the barotropic tide, the bouyancy tendency of the plume to spread into a thinner layer, and the Coriolis force.

Omitting the wind reduces the complexity somewhat, and there are many real cases where it is unimportant. Wind effects can be added later as a further refinement once the windless model has been sufficiently developed.

DIFFERENTIAL EQUATIONS DESCRIBING THE PLUME

This section deals with the derivation of the vertically integrated equations describing the motion of a thin layer of lighter water floating on and interacting with a very deep layer of denser water. Two sets of equations are derived - one for the entire water column, which reduce to the barotropic tidal equations in the absence of an upper layer, and a second set, which describe the motion of the upper layer.

Consider an upper layer, Figure 55, with density $\rho = \rho(z)$, velocity $u = u(z)$, salinity $s = s(z)$, and thickness $h = \eta - \xi$, where η and ξ are the upper and lower interfaces respectively. The z axis is positive upward, the mean value of η is 0, and the mean value of ξ is $-h$, the negative of the layer thickness. The lower layer has uniform properties ρ_0 , u_0 , s_0 . The equations will be derived for only one horizontal dimension; they are quite simply generalized to include the second horizontal dimension.

1. CONTINUITY EQUATION

For either layer, the continuity equation is

$$\frac{\partial u}{\partial x} + \frac{\partial w}{\partial z} = 0.$$

3.1.

Integrating equation 3.1 over the upper layer depth, we have

$$\int_{\xi}^{\eta} \frac{\partial u}{\partial x} dz + w_{z=\eta} - w_{z=\xi} = 0.$$

3.2a.

Expanding the integral, we get

$$\frac{\partial}{\partial x} \int_{\xi}^{\eta} u dz - u_{\eta} \frac{\partial \eta}{\partial x} + u_{\xi} \frac{\partial \xi}{\partial x} + w_{\eta} - w_{\xi} = 0.$$

3.2b.

We can apply the kinematic boundary condition at the upper surface $z=\eta$

$$\frac{D}{Dt} (\eta - z)_{z=\eta} = \frac{\partial \eta}{\partial t} + u_{\eta} \frac{\partial \eta}{\partial x} - w_{\eta} = 0,$$

3.3.

to simplify equation 3.2b. At $z=\xi$, $\frac{D}{Dt} (z - \xi)$ describes the motion of fluid relative to the interface $z=\xi$. As discussed earlier in this chapter, fluid crosses the interface, entering or leaving the plume, by means of entrainment and depletion. It is convenient to represent the net effect of these two competing processes as the sum of the two effects expressed separately. Writing entrainment as w_p , and depletion as w_n , we have

$$\frac{D}{Dt} (z - \xi) = w_p - w_n.$$

3.4.

Thus,

$$w_{z=\xi} = \frac{\partial \xi}{\partial t} + u_{\xi} \frac{\partial \xi}{\partial x} + w_p - w_n,$$

3.5.

and the continuity equation for the upper layer becomes:

$$\frac{\partial}{\partial x} \int_{\xi}^{\eta} u \, dz + \frac{\partial \eta}{\partial t} - \frac{\partial \xi}{\partial t} = w_p - w_n. \quad 3.6.$$

The continuity equation for the entire water column is

$$\frac{\partial}{\partial x} \int_{\xi}^{\eta} u \, dz + \frac{\partial}{\partial x} \int_{-D}^{\xi} u_0 \, dz + \frac{\partial \eta}{\partial t} = 0. \quad 3.7.$$

Adding and subtracting $\frac{\partial}{\partial x} \int_{\xi}^{\eta} u_0 \, dz$, we have

$$\frac{\partial \eta}{\partial t} + \frac{\partial}{\partial x} \int_{-D}^{\eta} u_0 \, dz = - \frac{\partial}{\partial x} \int_{\xi}^{\eta} (u - u_0) \, dz. \quad 3.8.$$

The left hand side of equation 3.8 is the continuity equation in a fluid with depth independent velocity, and the right hand side is a correction due to the presence of the river flow in the upper layer.

2. SALT EQUATION

Assuming molecular diffusion is negligible compared to turbulent effects the salt conservation equation is given by:

$$\frac{\partial s}{\partial t} + \frac{\partial}{\partial x} \langle u s \rangle + \frac{\partial}{\partial z} \langle w s \rangle = 0, \quad 3.9.$$

where $\langle u s \rangle$ includes the mean and turbulent fluxes in the horizontal direction, and $\langle w s \rangle$ denotes them in the vertical.

Integrating equation 3.9 over the upper layer, we have,

$$\frac{\partial}{\partial t} \int_{\xi}^{\eta} s \, dz - s_{\eta} \frac{\partial \eta}{\partial t} + s_{\xi} \frac{\partial \xi}{\partial t} + \frac{\partial}{\partial x} \int_{\xi}^{\eta} \langle u s \rangle \, dz$$

$$-\langle us \rangle_\eta \frac{\partial \eta}{\partial t} + \langle us \rangle_\xi \frac{\partial \xi}{\partial t} + \langle ws \rangle_\eta - \langle ws \rangle_\xi = 0.$$

3.10.

Assuming that $\langle us \rangle_\eta = (us)_\eta$, (where for notational simplicity quantities without angle brackets denote mean flow properties), that is, neglecting horizontal turbulent fluxes, and assuming that $\langle ws \rangle_\eta = (ws)_\eta$, we can use the kinematic boundary condition 3.3 to simplify 3.10. At the interface $z = \xi$, the quantity $\langle ws \rangle_\xi$ has two components. One is associated with motion of the interface, denoted by $w_{int} s_\xi$. The other is due to the flux of salt relative to the interface. The flux associated with entrainment we write $w_p s_o$, where s_o is the salinity of the lower layer; and the flux associated with depletion we write $w_n \bar{s}$, where \bar{s} is a salinity appropriate to the negative flux of salt due to depletion. Thus

$$\langle ws \rangle_\xi = w_{int} s_\xi + w_p s_o - w_n \bar{s},$$

3.11a

or

$$\langle ws \rangle_\xi = \left(\frac{\partial \xi}{\partial t} + u_\xi \frac{\partial \xi}{\partial x} \right) s_\xi + w_p s_o - w_n \bar{s}.$$

3.11b.

Using equation 3.11b and the kinematic boundary condition 3.3, 3.10 simplifies to :

$$\frac{\partial}{\partial t} \int_\xi^\eta s dz + \frac{\partial}{\partial x} \int_\xi^\eta us dz = s_o w_p - \bar{s} w_n.$$

3.12.

The salt equation is usually not included in barotropic tidal calculations, as the salinity is assumed uniform, so it is not written out here. However, it is interesting to note the salt equation for the lower layer alone takes the form

$$\frac{\partial}{\partial t} \int_{-D}^{\xi} s dz + \frac{\partial}{\partial x} \int_{-D}^{\xi} s u dz = -s_o w_p + \bar{s} w_n . \quad 3.13.$$

Thus, as one expects, the roles of entrainment and depletion are reversed for the lower layer, and the plume acts as both a source and a sink of salt (in different places of course) for the lower layer.

3. THE HYDROSTATIC EQUATION

It is assumed that the balance of vertical forces is adequately described by the hydrostatic equation,

$$\frac{\partial P}{\partial z} = -\rho g . \quad 3.14.$$

At a depth z in the upper layer,

$$p = - \int_{z'=x}^z \rho g dz' = \int_z^x \rho g dz' . \quad 3.15a.$$

At a depth z in the lower layer,

$$p = \int_x^x \rho g dz' + \int_z^{\xi} \rho_o g dz' . \quad 3.15b.$$

We should recall, from the salinity and sigma-T profiles presented in Chapter 2, that the density structure is controlled almost entirely by the salinity structure, and in fact,

$$\sigma_T = k s \quad 3.16.$$

is a very good approximation, with $k=0.8$. This equation of state was chosen for computational simplicity; comparison with

salinity and sigma-T traces shows it to be only close, not exact. The agreement is within 5% for winter conditions, but during summer, when the water is considerably warmer and not as isothermal, a reasonable value of k would vary from 0.55 near the surface to 0.6 near the bottom of the plume.

4. HORIZONTAL MOMENTUM EQUATION

The horizontal momentum equation, ignoring molecular diffusion, is :

$$\frac{\partial u}{\partial t} + \frac{\partial}{\partial x} \langle uu \rangle + \frac{\partial}{\partial z} \langle uw \rangle + \frac{1}{\rho} \frac{\partial p}{\partial x} - \frac{1}{\rho} \frac{\partial \tau_x}{\partial z} = 0, \quad 3.17.$$

where τ_x is the stress in the x-direction and p is the pressure.

Integrating over the upper layer, ignoring horizontal turbulent fluxes, and using the kinematic boundary condition 3.3, the first three terms become:

$$\frac{\partial}{\partial t} \int_{\xi}^{\eta} u dz + \frac{\partial}{\partial x} \int_{\xi}^{\eta} u^2 dz - w_p u_o + w_n \bar{u},$$

where u_o and \bar{u} have similar meaning to s_o and \bar{s} . Ignoring wind stress, the integral of the stress term becomes

$$-\int_{\xi}^{\eta} \frac{\partial \tau_x}{\partial z} dz = + \tau_x \Big|_{z=\xi}$$

This is the stress at the interface due to frictional forces and form drag in addition to $w_p u_o - w_n \bar{u}$ which is a momentum flux associated with mass transfer across the interface.

The remaining term to evaluate is the pressure gradient term,

$$\int_{\xi}^{\eta} \frac{1}{\rho} \frac{\partial}{\partial x} \left[\int_{z'=z}^{\eta} \rho(z') g dz' \right] dz .$$

Because the analysis becomes very complicated otherwise, we will assume that the density in the upper layer is vertically homogeneous, a form of the Boussinesq approximation. The pressure force in the upper layer is then:

$$\frac{g}{\rho} \left[\frac{1}{2} (\eta - \xi)^2 \frac{\partial \rho}{\partial x} + \rho (\eta - \xi) \frac{\partial \eta}{\partial x} \right] .$$

Thus, the upper layer momentum equation is :

$$\frac{\partial}{\partial t} \int_{\xi}^{\eta} u dz + \frac{\partial}{\partial x} \int_{\xi}^{\eta} u^2 dz + \frac{\tau_{\xi}}{\rho} - w_p u_0 + w_n \bar{u}$$

$$+ \frac{g}{\rho} \left[\frac{1}{2} (\eta - \xi)^2 \frac{\partial \rho}{\partial x} + \rho (\eta - \xi) \frac{\partial \eta}{\partial x} \right] = 0 .$$

3.18.

Note that for the upper layer we have 3 equations, 3.6, 3.12, and 3.18, and 4 independent variables, u , s , η , and ξ . In order to solve the upper layer equations, we require a relation between η and ξ , which we obtain from the equations for the barotropic tide. The simplest way to obtain the relation is by observing that in the deep water of the Strait, the horizontal pressure gradients must be those calculated in a barotropic tidal model, since the flows so calculated agree with observations (Crean, 1976). Thus,

$$\frac{\partial p}{\partial x} \Big|_{\text{lower layer}} = \rho_0 g \zeta_{\tau_x}$$

where ζ_{τ_x} is the surface slope obtained from a barotropic model.

Then using equation 3.15b for the pressure at a point in the

lower layer,

$$\frac{\partial}{\partial x} (\rho(\eta - \xi)) + \rho \xi_x = \rho_0 \xi_{\tau x} \quad 3.19a.$$

Defining $\delta = \rho_0 - \rho$, the above becomes, after rearranging,

$$\rho_0 \eta_x = [\delta(\eta - \xi)]_x + \rho \xi_{\tau x} \quad 3.20.$$

Equation 3.20 is the fourth equation required to complete the problem. The pressure gradient term in the integrated upper layer equation 3.18. becomes then (ignoring variations in ρ when not differentiated),

$$\frac{g}{\rho} \frac{\partial}{\partial x} \left(\frac{1}{2} (\eta - \xi)^2 \delta \right) + g (\eta - \xi) \xi_{\tau x} \quad 3.21.$$

Now to derive the momentum equation for the entire water column. All terms except the pressure gradient term are quite straightforward. The pressure term is:

$$\begin{aligned} & \int_{\xi}^{\eta} \frac{1}{\rho} \frac{\partial P}{\partial x} dz + \int_{-D}^{\xi} \frac{1}{\rho_0} \frac{\partial P}{\partial x} dz = \\ & \frac{g}{\rho} \left[\frac{\rho_x}{2} (\eta - \xi)^2 + \rho \eta_x (\eta - \xi) \right] \\ & + \frac{g}{\rho_0} \left[\rho_x (\eta - \xi) + \rho (\eta - \xi)_x + \rho_0 \xi_x \right] (\xi + D). \end{aligned} \quad 3.22a$$

Substituting $\rho = \rho_0 - \delta$, and doing a bit of rearranging, we get the above expression to equal:

$$\begin{aligned} & g(D + \eta) \eta_x + g \frac{(D + \eta)}{\rho_0} (\delta(\eta - \xi))_x \\ & + \frac{1}{2} \frac{g}{\rho_0} [\delta(\eta - \xi)^2]_x - g \frac{\delta}{\rho_0} \eta_x (\eta - \xi). \end{aligned} \quad 3.22b.$$

Note that if we consider the terms proportional to $D + \eta$, and require them to equal $\rho_0 g \xi_{\tau_x}$, we get

$$\eta_x - \frac{1}{\rho_0} (\delta(\eta - \xi))_x = \xi_{\tau_x}$$

as in equation 3.20.

The momentum equation for the entire water column is then

$$\begin{aligned} \frac{\partial}{\partial t} \int_{-D}^{\eta} u_0 dz + \frac{\partial}{\partial x} \int_{-D}^{\eta} u_0^2 dz + \frac{\tau_{bottom}}{\rho_0} + g(D + \eta) \eta_x = \\ g \frac{(D + \eta)}{\rho_0} (\delta(\eta - \xi))_x + \frac{g \delta}{\rho_0} (\eta - \xi) \eta_x \\ - \frac{1}{2} \frac{g}{\rho_0} (\delta(\eta - \xi)^2)_x - \frac{\partial}{\partial t} \int_{\xi}^{\eta} (u - u_0) dz - \frac{\partial}{\partial x} \int_{\xi}^{\eta} (u^2 - u_0^2) dz. \end{aligned}$$

3.23.

The left hand side represents the momentum terms in the barotropic tidal equation. The first term on the right hand side represents the correction made to $g(D + \eta) \eta_x$ because it contains the pressure gradient required to maintain the river flow. The pressure gradient associated with the river flow is $(g/\rho_0)(\delta(\eta - \xi))_x$, and this is subtracted from $g \eta_x$, in equation 3.23, to give $g \xi_{\tau_x}$, the gradient calculated in a model with no river effects. The second term on the right represents a correction to the barotropic pressure because the upper layer is somewhat lighter. The other terms, proportional to $\eta - \xi$ have little effect on the barotropic motion, whose driving terms, the left hand side of 3.23, are proportional to D . Thus the presence of the river flow has negligible effects on a barotropic model, and the surface slopes and velocities obtained from that model

may be used as forcing for the upper layer model.

To summarize, we will rewrite the equations for the upper layer in terms of a variable z which is zero at the bottom of the upper layer and increases upwards, and also will include the second horizontal dimension, and the Coriolis force. Note that the thickness of the upper layer is $h = \eta - \xi$.

CONTINUITY

$$\frac{\partial h}{\partial t} + \frac{\partial}{\partial x} \int_0^h u dz + \frac{\partial}{\partial y} \int_0^h v dz = w_p - w_n.$$

3.24.

SALT

$$\frac{\partial}{\partial t} \int_0^h s dz + \frac{\partial}{\partial x} \int_0^h u s dz + \frac{\partial}{\partial y} \int_0^h v s dz =$$

$$s_o w_p - \bar{s} w_n.$$

3.25.

X-DIRECTED MOMENTUM

$$\frac{\partial}{\partial t} \int_0^h u dz + \frac{\partial}{\partial x} \int_0^h u^2 dz + \frac{\partial}{\partial y} \int_0^h u v dz - f \int_0^h v dz + \frac{1}{\rho_o} \tau_{int,x}$$

$$+ \frac{1}{\rho_o} \frac{\partial}{\partial x} \left(\frac{1}{2} g \delta h^2 \right) = w_p \bar{u}_o - w_n \bar{u} - g h \mathcal{E}_{Tx}.$$

3.26

Y-DIRECTED MOMENTUM

$$\frac{\partial}{\partial t} \int_0^h v dz + \frac{\partial}{\partial x} \int_0^h u v dz + \frac{\partial}{\partial y} \int_0^h v^2 dz + f \int_0^h u dz$$

$$+ \frac{\tau_{int,y}}{\rho_o} + \frac{1}{\rho_o} \frac{\partial}{\partial y} \left(\frac{1}{2} g \delta h^2 \right) = w_p \bar{v}_o - w_n \bar{v} - g h \mathcal{E}_{Ty}$$

3.27.

There are several things which have yet to be specified in this model.

1. We have to provide the profiles of u , v , and s , so that, for example, we can relate $\int u^2 dz$ to $\int u dz$.

2. $w_p, w_n, \bar{u}, \bar{s}$, and τ_{int} must be specified in terms of flow properties such as the density and velocity differences between the upper and lower layer, and the thickness of the upper layer.

3. ξ_{rx}, ξ_{ry}, u_o , and v_o must be obtained from a barotropic tidal model (Crean, 1977), which is the solution of equations of the type 3.8, 3.23, with the right hand sides set to zero.

Items 1 and 2 above are related to properties of the flow, being related to the turbulent structure present, and can only be parameterized in terms of the large scale properties of the flow. Item 3 can be considered as external driving of the flow. However, the extent of the forcing produced by u_o and v_o depends on the type of turbulent interactions specified in items 1 and 2.

Having gone through considerable algebra to get to the above equations, we should check that they agree with the physics we want to model. First, consider the continuity and salt equations. As in the control volume approach described earlier, the quantity of water in the plume changes, $\partial h / \partial t$, because of horizontal divergences, in particular the river flow, and by fluxes relative to the boundary, w_p and w_n . Similarly, the salt content can change by internal rearrangement, or by influxes of salt, $w_p s_o$, and effluxes, $w_n \bar{s}$.

In the momentum equation, we see that the change in

momentum of a column of fluid is approximately given by:

$$\frac{D}{Dt} \int u dz =$$

buoyant spreading, $\partial/\partial x (1/2 g \delta h^2)$

+ frictional interaction, τ_{int}

+ gain or loss of water and its associated momentum, $w_p u_0 - w_n \bar{u}$,

+ forcing by the barotropic tidal slopes, $g \nabla \tau_x$.

It is difficult to estimate the relative importance of these terms, since the plume is spatially and temporally variable. However, Table 3 presents very coarse estimates of the order of magnitude of the terms in the momentum equation. The first part of the table lists the scaling parameters, and the second part lists the sizes of the various terms in the momentum equation, for the region near the river mouth, and for the far field. For the salinity and continuity equations, we notice that the ratio of the advective terms to the source terms is $uh/(wL)$, which is also given in Table 3. w_p is estimated from the numerical model of Chapter 5, where w_p was calculated according to the formula $w_p = 0.0001u$.

Except for the action of winds and possibly horizontal eddy viscosity and diffusivity, the equations derived in this chapter appear to have all the necessary terms to describe the plume.

BOUNDARY CONDITIONS

In solving any differential equation system, one has to specify the appropriate boundary conditions. The actual boundary conditions used will be discussed in chapter 5, but I would like to discuss here the theoretical boundary condition requirements. Consider a simplification of the above equations, in x-t space

only. (we define a new variable, $\Sigma = s_0 - s$, the salinity defect.)

$$\frac{\partial h}{\partial t} + \frac{\partial}{\partial x} (u h) = 0.$$

$$\frac{\partial}{\partial t} (\Sigma h) + \frac{\partial}{\partial x} (\Sigma u h) = 0.$$

$$\frac{\partial}{\partial t} (u h) + \frac{\partial}{\partial x} (u^2 h) + \frac{\partial}{\partial x} \left(\frac{1}{2} g' \Sigma h^2 \right) = 0.$$

These equations can be thought of as homogeneous equations the behaviour of whose solutions dictate the behaviour of the equations with forcing and dissipation, as long as the forcing and dissipation do not contain derivatives of the same or higher order. Writing $g' = g k$, these may be put in matrix form

$$\begin{pmatrix} h \\ \Sigma \\ u \end{pmatrix}_t + \begin{pmatrix} u & 0 & h \\ 0 & u & 0 \\ g' \Sigma & \frac{1}{2} g' h & 0 \end{pmatrix} \begin{pmatrix} h \\ \Sigma \\ u \end{pmatrix}_x = 0,$$

or $H_t + A H_x = 0$. The eigenvalues λ , and left eigenvectors, l_i , of A are:

$$\lambda = u, \quad l = (0, 1, 0).$$

$$\lambda = u \pm \sqrt{g' h \Sigma}, \quad l = \left(\frac{g' \Sigma}{\sqrt{g' h \Sigma}}, \frac{\frac{1}{2} g' h}{\sqrt{g' h \Sigma}}, 1 \right).$$

Multiplying the matrix form of the differential equations by l_i , we get:

$$l_i H_{i,t} + l_i A_{ij} H_{j,x} = 0.$$

Since $l_i A_{ij} = l_i \lambda \delta_{ij}$, there results

$$l_i H_{i,t} + \lambda l_i H_{i,x} = 0.$$

Thus, in the direction $dx/dt = \lambda$, $l_i \frac{d}{dt} H_i = 0$, the characteristic form of the differential equations. Explicitly,

the characteristic equations are :

$$\left(\frac{\partial}{\partial t} + u \frac{\partial}{\partial x} \right) \Sigma = 0 = \left(\frac{\partial}{\partial t} + u \frac{\partial}{\partial x} \right) s.$$

$$\left(\frac{\partial}{\partial t} + (u \pm c) \frac{\partial}{\partial x} \right) u \pm \frac{1}{\sqrt{h}} \left(\frac{\partial}{\partial t} + (u \pm c) \frac{\partial}{\partial x} \right) c \sqrt{h} = 0,$$

where $c = \sqrt{g' \epsilon h}$.

The reason for putting the equations in characteristic form is that the required boundary conditions at open boundaries become more obvious. The basic requirement is that one should prescribe as many boundary conditions as there are characteristics pointing into the region under consideration. Thus, one must prescribe salinity on an open boundary if its characteristic is directed into the region. Since the characteristic speed is u , the flow velocity, one must prescribe s on an inflow, and must devise a way for it to be determined at an outflow boundary by flow conditions in the interior of the computational region.

If $|u|$ is greater than c , and u is an inflow, then both $u+c$ and $u-c$ point into the computational region, and two independent pieces of information about u and c , in addition to s discussed above, must be specified. If $|u|$ is less than c , then one of $u+c$, $u-c$ points into the region, and one points out, so either u or c , or a relation between them, must be specified. If $u=c$, a very complicated situation arises, in which a boundary in $x-t$ space becomes a characteristic. This is a situation which becomes very tricky in problems with a time-dependent boundary condition, and requires recourse to further aspects of the physical system.

CHAPTER 4

AIDS TO INTUITION ABOUT THE PLUME

Before presenting the numerical model in the next chapter, it is worthwhile to look at some simple models of plume dynamics. These models do not include all terms in the equations of Chapter 3, so can't be expected to describe the plume adequately, but they are useful in clarifying various aspects of the plume's behaviour.

The first sub-model, the compressible flow analogy, shows that near the river mouth, the predictions of a frictionless model are at variance with observations, leading one to conclude that friction and entrainment are important features of the plume near the river mouth. The second model, a time-independent model of surfacing isopycnals, illustrates the roles of depletion and entrainment in causing the isopycnals to rise as one proceeds downstream in the plume. The third model, conditions at a strong frontal discontinuity, discusses the motion of the strongly contrasted colour fronts frequently found in the Strait, and suggests that these fronts induce considerable vertical circulation. The fourth model, a kinematic wave approach to frontal motion, is intended to illustrate, in a very simple manner, the way in which fronts arise in a time-dependent situation, due to the tidally varying river flow. The fifth model, mixing and fluxes across an interface, shows how an upper layer model, as developed in this thesis, is compatible with a diffusive (eddy diffusivity) model of the vertical salinity distribution. The sixth section, analogy with turbulent jets, is an attempt to motivate the use of entrainment and

depletion by showing how they arise in a more accessible system, a turbulent plane jet.

1. COMPRESSIBLE FLOW ANALOGY

There is an exact analogy between the frictionless flow of a compressible fluid and the frictionless flow of a liquid with a free surface. The method of solution of the equations derived below was developed for compressible flow (e.g. Shapiro and Edelman, 1947), and later adopted for use in hydraulic engineering (Ippen, 1951). Using this method, one is able to predict the velocity and thickness of a fluid discharged from a channel into an unbounded region. The solution for water flowing over a solid surface (as developed in Rouse et al, 1951) is identical to the solution for lighter fluid flowing over heavier fluid (as required in a plume theory), if g , the acceleration of gravity, is replaced by $g' = g \Delta \rho / \rho$, as shown in Chapter 3. This then is a buoyancy spreading model, representing a balance between the convective accelerations and the spreading tendency of the pressure gradient.

The equations of continuity and momentum conservation for a steady-state, frictionless plume are:

$$(hu)_x + (hv)_y = 0. \quad 4.1$$

$$u u_x + v u_y + g' h_x = 0. \quad 4.2$$

$$u v_x + v v_y + g' h_y = 0. \quad 4.3.$$

Fundamental to this method is the requirement that the vorticity of the flow be zero,

$$u_y - v_x = 0. \quad 4.4.$$

This approximation is assumed to be valid in a region around the river mouth.

The method of solution is as follows. From 4.2, 4.3, and 4.4 one obtains the Bernoulli equation,

$$\frac{u^2}{2} + \frac{v^2}{2} + c^2 = \text{constant} \quad 4.5.$$

where $c^2 = g'h$.

The continuity equation may be put in the form

$$(u^2 - c^2) m du + (v^2 - c^2) dv = 0, \quad 4.6.$$

$$\text{where } m = \frac{uv \pm c \sqrt{u^2 + v^2 - c^2}}{u^2 - c^2} >$$

$$du = \left(\frac{\partial u}{\partial x} + m \frac{\partial u}{\partial y} \right) dx,$$

$$dv = \left(\frac{\partial v}{\partial x} + m \frac{\partial v}{\partial y} \right) dx.$$

Thus, in the direction $dy/dx = m$, du and dv satisfy the ordinary differential equation 4.6. Since there are two types of m , depending on the sign of the square root, there are two equations, in addition to the Bernoulli equation, from which to obtain u , v , and c^2 . However, all this depends on m being real, that is on $u^2 + v^2$ being greater than c^2 . Thus, this model applies to supercritical flow only. There is a fair amount of evidence (Wright and Coleman, 1971; Garvine, 1977) that the flow at a river mouth is internally critical or supercritical, i.e. that $(u^2 + v^2) > c^2$. Thus, one can use equation 4.6 to obtain a solution around the river mouth, as long as $u^2 + v^2$ remains greater than or equal to c^2 .

Figure 56a illustrates the orientation of the two characteristics, $C+$ and $C-$ (defined by $dy/dx = m_+$ or m_-), and a streamline, with respect to an x - y coordinate system.

Defining $u = q \cos \theta$, $v = q \sin \theta$, $c = q \sin \mu$, and $\chi_{\pm} = \theta \pm \mu$, (Fig. 56a) one can eventually manipulate equation 4.6 into the form

$$\Theta \pm P(\mu) = \text{constant} \quad 4.7.$$

on $dy/dx = m_{\pm} = \tan \chi_{\pm}$, and

$$P(\mu) = \sqrt{3} \tan^{-1} (\sqrt{3} \tan \mu) - \mu.$$

One interesting thing about the above solution is that it is possible to integrate analytically the differential equations along the characteristics.

The problem is set up as follows. An opening in a solid wall is assumed, through which water is flowing with $v=0$, $u=c$. One then fills up the computational region with the two families of characteristics, and uses tabulated values of $P(\mu)$ to obtain values of u and v at the intersection of characteristics. (Fig. 56b).

Rouse et al, (1951), worked out by hand the solution to this problem, with $F = u/c = 1, 2, 4$, (Fig 57). The results, for the values of F examined, are all quite similar - as one proceeds outward from the river mouth, the upper layer thins and spreads. Since the downstream thinning of the layer constitutes a pressure gradient, the flow accelerates. In contrast to this model we observe, (Cordes, 1977), that the flow outward from the river mouth slows down, rather than speeds up. The inadequacy of the model in this respect points out the importance of retarding forces at the river mouth. The retarding forces could come from three sources:

- 1) an adverse pressure gradient in the barotropic tide, caused by the large geostrophic slope during the ebb cycle of the tide

in the Strait;

2) entrainment of water with zero momentum in the downstream direction of the plume;

3) frictional interaction between the upper layer and lower layer.

To determine how important these terms are, we first estimate $g'h_x$ from the analytical solution, Fig. 57. For $F^2=1$,

$$g'h_x = g' \left(\frac{\partial h}{\partial x} \right)_{\text{Fig. 57}} \times \left(\frac{h_0}{b_{1/2}} \right),$$

where $(\partial h / \partial x)_{\text{Fig. 57}}$ is measured from the diagram, h_0 is the initial depth of flow, and $b_{1/2}$ is the halfwidth of the river mouth. The factor $(h_0 / b_{1/2})$ converts from the non-dimensional units of the analytic solution to units appropriate to the Fraser River. Taking the width of the river to be 600 meters, and g' to be $10 \text{ m/sec}^2 \times 0.01 = 0.1 \text{ m/sec}^2$, and h_0 to be 8 meters, we can evaluate $\partial h / \partial x$ for the region along the centreline where h changes from 1 to 0.3, a distance of 2.5 halfwidths: $(\partial h / \partial x)_{\text{Fig. 57}} = 0.7 / 2.5$. Thus, $g'h_x \sim 7.5 \times 10^{-4} \text{ m/sec}^2$. In the region where h changes from 0.3 to 0.1, the pressure gradient, calculated in the same manner, is $2.0 \times 10^{-4} \text{ m/sec}$.

From the geostrophic relation, $fv = g\zeta_x$, the crosschannel pressure gradient for a current of 1 m/sec (an upper limit) is about $1 \times 10^{-4} \text{ m/sec}^2$. This slope results in the water level being higher on the western side of the Strait of Georgia during an ebb, which constitutes an adverse pressure gradient to the river flow in the vicinity of the river mouth. Thus it appears that the cross channel barotropic tidal slope is the same order of magnitude as the buoyant spreading pressure gradient.

One can estimate the relative effect of vertical entrainment as follows. If the contribution of entrainment to the continuity equation is written as

$$\frac{\partial h}{\partial t} = w,$$

and one considers the vertically integrated momentum equation,

$$\frac{\partial}{\partial t} (uh) = h \frac{\partial u}{\partial t} + u \frac{\partial h}{\partial t} = Q,$$

then the average momentum equation is

$$\frac{\partial u}{\partial t} = \frac{1}{h} Q - \frac{w}{h} u.$$

Thus, entrainment acts as linear friction, with friction coefficient w/h . We will assume $w=Eu$, and $E=2 \times 10^{-4}$ (Keulegan, 1966). This order of magnitude for E was verified by both Cordes (1977) and de Lange Boom (1976) for the Fraser River plume. An estimate of u from the Bernoulli equation is

$$u \sim [2g'h_0(3/2 - h/h_0)]^{1/2}.$$

At $h/h_0=0.6$, $u \sim 1.2$ m/sec. This is also a reasonable value for the measured speed near the river mouth. With this value for u , and $h=.6 \times 8$ m, the retarding force due to entrainment, wu/h , is 0.4×10^{-4} m/sec². This value is one full order of magnitude less than $g'h_x$ near the river mouth and somewhat closer to $g'h_x$ at points further downstream. It appears that entrainment has a significant but not dominant effect on the plume near the river mouth. There is an indirect effect also. As entrainment proceeds, g' , proportional to the density difference, decreases, and h has a tendency to increase. The actual pressure gradient driving u is $(1/2h) \frac{\partial}{\partial x} (g'h^2)$. Due to entrainment, since g' decreases, and h has a tendency to increase (opposed by its

buoyant spreading tendency) it is difficult to predict this pressure gradient without a more detailed model, such as that discussed in Chapter 5.

The third possible retarding force is friction. If one assumes quadratic friction, and equates $hg'h_x$ to $Ku|u|$, then to be important, Ku^2/h must be close to 7.5×10^{-4} m/sec². Assuming $Ku^2/h = 7.5 \times 10^{-4}$ m/sec², we get $K \sim 2 \times 10^{-3}$. This value of K is similar to the value of drag coefficient used in many calculations. For instance, the drag coefficient for wind over water is about 1.5×10^{-3} , and the drag coefficient for bottom friction in a tidal channel is about $2-4 \times 10^{-3}$, and the interfacial drag coefficient in a laboratory scale flow is of order 10^{-3} (Lofquist, 1960). Thus it appears that friction plays an essential role in the plume dynamics.

2. A TIME-INDEPENDENT MODEL OF SURFACING ISOPYCNALS

As demonstrated in Chapter 2, figures 15, 27a, and 27b in particular, the surfacing of isopycnals is a dominant feature of the plume in regions away from the river mouth. The model discussed here is an attempt to explain this phenomenon in terms of entrainment and depletion. This model applies to the region from around station c to station j, Fig. 27a. Here the plume is thought to be more or less uniform across the Strait, and advected back and forth by the tide, with a small mean velocity to carry river water out of the Strait. The tidal excursion in this area is about 10 km, so the plume is advected back and forth by the tide a rather large distance. One could imagine performing an average over a few tidal cycles and obtaining a set of data describing a stationary plume. One also needs to

perform averages across the Strait (and hence across the plume), or else assume lateral uniformity. The plume is fed water at its upstream end, and this water leaks out from the forward or leading end by means of the depletion mechanism discussed in Chapter 3. The equations for this model of the plume, a simplified form of 3.24, 3.25, and 3.26 are:

$$\frac{\partial U}{\partial x} + w_n - w_p = 0 ;$$

4.7.

$$\frac{\partial}{\partial x} (Us) + w_n s - w_p s_0 = 0 ;$$

4.8.

$$\frac{\partial}{\partial x} \left(\frac{1}{2} \gamma (s_0 - s) h^2 \right) + w_n \frac{U}{h} + K' \frac{U}{h} = 0 ;$$

4.9.

where $\gamma(s_0 - s) = g(\rho_0 - \rho)$ is an equation of state, U is a transport, (vertically integrated velocity), and K' is a coefficient of linear friction. A schematic drawing of the model is shown in Figure 58a. The use of linear friction is not unrealistic in that the tidal average of square law friction is linear in the residual flow (Gruen and Groves, 1966).

To make the solution of this model very easy, assume w_n and w_p are constants, and that $w_n > w_p$, which is valid near the outer edge of the plume.

The continuity equation, 4.7, has the immediate solution

$$U = U_0 - (w_n - w_p) x ,$$

where U_0 is the transport at $x=0$, and where $x=0$ is taken at the upstream boundary of the region of applicability of this model (Fig. 58a). Defining $\alpha = w_n - w_p$, and $L = U_0 / \alpha$, we have $U = \alpha(L - x)$. Note that $U=0$ at $x=L$, so the length of the plume is L .

The salt and continuity equation may be combined to give:

$$U s_x + w_p (s - s_0) = 0.$$

4.10.

Define $s - s_0 = \Sigma, < 0$; $y = L - x$. Then, the above equation becomes

$$-\alpha y \Sigma_y + w_p \Sigma = 0,$$

with solution $\Sigma = Ay^{w_p/\alpha}$; the salinity defect is proportional to the distance from the leading edge, y , to the power w_p/α . Imposing the boundary condition that at $x=0$ $s=s_1$, we get $A = (s_1 - s_0)^{-w_p/\alpha} L^{-w_p/\alpha}$.

In terms of the variables y and Σ , the momentum equation becomes

$$\frac{\partial}{\partial y} \left(\frac{1}{2} \gamma \Sigma h^2 \right) + \frac{w_n}{h} \alpha y + \frac{K'}{h} \alpha y = 0.$$

With $\Sigma = Ay^{w_p/\alpha}$, we get

$$h \frac{\partial}{\partial y} (A y^{w_p/\alpha} h^2) + \frac{2\alpha}{\gamma} (w_n + K') y = 0.$$

Trying a solution $h = By^\beta$ gives

$$A B^3 y^{3\beta + w_p/\alpha - 1} (2\beta + \frac{w_p}{\alpha}) + \frac{2\alpha}{\gamma} (w_n + K') y = 0.$$

Equating powers of y : $\beta = (2 - w_p/\alpha)/3$. And finding a value of B to make the left hand side equal to zero:

$$B = \left[\frac{2\alpha/\gamma (w_n + K')}{-A (2\beta + w_p/\alpha)} \right]^{1/3}.$$

Because it is a non-dimensional number, and perhaps the most important one for the plume, the internal Froude number is of some interest. It is given by:

$$F_i^2 = \frac{U^2}{g'h^3} = -\frac{U^2}{\gamma \Sigma h^3} = \frac{W_n - W_p}{6} \left(\frac{4 + W_p/\alpha}{K' + W_n} \right);$$

a constant.

To summarize the solution

$$U = \alpha (L - x)$$

4.11.

$$S = S_0 - (S_0 - S_1) \left(\frac{L - x}{L} \right)^{W_p/\alpha}$$

4.12.

$$h = \left[\frac{2\alpha/\gamma (W_n + K')}{(S_0 - S_1) L^{-W_p/\alpha} (4/3 + 1/3 W_p/\alpha)} \right]^{1/3} (L - x)^{\frac{2 - W_p/\alpha}{3}}$$

4.13.

And the velocity, u , is given by

$$u = \left[\frac{2\alpha/\gamma (W_n + K')}{(S_0 - S_1) L^{-W_p/\alpha} (4/3 + 1/3 W_p/\alpha)} \right]^{-1/3} (L - x)^{\frac{1 + W_p/\alpha}{3}}$$

4.14.

Thus, the transport, U , decreases in the downstream direction, as plume water becomes saltier and is redefined as lower layer water; the average salinity of the plume increases downstream; and the thickness of the layer decreases downstream. It is reassuring to note that the fluid velocity, u , also decreases downstream, going to zero at $x=L$.

The data for July 3, 1975 (Fig. 27a) seem a good choice for comparison with this model, in that the salinity section for that day shows the surfacing of isopycnals very clearly. Referring to Fig. 27a, consider station d as $x=0$. L is then 23 km, if the plume boundary is defined as the 25 ‰ contour. With

$s_0 = 25 \text{ ‰}$, the average salinity at station d, s_1 , is 18.6 ‰ , from an integration of the actual salinity profile. We need an estimate for U_0 . Assume that on average, half the river discharge leaves through the northern channels and half through the southern channels. Assuming that the river discharge is $8000 \text{ m}^3/\text{sec}$, and that by the time river water reaches station d it has entrained an equal volume of salt water then the transport to the south is $8000 \text{ m}^3/\text{sec}$, flowing along the axis of the Strait. At station d, the Strait is about 16000 m wide. Assuming uniform discharge across the Strait, $U_0 = (8000/16000) = 0.5 \text{ m}^2/\text{sec}$. Thus $\alpha = U_0/L = .5/(23 \times 10^5) = 2.2 \times 10^{-5} \text{ m/sec}$. We can get an estimate of w_p/α by fitting the salinity change from station d to station j. At station j, the average salinity in the upper layer is 23 ‰ and $x = 11 \text{ km}$. We obtain, from equation 4.12, $w_p/\alpha = 1.8$. With $\alpha = 2.2 \times 10^{-5} \text{ m/sec}$, we find $w_p = 4 \times 10^{-5} \text{ m/sec}$, and $w_n = 6 \times 10^{-5} \text{ m/sec}$. This fixes $h(x) = h_0 \left(\frac{L-x}{L} \right)^{0.2/3}$. Using $\gamma = g(\rho_0 - \rho)/(s_0 - s) = .83$, (average of salinity profiles for stations d, j, l) we calculate K' , the linear friction coefficient, to be $5.3 \times 10^{-3} \text{ m/sec}$. Equating $K'u$ and $Cu|u|$ at $x=0$, we get an equivalent $C = 2.6 \times 10^{-2}$. This is about 10 times the usual value of a drag coefficient, 3×10^{-3} . However, K' is really Cu_{rms} , (Groen and Groves, 1966), and the rms value of velocity is probably quite a bit higher than the tidal mean used here. The computed and observed distribution of h is shown in Figure 58b. The fit uses the two h points at the upstream and downstream ends of the plume, so there is only one point left to check the fit. To show the sensitivity of the fit, the curve $h = h_0 \left(\frac{L-x}{L} \right)^{1/3}$ is plotted as a dashed line.

The model is substantially correct in that it predicts the rising of isopycnals (modelled as a thinning of the layer and an increase in average salinity of the layer), but it would be extremely unlikely that the entrainment and depletion processes can be modelled very well by constant values of w_n and w_p . The model would be improved by obtaining data for fitting that were truly cross-channel and tidally averaged; and by obtaining, empirically, better formulae for w_n and w_p .

3. CONDITIONS AT A STRONG FRONTAL DISCONTINUITY

As discussed in Chapter 2, particularly with reference to the data of July 2, 1975, Fig. 31, there is often a distinct colour front bounding the plume. The purpose of this section is to clarify the role these fronts play in determining the motion of the water behind them. One would like to have a model of a front suitable for use with a larger scale model of the entire plume, and for these purposes a detailed model of the circulation at the front is not required, but rather relations between frontal velocity and the fluxes of mass, momentum and salt into the frontal region.

With reference to the dye experiment described in Chapter 2, on July 3, 1975, a "tank tread" model of frontal circulation suggests itself. Thus, if one considers a military tank moving over the ground at speed V , to an observer on the ground the upper tread is moving at $2V$, the tank at V , and the bottom tread is stationary. This is similar to the velocity profiles measured in the plume, eg. Fig. 40, where the bottom part of the plume is "attached" to the lower water, and the upper part is moving at a significantly different speed. Continuing with the tank

tread analogy, and changing the co-ordinate system to that of an observer sitting on the tank, the top tread is moving at V , the bottom at $-V$, and the tank itself appears stationary. Similarly, an observer travelling with the front sees water at the surface of the plume coming toward him (as the dye on the surface ran toward the front, July 2), and sees deeper water travelling away from him, on the under side of the plume (like the dye which was later found at depth, behind the front). Also, to an observer on the tank, the ground on which the tank is travelling is coming toward him, and then passing under him; similarly, to an observer at the front, the dark blue water appears to travel toward him, and then flow under the plume.

A model to describe this motion can be developed from a control volume approach. Consider a cross-section of the front, and draw a control volume around it, Fig. 59a. Assuming the front moves at $\dot{\sigma}$, the control volume also moves at $\dot{\sigma}$. Taking $z=0$ at the base of the plume, at some $z=h'$ (Fig. 59a), the water speed u (relative to a stationary co-ordinate system) equals the front speed $\dot{\sigma}$. Above this level, water is flowing into the control volume, and below this level, water is flowing out. The speed of water in the control volume or frontal co-ordinate system is $u-\dot{\sigma}$. Conservation of mass requires

$$\int_{h'}^h (u-\dot{\sigma}) dz + Q = \int_0^{h'} (\dot{\sigma}-u) dz,$$

or

$$\dot{\sigma} h - \int_0^h u dz - Q = 0.$$

4.15a.

Q represents a rate of entrainment specifically due to frontal processes and is entirely different from w_p discussed previously. w_p and w_n have been ignored because the control volume length is assumed very small, of order tens of meters, relative to the entire plume.

Similarly, conservation of salt requires:

$$\int_{h'}^h (u - \dot{\sigma}) s dz + Q s_0 + \int_0^{h'} s (u - \dot{\sigma}) dz = 0,$$

or

$$\dot{\sigma} \int_0^h s dz - \int_0^h u s dz - Q s_0 = 0.$$

4.16a.

Conservation of momentum requires:

$$\int_{h'}^h (u - \dot{\sigma})^2 dz + \int_0^{h'} (u - \dot{\sigma})^2 dz - Q \dot{\sigma} + \Delta p - K = 0,$$

or, using the continuity equation,

$$\int_0^h u^2 dz - \dot{\sigma} \int_0^h u dz + \Delta p - K = 0.$$

4.17a.

Here, K is the excess momentum reaction at the front, due mainly to form drag.

As derived in Chapter 3, the net pressure force is $1/2 g h^2 \frac{\Delta \rho}{\rho}$, if ρ is independent of depth in the layer. It is possible to obtain the pressure force fairly simply for a

variable $\rho(z)$. Consider a plume of thickness h , with its base at $z = -(h - \Delta h)$ (Fig. 59b). For zero pressure gradient at depth, (the assumed condition in the water beneath the plume), we require

$$\int_0^h \rho dz = \rho_0 (h - \Delta h),$$

or $\Delta h = \frac{(\rho_0 - \bar{\rho}) h}{\rho_0}$ where $\bar{\rho} = \frac{1}{h} \int_0^h \rho dz$.

The net pressure force, divided by the average density $\bar{\rho}$ is:

$$\frac{1}{\bar{\rho}} \left[\int_0^h \int_0^z \rho g dz' dz - \rho_0 g \left(\frac{h - \Delta h}{2} \right)^2 \right] =$$

$$\frac{1}{\bar{\rho}} \left[\int_0^h \int_0^z \rho g dz' dz - g \frac{h^2}{2} \frac{\bar{\rho}^2}{\rho_0} \right].$$

4.18.

For the case $\rho = \bar{\rho} = \text{a constant}$, this becomes

$$\frac{1}{\bar{\rho}} \frac{g h^2}{2} \left[\bar{\rho} - \frac{\bar{\rho}^2}{\rho_0} \right] = g \frac{h^2}{2} \frac{\Delta \rho}{\rho},$$

as in Chapter 3.

If $\rho = \rho_s + (\rho_0 - \rho_s) z/h$, a linear profile, then the net pressure force is $1/12 g h^2 (\rho_0 - \rho_s) / \rho_0$, correct to first order in $\rho_0 - \rho_s$.

If we had used the average density in the formula $1/2 g h^2 \Delta \rho / \rho$, we would have $1/4 g h^2 (\rho_0 - \rho_s) / \rho_0$, significantly different from $1/12 g h^2 (\rho_0 - \rho_s) / \rho_0$.

Now, to apply the equations to some field data. On July 23, 1975, we measured a current profile and a salinity profile at about 200 meters from the front, in the plume. (Fig. 39 and Fig.

40). The current profile was actually a speed profile, so the zero crossing and direction were only inferred. Referring the velocities to 17m, the deepest measured, the resulting front speed $\bar{\sigma}$ is that relative to tidally moving deep water. Assuming a plume depth of 6m, $\rho_o = 1.017$, $\rho_s = 1.003$, and assuming a linear density profile, $\rho = \rho_s + (\rho_o - \rho_s) z/h$, the pressure term 4.18, turns out to be $.42 \text{ m}^2 \text{ s}^{-2}$.

The integrals of u and s are:

$$\int_0^h u dz = 1.25 \text{ m}^2/\text{s}$$

$$\int_0^h u^2 dz = 0.72 \text{ m}^3/\text{s}^2$$

$$\int_0^h s dz = 100 \text{ m ppt}$$

$$\int_0^h u s dz = 12.9 \text{ ppt m}^2/\text{s}.$$

With $s = 23.4$, we get, by solving equations 4.15a, 4.16a, 4.17a,

$$\bar{\sigma} = .41 \text{ m/s}$$

$$Q = 1.21 \text{ m}^2/\text{s}$$

$$K = 0.63 \text{ m}^3/\text{s}^2;$$

recalling that $\bar{\sigma}$ is the front speed, Q is the extra frontal entrainment, and K is the extra form drag associated with propagation of the front.

Note that the front speed is considerably larger than the average speed, $1.25/6 = .21 \text{ m/s}$. Also note that $Q \sim \int u dz$. That is, a front extends itself, or propagates, by mixing equal parts of plume water and salt water. Also, one could write $K = 1/2 C_f \bar{\sigma}^2 h$,

where C_0 is a drag coefficient, which turns out to be 1.2 in this case. Since values of C_0 for flow over blunt objects such as cylinders are about 1, it appears that K may be identified with the drag exerted by the salt water as it flows under the blunt leading edge of the plume.

It is informative to re-derive eqns. 4.15a, 4.16a, and 4.17a from the differential form of the equations, Chapter 3. Thus, in one horizontal dimension, suppose that for $x < \sigma(t)$, there exists a plume satisfying the equations:

$$\frac{\partial h}{\partial t} + \frac{\partial}{\partial x} \int_0^h u dz + w_n - w_p - Q \delta(x - \sigma) = 0. \quad 4.19.$$

$$\frac{\partial}{\partial t} \int_0^h s dz + \frac{\partial}{\partial x} \int_0^h u s dz + w_n s - w_p s - Q s_0 \delta(x - \sigma) = 0. \quad 4.20.$$

$$\begin{aligned} \frac{\partial}{\partial t} \int_0^h u dz + \frac{\partial}{\partial x} \int_0^h u^2 dz + \frac{\partial}{\partial x} \left(\frac{1}{2} g' h^2 \right) + R u |u| \\ + w_n \bar{u} - w_p u_0 + K \delta(x - \sigma) = 0. \end{aligned} \quad 4.21.$$

$\delta(x - \sigma)$ is the Dirac delta function, used to make the quantities Q , Qs_0 , and K non-zero only at the front, $x = \sigma(t)$. We shall integrate equations 4.19, 4.20, and 4.21 from $x = \sigma - \epsilon$ to $x = \sigma + \epsilon$; set quantities at $x = \sigma + \epsilon$ equal to zero, since there is no plume ahead of the front; and finally take $\epsilon \rightarrow 0$. There results:

$$\dot{\sigma} h - \int_0^h u dz - Q = 0. \quad 4.15b.$$

$$\dot{\sigma} \int_0^h s dz - \int_0^h u s dz - Q s_0 = 0. \quad 4.16b.$$

$$\dot{G} \int_0^h u dz - \int_0^h u^2 dz - g \Delta \frac{h^2}{2} + K = 0.$$

4.17b.

Notice that the quantities involving w_p , w_n , and $Ru|u|$ disappear, since they are proportional to ϵ , which approached zero. The justification for this procedure is that as one proceeds from Sand Heads to the front, properties change only gradually, and are appropriately related to each other by partial differential equations. Then, at the front, the fields of thickness, velocity and salinity change drastically in a very short distance, of the order of a small boat length, and can only be related to each other in terms of weak solutions. (A weak solution is a set of relations between the changes of various properties across a discontinuity, Whitham, 1974).

We can compare (approximately) the speed of the front to the calculated speed, 0.41 m/s. Referring to Fig. 38a, all three drogues were inserted at the front, and the shallow drogue, S, stayed with the front. Assuming the deep drogue travelled with the bottom water (not exactly true), the relative speed is about .33 m/s. This is 80% of the calculated speed, but the drift time of the drogues, 1.5 and 2 hours, is not very small compared to the tidal period, (nor was the current profile measurement time), so great accuracy can't be expected.

Summary of frontal circulation

The following description of a front emerges from the equations derived above. The front is a mixing region of water which is pushed outward by the momentum flux and the pressure gradient, and retarded by the mixing of ambient water and the

form drag it experiences from the ambient water. The intense mixing at the front can be visualized as follows. Relative to the depth at which $u=\bar{u}$, quite fresh water above this level flows into the mixing region at the front. Water below this level, flowing away from the front, is quite salty, and could only have picked up this salt by an intense, churning mixing at the front.

4. KINEMATIC WAVE APPROACH TO FRONTAL MOTION

The following model is intended to demonstrate, as simply as possible, the way in which fronts, described in Chapter 2, develop in a time-dependent plume model. We consider a one dimensional model. The continuity equation, without entrainment,

is
$$\frac{\partial h}{\partial t} + (uh)_x = 0.$$
 4.22.

We further suppose that all the dynamics governing the plume can be characterized by

$$\frac{u^2}{h} = F,$$
 4.23.

where F is a constant. F is similar to a Froude number, but has the dimensions of an acceleration to simplify subsequent mathematical expressions. Although the assumption that F is constant may not be a good approximation for the plume, for the present purposes the simplicity of the resulting mathematical analysis more than compensates for the physical inadequacy of that assumption. The approach used here is called the kinematic wave method because all the dynamic interactions are summarized in a simple rule, equation 4.23, and we look at the motion prescribed by the continuity equation 4.22 (Whitham, 1974).

Substituting for u in the continuity equation we find:

$$\left(\frac{\partial}{\partial t} + \frac{3}{2} F^{1/2} h^{1/2} \frac{\partial}{\partial x} \right) h = 0,$$

$$\text{or } dh/dt = 0 \text{ on } \frac{dx}{dt} = \frac{3}{2} F^{1/2} h^{1/2} = \frac{3}{2} u. \quad 4.24.$$

The lines $dx/dt = (3/2)u$ are the characteristics. At $x=0$, representing the river mouth, assume the velocity versus time graph is a series of triangles, representing tidal modulation of river flow (plotted along the time axis, Fig. 61).

Thus, on $x=0$:

$$u = (2/3)t; \quad 0 < t < 3$$

$$u = 4 - (2/3)t; \quad 3 < t < 6$$

$$u = (2/3)t - 4; \quad 6 < t < 9. \quad 4.25.$$

The implicit solution of 4.23, 4.24. And 4.25 is

$$h = h_0(\tau),$$

$$u = u_0(\tau),$$

$$\text{on the line given by } x = (3/2)u_0(\tau)(t - \tau) \quad 4.26.$$

where $h_0(\tau)$ and $u_0(\tau)$ are the values of u and h at $x=0$, $t=\tau$.

The solution is displayed in a characteristic diagram in the $x-t$ plane - fig. 60a. However, two complications arise.

1). We will assume here that initially there is no fresh water in the Strait (perhaps because of a windy period before model time $t=0$), so that water issuing from $x=0$ in this model forms a front. This front is a boundary to the region of validity of the plume equations, 4.26, and its motion must be found. Referring to Fig. 60b, at a point (s,t) on the front, $ds/dt = \text{front speed} = u$, the local water speed. Since the point (s,t) is a termination point for a characteristic, s and t are related by

the implicit solution 4.26. For $\tau < 3$, that is for water discharged before $t=3$, the front is given by

$$s = (t - \tau)(\tau) \quad 4.27.$$

$$\frac{ds}{dt} = u = \frac{2}{3}\tau - \frac{1}{3}(t + \sqrt{t^2 - 4s}) \quad 4.28.$$

Equation 4.28, with initial condition $s=t=0$ has solution $s=2/9t^2$. To continue the front beyond $\tau=3$, different formulae than 4.27 and 4.28 must be used, reflecting the fact that the functional form $u(\tau)$ has changed. Equation 4.28 must then be integrated numerically, as solutions can't be found analytically.

2). The other complication is the formation of shocks or hydraulic jumps. These occur whenever a faster moving characteristic overtakes a slower moving one. For example, the characteristics for $\tau > 6$ have speeds which are increasing functions of time, whereas those for $\tau < 6$ decrease. Consider two characteristics, one for $\tau > 6$, the other for $\tau < 6$. (Figure 60c) The curve (s, t) , the path of the hydraulic jump, must satisfy both characteristic relations:

$$s = (-\tau_1 + 6)(t - \tau_1) \quad 4.29.$$

$$s = (\tau_2 - 6)(t - \tau_2) \quad 4.30.$$

We further require a jump relation. Integrating the continuity equation across this jump:

$$\int_{s-\epsilon}^{s+\epsilon} \frac{\partial h}{\partial t} dx + \int_{s-\epsilon}^{s+\epsilon} \frac{\partial}{\partial x} (uh) dx = 0,$$

or

$$\frac{\partial}{\partial t} \int_{s-\epsilon}^{s+\epsilon} h dx + h_{s-\epsilon} \dot{s} - h_{s+\epsilon} \dot{s} + (uh)_{s+\epsilon} - (uh)_{s-\epsilon} = 0.$$

The integral approaches zero as ϵ tends to zero, and we are left with

$$\dot{s} = \frac{ds}{dt} = \frac{(uh)_{s-\epsilon} - (uh)_{s+\epsilon}}{h_{s-\epsilon} - h_{s+\epsilon}} = \frac{[u^3]}{[u^2]}, \quad 4.31.$$

for $u^2/h = F$.

The solution to eqn. 4.29, 4.30, and 4.31 is $s = .229... (t-6)^2$.

These internal jumps may represent some of the weaker discontinuities one sees in the plume, for instance at station q, r July 2, 1975, Figure 26. Since the water on either side of the jump took different times to arrive at the discontinuity (t_1 is less than t_2), the amount of silt in suspension, and hence the colour, will be different. These fronts have been termed internal fronts, to distinguish them from the true front, which is the boundary of validity of the plume equations.

Proceeding on in this manner, the diagram in Figure 61 may be drawn. Figure 62 is a plot of u versus x at $t=14$ - an instantaneous photograph of the distribution of downstream velocity in the plume. Recall that h is proportional to u^2 , so this is also a plot of plume thickness. Using a rather mixed but convenient set of units, x could be measured in nautical miles, t in hours, u in knots, and h in meters. F would then be in $(\text{knot})^2/\text{m}$. In Figure 61, there is a strong colour front, bounding the region of solution. At $s = 30.5$, the front speeds up, since faster water, originating from $t=9.9$ catches up with

it. There are hydraulic jumps originating from $\tau=6, \tau=12$, etc. Looking at Figure 62, one could imagine the following sequence of observations, proceeding out from the river mouth. At $s=1$, there is an internal front, corresponding to faster moving water catching up with slower moving water. The slow water has spent more time since it left the river mouth, so silt could have settled out, and this front might show up as a colour discontinuity. Again, at $s=11.8$, another internal front appears, and at $s=19.6$ the true front is found. The front at $s=19.6$ is still quite strong, although in reality, because of dissipation and spreading, it would be very weak.

As mentioned at the beginning of the section, the model described here is based on grossly oversimplified dynamics. However, it clarifies mathematically the formation of fronts in a time dependent system.

5. MIXING AND FLUXES ACROSS AN INTERFACE

The introduction of an isohaline as a boundary for our plume model presents complications in trying to model the vertical fluxes of salt, water, and momentum across that interface. In many fluid mechanics calculations the turbulent mixing of a scalar quantity is assumed to be governed by a diffusion term, $\partial/\partial x_i (K \partial s/\partial x_i)$ where one attempts to choose K in such a way that $\partial/\partial x_i (K \partial s/\partial x_i) = -\frac{\partial}{\partial x} (\overline{u' s'})$, where the primes refer to 'turbulence' quantities. In this section we will assume that a diffusion equation governs the distribution of salt,

$$\frac{Ds'}{Dt'} = \frac{\partial}{\partial z'} \left(K' \frac{\partial s'}{\partial z'} \right),$$

4.32

where

$$\frac{D}{Dt'} = \frac{\partial}{\partial t'} + u' \frac{\partial}{\partial x'} + v' \frac{\partial}{\partial y'},$$

and where here primes denote dimensional quantities and u' and v' are components of some appropriate advection velocity. Thus 4.32 describes the downstream evolution of a salinity profile. Equation 4.32 will be solved numerically, (in a co-ordinate system travelling at (u', v') , so D/Dt' is replaced by $\partial/\partial t'$); then choosing 0.8 times the maximum salinity as the bottom of the upper layer we obtain, from the numerical solution, $\partial h/\partial t$ and $\partial s/\partial t$ for this upper layer. We then try to model the evolution of the upper layer thickness and salinity using the two fluxes discussed in Chapter 3, entrainment and depletion.

Two choices of K are considered in the solution of 4.32; $K = \text{a constant}$ and $K = az^2$, where z represents the vertical distance from the free surface, positive downwards. Scaling s' with S_0 , the maximum salinity, and t' with T_0 , a characteristic time, and z' with Z_0 , the depth where the salinity is approximately constant, we want to solve

$$\frac{\partial s}{\partial t} - \frac{\partial}{\partial z} \left(K \frac{\partial s}{\partial z} \right) = 0, \quad 4.33.$$

where $s' = sS_0$, $t' = tT_0$, $z' = zZ_0$, and $K' = KZ_0^2/T_0$, quantities without primes being dimensionless. The initial conditions are:

$$s=0 \text{ for } z < .2, \quad t=0$$

$$s=1 \text{ for } .2 < z < 1, \quad t=0.$$

Thus initially there is an upper layer $0.2Z_0$ thick, composed of fresh water, floating on a layer $0.8Z_0$ thick, of salinity S_0 .

At $z=0$, the free surface, the condition of no flux $K \partial s / \partial z = 0$, was imposed; at $z=1$, representing the deep, well-

mixed water, $s=1$.

Equation 4.33 with the above boundary and initial conditions was solved numerically. Figure 63a shows the results for $K=z^2/(.2)^2$, at times 0, $20\Delta t$, $120\Delta t$, $220\Delta t$, and $320\Delta t$, where $\Delta t=.4(\Delta z)^2$, and Δz , the vertical grid size, equals 0.02. Figure 63b shows the results for $K=1$, at times 0, $20\Delta t$, $220\Delta t$, $580\Delta t$, and $920\Delta t$. To compare these profiles with quantities available in an upper layer model of the plume, I chose $0.8S$ to be the salinity characterizing the base of the upper layer. Thus, Figure 64a shows the depth of the upper layer versus time for the variable K case, and Figure 64b shows the total salt content S , $\int s dz$ above the level $s=.8S_0$, versus time. As is evident from Figure 64a, the upper layer initially increases in thickness, then decreases - remember that at $t=0$ its thickness was $0.2Z_0$.

There is considerable difference in the s versus t curves of Fig. 63a and 63b, with Fig. 63a, $K \propto z^2$ appearing to be more like the observed profiles of salinity. It is interesting to speculate why this is so. First, $K \propto z^2$ is partially the functional form prescribed by Prandtl's mixing length hypothesis (Launder and Spalding, 1972). Since we are not dealing with a velocity profile, we can't however define a characteristic time such as $(\frac{\partial u}{\partial z})^{-1}$ to complete the specification of K in terms of mean flow properties as in the complete Prandtl mixing length theory, where $K \sim l_m^2 \frac{\partial u}{\partial z}$. Second, the $K \propto z^2$ form implicitly accounts for the effects of vertical stratification - near the surface the stratification is strongest, and hence mixing is inhibited the most and the supply of fresh water due to the velocity shear is greatest. For both these reasons, the

effective value of K should be relatively small near the surface, as it is when K is proportional to z^2 .

We wish to model the behaviour of s and h by the two equations, simplifications of eqns. 3.24 and 3.25,

$$\frac{dh}{dt} = w_p - w_n$$

4.34.

$$\frac{ds}{dt} = \alpha w_p - \beta w_n$$

4.35.

where w_p is the entrainment velocity, w_n is the depletion velocity, α is a salinity greater than $0.8S_0$, and β is a salinity less than or equal to $0.8S_0$. S denotes the total salt content in the layer, $\int s dz$. The quantities dh/dt and ds/dt were obtained from the $K=z^2/(.2)^2$ solution and plotted versus s , the average salinity in the upper layer. They were roughly fitted with

$$w_p = 1150$$

$$w_n = 2600s \text{ if } s < .5$$

$$w_n = 2600s - 8000(s - .5)^2 \text{ if } s > .5$$

$$\alpha = 0.9, \beta = 0.8.$$

w_p and w_n are converted to dimensional units by multiplying by the ratio $\Delta z/T_0$, where T_0 is of order 8 hours, and Δz is of order 0.5 m. The results of numerical integration of 4.34 and 4.35 using the above w_p , w_n , α , and β , are shown as the dashed curves of Fig. 64a and 64b. There is qualitative agreement with the results from the diffusion equation. There is not much point adjusting w_p , w_n , α , and β to make the agreement better because in the real world we don't know $K(z)$, and there are important effects due to velocity shear. However this example demonstrates

the use of two types of exchange across an interface (w_p and w_n) to model a mixing situation.

6. ANALOGY WITH TURBULENT JETS

Another way to view the phenomenon of entrainment and depletion, with reference to the plume, is to consider a turbulent plane jet (Abromovitch, 1963). Figure 65 shows a plot of an isoconcentration curve of a passive scalar discharged by the jet, (X is downstream, Y is cross-stream), and velocity vectors at various points. We see that for X less than about 5, the net flow across the isoconcentration curve is into the jet as defined by the iso-concentration curve; whereas for X greater than 5, the net flow is out of the jet region. Schematically, the situation is shown in Figure 66a. The curves AD and A'D' are the usually defined boundaries of the jet, representing the interface between turbulent and non-turbulent flow. If one wanted to consider only a region where there are significantly characteristic properties of the jet, as defined for instance by the concentration of a scalar quantity discharged by the jet, that region would be bounded by ABCB'A'. As Fig. 65 indicates, along AB and A'B' there is net flow into the jet, and along BCB' there is net flow out.

How does this concept apply to the plume? Consider a section through the plume, Fig. 66b. Because we are going to solve the plume equations in a finite region, a computational open boundary is indicated in Figure 66b. If we choose $s=25\%$ as our plume boundary then all of the Fraser River water, plus entrained water, flows out of the plume solely by means of the depletion mechanism, since the flow components (u, v) do not

cross the interface in the shallow water equations developed here. If, however, we choose $s=28\text{‰}$ as the plume boundary, part of the inflow is balanced by depletion, but there is also horizontal outflow over the depth h .

The computational aspects of these two choices are considerably different. For the case where the iso-haline comes to the surface within the computational region, the actual computational boundary becomes the line along which the isohaline intersects the surface. Thus, one has to numerically move this boundary across the grid system - a not impossible feat (Kasahara, Isaacson and Stoker, 1965), but a complicated one. For the case where the iso-haline does not surface, one then has the problem of an open boundary, and in particular the problem of specifying u , s , and h on an inflow, and also the problem of generation and reflection of false waves at the boundary.

CHAPTER 5

NUMERICAL MODELLING OF THE FRASER RIVER PLUME

The numerical modelling described below falls into 2 categories. First a model for a small rectangular region was developed. This model had the benefit of being inexpensive to run, and quick to show up any problems at boundaries, particularly the open outflow boundaries. Once all the terms described in Chapter 3 were in the small model, a few runs using a larger model simulating the real Strait of Georgia geometry were made. The aim of this chapter is to demonstrate that a reasonably flexible model has been developed, which has the potential to become an accurate tool in understanding the circulation in the Strait of Georgia.

The equations used in this model are 3.24 - 3.27, with the simplification that all properties were assumed homogeneous in the upper layer. Thus:

$$\frac{\partial h}{\partial t} + \frac{\partial U}{\partial x} + \frac{\partial V}{\partial y} = W_P - W_N$$

5.1.

$$\frac{\partial S}{\partial t} + \frac{\partial}{\partial x} \frac{US}{h} + \frac{\partial}{\partial y} \frac{VS}{h} = W_P S_o - W_N \frac{S}{h}$$

5.2.

$$\begin{aligned} \frac{\partial U}{\partial t} + \frac{\partial}{\partial x} \left(\frac{U^2}{h} \right) + \frac{\partial}{\partial y} \left(\frac{UV}{h} \right) + \frac{\partial}{\partial x} \left(\frac{1}{2} g' h^2 \right) \\ - fV + \frac{K U_R \sqrt{U_R^2 + V_R^2}}{h^2} + h \frac{\partial}{\partial x} \left(A \frac{\partial}{\partial x} \left(\frac{U}{h} \right) \right) \end{aligned}$$

$$+ h \frac{\partial}{\partial y} \left(A \frac{\partial}{\partial y} \left(\frac{U}{h} \right) \right) = u_c W_P - \frac{U}{h} W_N - gh \frac{\partial \zeta}{\partial x}$$

5.3.

$$\frac{\partial V}{\partial t} + \frac{\partial}{\partial x} \left(\frac{UV}{h} \right) + \frac{\partial}{\partial y} \left(\frac{V^2}{h} \right) + \frac{\partial}{\partial y} \left(\frac{1}{2} g' h^2 \right) + fU$$

$$+ \frac{K V_R \sqrt{U_R^2 + V_R^2}}{h^2} + h \frac{\partial}{\partial x} \left(A \frac{\partial}{\partial x} \left(\frac{V}{h} \right) \right)$$

$$= v_o W_P - \frac{V}{h} W_N - gh \frac{\partial \zeta}{\partial y}$$

5.4.

where

U, V are vertically integrated transports,

$$g' = g \Delta \rho / \rho = 24 - 0.8S/h$$

A = horizontal eddy viscosity, discussed later in this chapter

ζ = barotropic tidal elevation

S = vertically integrated salinity

u_o, v_o = tidal streams

U_R, V_R = relative transports = $U - u_o h, V - v_o h$.

K = quadratic friction coefficient

w_p = entrainment velocity

w_n = depletion velocity

s_o = salinity of water underneath the plume

h = plume thickness

f = Coriolis parameter

It should be noted that the equations to be modelled are in divergence form. That is, they are of the form

$$\frac{\partial \vec{P}}{\partial t} + \nabla \cdot \vec{F}(\vec{P}) + \vec{Q}(\vec{P}) = 0,$$

where all spatial derivatives are exact differentials. This form of the differential equations allows one to write the finite difference equations in such a way that there are no spurious

sources or sinks in the derivative terms.

The numerical scheme used as a starting point was the semi-implicit scheme of Heaps (Flather and Heaps, 1975). Although this scheme works very well for tidal calculations, there was some doubt about how well it would work with the upper layer model, in which the fluid velocity is close to the internal small amplitude gravity wave velocity. However, there is no indication that high flow velocities (internal Froude numbers close to one) are a problem, as long as one satisfies the stability requirements of the scheme.

A typical element of the computational grid is shown in Figure 67, and Figure 68 shows the entire computational grid for the rectangular model. Note in Figure 68 that an extra row of meshes is provided around the outer edge of the mesh area, to facilitate calculations near boundaries. Also note in Figure 67 that only one subscript is used to denote the physical location of a mesh point. The systematics of this indexing scheme is apparent in Figure 68, and the reason for its use is to increase computational efficiency.

Certain spatial averages are defined below, for use in the finite difference equations which follow. All fields are considered to be at the same time level, and recall that changing a subscript by n , the number of columns in the grid, changes the row, a change of 1 unit in the y -direction.

The averaging operations for the finite difference formulations are defined as follows:

$$\bar{U}_i^x = \frac{1}{2} (U_i + U_{i+1})$$

$$\bar{U}_i^y = \frac{1}{2} (U_i + U_{i-n})$$

$$\begin{aligned}
\bar{v}_1^x &= \frac{1}{2} (v_1 + v_{i+1}) \\
\bar{v}_1^y &= \frac{1}{2} (v_1 + v_{i-n}) \\
\bar{z}_1^x &= \frac{1}{2} (z_1 + z_{i+1}) \quad [Z = h] \\
\bar{z}_1^y &= \frac{1}{2} (z_1 + z_{i-n}) \\
\bar{u}_1 &= \frac{1}{4} (u_1 + u_{i-1} + u_{i+n} + u_{i-n}) \\
\bar{v}_1 &= \frac{1}{4} (v_1 + v_{i+1} + v_{i-n} + v_{i-n+1}) \\
\bar{z}_1 &= \frac{1}{4} (z_1 + z_{i+1} + z_{i-n} + z_{i-n+1}) \\
\bar{z}_1^x &= \frac{1}{4} (z_1 + 2z_{i+1} + z_{i+2}) \\
\bar{z}_1^y &= \frac{1}{4} (z_{i-n} + 2z_i + z_{i+n})
\end{aligned}$$

With $\Delta \ell$ as the spatial grid size, Δt as the timestep, we obtain the following set of finite difference equations.

The finite difference representation of the continuity equation is:

$$\begin{aligned}
&[Z_1(t+\Delta t) - Z_1(t)] \, 1/\Delta t = \\
&- [U_1(t) - U_{i-1}(t) + v_{i-n}(t) - v_i(t)] \, 1/\Delta \ell \\
&+ WP_1(t) + WN_1(t)
\end{aligned}$$

The finite difference representation of the salt equation is:

$$\begin{aligned}
 [S_1(t+\Delta t) - S_1(t)] 1/\Delta t = & \\
 & - \left[\frac{U_1(t)}{\bar{Z}_1^x(t)} \bar{S}_1^x(t) - \frac{U_{i-1}(t)}{\bar{Z}_{i-1}^x(t)} \bar{S}_{i-1}^x(t) \right. \\
 & \left. + \frac{V_{i-n}(t)}{\bar{Z}_1^y(t)} \bar{S}_1^y(t) - \frac{V_1(t)}{\bar{Z}_{i+n}^y(t)} \bar{S}_{i+n}^y(t) \right] \\
 & + WP_1(t) S_o - WN_1(t) \frac{S_1(t)}{\bar{Z}_1(t)}
 \end{aligned}$$

5.6

The finite difference representation of the reduced gravity calculation is:

$$G_1(t+\Delta t) = 24 - .8 \frac{S_1(t+\Delta t)}{Z_1(t+\Delta t)}$$

5.7

The finite difference representation of the x-directed momentum equation is:

$$\begin{aligned}
 [U_1(t+\Delta t) - U_1(t)] 1/\Delta t = & f \bar{V}_1(t) \\
 & - \frac{1}{2\Delta l} \left[G_{i+1}(t+\Delta t) (Z_{i+1}(t+\Delta t))^2 - G_1(t+\Delta t) (Z_1(t+\Delta t))^2 \right] \\
 & - K \left[\frac{(U_1(t) - U_T(t) \bar{Z}_1^x(t))}{(\bar{Z}_1^x(t))} \right. \\
 & \left. \sqrt{(U_1(t) - U_T(t) \bar{Z}_1^x(t))^2 + (\bar{V}_1(t) - V_T(t) \bar{Z}_1^x(t))^2} \right] \\
 & - \frac{1}{\Delta l} \left[\frac{(\bar{U}_1^x(t))^2}{\bar{Z}_1(t)} - \frac{(\bar{U}_{i-1}^x(t))^2}{\bar{Z}_{i-1}^x(t)} \right] \\
 & - \frac{1}{\Delta l} \left[\frac{\bar{U}_1^y(t) \bar{V}_{i-n}^x(t)}{\bar{Z}_1} - \frac{\bar{U}_{i+n}^y(t) \bar{V}_1^x(t)}{\bar{Z}_{i-n}} \right]
 \end{aligned}$$

$$\begin{aligned}
& -g \text{TSX}_i(t) + \overline{\text{WP}}_i^x(t) U_0(t) - \overline{\text{WN}}_i^y(t) \frac{U_i(t)}{\bar{Z}_i^x(t)} \\
& + \frac{\bar{Z}_i^x}{(\Delta \ell)^2} \left[A_{i+1} \left(\frac{U_{i+1}(t)}{\bar{Z}_{i+1}^x(t)} - \frac{U_i(t)}{\bar{Z}_i^x(t)} \right) \right. \\
& + A_{i-1} \left(\frac{U_{i-1}(t)}{\bar{Z}_{i-1}^x(t)} - \frac{U_i(t)}{\bar{Z}_i^x(t)} \right) + A_{i+n} \left(\frac{U_{i+n}(t)}{\bar{Z}_{i+n}^x(t)} - \frac{U_i(t)}{\bar{Z}_i^x(t)} \right) \\
& \left. + A_{i-n} \left(\frac{U_{i-n}(t)}{\bar{Z}_{i-n}^x(t)} - \frac{U_i(t)}{\bar{Z}_i^x(t)} \right) \right]
\end{aligned}$$

5.8

The finite difference representation of the y-directed momentum equation is:

$$\begin{aligned}
& \left[v_i(t+\Delta t) - v_i(t) \right] 1/\Delta t = f \bar{U}_i(t+\Delta t) \\
& - \frac{1}{2\Delta \ell} \left[G_i(t+\Delta t) (Z_i(t+\Delta t))^2 - G_{i+n}(t+\Delta t) (Z_{i+n}(t+\Delta t))^2 \right] \\
& - K \frac{(v_i(t) - v_T(t) \bar{Z}_{i+n}^y(t))}{(\bar{Z}_{i+n}^y(t))^2} \\
& \sqrt{(v_i(t) - v_T(t) \bar{Z}_{i+n}^y(t))^2 + (\bar{U}_i(t) - U_T(t) \bar{Z}_{i+n}^y(t))^2} \\
& - \frac{1}{\Delta \ell} \left[\frac{\bar{U}_{i+n}^y(t) \bar{V}_i^x(t)}{\bar{Z}_{i+n}^y(t)} - \frac{\bar{U}_{i+n-1}^y(t) \bar{V}_{i-1}^x(t)}{\bar{Z}_{i+n-1}^y(t)} \right] \\
& - \frac{1}{\Delta \ell} \left[\frac{(\bar{V}_{i+n}^y(t))^2}{\bar{Z}_{i+n}^y(t)} - \frac{(\bar{V}_i^y(t))^2}{\bar{Z}_i^y(t)} \right]
\end{aligned}$$

$$\begin{aligned}
& + \overline{WP}_{i+n}^y(t) V_0(t) - \overline{WN}_{i+n}^y(t) \frac{V_i(t)}{\bar{z}_{i+n}^y(t)} - g \text{TSY}_i(t) \\
& + \frac{\bar{z}_{i+n}^y(t)}{(\Delta z)^2} \left[A_{i+1} \left(\frac{V_{i+1}(t)}{\bar{z}_{i+n+1}^y(t)} - \frac{V_i(t)}{\bar{z}_{i+n}^y(t)} \right) \right. \\
& + A_{i-n} \left(\frac{V_{i-1}(t)}{\bar{z}_{i+n-1}^y(t)} - \frac{V_i(t)}{\bar{z}_{i+n}^y(t)} \right) + A_{i+n} \left(\frac{V_{i+n}(t)}{\bar{z}_{i+2n}^y(t)} - \frac{V_i(t)}{\bar{z}_{i+n}^y(t)} \right) \\
& \left. + A_{i-n} \left(\frac{V_{i-n}(t)}{\bar{z}_i^y(t)} - \frac{V_i(t)}{\bar{z}_{i+n}^y(t)} \right) \right]
\end{aligned}$$

5.9.

where TSX_i and TSY_i are the slopes of the water surface as obtained from a barotropic tidal model of the same area.

The time structure of these equations is quite important. In each computational cycle, the thickness Z_i and salt content S_i are calculated using values of the derivatives of U_i and V_i from the previous timestep. Then, U_i are calculated, using the derivatives of Z_i and S_i (or g_i) from the current timestep, and the previous values of V_i in the Coriolis term. Finally, V_i are calculated, using derivatives of the current Z_i , and S_i , and also the current U_i in the Coriolis term. In the entrainment, depletion, and friction functions, and the non-linear and eddy viscosity terms, the values of U_i , V_i , and S_i from the previous timestep are always used.

When using finite difference methods to solve non-linear partial differential equations, one is always concerned with the accuracy of the solution and under what conditions the scheme chosen is stable. Accuracy is best assessed by comparing the

numerical solution to an analytic solution, or possibly to real observed data. Stability analysis, discussed in the appendix, is usually done for the linearized equations, in the hope that the requirements in the non-linear case are not much different (local stability, Richtmyer and Morton, 1967).

THE SQUARE BOX MODEL

Modelling was started using a linearized form of the equations without tidal forcing, and with constant density:

$$\frac{\partial h}{\partial t} + \frac{\partial u}{\partial x} + \frac{\partial v}{\partial y} = 0.$$

$$\frac{\partial u}{\partial t} + g' h \frac{\partial h}{\partial x} + r u = 0.$$

$$\frac{\partial v}{\partial t} + g' h \frac{\partial h}{\partial y} + r v = 0.$$

The river flow was specified by $U_0 \tanh(t/T_0)$, where T_0 was 200 timesteps. U_0 was 50,000 cm²/sec, Δx was 10⁵ cm, so that $U \Delta x$, the river discharge, was 5000 m³/sec, approximately one half the freshet value. g' was 10 cm/sec², and the timestep was 480 sec. With friction given by $r = .005/h$ sec⁻¹ the thickness over the entire area varied only between 503 and 515 cm, and velocities varied from 30 cm/sec at the river mouth to 3-5 cm/sec at the outflow boundaries. These are not unreasonable values of velocity and thickness for a time-averaged plume - Chapter 2. Figure 69 shows a plot of the flux out of the open ends versus time, illustrating the initially rapid, and then very slow, approach to equilibrium. At the open ends, the boundary condition used was $\partial^2 h / \partial n^2 = 0$, where n is the direction normal to the outflow boundary (y -direction in this case). This boundary

condition was chosen as being the simplest one which stated that there was little spatial change of important flow properties near the open boundary, and still allowed there to be time-varying conditions at these open boundaries. The river mouth boundary condition was the specification of a transport. We are thus assuming subcritical flow, since only one boundary condition is specified. The internal Froude number is $\sqrt{30^2/(10 \times 500)} = 0.45$, so the flow, as determined by the friction in the system, is indeed subcritical.

The next step was to add the convective acceleration terms to the equations of motion. Since the real plume is near critical near the river mouth, the gradient of u^2 is as important as the gradient of $1/2g'h^2$. When these terms were added, the grid adjacent to the river mouth became very unstable, with the depth rapidly decreasing and the velocity rapidly increasing as the river flow was turned on. When square law friction and entrainment were added, this problem was eliminated. The entrainment was written as $w_p = 0.0064U^2/(g'h^3)$. This is a deviation from the intent that w_p should be written as Eu , where E is a constant times the Froude number squared, $U^2/(g'h^3)$, which would make w_p proportional to U^3 (Long, 1975a). Interestingly, the real geometry model, discussed later, indicated that 2 was too large a power of U in the entrainment formula. Values of the friction coefficient between 0.001 and 0.007 were used in the course of the modelling discussed below.

With the addition of these two momentum dissipators, (entrainment and square law friction), the region around the river mouth was stable. However, the outflow boundary was now

unstable. This problem was cured by specifying the Froude number at the outflow to be a constant. Figures 70, 71, and 72 show the flow field produced by the model at this stage. Δx was .33 km, Δt was 120 sec, g' was 10 cm/sec. The river discharge was given by $U=0.5xU_0(1-\cos(2 t/T_0))$, attaining its maximum value of 2000 m³/sec at 6 hours, and remaining at that value thereafter. This river inflow was divided among three grid meshes, for a river mouth width of 1 km. The outflow Froude number was 0.333, and the friction constant was 0.001.

When the model incorporating the non-linear terms was run for an extended period of time, it developed what was presumably the well-known non-linear instability - the production of short waves by the non-linear terms, and their retention within the system because of their slow phase speed. Note the noodling of velocity vectors in Fig. 72, particularly along the solid boundaries. As discussed in the appendix, for the system used here, the phase speed is $\sqrt{g'h_0} \frac{\sin K\Delta/2}{K\Delta/2}$. For $\lambda=2\Delta$, this is $0.6\sqrt{g'h_0}$. Figure 73a shows the effect these small scale oscillations have on the influx to the system (river flow plus total entrainment), and the total efflux out of the open boundaries. We would like the two curves to approach each other, and then remain flat. To achieve a steady state, horizontal eddy viscosity was introduced. At solid boundaries the eddy viscosity was taken to be zero; elsewhere 10³ cm²/sec, so that there was no net change in the momentum of the system due to sidewall friction. Figure 74 and 75 show the resulting model velocity fields at two times, with other conditions identical to Figures 70 and 71. Figure 73b shows how the influx and efflux quickly

approach an equilibrium level.

The question arises, what is the correct value to specify as the outflow Froude number? It turns out that it doesn't matter very much. Figure 76 shows the result of allowing an initial hump of water (the distribution of elevation is $h=50\exp(-y^2/6^2)$, with y measured in units of Δl), shown as small dashes, to propagate outward (elevations were uniform in the x -direction, the greatest thickness being off the river mouth). The large dashes show the hump just as it is passing through the open boundary, 12 meshes from $y=0$, for $F^2=0.33$. For $F^2=1$, the curve is identical, except that the depth in the last mesh, indicated by a solid dot, is 11 cm less than for $F^2=0.33$. Similarly, the velocity curves (solid line) were identical, except for the last mesh, where the velocity was 2 cm/sec faster for the $F^2=1$ case. It appears that a flow like the plume travels like a kinematic wave - the dynamics are mainly controlled by friction, and we need prescribe a boundary condition at the upstream end only. This of course applies only if the flow is reasonably strongly outward at the open boundaries. In his book, Whitham (1974) describes how the effective order of a partial differential equation decreases, under the effect of friction, for a linear case, and the plume seems to be an example of this phenomenon for a non-linear case.

We are concerned with dispersion in a numerical scheme. In the linear case, we want, for example, all disturbances to propagate at $\sqrt{g'h}$. It is difficult to check how well a scheme is working in the non-linear case, because of the lack of analytic solutions. However, we know that if there is a disturbance

propagating into a region, with the fields continuous, but their spatial derivatives discontinuous, then that disturbance travels at the local characteristic speed, before it breaks (Whitham, 1974). Thus, a "gentle" disturbance propagates at $u + \sqrt{g'h}$. We can see this in Figure 77, which is a plot, in the direction normal to the river opening, of u and h from Figure 74. The disturbance is a bulge of water propagating out from the river mouth. It has travelled about $10\Delta x$, and $(u + \sqrt{g'h}) 100\Delta t$, evaluated at the front, is $9.95\Delta x$. The agreement in the calculation of the position of the front is of course a crude verification, but it is encouraging to note the front of the disturbance moving at a speed greater than $\sqrt{g'h}$. U is about 25% of $\sqrt{g'h}$, so the faster propagation speed due to the non-linear effect should be apparent, which it is. We have implicitly assumed that u and h at the front were constant at all times. Figure 77 is drawn for timestep 100. At timestep 50, u was 5 cm/sec (the same as at timestep 100), and h was 42 cm (versus 44 cm at timestep 100), so there is little temporal variation of properties at the front.

Another question, related to dispersion, concerns the effect of grid size on the solution. In Figures 78, 79, 80, and 81 we compare the results of two different solutions to the same problem. Part A of each figure shows the distribution of h , w , u , and v from the model discussed so far ($\Delta x = 0.33$ km, $\Delta t = 120$ sec, $Q_{max} = 2000 \text{ m}^3/\text{sec}$), and part B shows the same fields at the same time for a larger-scale model ($\Delta x = 1$ km, $\Delta t = 240$ sec, $Q_{max} = 2000 \text{ m}^3/\text{sec}$). Each number in part A was obtained by averaging over 9 meshes, corresponding to 1 mesh for the part B fields. In

general, the agreement is better than 10%, except in the outer meshes of the plume. Here, one is getting close to the boundary in the 0.33 km mesh model, and the 1 km mesh model is having trouble resolving the situation at the front.

TIDAL EFFECTS IN THE BOX MODEL

The next items to be included were the tidal effects. First the effects of tidal elevations, then tidal currents, and finally varying river flow were introduced. The phases and amplitudes of the tide approximated those in the Strait of Georgia, for an M2 constituent only. The period was taken to be 12 hours, for computational ease. The tidal parameters chosen were:

$$\zeta = \zeta_0 \cos(\omega t - 24^\circ);$$

$$v = 20 \cos(\omega t - 132^\circ);$$

$$U_{\text{river}} = U_0/2 (1 - \cos \omega t);$$

$$\frac{\partial \zeta}{\partial y} = \frac{10}{24 \Delta x} \cos(\omega t - 204^\circ).$$

Note that low water corresponds to maximum $\partial \zeta / \partial y$, maximum river flow occurs about 0.7 hours (24 degrees of phase) before low water (as determined from the surface current meter, Chapter 2), and maximum streams lead the elevation by 72 degrees, a typical value for the Strait. Cross channel slopes and streams were assumed to be zero, for simplicity only.

When these tidal effects were added, it was found that the flows near boundaries were anomalous. Figure 82 shows the flow

field from a model with the constant Froude number boundary condition and Coriolis force. The presence of the Coriolis force causes the flow to have a large cross-channel component which would not be present if a more realistic tide with cross-channel slopes were prescribed. The flow near the inflow boundary bears little relation to the flow in the interior flow field. The object in selecting a boundary condition was that the flow at the open boundaries should look like a smooth extrapolation of the flow in the interior. It was found that specifying $\partial^2 F^2 / \partial n^2 = 0$ at the open boundary was a satisfactory boundary condition in this respect - the flow reversed directions (due to tidal forcing) at about the same time everywhere in the model, and didn't pile up at the boundaries. Figure 83 shows the flow field with this boundary condition, with tidal elevations, Coriolis force, and constant river flow. Figure 84 shows the same flow field, but for much lower friction ($K=0.005$ in the first case, 0.001 in this case.) During the course of subsequent experiments, it was found that a better outflow boundary condition (in terms of the uniformity of the flow field) was to calculate the velocity based on $\partial^2 F^2 / \partial n^2 = 0$, and then average this with the velocity one mesh in from the boundary.

SALINITY CALCULATION

At this point, the calculation of the salinity distribution was started. Initially, the leapfrog scheme was used, but was dropped, because of the computational mode, discussed in the Appendix. It was intended to use the Richtmeyer scheme, but due to a programming error, the second order correction was omitted, so in effect only a first order scheme was used for the salt

advection equation. The inclusion of the density effect of the salt introduced no problem, as long as the variable g' was used in the calculation of the Froude number for the outflow boundary condition. The salinity boundary condition was that on inflow the salinity took on the value it had on the last outflow.

Figures 85 to 91 show a sequence of vector diagrams for a run with tidal elevations, constant river flow, density based on salinity, and no Coriolis force. The friction constant was 0.005, Δt was 120 sec. Δx was 10^5 cm, (1 km), the river flow was $2000 \text{ m}^3/\text{sec}$, and the entrainment flux varied between 2000 and $7000 \text{ m}^3/\text{sec}$, depending on the stage of the tide. Figures 92 to 95 show how the velocity field advected the salinity and thickness fields back and forth due to the tide. There should be perfect left-right symmetry between figures 92 and 93, and between 94 and 95, in the absence of a Coriolis force, and with a 12 hour tide. It was found later that specifying a somewhat high (20 ppt) salinity on inflow removed some of the asymmetry present, but there was still some left (presumably a start-up transient that persists, which we don't as yet know how to damp out effectively).

ROLE OF DEPLETION

It was at this stage that the requirement of the depletion mechanism was becoming apparent. The first clue was that with w_p proportional to $1/g'$, there was too much entrainment in the far field, where g' was small. The plume increased in both thickness and salinity as one proceeded out from the river mouth - Figures 92 to 95. The rate of increase of volume was decreased somewhat by replacing $1/g'$ with $1/24$ in the entrainment function. There

are two sources of water to the plume, river flow and entrainment, and there was no loss in the model, so the plume continually got thicker, in the absence of depletion. In an effort to improve this situation, I specified that the outflow be a slight bit larger (outflow Froude number increased by 0.03) than that calculated by $\partial^2 F^2 / \partial n^2 = 0$. The results are interesting. Figure 96 shows drogue tracks released into a flow in which $\partial^2 F^2 / \partial n^2 = 0$ was the boundary condition; the flow field was that of the series in Figs. 85 to 91. Figure 97 shows the resulting drogue tracks when the open boundary Froude number was calculated to make $\partial^2 F^2 / \partial n^2 = 0$, and then had 0.03 added to it during outflow conditions. This was done to create an extra flow on the outflow stage, to balance the entrainment. Figure 98 shows a typical velocity field. One cannot help but feel that the way in which the drogues diverge in Figure 97 is very unlike their behaviour in the plume as shown in Figure 99 from Cordes (1977). Part of the reason for the divergence is that the excess outflow drained the system, so that the average depth was 250 cm for Fig 97, and about 450 cm for Fig. 96. This would tend to favour any buoyant spreading tendency in Fig 97. It seems that depletion might do a better job, in that it removes mass and momentum at the same rate, leaving the velocity field unchanged.

If

$$\frac{\partial h}{\partial t} = -w_n, \quad \frac{\partial uh}{\partial t} = -uw_n,$$

then

$$\frac{\partial u}{\partial t} = \frac{1}{h} \left(\frac{\partial uh}{\partial t} - u \frac{\partial h}{\partial t} \right) = \frac{1}{h} (-u w_n + u w_n) = 0.$$

As mentioned with respect to the salinity distribution, it was difficult to get rid of the left-right asymmetry in the density, elevation and velocity fields. One expects, in the absence of the Coriolis force, that there should be only a 6 hour periodicity in the total discharge out of the model with constant river flow. Figure 100 is a plot of the discharge out of a model with constant river flow and no Coriolis force, but with tidal streams and elevations. The amplitude of the 12 hour periodicity is decreasing but not as fast as one would like.

As a final test of the square box model without depletion, drogues were released into the flow at four different stages of the tide - Figures 101 to 104. The model had variable river flow, Coriolis force, and tidal slopes and streams. The drogue paths are not very similar to those of figure 99. There are two reasons for this. First, the average river discharge, 1000 m³/sec, is much lower than the freshet conditions the drogue tracks apply to. Second, because there was no depletion, the upper layer had grown very thick over the time before the drogues were installed (about 10 meters), so the river momentum was rather insignificant compared to the tidal momentum. It is nevertheless interesting to note that drogues released at different stages of the tide occupy different regions of the model Strait.

TESTING DEPLETION

In an effort to understand the effects of adding depletion, w_n , a few experiments were carried out. The entrainment velocity, w_p , was kept the same, and the depletion velocity was specified as $w_n = .0001S/200$. Thus, depletion was proportional to the product of salinity and thickness. As predicted, it served to thin the plume in the outer regions. A run was done with tidal elevations, constant river flow, and no Coriolis force. Conditions are the same as for figures 85 to 91, and since the velocity fields are almost identical, only one is shown. The velocity field at 62 hours, corresponding to the same tidal phase as Figure 86, is shown in Figure 105, and Figure 106 shows the drogue tracks corresponding to Figure 96. Figure 107 shows the elevation field corresponding to Figure 94, and Figure 108 corresponds to 95. The depletion velocity was rather large, but the object of these runs was to obtain a very significant depletion effect for demonstration purposes. Since Figures 107 and 108 show a thinning plume it is apparent that depletion is having its predicted effect. The drogue tracks spread out more than we would perhaps like, but this is due to the excessive thinning produced by depletion, giving buoyant spreading greater relative importance. The fact that Figures 107 and 108 are mirror images of each other whereas 94 and 95 are not indicates that depletion is perhaps an effective way to damp out startup transients which arise when one turns on tidal forcing.

REAL GEOMETRY MODEL

Since all the terms essential to the plume dynamics had been investigated with the square box model, it appeared appropriate to investigate the behaviour of the model in a real geometry situation. Unfortunately, the physical transfer of tidal forcing from the barotropic model had not been worked out in time, so an ad hoc approximation to the M2 tide was used. (the tidal forcing was similar to that in the square box model, with the tidal slopes and streams being increased in the region of the river mouth, to model the effect of the narrowing of the Strait in that area. In reality there is a larger cross-channel slope than down-channel, but the M2 tide used had only a downchannel slope.) The grid size used was 2 km which was the same as the tidal model of Crean (1977). Only two passes in the south were kept open- Haro Strait and Boundary Pass, and the shallow banks near Sand Heads were replaced with solid walls. The mean river flow was $4000 \text{ m}^3/\text{sec}$. Figure 109 shows a plot of velocity vectors at the time of maximum river flow. Figures 110 and 111 show the growth and advection of a bulge of water during 6 hours of flood tide. Figure 112 shows the drogue tracks, for drogues released at maximum river flow.

It was found when working with the larger river velocities of this model that the square-law entrainment was too large near the river mouth - starting with 0 ‰ salinity everywhere, the model was entraining more salt water in the mesh adjacent to the river than there was fresh water flowing in. It was decided to switch to an entrainment velocity which was linearly proportional to the flow velocity, based on the following

argument. During the summer, the plume is fastest and freshest. Thus, $s \propto u^{-\mu}$, where μ is probably smaller than 1. The salinity is approximately given by $s \sim w_p/u$, the ratio of entrainment velocity to flow rate. Combining these we get

$$w \sim s u \sim u^{1-\mu},$$

not $w \propto u^2$, and closer to $w \propto u^1$.

The entrainment velocity was given by $w_p = 0.0001 \sqrt{u^2 + v^2}$, where u_r and v_r are the velocities relative to the tidal streams. The depletion velocity was given by

$$w_n = 0 \text{ if } g' > 12;$$

$w_n = 0.00025(24 - g')$ if $g' < 12$. Thus, depletion is assumed to act only when the salinity is greater than 15 ‰, ($g' = 12$ at $s = 15$ ‰), and increases as the salinity increases.

The eddy viscosity was increased to $10^4 \text{ cm}^2/\text{sec}$.

The river mouth boundary condition was to specify two components of transport, U and V , in the ratio such that $U/V = \tan I$, where I is the inclination of the Sand Heads jetty to the grid system. For the momentum equations one mesh downstream (in both x and y directions), a correction, corresponding to replacing $\partial/\partial x (U^2/h)$ with $1/b \partial/\partial x (U^2 b/h)$ was made, where b is the projected width of the river in each direction (a very ambiguous quantity). It was further necessary to set the cross-stream transport of downstream river momentum ($\partial/\partial y (UV/h)$) equal to zero for the two velocity locations adjacent to, but not downstream of, the river mouth, (essentially because the grid could not resolve the very sharp cross-stream gradient of downstream velocity, transporting too much momentum to the two adjacent meshes, and draining them).

The final test of the model was to specify a tide made up of the two most important constituents in the Strait of Georgia, M2 and K1, and to use a mean river flow of 8000 m³/sec, to match the conditions of Cordes' experiment (1977). Figure 113 shows the tidal elevations (proportional to the negative of the downchannel slopes), tidal streams (proportional to the crosschannel slopes by the geostrophic relation, since the cross-stream velocity is very small), and river flow used in this run. The elevations and velocities were normalized so that the M2 constituent had amplitude unity; the river discharge was normalized so that the mean mass discharge rate was unity. The slopes and velocities used in this experiment were obtained by multiplying the normalized value by an approximate magnitude, obtained by dividing the model into 7 areas and determining the magnitudes of slopes and streams by visual inspection of the output from Crean's (1977) model. Figure 114 shows the distribution of velocities (cm/sec) and slopes (cm/2km) to be multiplied by the phase factor of Figure 113 to obtain the tidal forcing used. The velocity fields and drogue tracks are shown in figures 115 to 122. The drogue tracks were still not quite like those of Figure 99. The tracks of Figure 122 were repeated using a correction for the fact that the drogues were travelling in a vertically sheared flow. As shown by Buckley (1977), a drogue travelling in a linearly sheared flow travels at the average velocity over its depth. It can be shown that if the drogue is not as deep as the upper layer, and one assumes a linear shear, with the velocity at the bottom of the upper layer being the tidal velocity, the speed of the drogue is given by

$$U_{\text{drogue}} = U_{\text{mean}} + (1 - z/h)(U_{\text{mean}} - U_0)$$

With this correction, the drogue tracks of figure 123 were obtained. Figure 124 is a replotting of Figure 123, to coincide with Figure 99. There is considerable agreement between Figures 99 and 124. Figures 125 to 129 show the growth and break-up of a bulge of water discharged by the river.

Although the model has not been verified in all respects, it appears to be capable of adjustment to fit Nature. The top priority is to work out the logistics of using actual tidal forcing from the model of Crean (1977). The ad hoc tidal parameterization used to generate Figures 115-129 was unfortunate in that the tidal streams prescribed tended to pull upper layer water away from coastlines perpendicular to the main axis of the Strait. Consequently, several areas had to be removed from the model, resulting in the blank area north of Haro Strait in, for example, Figure 117-119.

CHAPTER 6

CONCLUDING DISCUSSION

It is difficult to draw precise conclusions from the work described in this thesis; since the dynamics of the upper layer are very complicated, the work described here can only be considered as a first stage. With the above qualification, I would like now to summarize what this thesis accomplished, and then discuss what types of work it leads to.

Considerable insight into the plume was obtained by acquiring the fairly synoptic STD sections of Chapter 2. The velocity profiles obtained, although few in number, were crucial in deciding that the plume could be modelled successfully as a separate upper layer. The simple model of a discontinuous front, Chapter 4, section 2, pointed out the possibility of a great deal of mixing at a front, and the large form drag at the front. Many models of plumes and jets have used the concept of entrainment across a permeable interface, but the concept of depletion is, I think, relatively recent (Winter, Pearson, and Jamart, 1977; Stronach, Crean, and Leblond, 1977). Finally, the development of a numerical model was a major effort of this work. The immediate aim in developing the model was to have a system of equations, and the corresponding computer code, which included all the terms which were thought of significance (with the exception of winds); and to learn how to deal with open outflow boundaries in a non-linear flow. These goals appear to have been successfully accomplished. Indeed, the drogue tracks produced by the model compare quite favorably to those of Cordes (1977), when a reasonable approximation to the barotropic tide

is used, and without any adjustment of the parameters of the model other than those required to obtain stability of the solution.

Now, to discuss the most immediate improvements to be considered. First, one can always use more field measurements in refining a model. There are two regions where the dynamics are particularly puzzling. One is in the vicinity of the outflow boundaries, where we really know very little of the temporal nature of the upper layer fluxes of mass, momentum, and salt. The other area is the complicated geometry around the river mouth (Figure 4). We would like to include the other minor openings (Canoe Pass, North Arm, Middle Arm), and also include, in some way, the effects of the flow of shallow, brackish water over the banks, particularly Roberts Bank. Even putting aside these geometrical complications, in the model developed here, we did not use a critical or supercritical boundary condition at the river mouth. There is probably an entraining hydraulic jump at the river mouth, followed by subcritical flow downstream of the jump, so that specification of only one flow parameter at the river mouth, (the discharge), is perhaps adequate. However, since there is such intense mixing due to this presumed jump at the river mouth, one would like to have a better idea of what is going on there. Since we observe (Fig. 25b) considerable change over a short distance near the river mouth, and are using a rather coarse grid, a description of the river mouth dynamics, suitable for a coarse grid model, needs to be developed.

As far as the numerical model is concerned, the specification of friction, entrainment, and depletion is always

open to question. To a certain extent, we don't even know the functional forms to give to these effects, let alone the constant in front. The closeness of the model predictions and field results indicate that we have the sizes of these effects approximately correct. We would like to incorporate the effects of winds in the model. The simplest thing is to put all the wind stress, $1/2 C_D U^2$, into the upper layer. Complications arise, for example, if the wind blows for too long, and mixes away the plume, a problem which cannot be handled at this stage of model development.

It has recently been observed, (Chang, 1976), that there is considerable energy in low frequency (periods greater than 4 days) oscillations. The effect of this temporal variability on plume motion needs to be assessed, as does the amount and effect of baroclinicity in the currents and pressure gradients beneath the plume.

As mentioned in Chapter 4, section 6, there is a possibility that we should learn how to deal with surfacing isopycnals in the model. This brings up the intriguing possibility of a 2-layer plume, a section through which is shown in Figure 130. For arguments sake, we will assume that at the northern end of the plume, there is an outflow boundary, a situation we have dealt with in the model so far. At the southern end, there is a surfacing isopycnal, and some development of the model must be done to accomodate this situation. There may be an additional boundary, indicated NP in Figure 130. This is the boundary between the existing plume (representing several days discharge), and the much fresher

water discharged during the current tidal cycle. The boundary of this current plume would be the intense colour front found in the Strait. Numerically, we would have to learn how to move this front, and how to eventually incorporate "new plume" into "existing plume". When the upper layer model is thought to be adequately refined, it could be used as the upper layer of a conventional 3-dimensional model (Leendertse, Alexander, and Liu, 1973). The topmost layer of the of the 3-dimensional model would have as its free surface the interface between the upper and lower layers as defined in this research. The interfacial fluxes of mass, salt and momentum found in the plume model would then be applied to the 3-dimensional model, with of course their signs reversed. In this way one is letting the physics of the situation (a strong pycnocline at a variable depth) dictate the type of numerical schemes employed to model it.

REFERENCES CITED

Abramovich, G. N. 1963. The Theory of Turbulent Jets. The M.I.T. Press, Cambridge, Mass. 671p.

Bondar, C. 1970. Considerations theorique sur la dispersion d'un courante liquide de densite reduite et a niveau libre, dans un bassin contenant un liquid d'un plus grand densite. Symposium on the Hydrology of Deltas, UNESCO, 11, 246-256.

Buckley, J. R. 1977. Currents, Wind, and Tide in Howe Sound. Ph.D. Thesis. University of British Columbia. 255 p.

Charney, J. G. 1955. The Gulf Stream as an inertial boundary layer. Proceedings of the National Academy of Sciences. 41, 731-740.

Chang, P. Y. K. 1976. Subsurface currents in the Strait of Georgia, west of Sturgeon Bank. M.Sc. Thesis. University of British Columbia. 181 p.

Cordes, R. E. 1977. Measurements of the velocity field in the Fraser River plume. M.Sc. Thesis. University of British Columbia. 137 p.

Crean, P. B. 1976. Numerical model studies of the tides between Vancouver Island and the mainland coast. J. Fish. Res. Bd. Canada. 33. 2340-2344.

Crean, P. B. 1977. A numerical model simulation of barotropic mixed tides in the water between Vancouver Island and the mainland and the relevance to the estuarine circulation. To appear in Proceedings of the 9th Liege Colloquium on Ocean Hydrodynamics. Elsevier, Amsterdam.

Crean, P. B. And A. B. Ages. 1971. Oceanographic records from twelve cruises in the Strait of Georgia and Juan de Fuca Strait, 1968. Department of Energy, Mines and Resources, Marine Sciences Branch, Victoria.

De Lange Boom, B. R. 1976. Mathematical modelling of the chlorophyll distribution in the Fraser River plume, British Columbia. M. Sc. Thesis. University of British Columbia. 140 p.

Flather, R. A., and N. S. Heaps. 1975. Tidal computations for Morecambe Bay. Geophys. J. R. Astr. Soc. 42: 487-517.

Garvine, R. W. 1974. Dynamics of small-scale oceanic fronts. J. Phys. Oceanogr. 4: 557-569.

Garvine, R. W. 1977. Observations of the motion field of the Connecticut River plume. J. Geophys. Res. 83: 441-454.

Garvine, R. W., and J. D. Monk. 1974. Frontal Structure of a river plume. J. Geophys. Res. 79: 2251-2259.

Giovando, L. F. And S. Tabata. 1970. Measurements of surface

flow in the Strait of Georgia by means of free-floating current followers. Fish. Res. Bd. Canada, technical report no. 163. 69 p.

Godin, G. 1972. The Analysis of Tides. University of Toronto Press, Toronto. 264 p.

Herlinveaux, R. H., and J. P. Tully. 1961. Some oceanographic features of Juan de Fuca Strait. J. Fish. Res. Bd. Canada. 18:1027-1071.

Hodgins, D. O. 1974. Salinity intrusion in the Fraser River, British Columbia. Ph. D. Thesis. University of British Columbia. 147 p.

Ippen, A. T. Mechanics of Supercritical flow. Trans. of the American Soc. Civil Engineers. 116: 268-295.

Kasahara, A., E. Isaacson, and J. J. Stoker. 1965. Numerical studies of frontal motion in the atmosphere. Tellus 17: 261-276.

Koh, R. C. Y., and L-N. Fan. 1970. Mathematical models for the prediction of temperature distributions resulting from the discharge of heated water into large bodies of water. Water Quality Office, Environmental Protection Agency, Washington, U. S. A. 219 p.

Launder, B. E., and D. B. Spalding. 1972. Lectures in

mathematical models of turbulence. Academic Press, London and New York. 169 p.

Leendertse, J. J., R. C. Alexander, and S-K. Liu. 1973. A three dimensional model for estuaries and coastal seas: vol. 1, principles of computation. The Rand Corporation, R-1417. 57p.

Lofquist, K. 1960. Flow and stress near an interface between stratified fluids. The Physics of Fluids. 3: 158 - 175.

Long, R. R. 1975a. The influence of shear on mixing across density interfaces. J. F. M. 70: 305 - 320.

Long, R. R. 1975b. Circulation and density distributions in a deep, strongly stratified, 2 layer estuary. J. F. M. 71: 529-540.

Richtmyer, R. D., and K. W. Morton. 1967. Difference Methods for Initial Value Problems. Interscience Publishers, New York. 405 p.

Rouse, H., B. V. Bhoota, and E-Y. Hsu. 1951. Design of Channel Expansions. Trans. of the American Soc. Civil Engineers. 116: 347-363.

Shapiro, A. H., and G. M. Edelman. 1947. Method of characteristics for two dimensional supersonic flow - graphical and numerical. Journal of Applied Mechanics. Pp A154-A162. (part

of Trans. Am. Soc. Mech. Eng. Vol. 69.)

Stolzenbach, K. D., and D. P. Harleman. 1971. An analytic and experimental investigation of surface discharge of heated water. Ralph M. Parsons Laboratory for Water Resources and Hydrdynamics, MIT, Report no. 135. 212 p.

Stronach, J. A., P. B. Crean, and P. H. Leblond. 1977. An upper layer model of the Fraser River plume. Paper presented at the 9th Liege Colloquim on Ocean hydrodynamics.

Tabata, S. 1972. The movement of Fraser River -influenced water as deduced from a series of aerial photographs. Marine Sciences Branch, Pacific Region, Pacific Marine Science Report no. 72-6. 69 p.

Takano, K. 1954a. On the velocity distribution off the mouth of a river. J. Oceanogr. Soc. Japan. 10: 60-64.

Takano, K. 1954b. On the salinity and velocity distribution off the mouth of a river. J. Oceanogr. Soc. Jap. 10: 92-98.

Takano, K. 1955. A complimentary note on the diffusion of the seaward flow off the mouth of a river. J. Oceanogr. Soc. Japan. 11: 1-3.

Turner, J. S. 1973. Buoyancy Effects in Fluids. 1973. Cambridge (England) Univ. Press. 367 p.

Waldichuk, M. 1957. Physical oceanography of the Strait of Georgia, British Columbia. J. Fish. Res. Bd. Canada. 14: 321-486.

Whitham, G. B. 1974. Linear and Non-linear Waves. Wiley-Interscience, New York. 636 p.

Winter, D. F., Pearson, C. E., and B. M. Jamart. 1977. Two layer analysis of steady circulation in stratified fjords. Paper presented at the 9th Liege Colloquium on Ocean Hydrodynamics.

Wright, L. D., and J. M. Coleman. 1971. Effluent expansion and interfacial mixing in the presence of a salt wedge, Mississippi River delta. J. Geophys. Res. 76: 8649-8661.

APPENDIXLINEAR STABILITY ANALYSIS

Certain parts of the following discussion are based on unpublished notes by R. Flather.

Consider the set of equations:

$$\frac{\partial h}{\partial t} + \frac{\partial u}{\partial x} + \frac{\partial v}{\partial y} = 0.$$

$$\frac{\partial u}{\partial t} + gh_0 \frac{\partial h}{\partial x} + fv + ru = 0.$$

$$\frac{\partial v}{\partial t} + gh_0 \frac{\partial h}{\partial y} - fu + rv = 0.$$

If Δ is half the grid spacing, and τ the timestep, the scheme under consideration is:

$$h^{t+\tau} = h^t - \tau/2\Delta (u_{x+\Delta}^t - u_{x-\Delta}^t + v_{y+\Delta}^t - v_{y-\Delta}^t).$$

$$u^{t+\tau} = u^t - \frac{\tau gh_0}{2\Delta} (h_{x+\Delta}^{t+\tau} - h_{x-\Delta}^{t+\tau}) - f v^t \tau - r u^t \tau.$$

$$v^{t+\tau} = v^t - \frac{\tau gh_0}{2\Delta} (h_{y+\Delta}^{t+\tau} - h_{y-\Delta}^{t+\tau}) + f u^t \tau - r v^t \tau.$$

Assume that at any time, the fields of h , u , and v are written as Fourier series, i.e.,

$$u = \sum_{k,l} u_{kl} e^{ikx + ily}.$$

Then consider only one Fourier component, and also define a new h_{kl} equal to $-\sqrt{gh_0} h_{kl}$. Defining

$$ia = \frac{\tau \sqrt{gh_0}}{\Delta} i \sin k\Delta, \quad ib = \frac{\tau \sqrt{gh_0}}{\Delta} i \sin l\Delta,$$

and dropping the k, l subscripts, we have:

$$\begin{pmatrix} h \\ u \\ v \end{pmatrix}^{t+\tau} = \begin{pmatrix} 1 & ia & ib \\ ia & 1-r\tau-a^2 & -ab+f\tau \\ ia f\tau+ib & -ab-a^2 f\tau+f\tau-rf\tau^2 & 1-b^2-abf\tau+f^2\tau^2-r\tau \end{pmatrix} \begin{pmatrix} h \\ u \\ v \end{pmatrix}^t.$$

If we consider the case $r=f=0$, we are left with the simpler system:

$$\begin{pmatrix} h \\ u \\ v \end{pmatrix}^{t+\tau} = \begin{pmatrix} 1 & ia & ib \\ ia & 1-a^2 & -ab \\ ib & -ab & 1-b^2 \end{pmatrix} \begin{pmatrix} h \\ u \\ v \end{pmatrix}^t.$$

This is of the form $\vec{s}^{t+\tau} = G \vec{s}^t$, where

$$\vec{s} = h \begin{pmatrix} 1 \\ 0 \\ 0 \end{pmatrix} + u \begin{pmatrix} 0 \\ 1 \\ 0 \end{pmatrix} + v \begin{pmatrix} 0 \\ 0 \\ 1 \end{pmatrix},$$

and G is the above matrix. If we find a set of eigenvalues λ , and a set of eigenvectors \vec{E}_i for G , then the time structure becomes

$$\vec{E}_i^{t+\tau} = \lambda_i \vec{E}_i^t$$

and

$$\vec{E}_i^{n\tau} = (\lambda_i)^n \vec{E}_i^{t=0}.$$

Clearly, for the solution to be bounded λ_i^n must be bounded, which is true if $|\lambda_i| \leq 1 + O(\tau)$, which is the von Neumann stability condition (Richtmeyer and Morton, 1967). The term of $O(\tau)$ allows for the possibility of exponential growth, which

one would not in general want to exclude. Note that E_i is a quantity of the form

$$\vec{E}_i = \alpha_i h \begin{pmatrix} 1 \\ 0 \\ 0 \end{pmatrix} + \beta_i u \begin{pmatrix} 0 \\ 1 \\ 0 \end{pmatrix} + \gamma_i v \begin{pmatrix} 0 \\ 0 \\ 1 \end{pmatrix},$$

so that knowing $\alpha_i, \beta_i, \gamma_i$, (which is readily done), one could obtain h, u , and v from the three \vec{E}_i 's. Calculating the λ_i according to $\det(G - \lambda \mathbb{1}) = 0$, we obtain:

$$\lambda_1 = 1$$

$$\lambda_{2,3} = 1 - \frac{a^2 + b^2}{2} \pm \sqrt{\left(1 - \frac{a^2 + b^2}{2}\right)^2 - 1}.$$

If $\frac{a^2 + b^2}{2}$ is less than 2, the modulus of $\lambda_{2,3}$ turns out to be exactly one. This is what we want in that the time factor for the analytic case, going from t to $t + \tau$ must be $e^{\pm i\omega\tau}$ for a system without friction, and the modulus of $e^{\pm i\omega\tau}$ is one. $\lambda_1 = 1$ is associated with the eigenvector $-bu + av$, which can be identified with $\tau \sqrt{gh_0} \left(\frac{\sin l\Delta}{\Delta} u - \frac{\sin k\Delta}{\Delta} v \right)$, which for small $k\Delta, l\Delta$, (large wavelengths), can be identified with $\partial u / \partial y - \partial v / \partial x$, the vorticity, which is an invariant since the Coriolis force is absent. We can compare $\lambda_{2,3}$ with $e^{\pm i\omega\tau}$. ω is given by $\sqrt{gh_0} (l^2 + k^2)^{1/2}$. Thus,

$$e^{\pm i\omega\tau} = 1 \pm i \sqrt{gh_0} \tau (l^2 + k^2)^{1/2} - gh_0 \tau^2 (l^2 + k^2) / 2!$$

$$+ i (gh_0)^{3/2} \tau^3 (l^2 + k^2)^{3/2} / 3! \dots$$

$$\lambda_{2,3} = 1 - 1/2 \left[\left(\tau \sqrt{gh_0} \frac{\sin k\Delta}{\Delta} \right)^2 + \left(\tau \sqrt{gh_0} \frac{\sin l\Delta}{\Delta} \right)^2 \right] \\ \pm \frac{i \tau \sqrt{gh_0}}{2\Delta} \left[(2 \sin k\Delta)^2 + (2 \sin l\Delta)^2 \right] (1 - 1/8 (a^2 + b^2) \dots).$$

For $k\Delta \ll 1$, $l\Delta \ll 1$, we have

$$\lambda_{2,3} = 1 \pm i \tau \sqrt{gh_0} (k^2 + l^2)^{1/2} - 1/2 \tau^2 gh_0 (k^2 + l^2) \\ + 1/8 i \tau^3 (gh_0)^{3/2} (k^2 + l^2)^{3/2} \dots$$

Thus the numerical and analytic factors differ in the third order, so one could say the scheme is of second order accuracy in time. This is only true if we can replace $\sin(k\Delta)$ with $k\Delta$, and $\sin(l\Delta)$ with $l\Delta$; that is if there are many meshes per wavelength. Thus, the accuracy of the space differencing (which gave rise to the term $i \sin k\Delta/\Delta$, rather than ik , for the analytic expression for the logarithmic derivative of a sinusoid e^{ikx}) affects our time factor. One could also consider $\lambda_{2,3}$ as the expansion of $e^{i\tau ck}$ (in one dimension), where c is the computational phase speed, which turns out to be $\sqrt{gh_0} \frac{\sin k\Delta}{k\Delta}$.

The requirement that $a^2 + b^2 < 4$ is satisfied if

$$\left(\frac{\tau \sqrt{gh_0}}{\Delta} \right)^2 + \left(\frac{\tau \sqrt{gh_0}}{\Delta} \right)^2 < 4$$

or $\tau \sqrt{gh_0} < \sqrt{2} \Delta$. Realizing that Δ is one half the grid spacing Δl , we get as a stability criterion $\sqrt{2} \tau \sqrt{gh_0} < \Delta l$. This is the stability requirement for a linear model, and we would like to expand it now to a non-linear one. The most straightforward way is to recognize $\sqrt{gh_0}$ as the wavespeed for the linear case, and replace it with $(\sqrt{u^2 + v^2} + \sqrt{gh})_{\max}$, the maximum expected wave speed for the non-linear case. Thus, our final condition is

$$\sqrt{2} \tau (\sqrt{u^2 + v^2} + \sqrt{gh})_{\max} < \Delta l.$$

If $r=0$, $f \neq 0$, the stability requirement can be shown to be:

$$2\tau (\sqrt{u^2+v^2} + \sqrt{gh_0})_{max} < \sqrt{2-f^2} \Delta l.$$

As long as $f\tau \ll 1$ (a very easy condition to satisfy), the Coriolis force places no restriction on the scheme.

If $f=0$, $r \neq 0$, it can be shown that the requirements imposed by friction are $r\tau < 2$, and

$$\sqrt{2}\tau (\sqrt{u^2+v^2} + \sqrt{gh_0})_{max} < \sqrt{1-r\tau/2} \Delta l,$$

which is a more severe form of the $\tau - \Delta l$ relation. One can also see the requirements imposed by friction as follows. Consider the simple equation

$$\frac{\partial u}{\partial t} = -ru$$

with the finite difference approximation

$$u^{t+\tau} = u^t - r\tau u^t.$$

Writing $u^{t+\tau} = \lambda u^t$, we can obtain $\lambda = 1 - r\tau$. Note that these are the first two terms in the expansion of $e^{-r\tau}$, the analytic value for λ . If $r\tau$ is 2, the error in λ is $e^{-2} - (1-2) = 1.14$, about 7 times the true value of λ . If $r\tau = 1$, the error is .37, about the same size as λ . If $r\tau = .5$, the error is .1, about 16% of λ . Thus for accuracy, one wants $r\tau$ to be considerably less than one. Physically, friction cannot remove more momentum from a system than was initially present. Thus, λ should never be negative, and we should minimally replace $r\tau < 2$ with $r\tau < 1$. When applied to the case of non-linear friction, ru is replaced with $Cu|u|$. Thus we require $C\sqrt{u^2+v^2}_{max}\tau < 1$.

We can also look at the effect of entrainment. Consider the set of equations

$$\frac{\partial h}{\partial t} + \frac{\partial u}{\partial x} - wu = 0.$$

$$\frac{\partial u}{\partial t} + gh_0 \frac{\partial h}{\partial x} = 0.$$

In the scheme adopted here these have finite difference representation

$$h^{t+\tau} = h^t - \tau/2\Delta (u_{x+\Delta}^t - u_{x-\Delta}^t) + w\tau/2 (u_{x+\Delta}^t + u_{x-\Delta}^t).$$

$$u^{t+\tau} = u^t - \frac{gh_0}{2\Delta} (h_{x+\Delta}^{t+\tau} - h_{x-\Delta}^{t+\tau}).$$

Proceeding as before we get

$$\begin{pmatrix} h \\ u \end{pmatrix}^{t+\tau} = \begin{pmatrix} 1 & ia - b \\ ia & 1 - a^2 - iab \end{pmatrix} \begin{pmatrix} h \\ u \end{pmatrix}^t,$$

where

$$a = \frac{\tau \sqrt{gh_0}}{\Delta} \sin k\Delta, \quad b = w \tau \sqrt{gh_0} \cos k\Delta.$$

The eigenvalues are

$$\lambda_{1,2} = 1 - \frac{a^2}{2} - \frac{iab}{2} \pm \sqrt{\left(1 - \frac{a^2}{2} - \frac{iab}{2}\right)^2 - 1}.$$

The question is, do these eigenvalues satisfy the von Neumann stability criterion, $|\lambda| < 1 + O(\tau)$? We will assume b is small (for accuracy) and expand about $b=0$. Thus

$$\begin{aligned} \lambda_{1,2} &\sim 1 - \frac{a^2}{2} - \frac{iab}{2} \pm \sqrt{\frac{a^4}{4} - a^2 + b(-ia + \frac{ia^3}{3})} \\ &\sim 1 - \frac{a^2}{2} - \frac{iab}{2} \pm ia \sqrt{1 - a^2/4} \left\{ 1 - \frac{ib}{a^2} \frac{1 - a^2/2}{a^2/4 - 1} \right\} \\ &\sim \underbrace{1 - \frac{a^2}{2} \pm ia \sqrt{1 - a^2/4}}_C + b \underbrace{\left(\frac{-ia}{2} \pm \frac{1}{2a} \frac{1 - a^2/2}{\sqrt{1 - a^2/4}} \right)}_D. \end{aligned}$$

Now $|C|=1$, and $|D|=O(\tau)$, since b is $O(\tau)$ and a is $O(\tau/\Delta)$, which is $O(1)$. Thus since $|\lambda| < |C| + |D|$, the inclusion of entrainment results in a stable scheme if the entrainment is small.

We further should be aware of the stability limitations imposed by the eddy viscosity equation. Consider

$$\frac{\partial u}{\partial t} - A \frac{\partial^2 u}{\partial x^2} = 0,$$

with finite difference representation

$$u^{t+\tau} = u^t + \frac{A\tau}{\Delta^2} (u_{x+\Delta}^t - 2u_x^t + u_{x-\Delta}^t).$$

Again, $u = ue^{ikx}$ gives

$$\lambda = 1 + \frac{2A\tau}{\Delta^2} (\cos(k\Delta) - 1).$$

$\cos(k\Delta) - 1$ varies from 0 to -2, thus λ varies from 1 to $1 - 4\frac{A\tau}{\Delta^2}$, and for stability, we want $\frac{2A\tau}{\Delta^2} < 1$.

Because it involves only one equation (assuming u is known perfectly) the salt advection equation is useful to demonstrate the phase error introduced by numerical schemes. In order to see what kind of accuracy to expect, and as an aid in selecting a finite difference scheme, several schemes were tried in a one-dimensional prototype. The equation solved was $\frac{\partial s}{\partial t} + U \frac{\partial s}{\partial x} = 0$. U was taken to be 40 cm/s, $\Delta T = 120$ sec., $\Delta X = 1 \text{ km} = 10^5$ cm. At $x=0$, the salinity grew linearly from 0 to 30 in 180 timesteps (6 hours), and then decreased linearly back to zero in the next 180 timesteps, after which it remained zero. This triangular shaped pulse then propagated along in the direction of increasing x , since U was positive.

All the schemes tested conserved salt, but some appeared more stable than others. In all of them, it was possible to see that waves of different wavelength propagated at different velocities, so that the original triangular shape was dispersed

into a rounded bump, with either leading or trailing ripples, depending on the sign of the phase error. This dispersion is produced by the phase error of the finite difference scheme.

1. Forward time differencing

The finite difference form is

$$S_j^{t+\tau} = S_j^t - \frac{u\tau}{2\Delta} (S_{j+1}^t - S_{j-1}^t).$$

Thus if

$$S_j^{t+\tau} = \lambda S_j^t = \lambda S e^{i(j\Delta x)},$$

and

$$\lambda = 1 - \frac{i u \tau}{\Delta} \sin k \Delta.$$

$$\text{For small } k\Delta, \lambda \sim 1 - i u \tau k - \frac{i u \tau}{\Delta} \frac{k^3 \Delta^3}{3!} \dots$$

The analytic λ is

$$e^{-i k u \tau} = 1 - i u \tau k - \frac{k^2 u^2 \tau^2}{2!} \dots$$

Thus this scheme is only first order accurate. Identifying the computational λ with an expansion of $e^{-i k u \tau \frac{\sin k \Delta}{k \Delta}}$, we see that the computational phase speed is $u \frac{\sin k \Delta}{k \Delta}$, and that therefore smaller waves, with larger k , travel slower. Thus, we predict ripples (short waves) emerging from the trailing edge of the salt pulse. As we see in Figure 131, this is indeed the case. Checking for stability, we see that $|\lambda| = 1 + O(\tau^2)$. Thus, although the system conserves salt, the amplitude of the various Fourier components grows with time. Since there is no source term in the original equation, this growth of the various modes is an error.

2. Leapfrog time

The scheme used is

$$\frac{s_j^{t+\tau} - s_j^{t-\tau}}{2\tau} = \frac{-u}{2\Delta} (s_{j+1}^t - s_{j-1}^t).$$

Defining $S = Se^{ikx}$, $a = 2(\sin k\Delta)\frac{u\tau}{\Delta}$, we get

$$\lambda = -\frac{ia}{2} \pm \frac{1}{2} \sqrt{4 - a^2},$$

and if $a^2 < 4$, $|\lambda| = 1$. Thus none of the waves grows in amplitude, which is what we want. Expanding λ , we get

$$\lambda = \pm \left(1 - \frac{\sin^2 k\Delta}{2} \left(\frac{u\tau}{\Delta} \right)^2 + \dots \right) - \frac{ia\tau}{\Delta} \sin k\Delta.$$

The leading term is $\pm 1 - \frac{ia\tau}{\Delta} \sin k\Delta$. There are two λ 's, with leading terms

$$\lambda_1 = 1 - \frac{ia\tau}{\Delta} \sin k\Delta, \quad \lambda_2 = -1 - \frac{ia\tau}{\Delta} \sin k\Delta.$$

λ_1 we associate with the real physical wave, with true $\lambda = e^{-i\omega\tau} = e^{-iuk\tau}$. We see that for this λ , again the short waves travel slowest, as Fig. 132 shows. λ_2 is associated with the computational mode, and is approximately $-e^{i\omega\tau}$, thus it is associated with a high frequency (period = 2τ) sign alternation. From the dispersion relation $\omega = uk$, the wavelength associated most strongly with this mode is

$$\lambda = 2\pi u / \omega = 2\pi u / 2\pi / \tau = u\tau = O(\Delta);$$

that is the shortest wave. The computational scheme does not initiate the computational mode, but if there are short wavelengths present, they will excite this mode. One usually plans on doing a bit of filtering to eliminate this problem.

3. Richtmeyer scheme (Richtmyer and Morton, 1967)

This is in some sense an iterative scheme. The basic idea is to calculate $\frac{s^{t+\tau} - s^t}{\tau}$ as a function of spatial derivatives of s at $t+1/2\tau$. Thus

$$s_{j+1/2}^{t+1/2} = s_{j+1/2}^t - 1/2 \tau u / \Delta (s_{j+1}^t - s_j^t)$$

$$s_{j-1/2}^{t+1/2} = s_{j-1/2}^t - 1/2 \tau u / \Delta (s_j^t - s_{j-1}^t)$$

$s_{j+1/2}^t$ is approximated as $1/2 (s_j^t + s_{j+1}^t)$. We obtain for $s_j^{t+\tau}$:

$$s_j^{t+\tau} = s_j^t - \frac{u\tau}{2\Delta} (s_{j+1}^t - s_{j-1}^t - \frac{u\tau}{\Delta} (s_{j+1}^t - 2s_j^t + s_{j-1}^t)).$$

With $\mu = \frac{u\tau}{\Delta}$, we get for λ

$$\lambda = 1 - i\mu \sin k\Delta + \mu^2 (\cos(k\Delta) - 1).$$

Again we see that small waves travel slower.

$$|\lambda|^2 = 1 - 4\mu^2(1 - \mu^2) \sin^2(1/2 k\Delta),$$

so that numerical dissipation is present. The shape of the s distribution for this scheme is identical to the Leapfrog scheme and is not shown.

APPLYING A FINITE DIFFERENCE SCHEME TO THE PLUME MODEL

A problem develops when one tries to apply a finite difference scheme to the plume model. U is not constant, so the formulae look messier. The leapfrog scheme is the most direct, since one doesn't have to interpolate spatial derivatives as in the Richtmeyer scheme. However, it was not used in the model because of its extra time level requirement - it is a three level scheme. Also, in developing a model, one often runs for a few timesteps with a certain set of conditions, then saves the output as initial conditions for a further run. If the succeeding run involves considerable changes (which one hopes are improvements) there is a very good opportunity to generate a

computational mode. For this reason it was intended to use the Richtmeyer scheme. However, because of a programming error, discovered after the modeling discussed here was completed, in fact only a first order accurate scheme for the salt advection equation was used. This probably accounts for the considerable small scale fluctuations present after a long run, showing up in particular as small negative salinities. Thus the solution of the convective equation in a 2-dimensional, spatially and temporally varying flow has not been carried out as well as one would like. The problems are two-fold:

- 1) getting a high enough order accurate scheme;
- 2) applying this scheme to the already existing grid of staggered transports and thicknesses.

There is a further, more subtle, point about the salinity equation. The salinity advection equation is also a density advection equation, and thus affects the momentum equation. It was assumed, and confirmed only by the limited experience discussed in this thesis, that a stable scheme would result if the salinity field were treated the same as the elevation field, as far as time levels in the numerical scheme were concerned. Thus, the old velocity field is used to update the salinity field, and the new density field is used in to update the velocity fields.

TABLE I
HARMONIC ANALYSIS OF RIVER SPEEDS

NAME	FREQUENCY cycle/day	AMPLITUDE cm/sec	PHASE degree	
Z0	0.0	0.0860	0.00	
NM	0.03629164	0.2318	274.16	
MSP	0.06772637	0.4556	176.66	
2Q1	0.85695237	2.8886	28.19	
Q1	0.89324397	3.3717	167.73	
O1	0.92953563	24.0625	280.06	
NO1	0.96644622	8.2796	59.74	
P1	0.99726212	10.7181	304.67	INFERRED (K1)
S1	1.00000000	1.7835	257.24	
K1	1.00273705	33.1047	302.74	
J1	1.03902912	2.7960	169.53	
OO1	1.07594013	4.7931	197.50	
MNS2	1.82825470	2.5522	7.42	
MU2	1.86454678	6.4664	108.74	
N2	1.89598083	6.7790	234.64	
NU2	1.90083885	1.3024	239.74	INFERRED (N2)
M2	1.93227291	48.3670	311.66	
L2	1.96856499	25.7985	320.57	
T2	1.99726295	0.8353	313.44	INFERRED (S2)
S2	1.99999905	13.2946	336.78	
K2	2.00547504	3.5766	335.88	INFERRED (S2)
2SM2	2.06772518	5.8606	183.44	
MO3	2.86180973	5.7899	154.61	
M3	2.89841080	1.5712	325.21	
MK3	2.93500996	10.6364	173.79	
SK3	3.00273800	3.2154	171.84	
MN4	3.82825470	1.0384	178.85	
M4	3.86454678	4.3592	346.81	
SN4	3.89598179	2.3171	166.22	
MS4	3.93227291	6.3899	189.51	
S4	4.00000000	2.8767	172.03	
2MN6	5.76052761	1.4951	44.20	
M6	5.79681969	1.9540	185.45	
MSN6	5.82825565	1.1174	19.73	
2MS6	5.86454582	2.2803	129.23	
2SM6	5.93227386	1.2324	329.69	
3MN8	7.69280148	0.2242	167.19	
M8	7.72909451	1.0761	180.33	
3MS8	7.79681969	0.2408	248.67	
M12	11.59364128	0.0446	263.10	

TABLE II
HARMONIC ANALYSIS OF POINT ATKINSON ELEVATIONS

NAME	FREQUENCY cycle/day	AMPLITUDE cm	PHASE degree	
Z0	0.0	302.087	0.0	
MM	0.03629164	5.304	349.62	
MSF	0.06772637	2.762	323.83	
2Q1	0.85695237	1.381	141.43	
Q1	0.89324397	8.231	137.91	
O1	0.92953563	45.787	153.47	
NO1	0.96644622	4.997	220.03	
P1	0.99726212	27.801	166.24	INFERRED (K1)
S1	1.00000000	4.626	118.81	INFERRED (K1)
K1	1.00273705	85.8747	164.31	
J1	1.03902912	5.079	200.06	
OO1	1.07594013	2.411	238.04	
MNS2	1.82825470	0.883	336.40	
MU2	1.86454678	4.137	94.61	
N2	1.89598083	19.242	131.42	
NU2	1.90083885	3.697	136.52	INFERRED (N2)
M2	1.93227291	91.281	159.49	
L2	1.96856499	5.429	209.59	
T2	1.99726295	1.426	155.02	INFERRED (S2)
S2	1.99999905	22.720	178.25	
K2	2.00547504	6.112	177.35	INFERRED (S2)
2SM2	2.06772518	0.454	110.66	
MO3	2.86180973	0.136	90.45	
M3	2.89841080	0.180	263.58	
MK3	2.93500996	0.160	167.06	
SK3	3.00273800	0.103	152.38	
MN4	3.82825470	0.096	168.62	
M4	3.86454678	0.336	161.73	
SN4	3.89598179	0.077	43.39	
MS4	3.93227291	0.276	232.26	
S4	4.00000000	0.093	51.69	
2MN6	5.76052761	0.502	49.46	
M6	5.79681969	0.657	66.51	
MSN6	5.82825565	0.200	38.74	
2MS6	5.86454582	0.787	100.55	
2SM6	5.93227386	0.204	105.99	
3MN8	7.69280148	0.074	325.71	
M8	7.72909451	0.160	141.13	
3MS8	7.79681969	0.072	240.77	
M12	11.59364128	0.075	164.79	

TABLE III
SCALE ANALYSIS OF TERMS IN THE EQUATION OF MOTION

parameter	river area (cgs)	far field (cgs)
u , flow velocity	100	20
u_0 , tidal stream	20	20
h , plume thickness	400	100
L , horizontal length scale	10^5	10^6
T , time scale	4×10^4	4×10^4
f , Coriolis parameter	10^{-4}	10^{-4}
g , reduced gravity	20	10
w_p , entrainment velocity	400×10^{-4}	10×10^{-4}
$\partial u h / \partial t$, time derivative	1	.05
$\partial(u^2 h) / \partial x$, advective term	40	0.04
$\partial(g' h^2 / 2) / \partial x$, pressure gradient	16	0.1
$f u h$, Coriolis term	4	0.2
$K u^2$, ($K=0.001$), interfacial friction	10	0
$w_p u_0$, entrained momentum flux	4	0.02
$g h \zeta_x$, barotropic tidal forcing	4	4
$u h / L w$, advection/entrainment	10	2

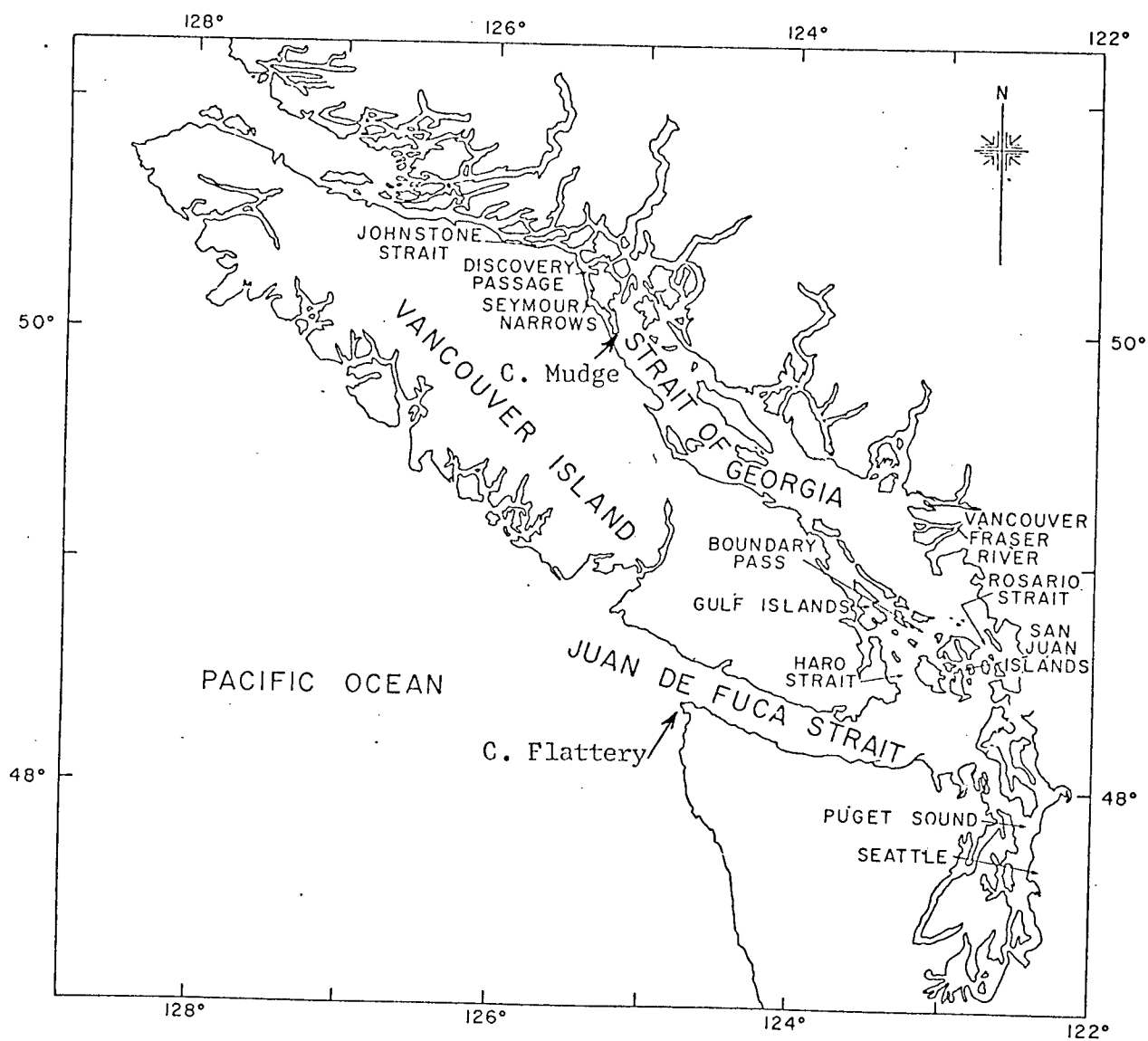


FIGURE 1. Chart showing the Straits of Georgia and Juan de Fuca, and the Fraser River.

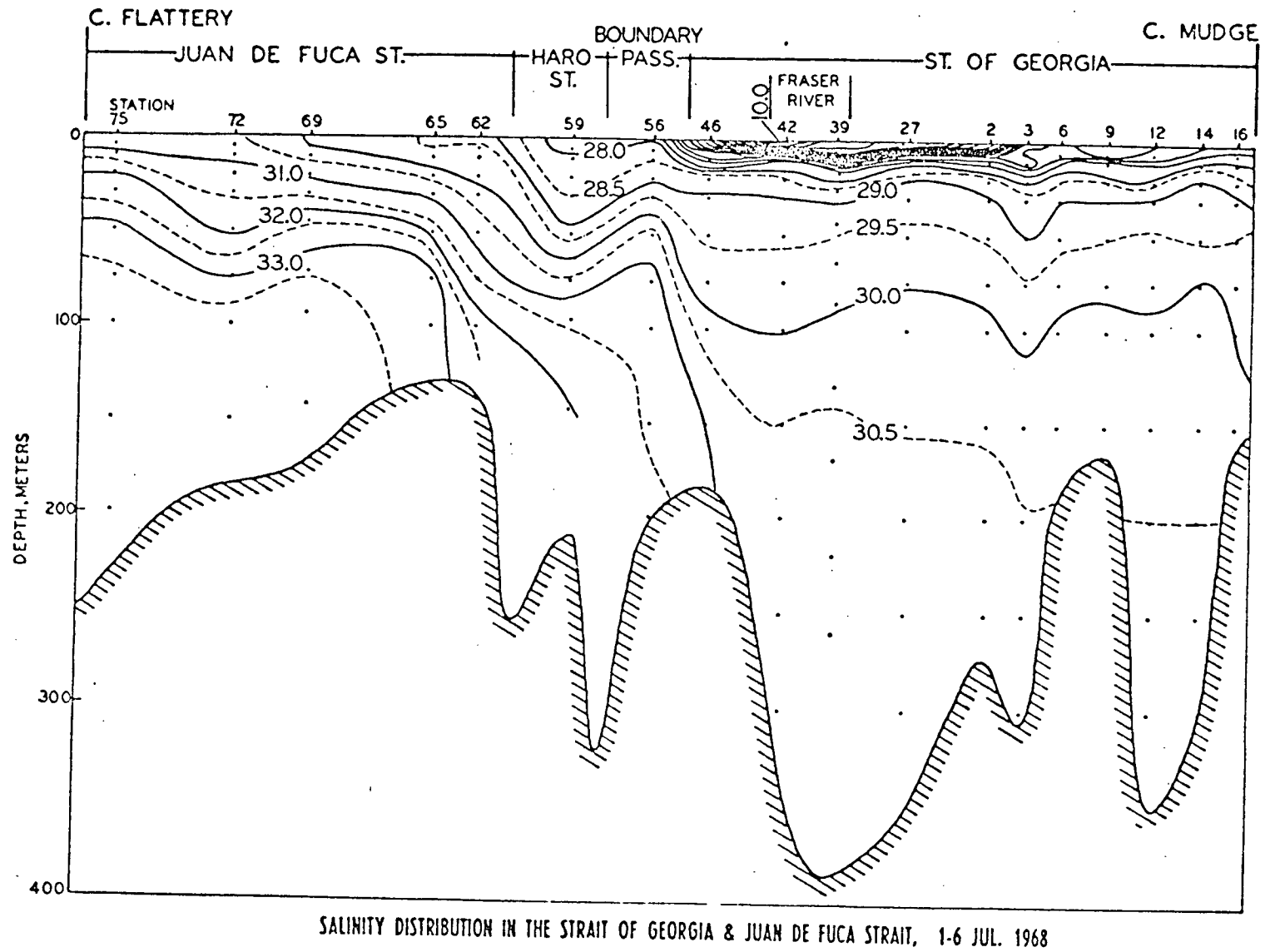
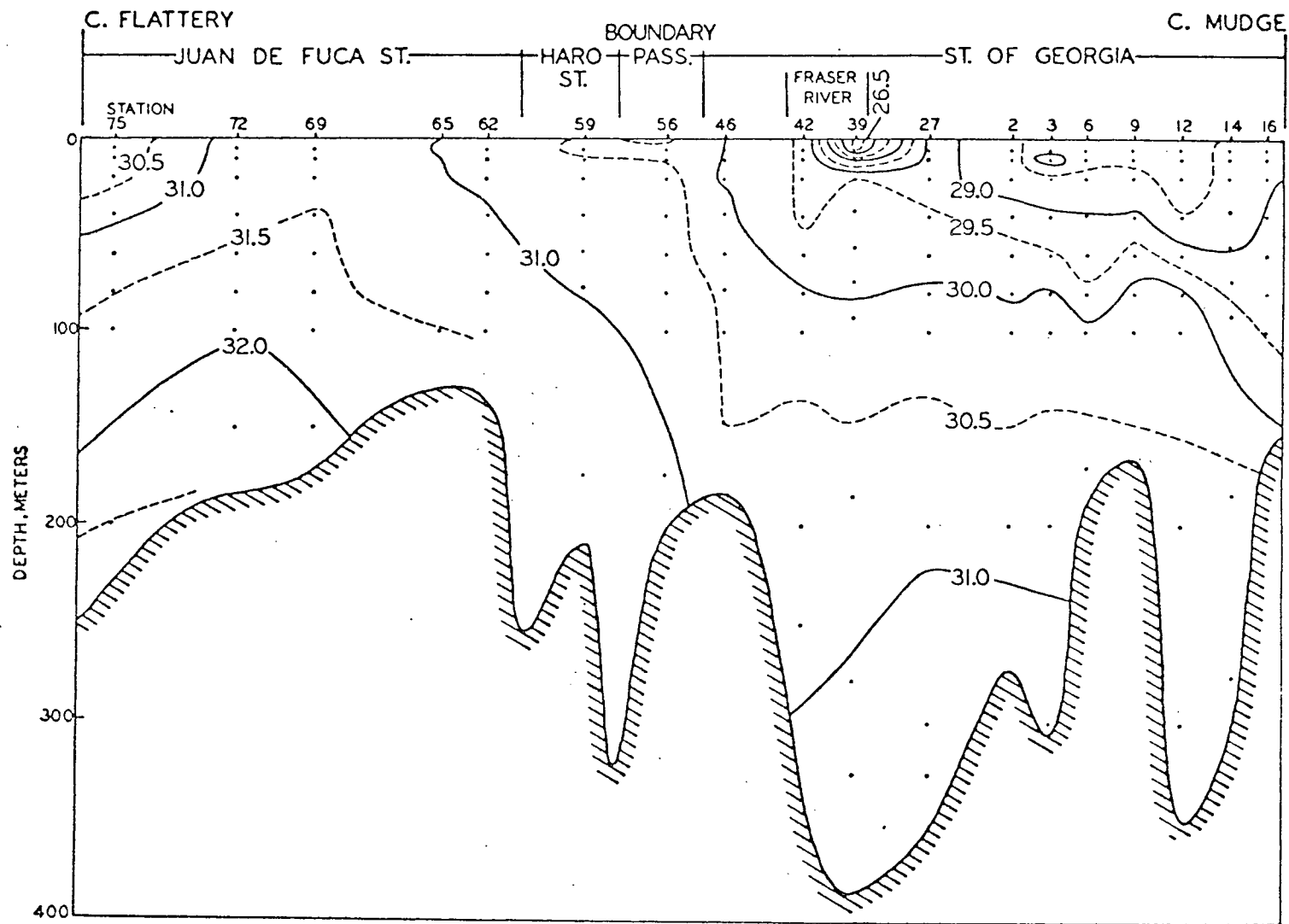


FIGURE 2. Taken from Crean and Ages(1971).



SALINITY DISTRIBUTION IN THE STRAIT OF GEORGIA & JUAN DE FUCA STRAIT, 4-8 DEC. 1967

FIGURE 3. Taken from Crean and Ages(1971).

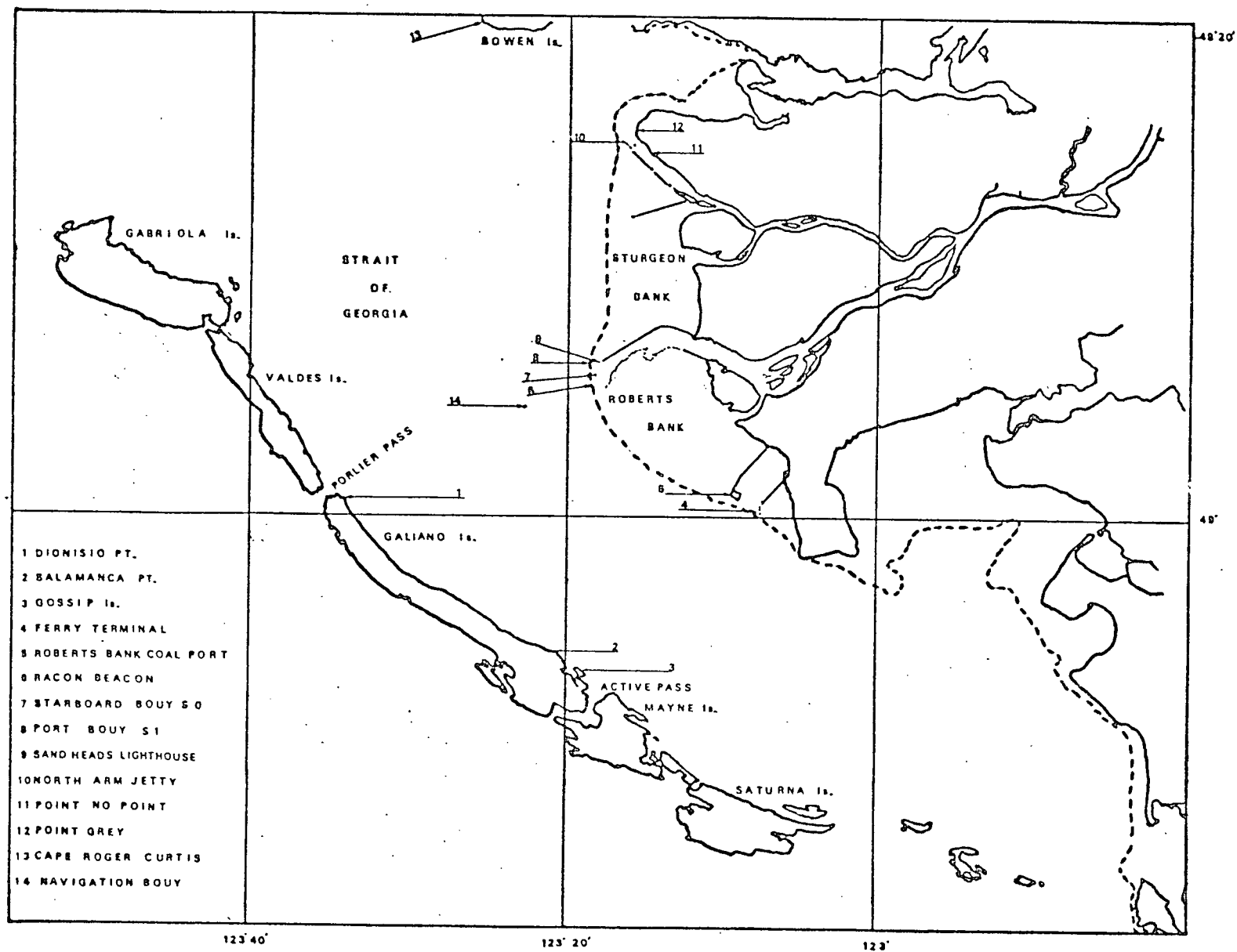


FIGURE 4. Chart showing the Fraser delta. Dashed line is the 12 m depth contour.

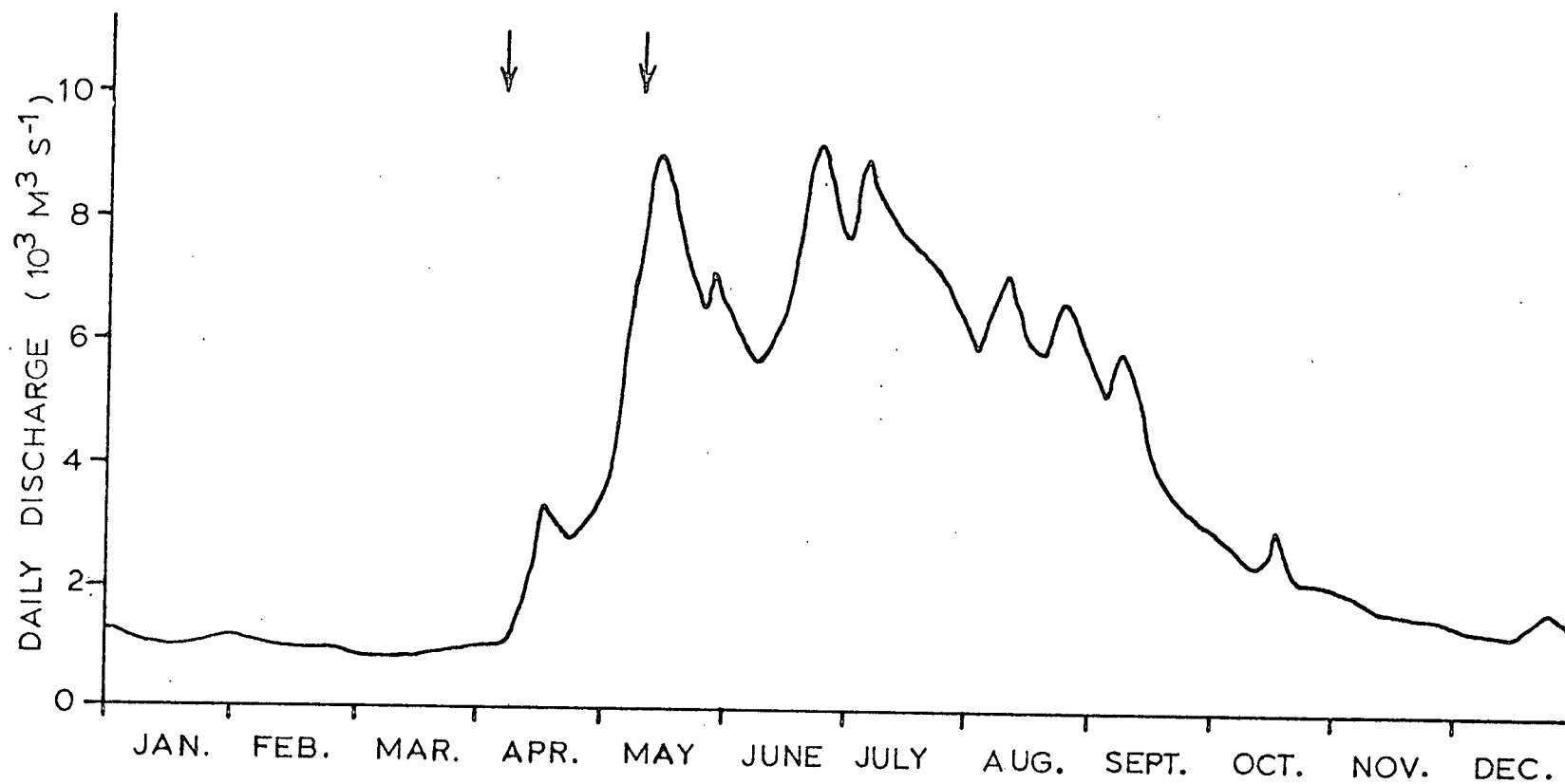


FIGURE 5. The daily Fraser River discharge for 1976, measured at Hope. The two arrows indicate the period during which a current meter, described in Chapter 2, was installed.

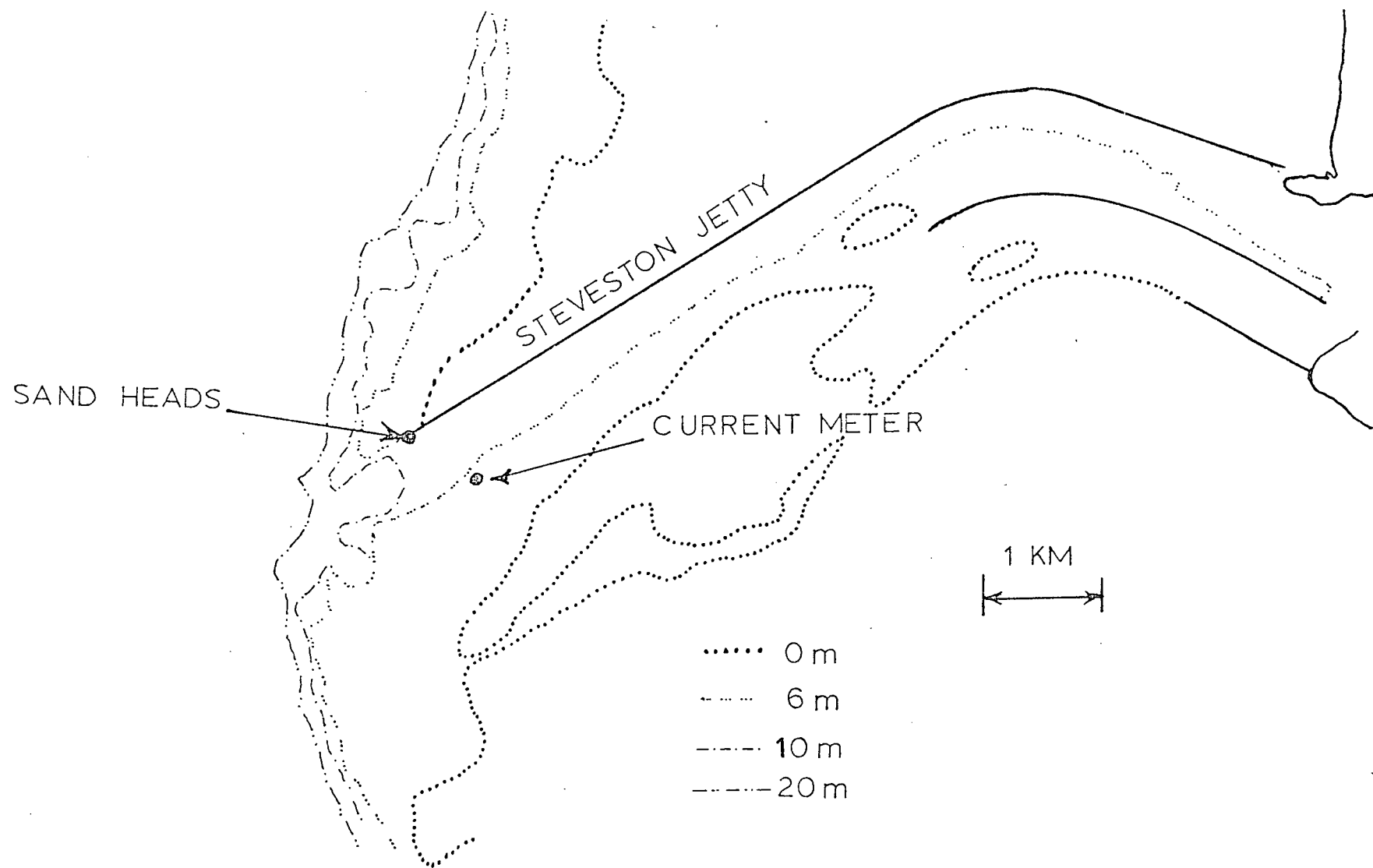


FIGURE 6. Chart of the river mouth area, showing the location of the current meter mooring.

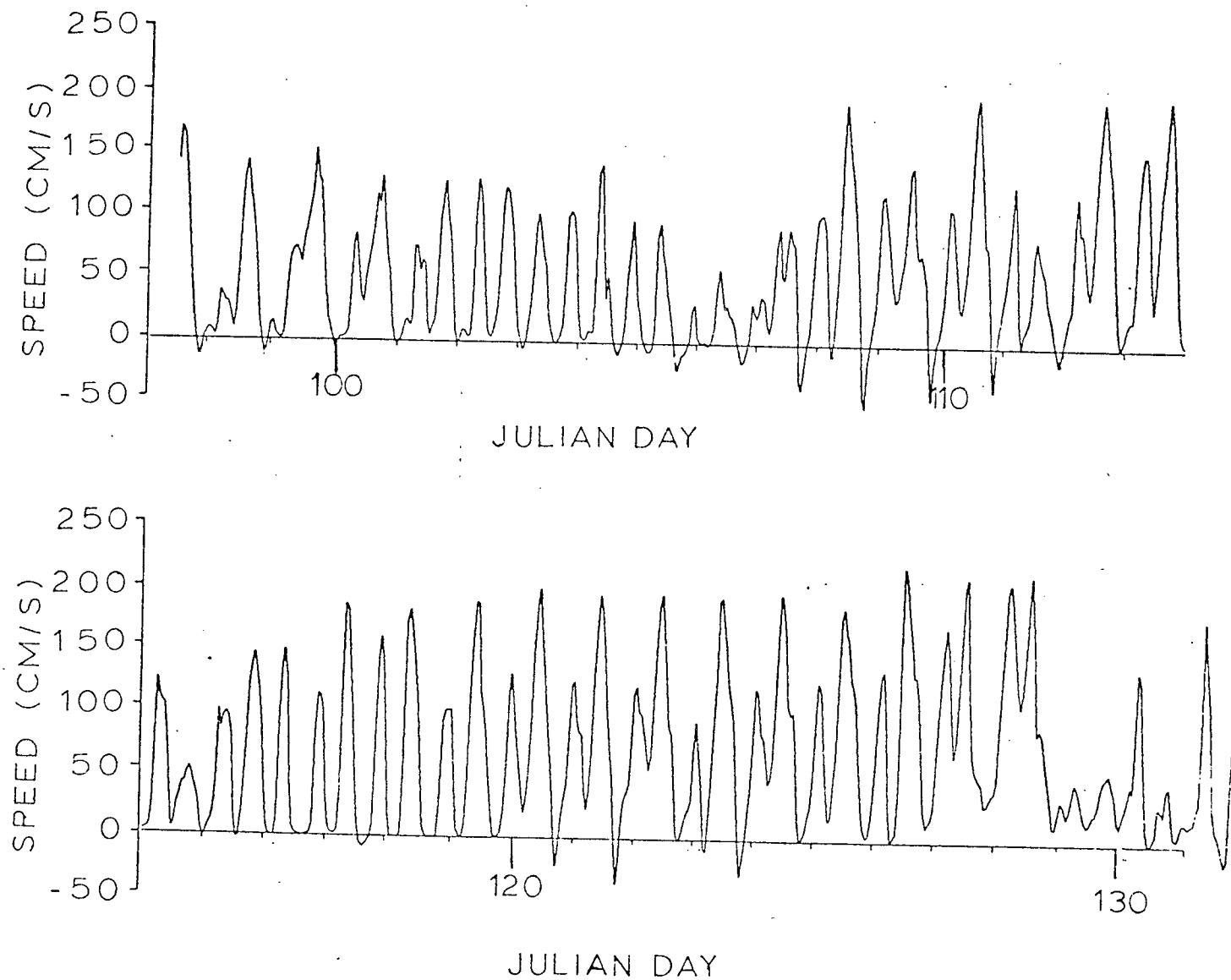


FIGURE 7. Smoothed current meter record obtained by using the angular correction and the smoothing filter $A_6A_6A_7/(6.6.7)$. The break in the time axis occurs at day 114.

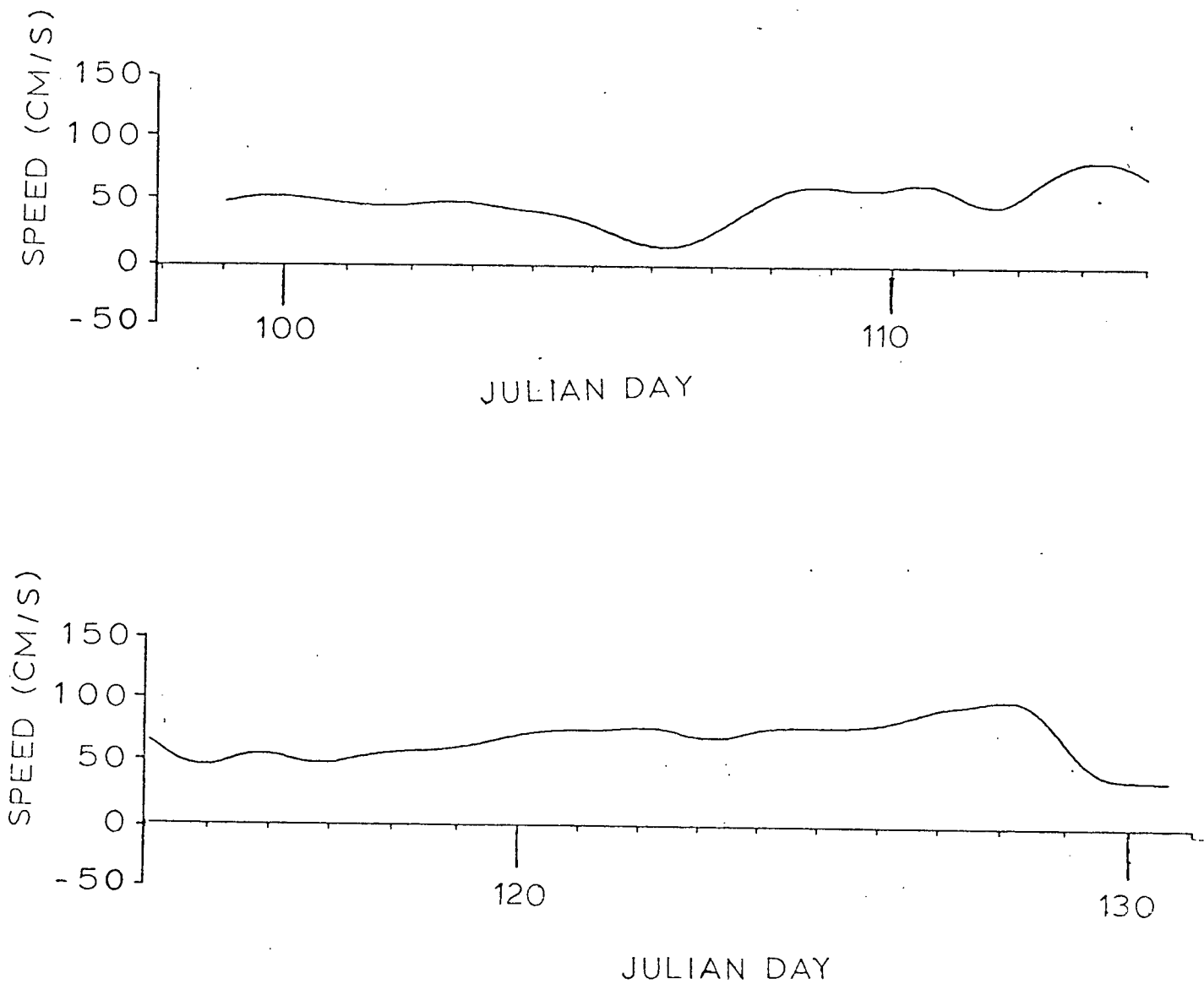


FIGURE 8. The low frequency component of the current meter record, obtained by using the $A_{24}A_{24}A_{25}/(24 \cdot 24 \cdot 25)$ filter. The break in the time axis occurs at day 114.

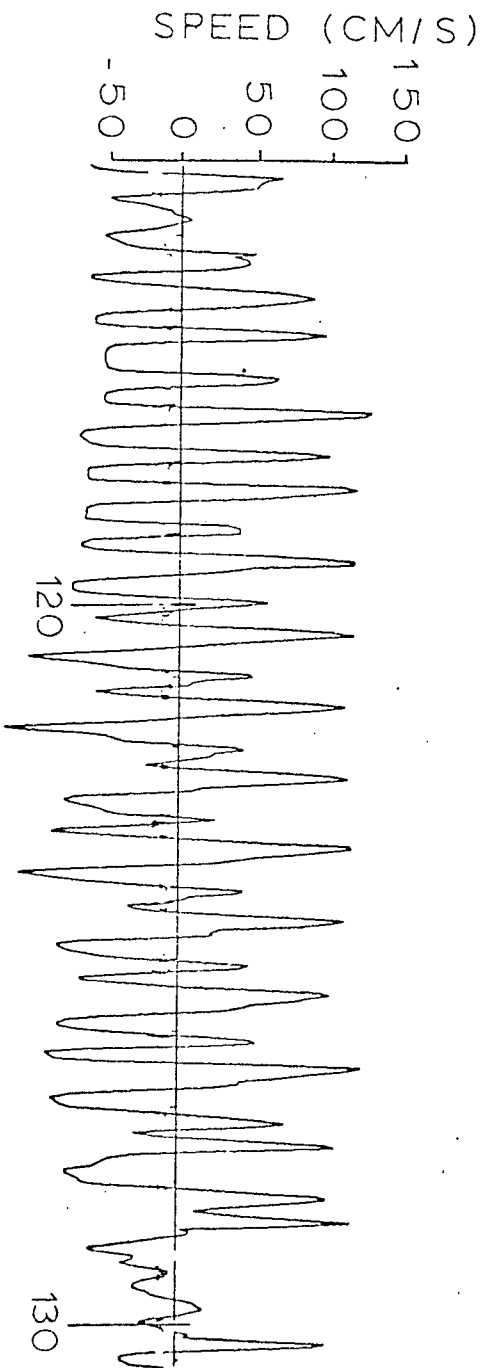
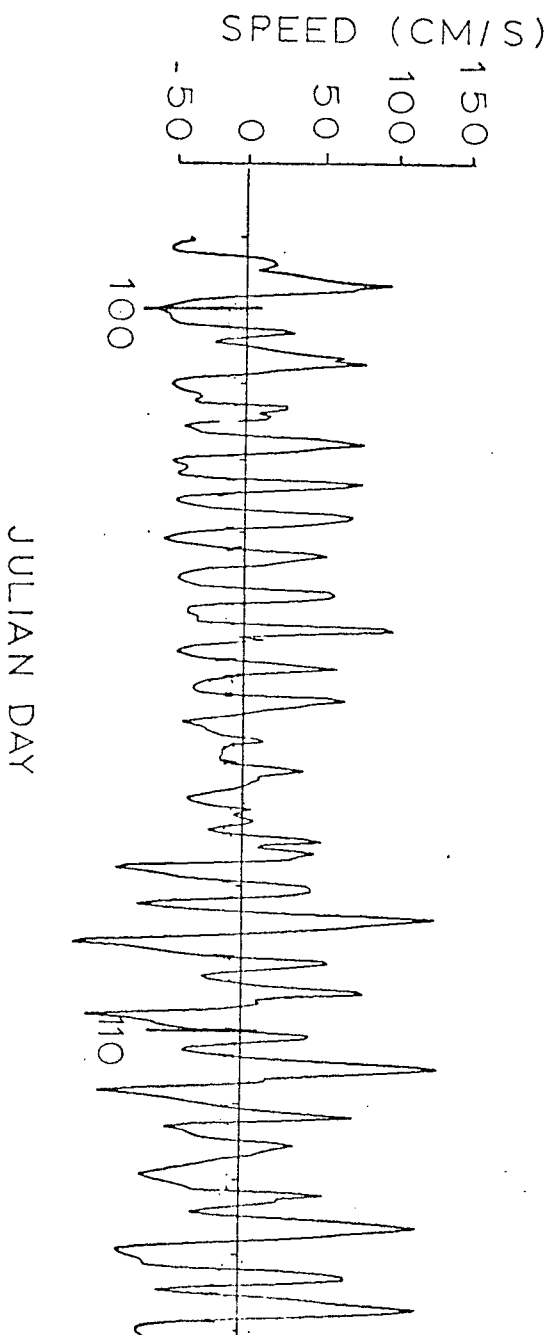


FIGURE 9. The tidal part of the current meter record, obtained by subtracting the low frequency signal from the smoothed signal. The break in the time axis occurs at day 114.

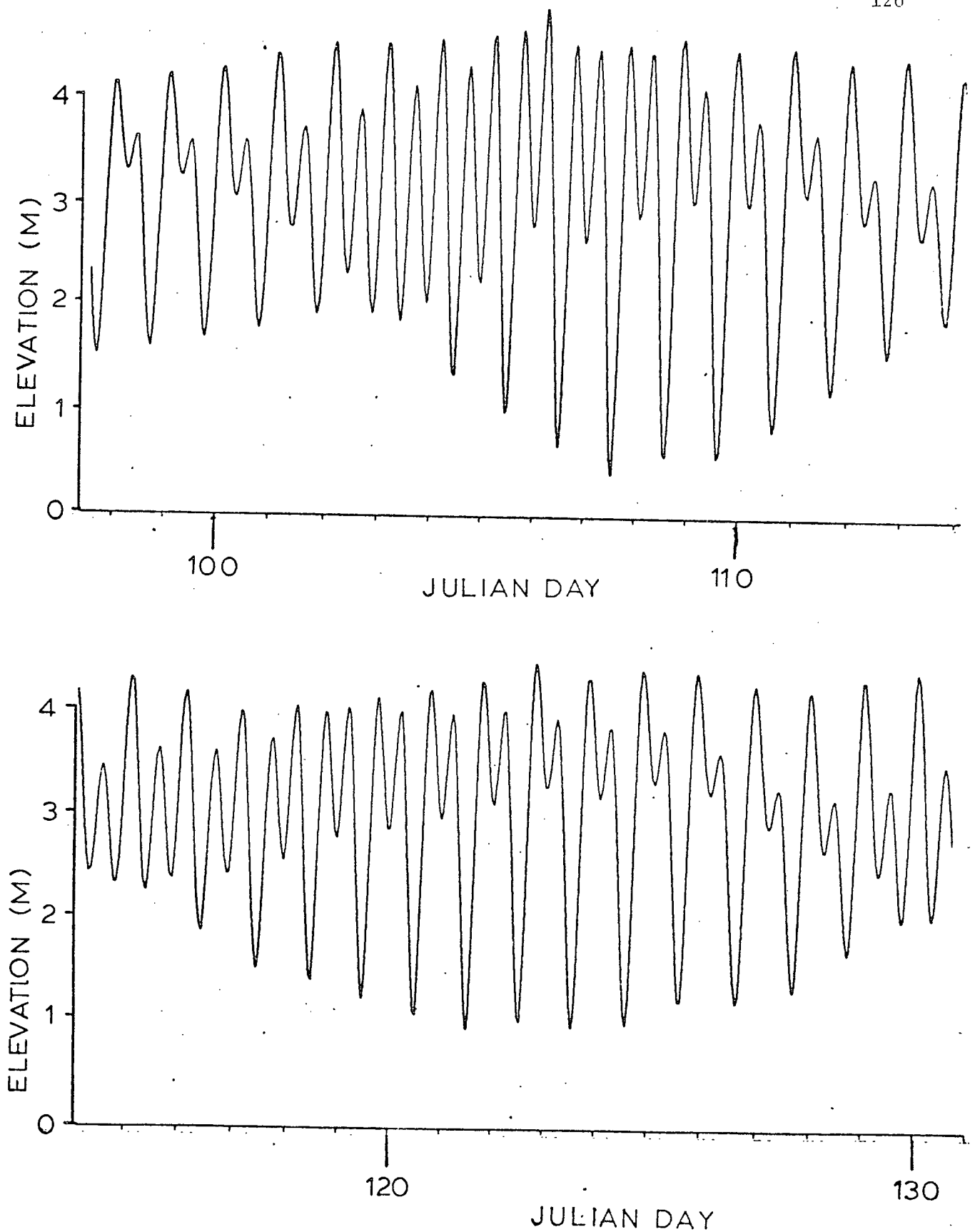


FIGURE 10. Tidal elevations at Point Atkinson during the time the current meter was in operation. The break in the time axis occurs at day 114.

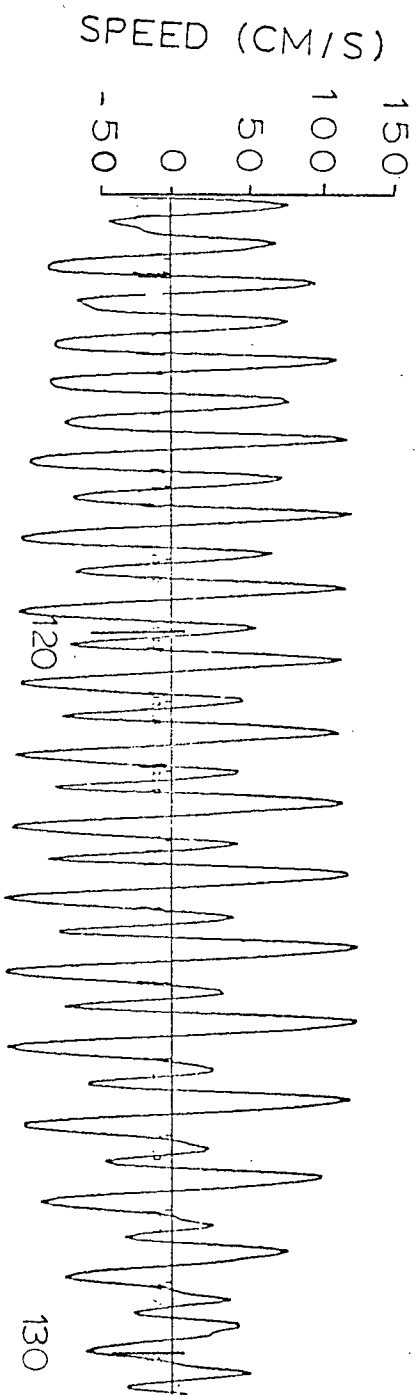
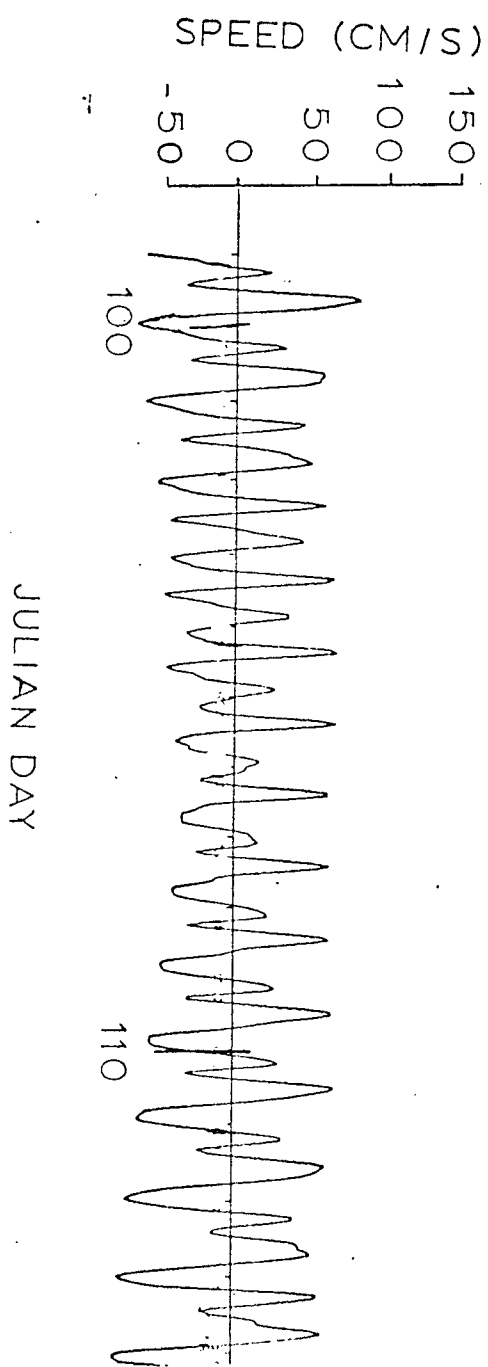


FIGURE 11. A reconstruction of the tidal signal from constituents obtained by harmonic analysis. The break in the time axis occurs at day 114.

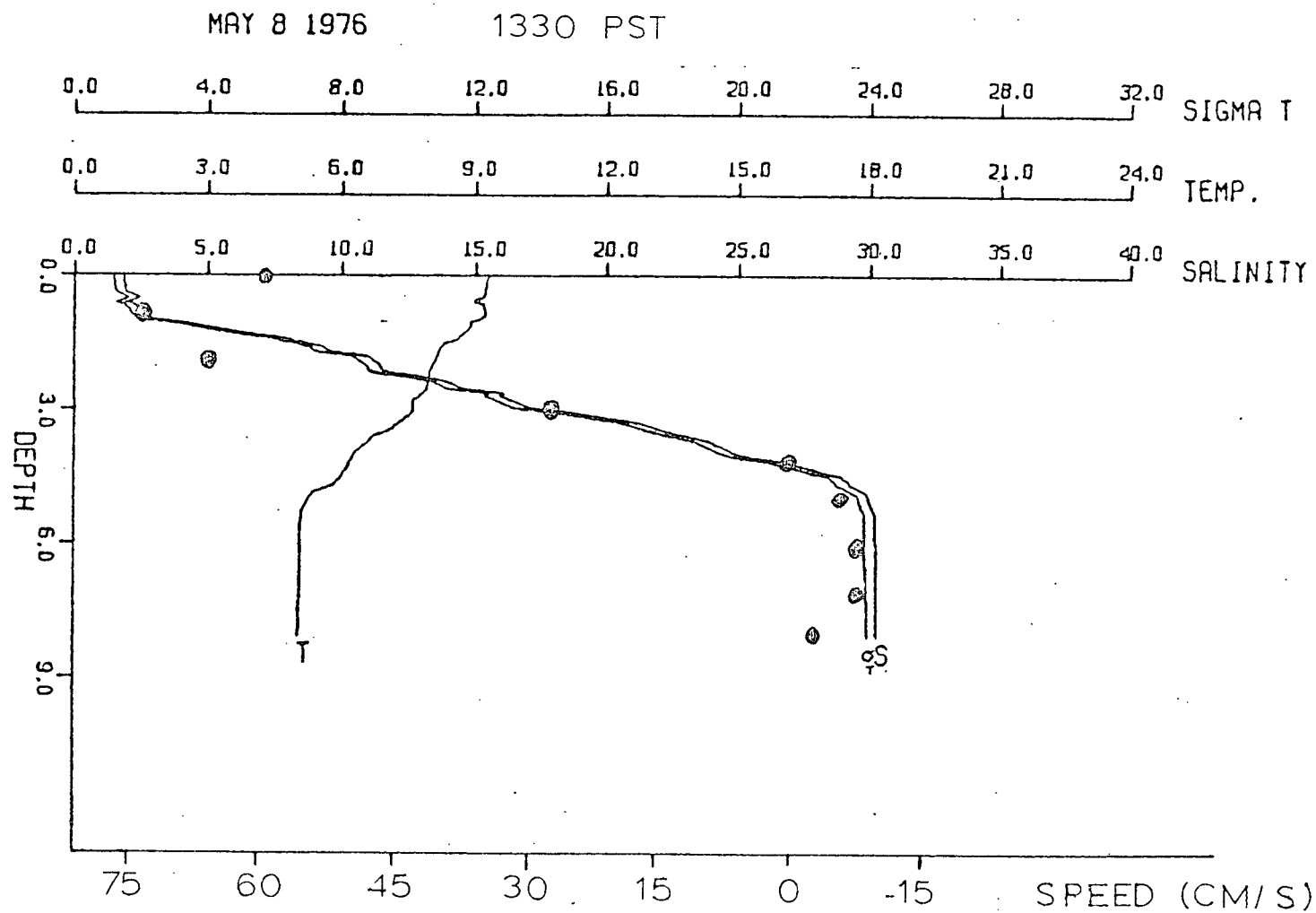


FIGURE 12. Profiles of S,T,sigma t. and current speed (indicated by dots) for 1330 PST.
 May 8, 1976, at the current meter mooring.

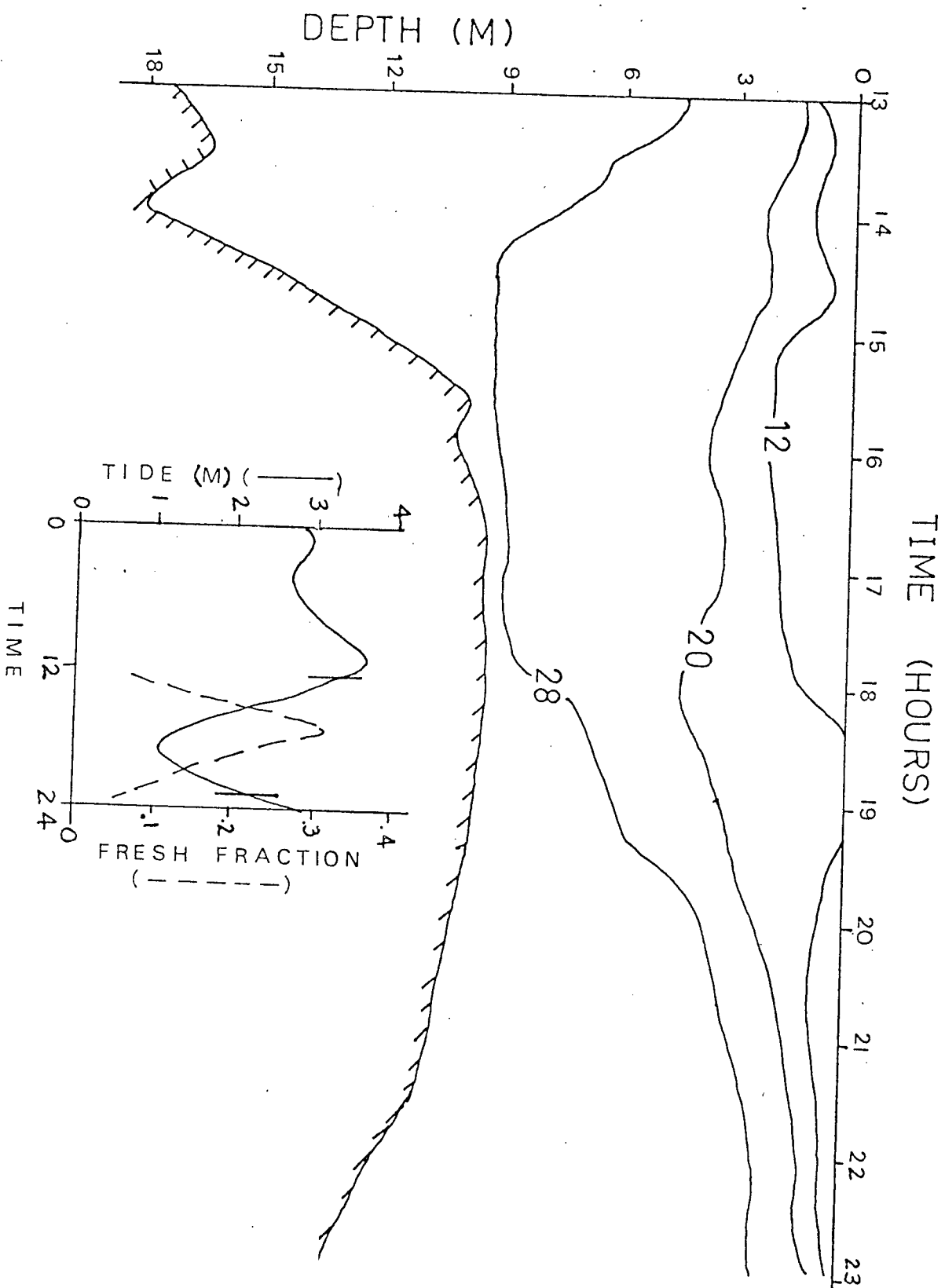
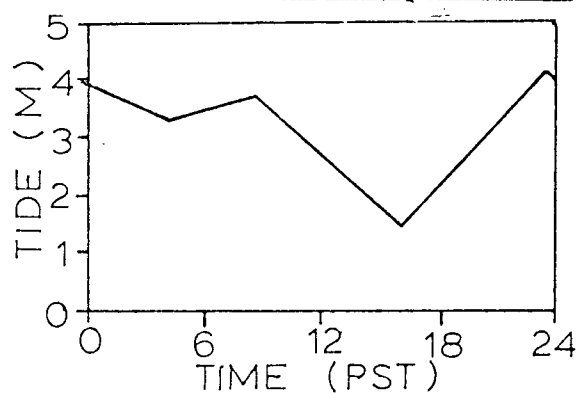
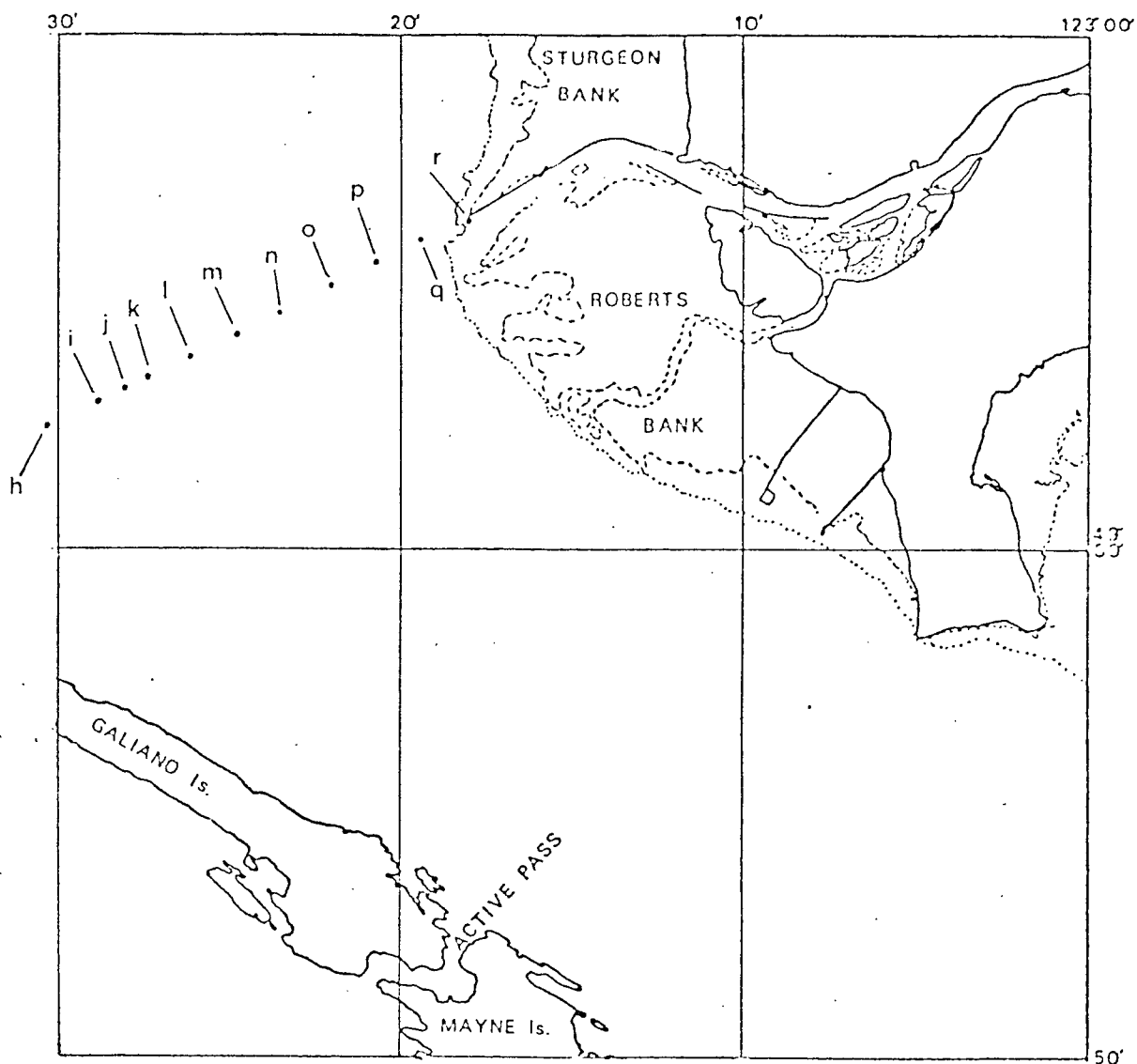


FIGURE 13. The salinity distribution as a function of time at the river mouth, January 21, 1975.



WINDS AT SAND HEADS

0000	E18
0500	E18
0700	E16
0900	SE12
1200	SE6
1500	E6
1800	calm

STATION TIMES

h	1730	l	1758	p	1832
i	1732	m	1805	q	1842
j	1744	n	1814	r	1849
k	1750	o	1822		

FIGURE 14. Station positions and times, wind and tide for April 6, 1976.

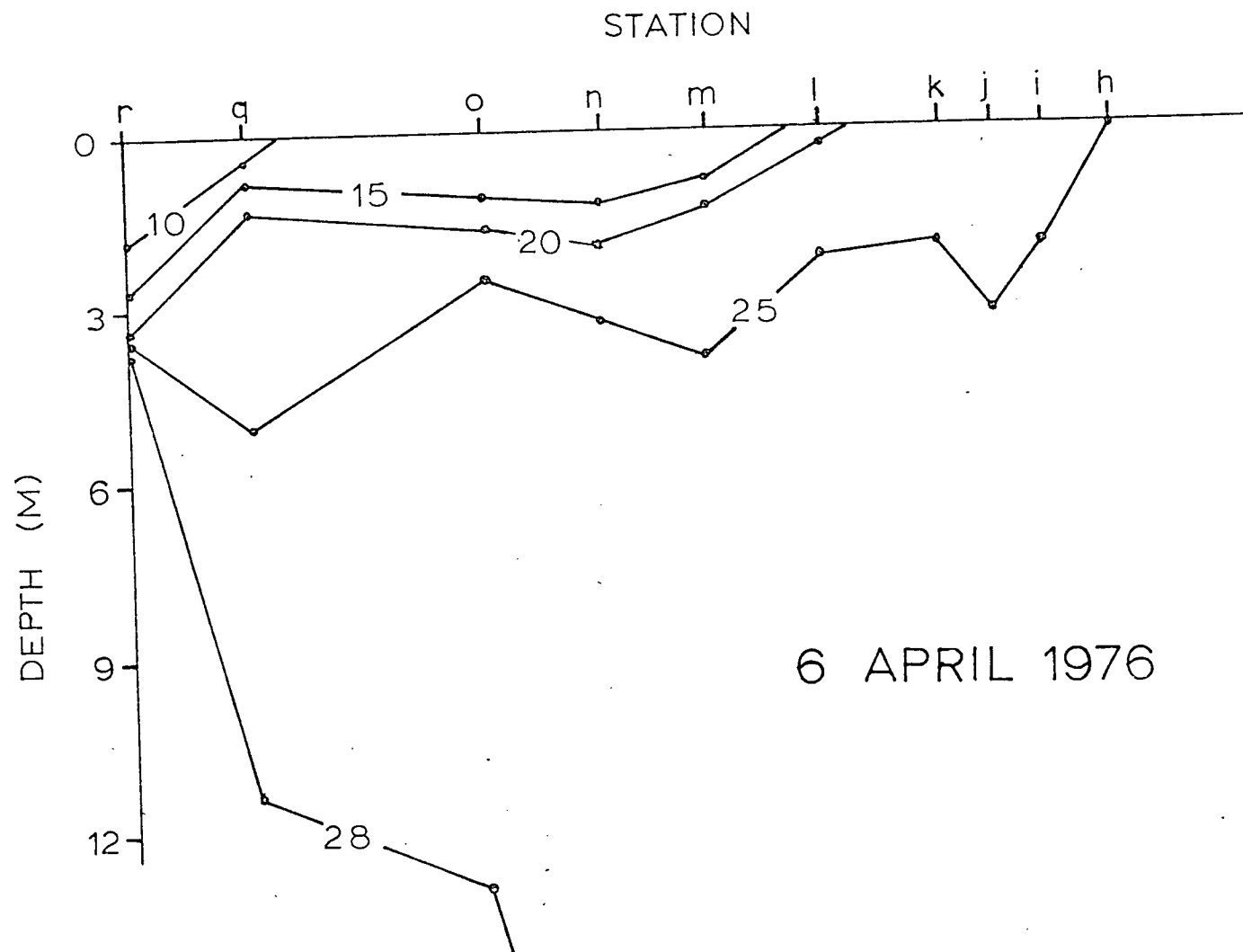


FIGURE 15. Salinity section along line h - r for April 6, 1976.

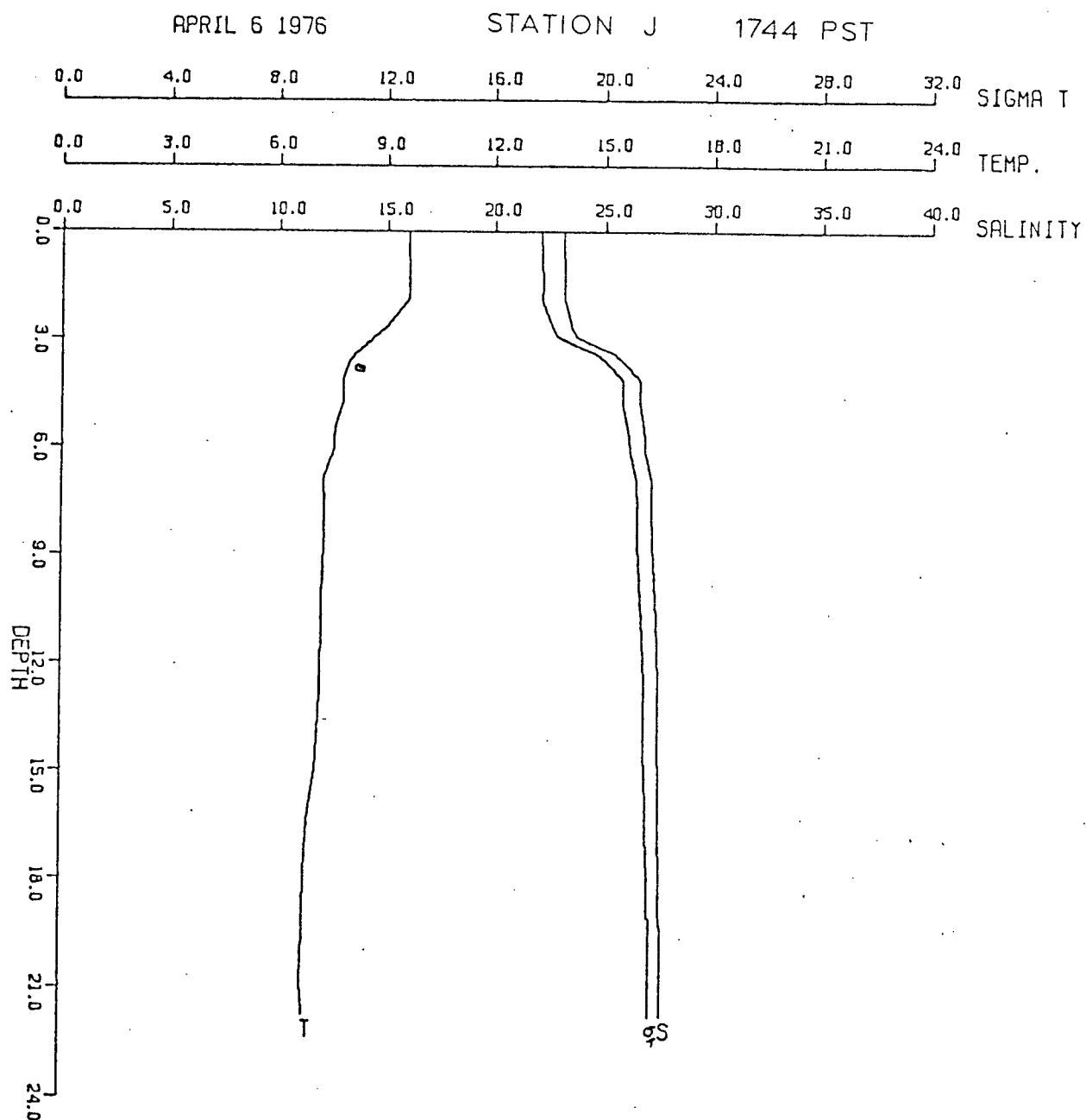


FIGURE 16. S, T, sigma t profiles at station j, 1744 PST, April 6, 1976.

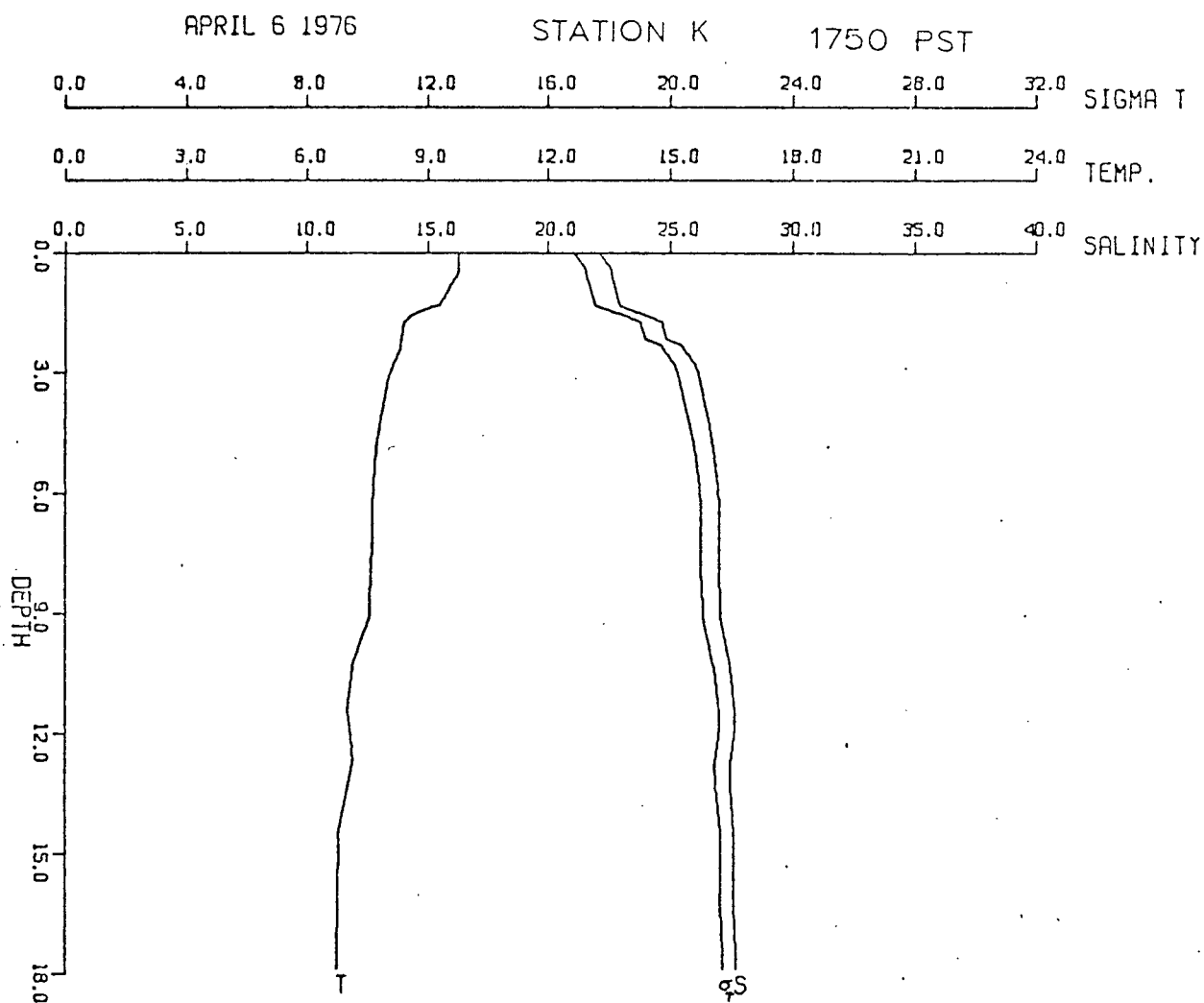


FIGURE 17. S, T, sigma t profiles at station k, 1750 PST, April 6, 1976.

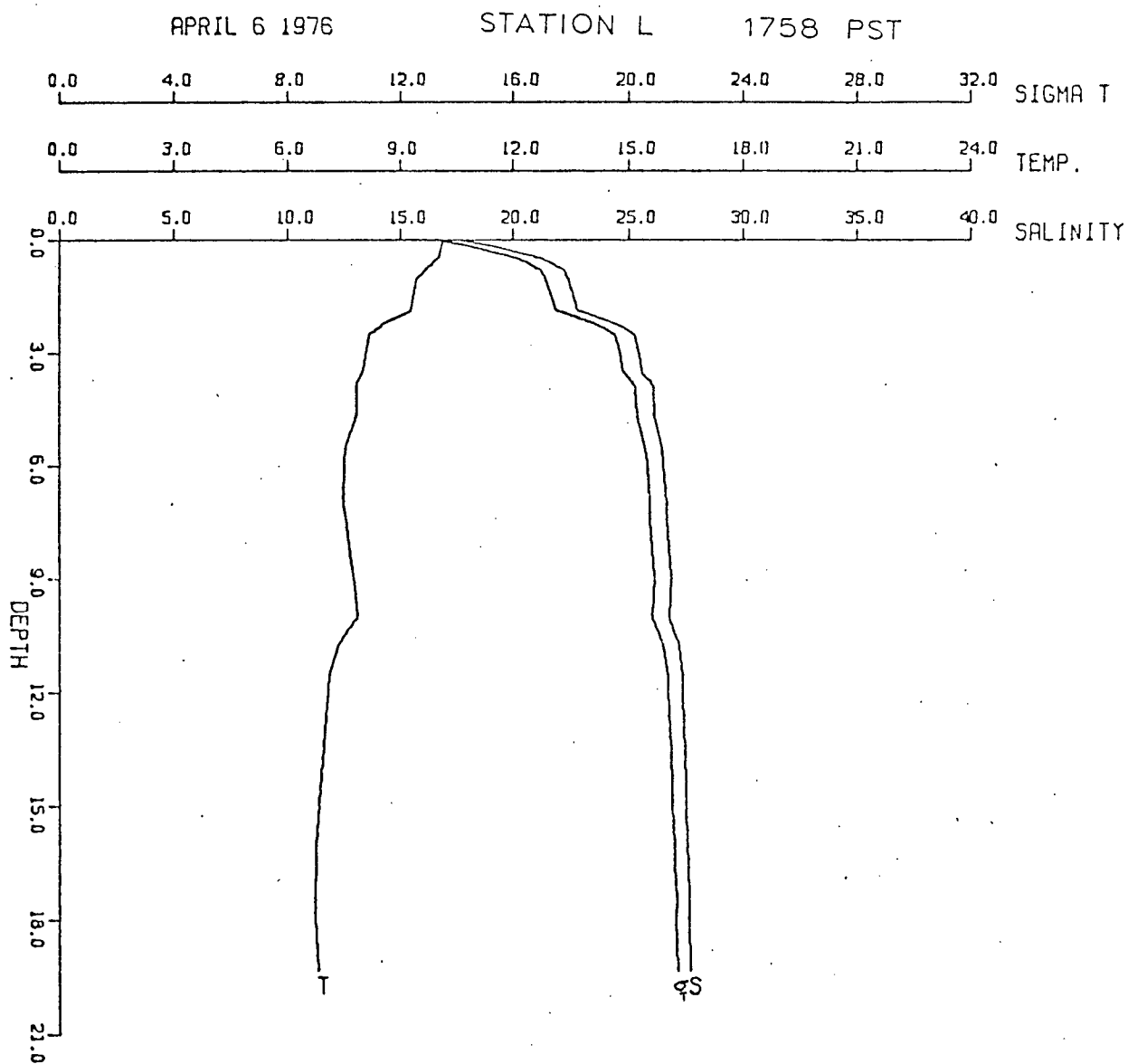
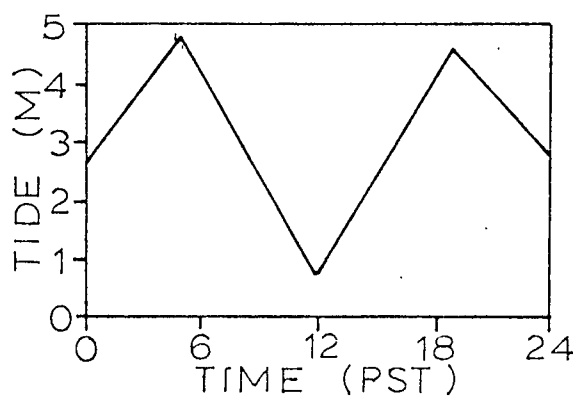
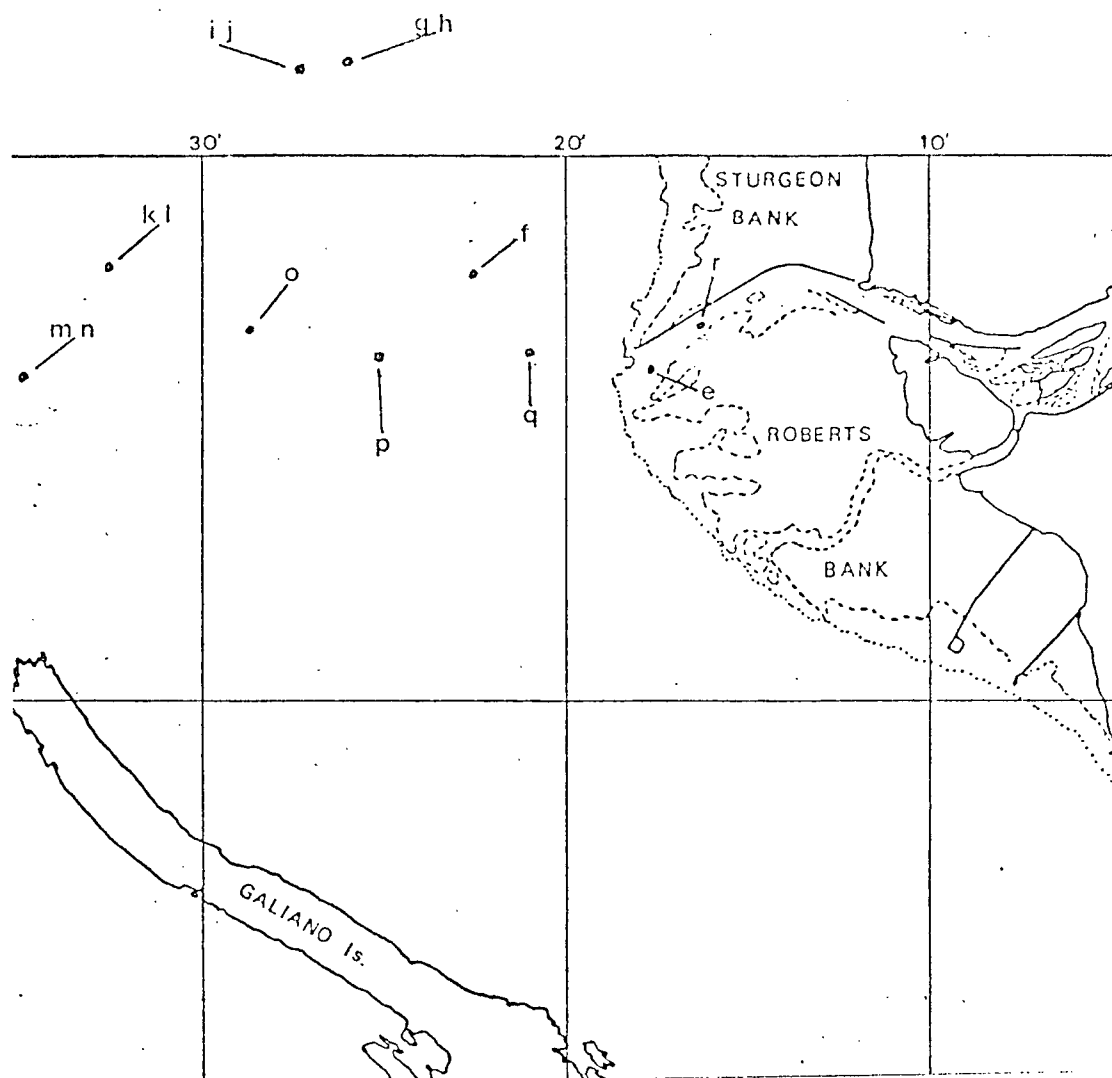


FIGURE 18. S, T, sigma t profiles at station 1, 1758 PST, April 6, 1976.



WINDS AT SAND HEADS

0000 NW52
 0400 NW44
 0700 NW42
 0800 NW36
 1200 N8
 1800 SE6

STATION TIMES

e 1513	i 1620	m 1730	q 1831
f 1535	j 1625	n 1732	r 1844
g 1553	k 1710	o 1755	
h 1558	l 1713	p 1818	

FIGURE 19. Station positions and times, wind and tide for April 15, 1976.

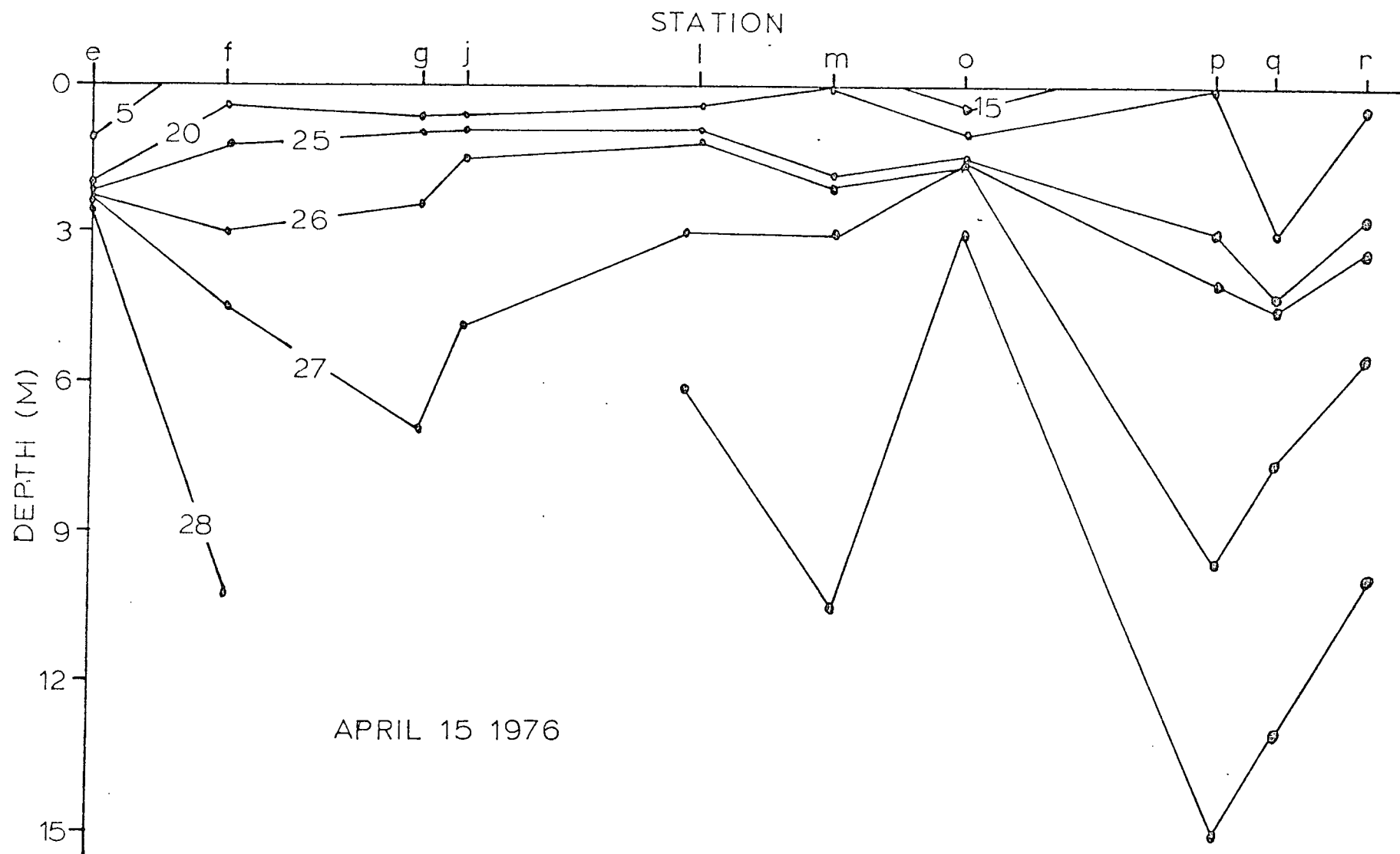


FIGURE 20. Salinity distribution along line e-m and along line m-r for April 15, 1976.

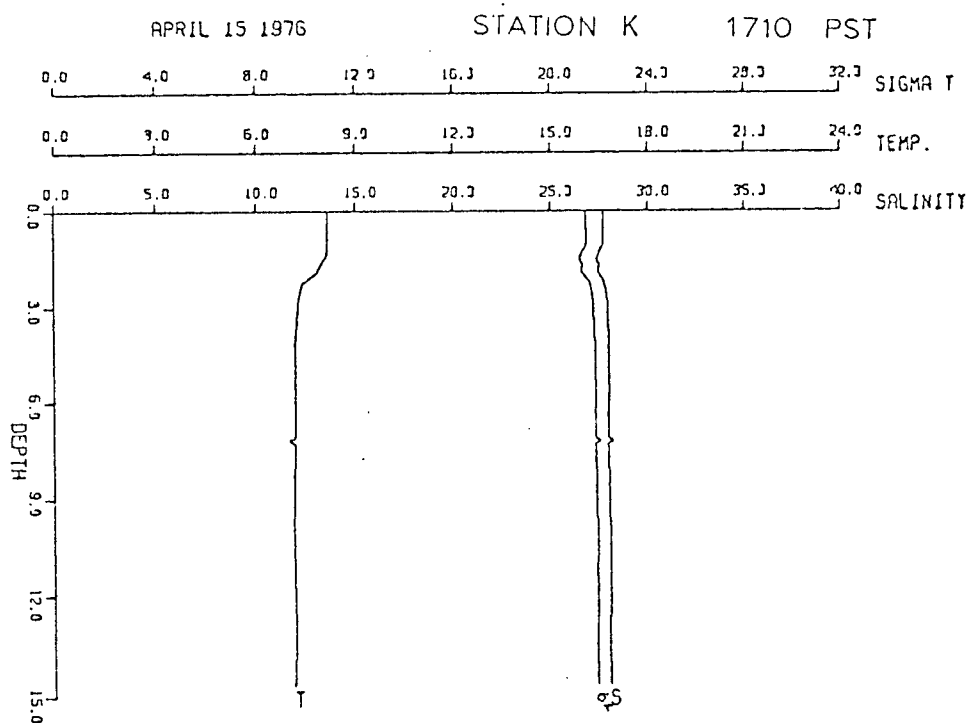


FIGURE 21a. S, T, sigma t profiles at station k, 1710 PST, April 15, 1976.

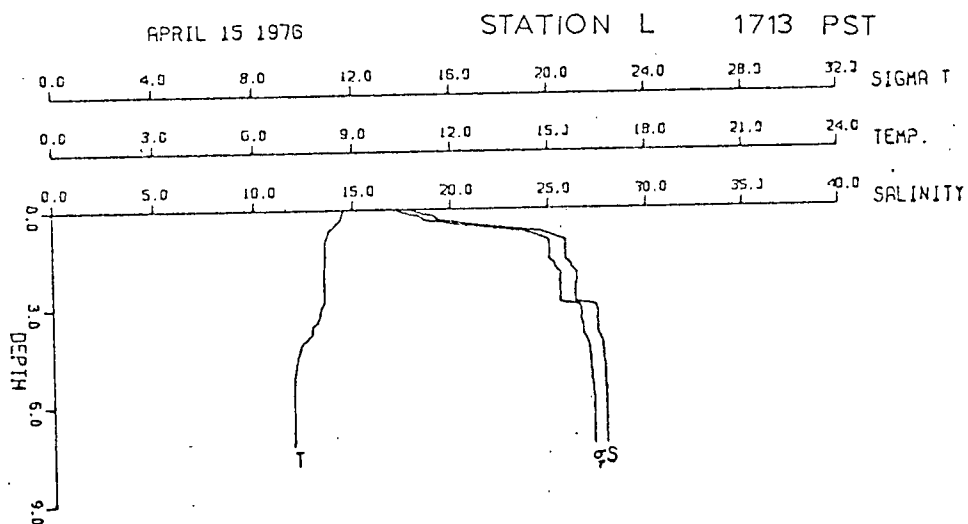
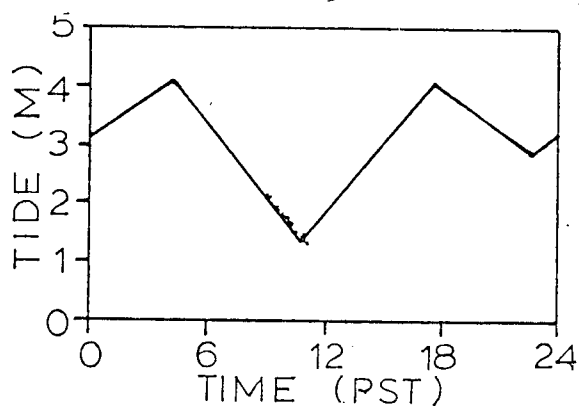
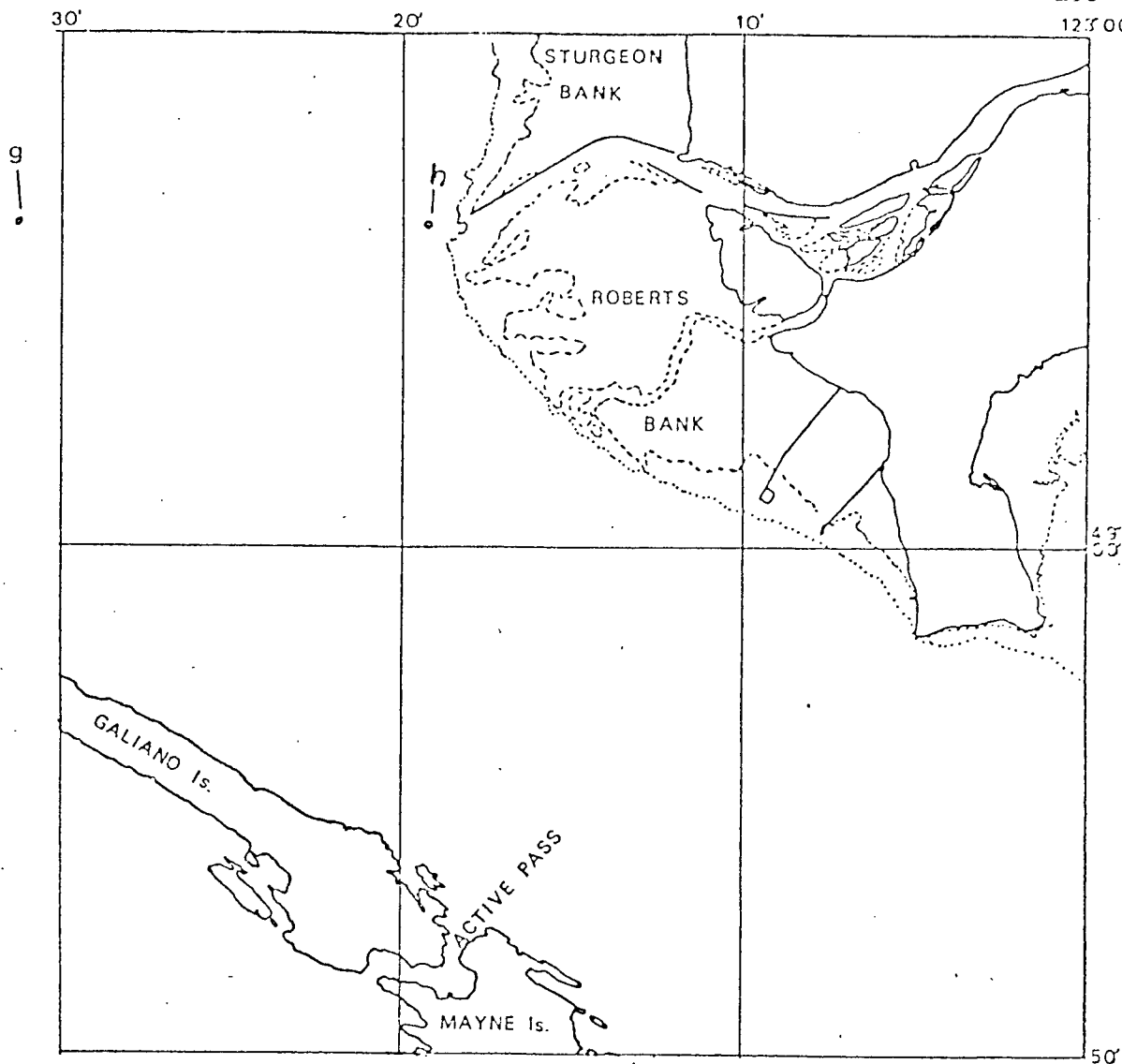


FIGURE 21b. S, T, sigma t profile at station l, 1713 PST, April 15, 1976.



WINDS AT SAND HEADS

0000	E10
0400	E4
0700	calm
0900	W4
1200	NW8
1800	N10

STATION TIMES

g 1623
h 1714

FIGURE 22. Station positions and times, wind and tide for April 28, 1976.

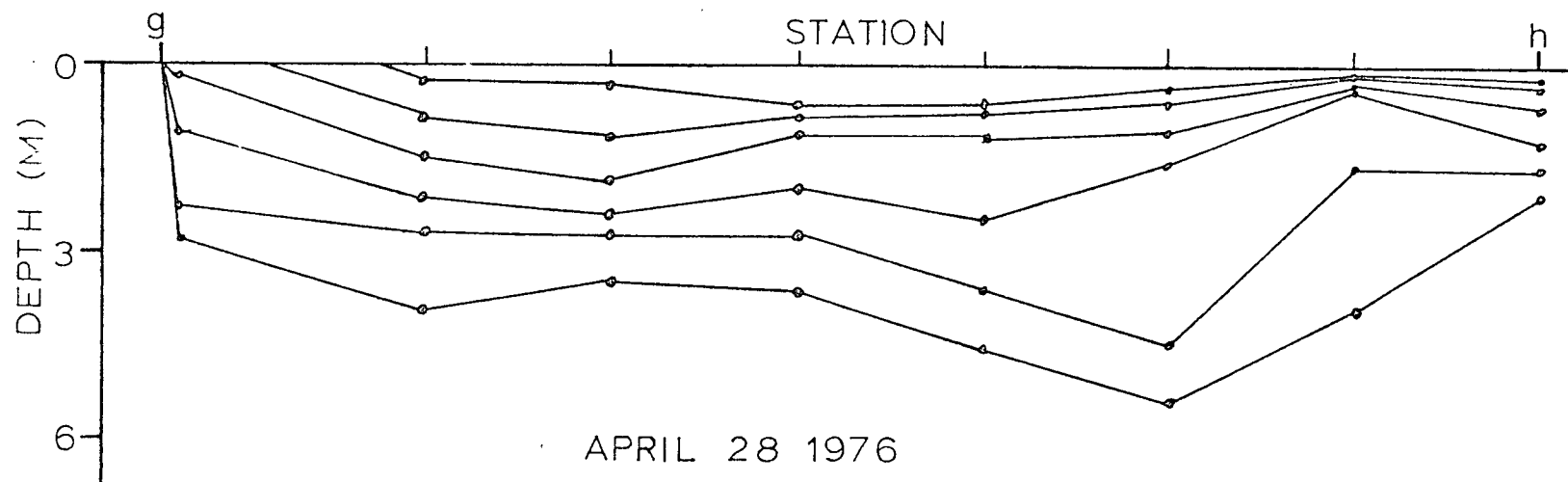


FIGURE 23. Salinity section for April 28, 1976, along a line from a front at station g to station h. The salinity isopycnals are 15, 17.5, 20, 22.5, 25, and 26 parts per thousand.

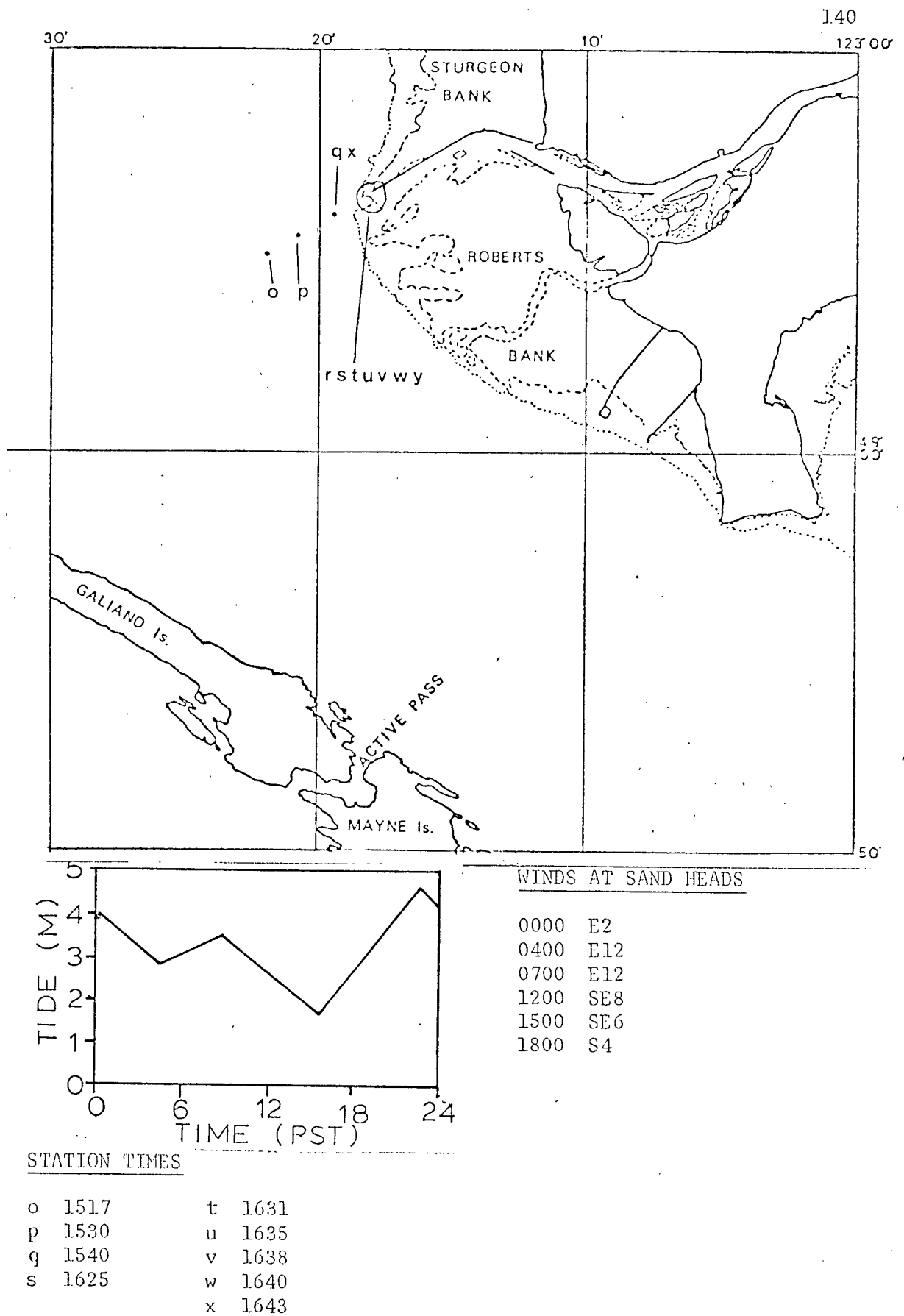


FIGURE 24. Station positions and times, wind and tide for June 4, 1976.

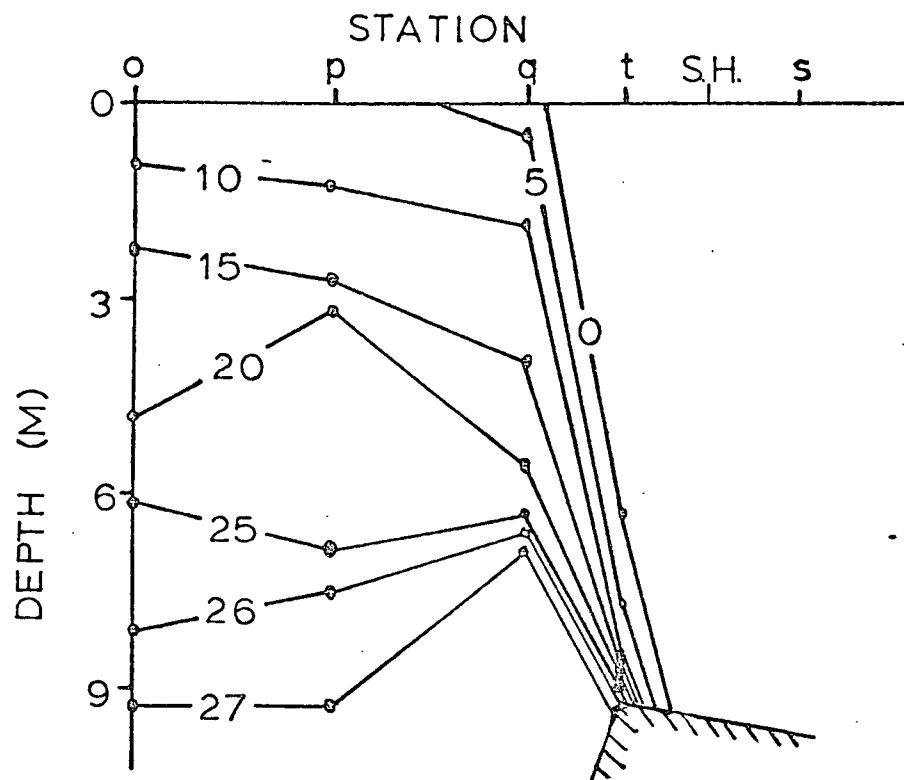


FIGURE 25a. Salinity section along line o-s, June 4, 1976. S.H. indicates the location of Sand Heads.

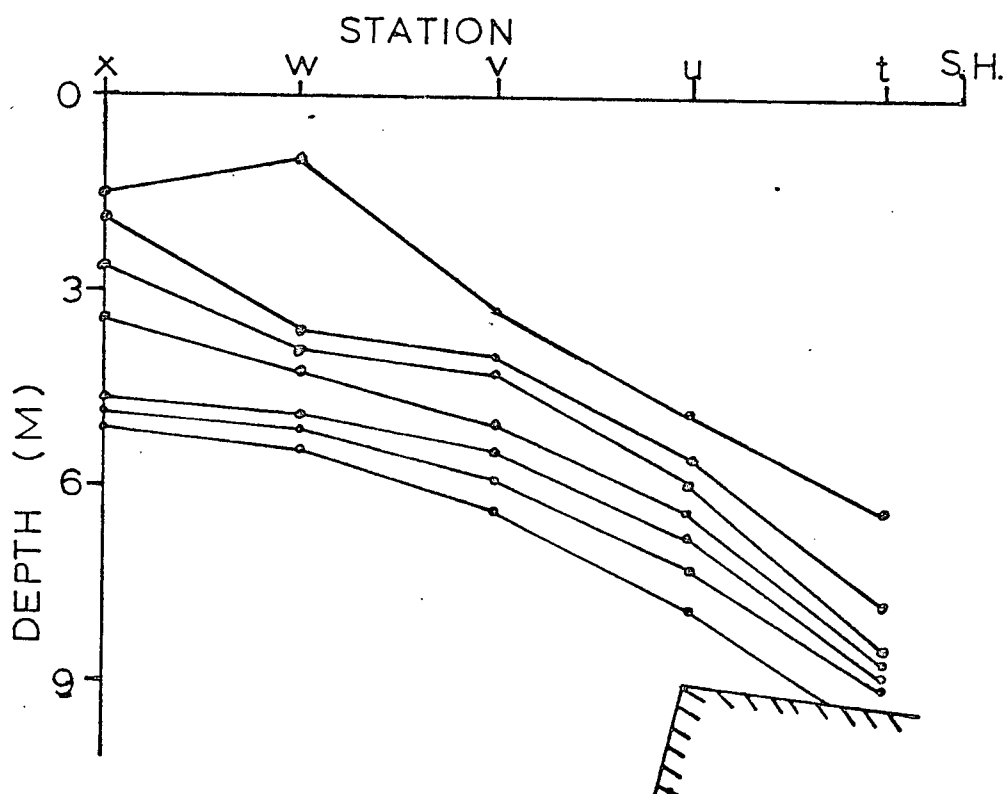
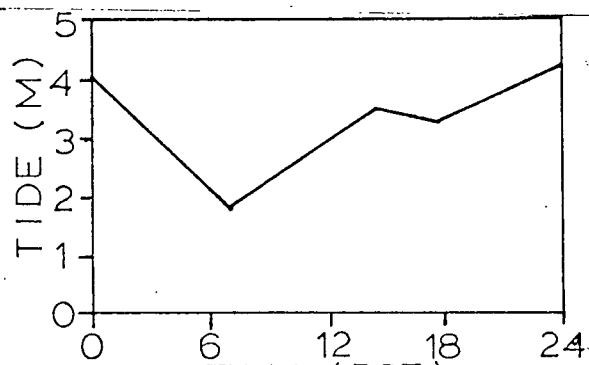
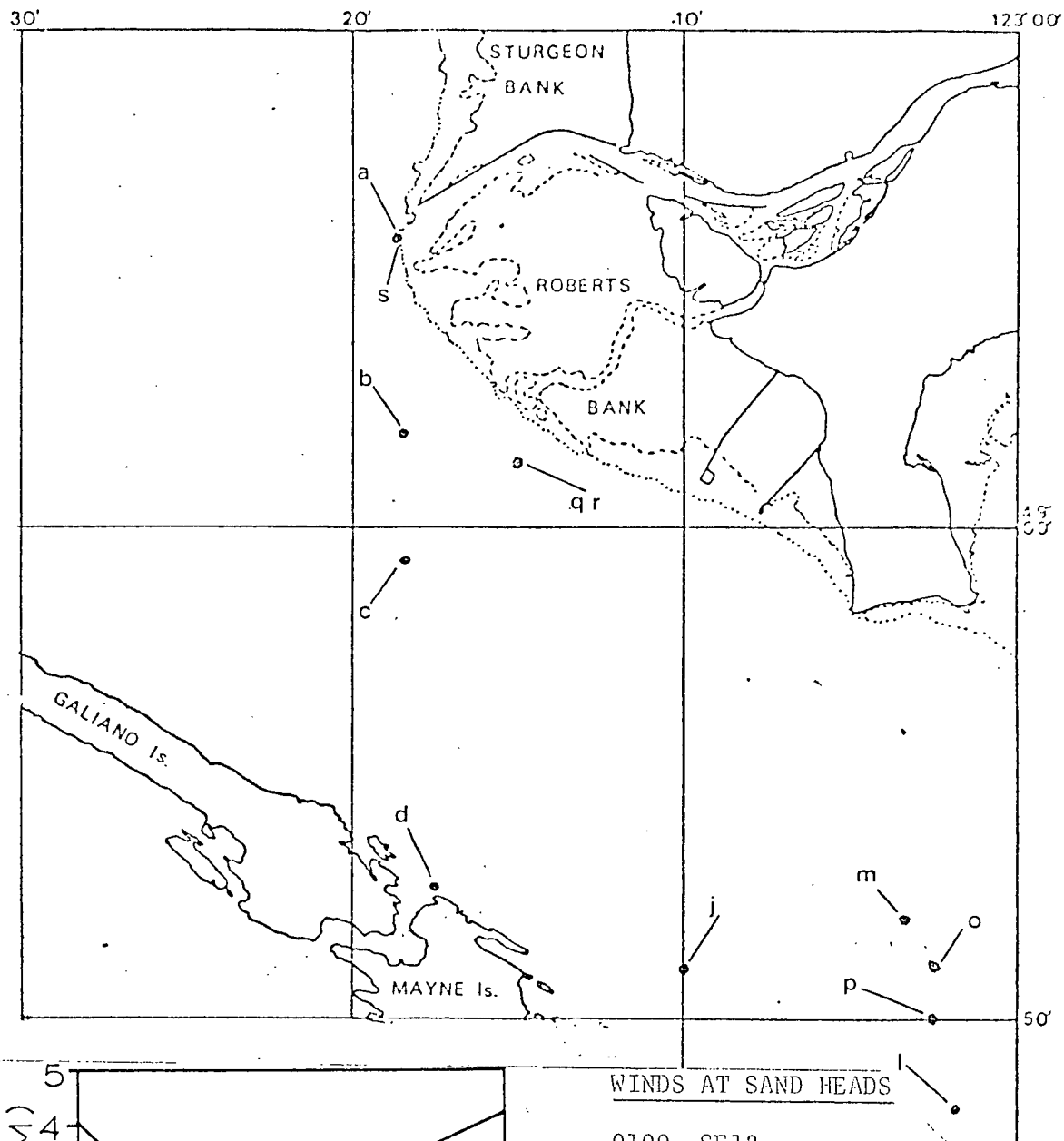


FIGURE 25b. Salinity section along line x-t, June 4, 1976. Isohalines shown are 5, 10, 15, 20, 25, 26, 27‰. S.H. indicates the location of Sand Heads.



WINDS AT SAND HEADS

0100 SE13
 0500 E10
 0900 SE6
 1300 S4
 1700 SE11

STATION TIMES

a 0642	j 1106	p 1329	s 1625
b 0709	l 1230	q 1447	
c 0733	m 1302	q 1457	
d 0916	o 1319	r 1540	

FIGURE 26. Station positions and times, wind and tide for July 3, 1975.

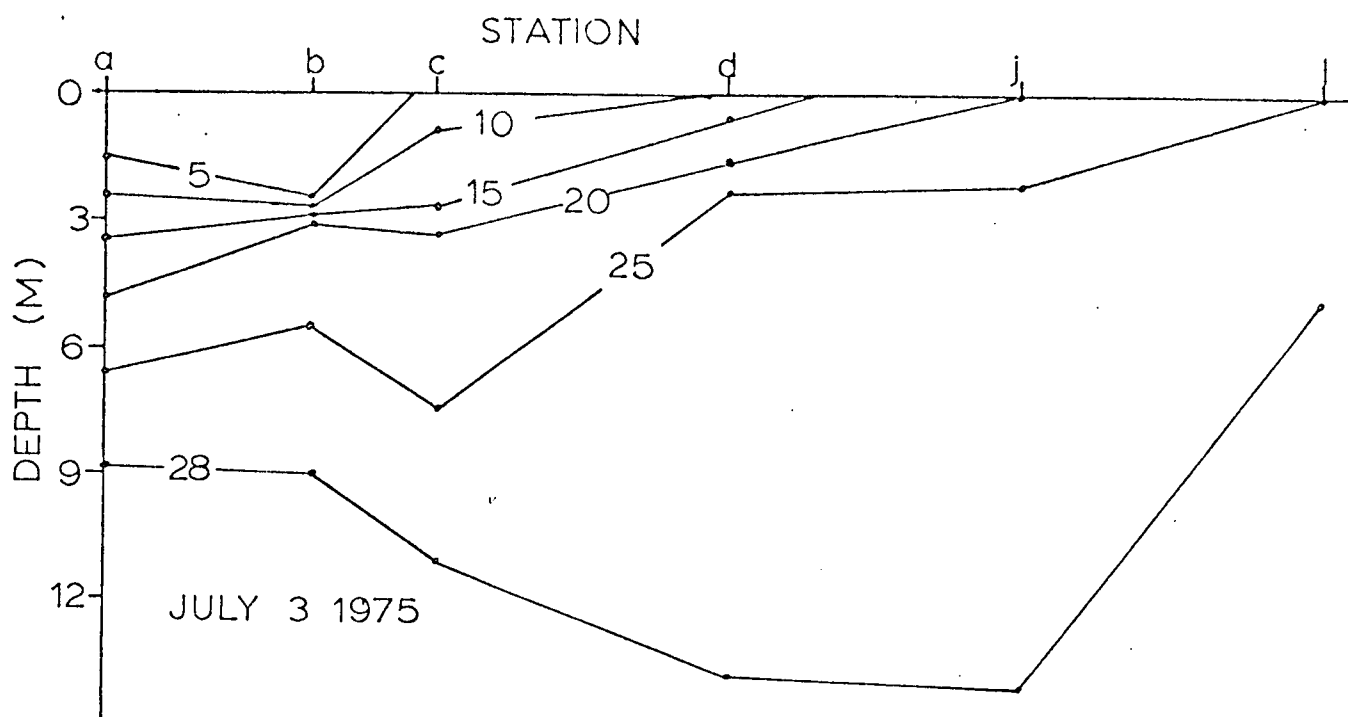


FIGURE 27a. Salinity section along line a-l, July 3, 1975.

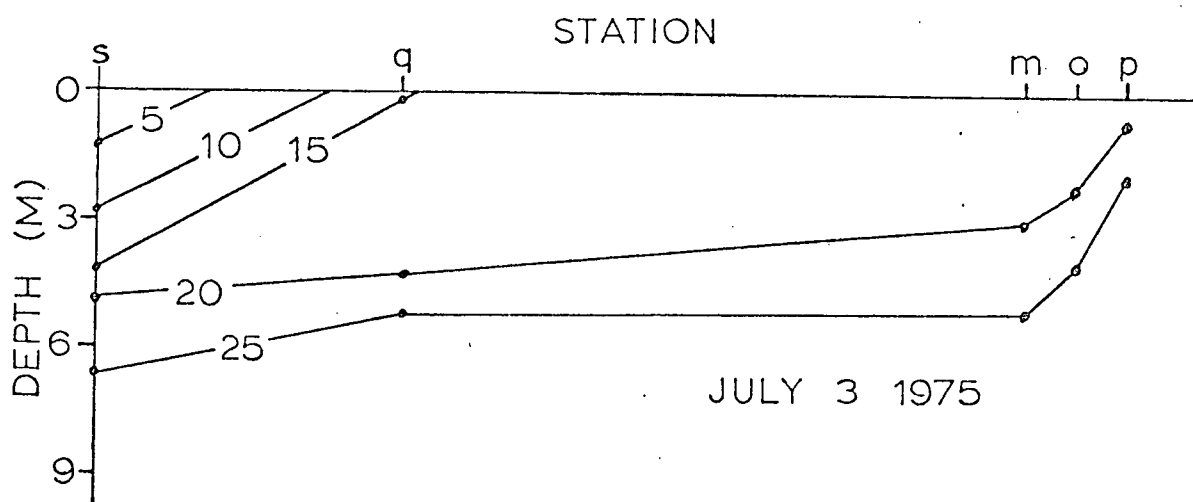


FIGURE 27b. Salinity section along line p-s, July 3, 1975.

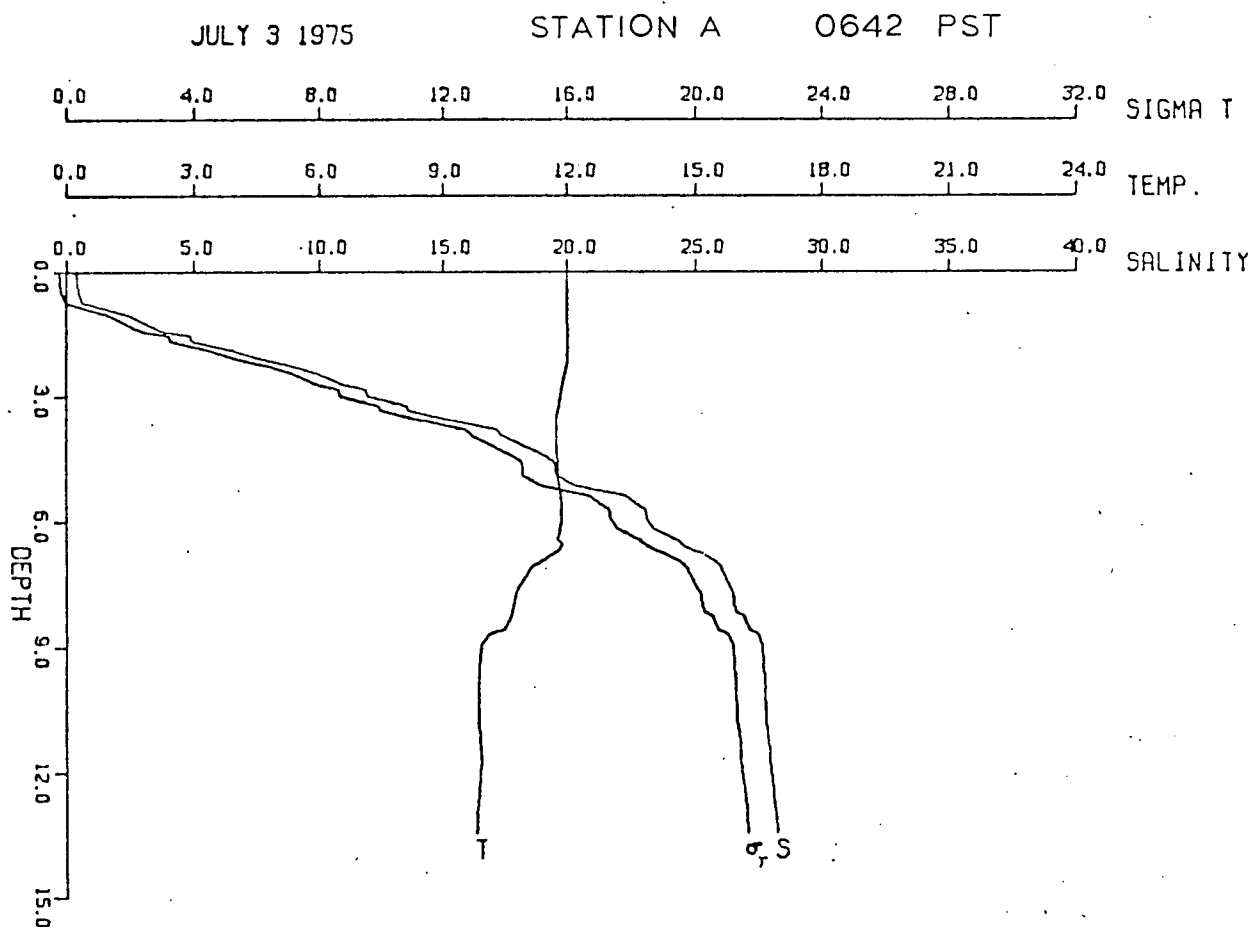


FIGURE 28. S, T, sigma t profiles at station a, 0642 PST, July 3, 1975.

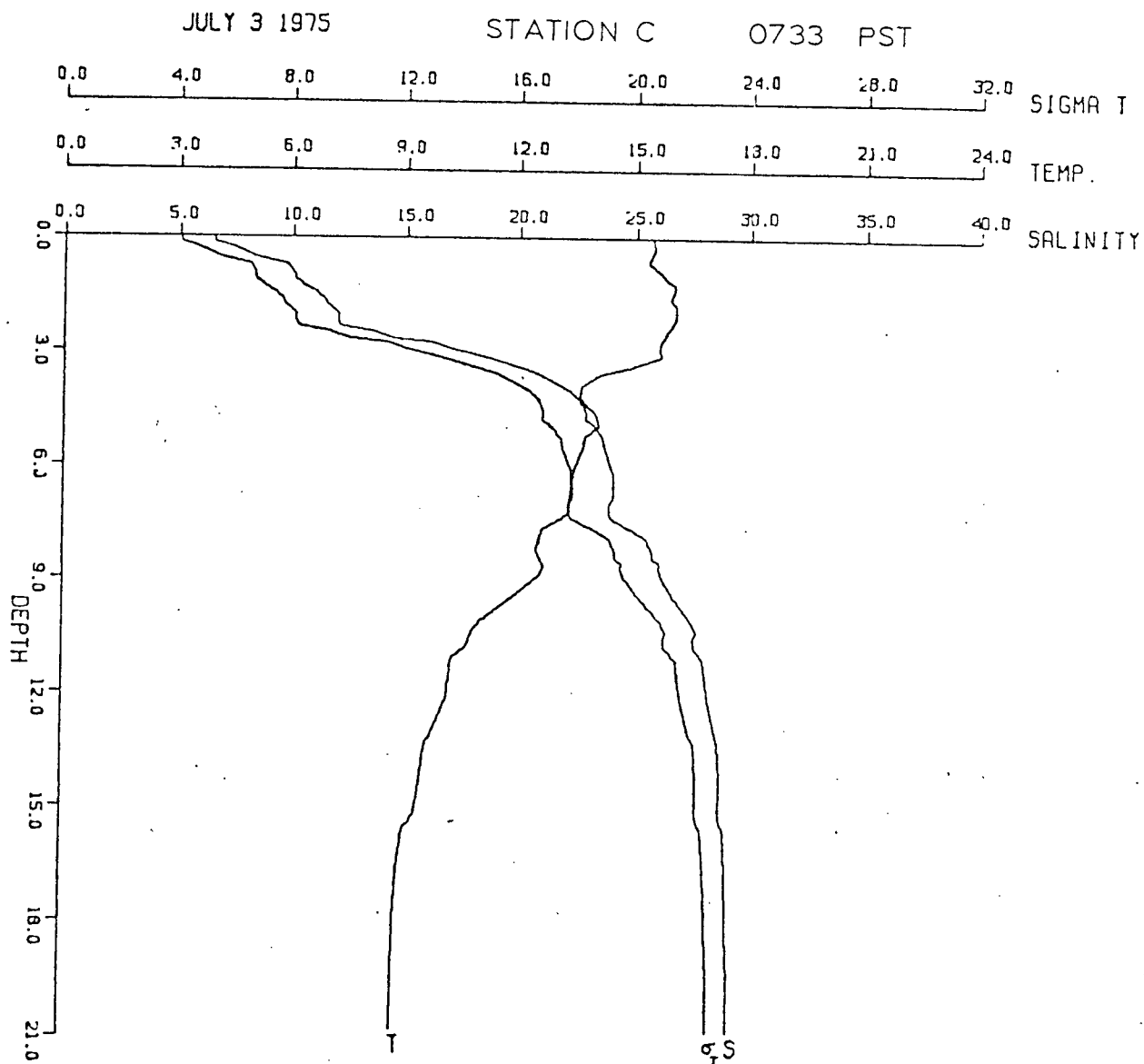


FIGURE 29. S, T, sigma t profiles at station c, 0733 PST,
July 3, 1975.

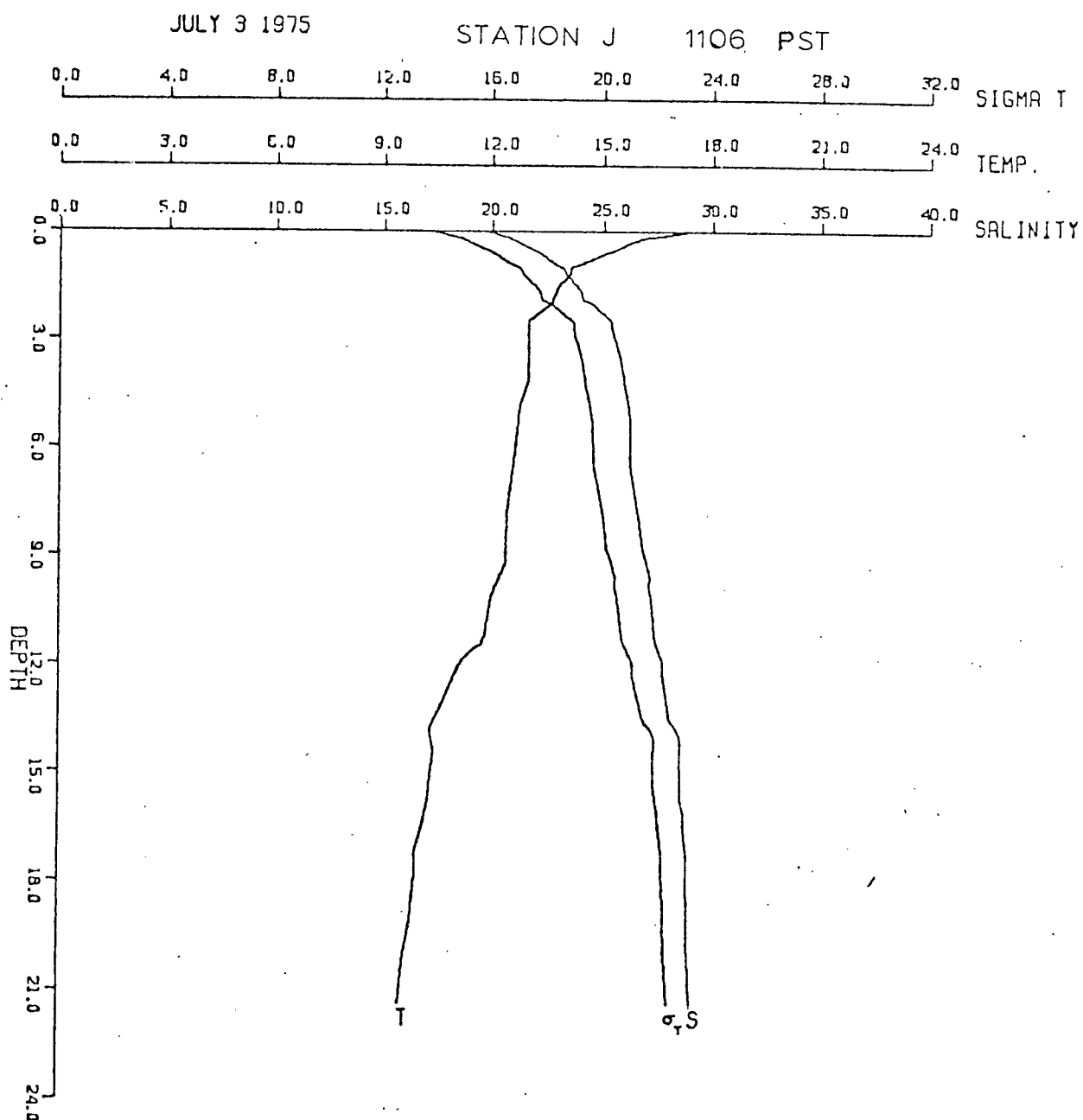


FIGURE 30. S, T, sigma t profiles at station j,
1106 PST, July 3, 1975.

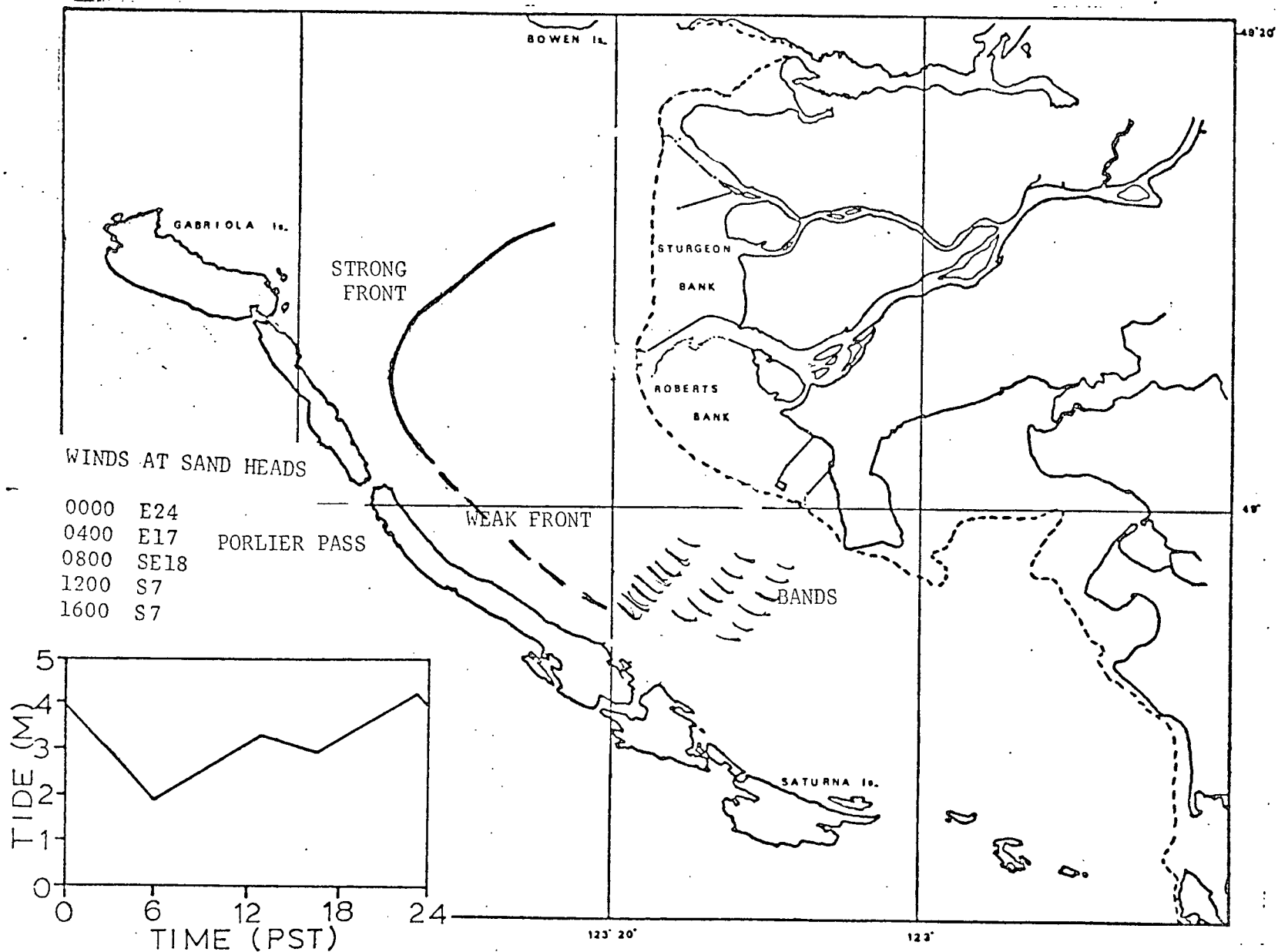


FIGURE 31. Sketch of the plume observed by aerial survey, 0900 PST, July 2, 1975.

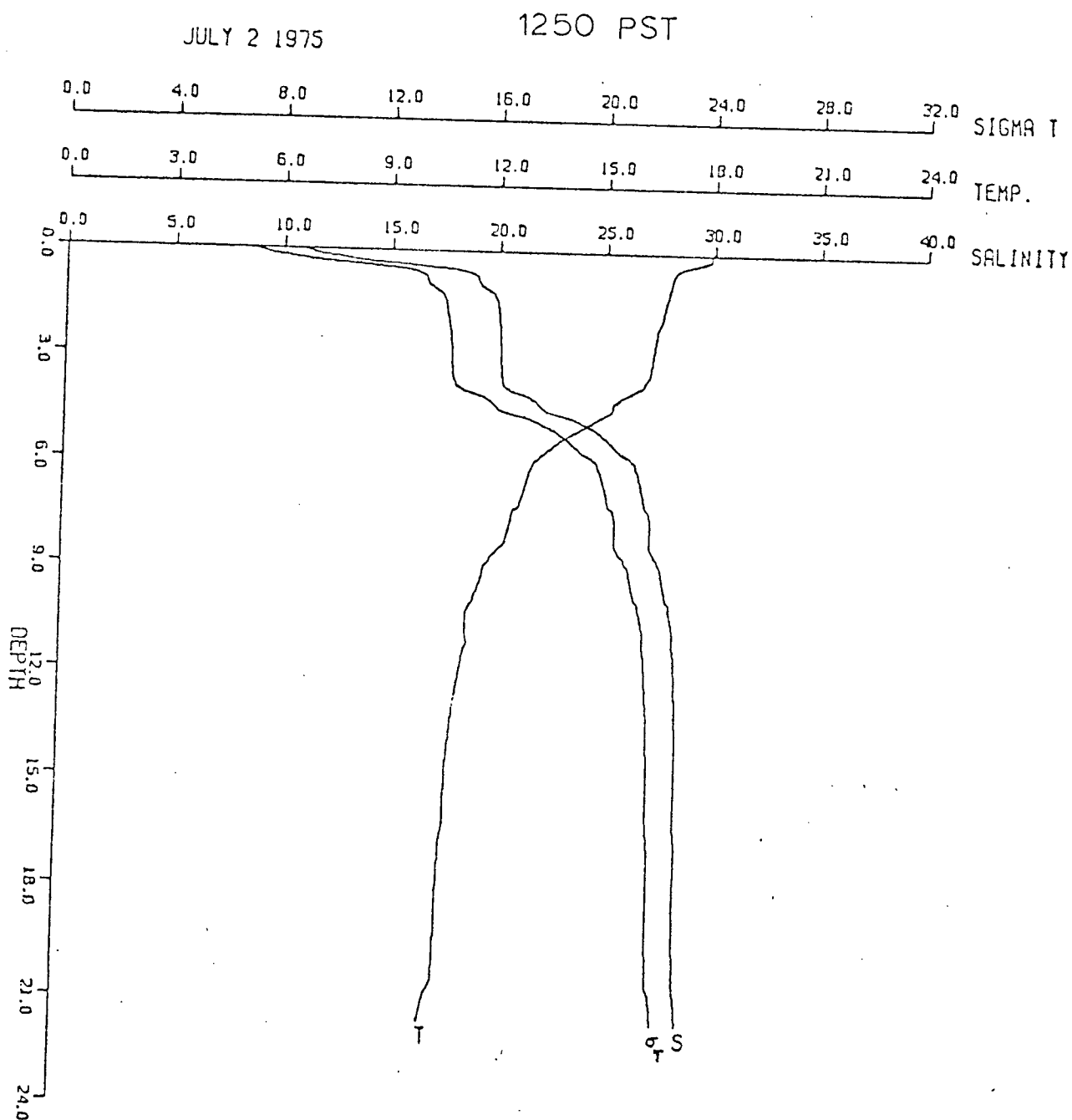


FIGURE 32. S, T, sigma t profile on the silty side of the front,
1250 PST, July 2, 1975..

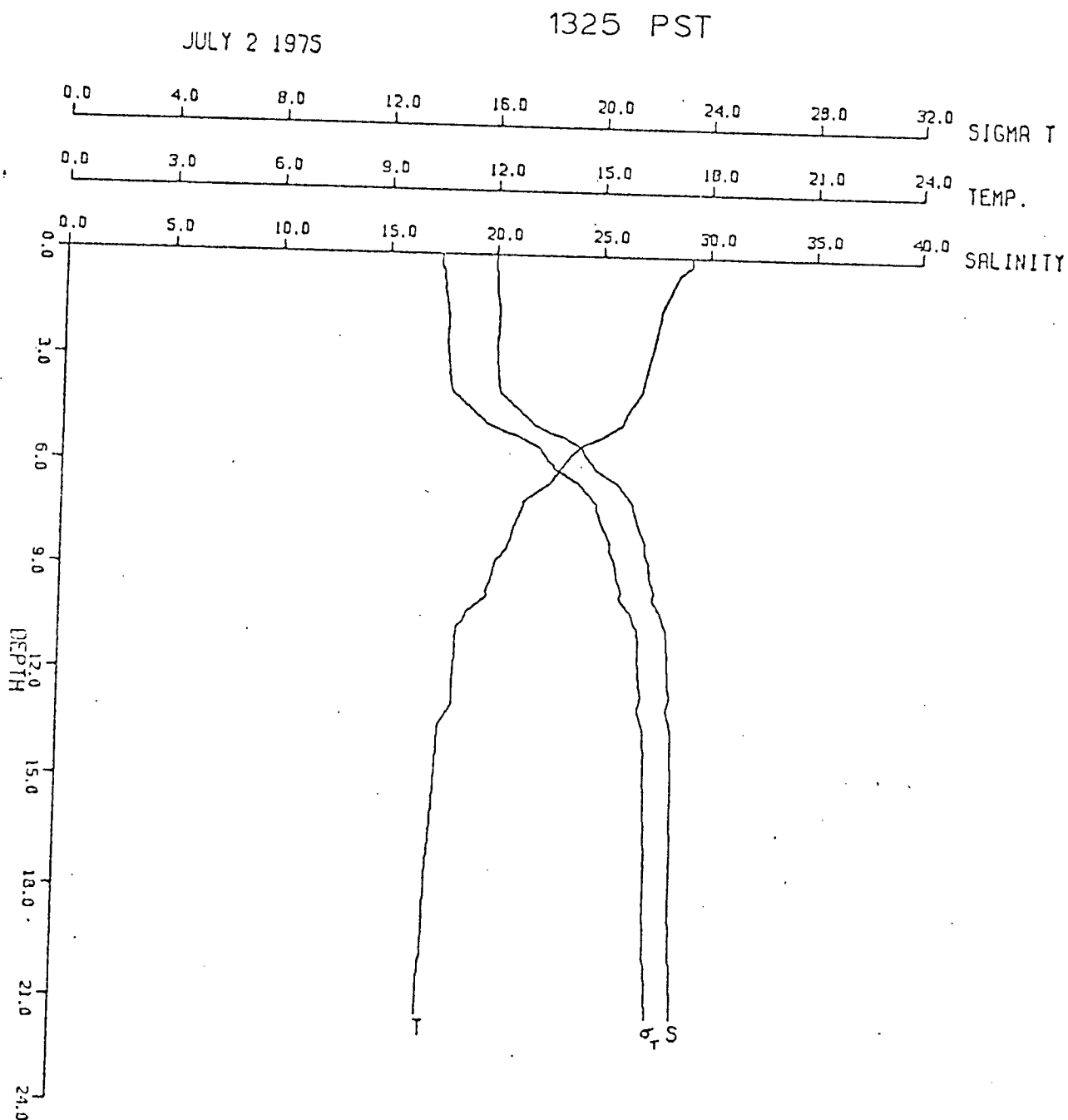


FIGURE 33. S, T, sigma t profiles on deep blue side of front,
1325 PST, July 2, 1975.

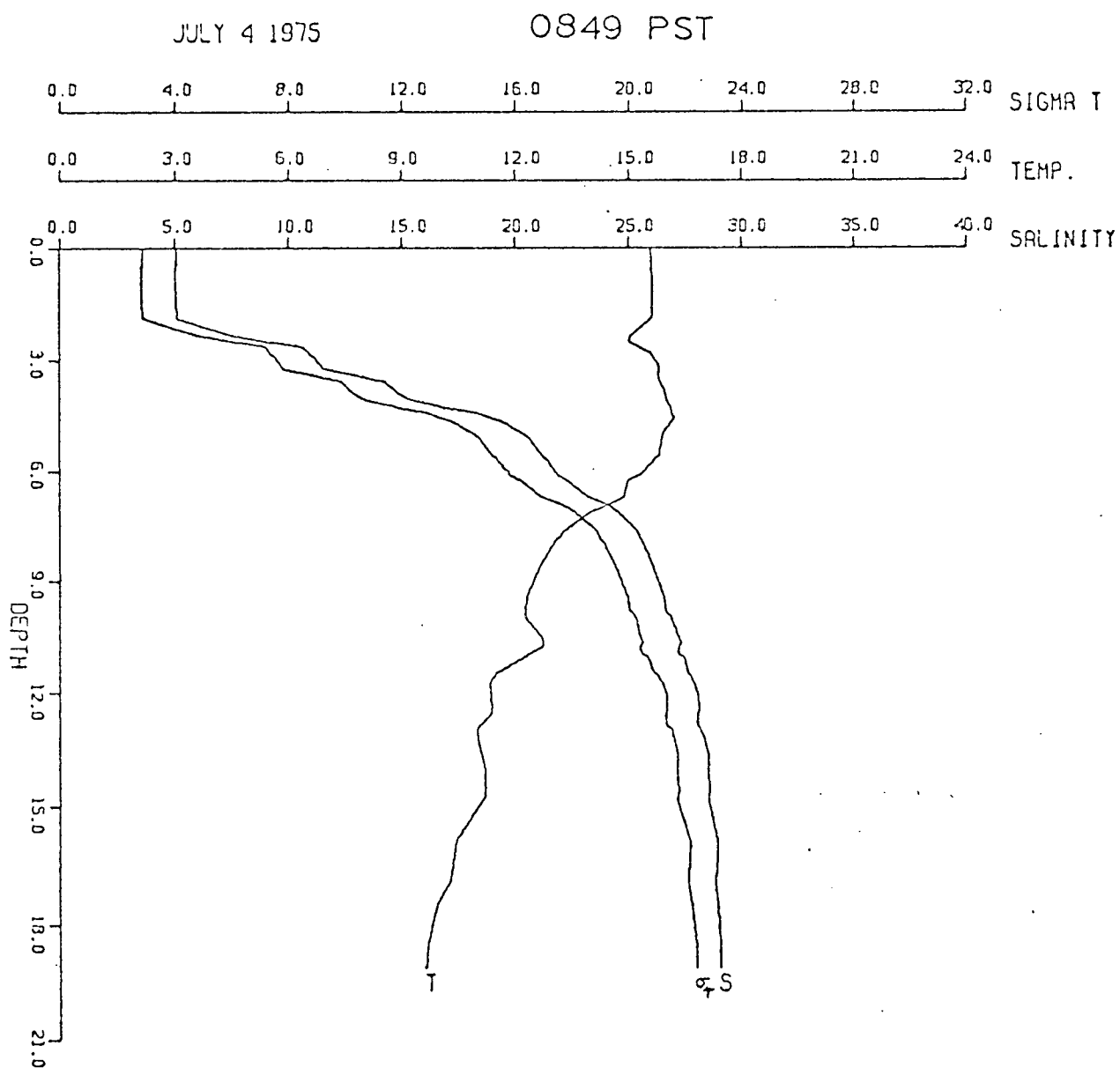


FIGURE 34. S, T, sigma t profiles on silty side of front,
0849 PST, July 4, 1975.

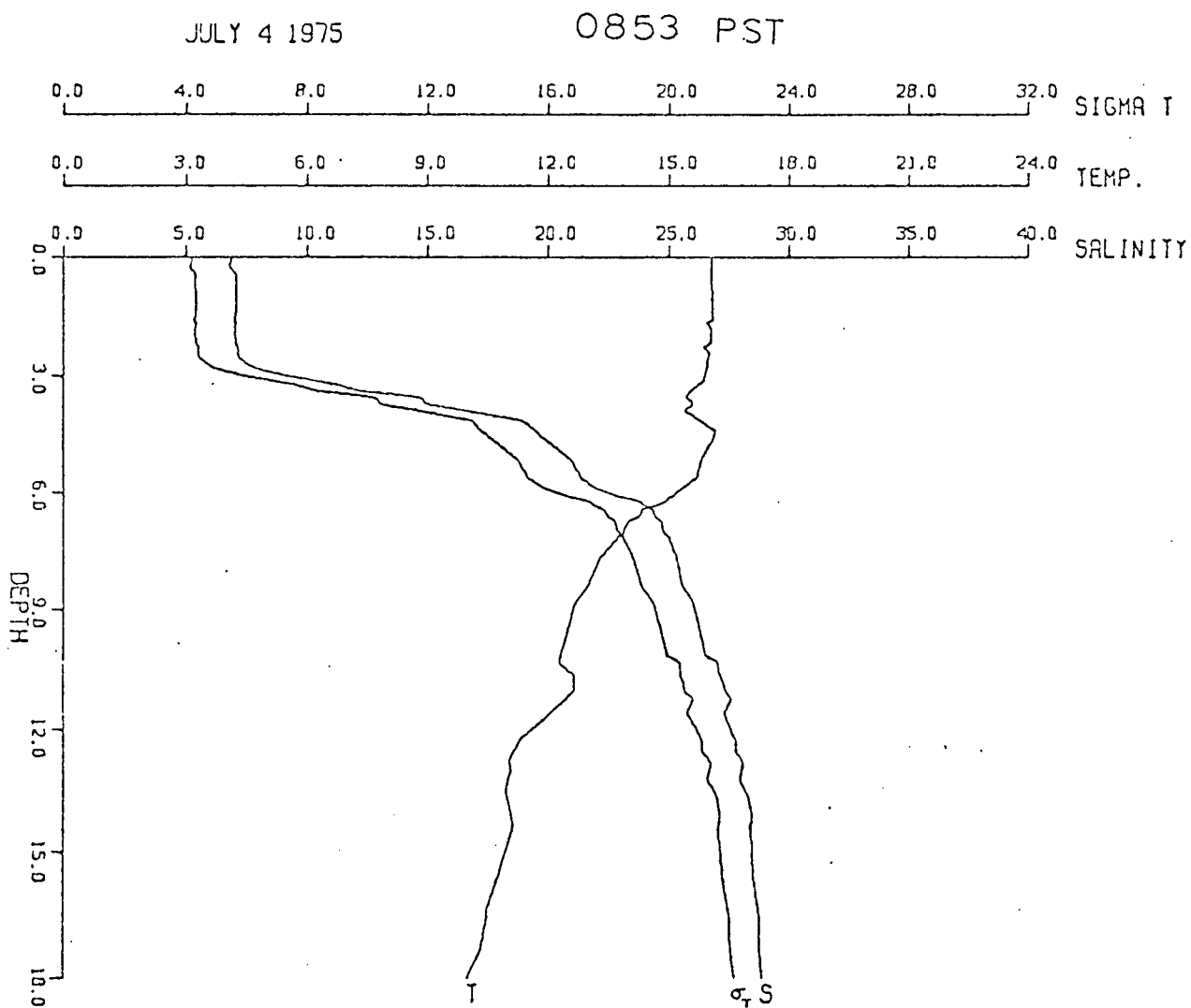


FIGURE 35. S, T, sigma t profiles on deep blue side of front,
0853 PST, July 4, 1975.

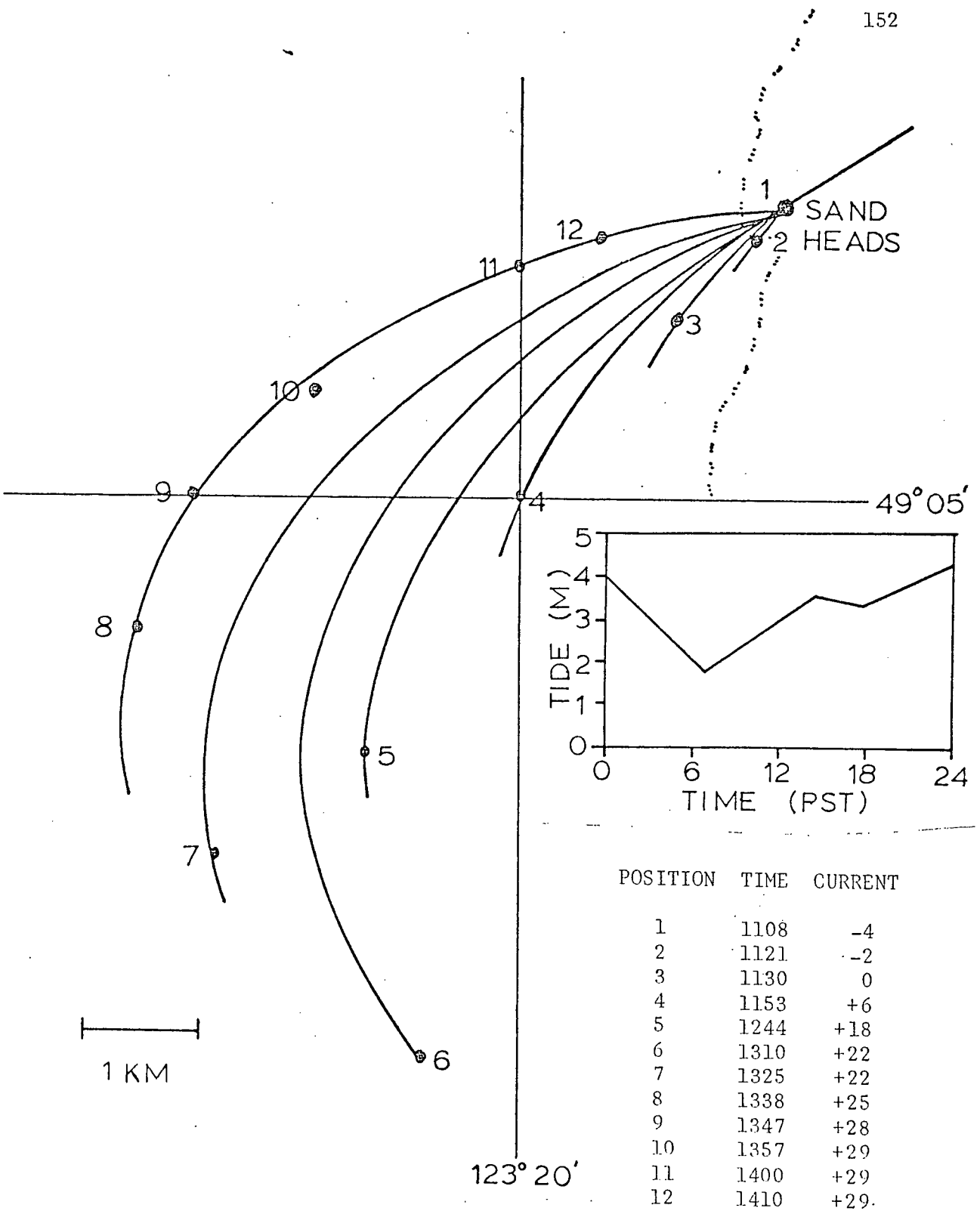
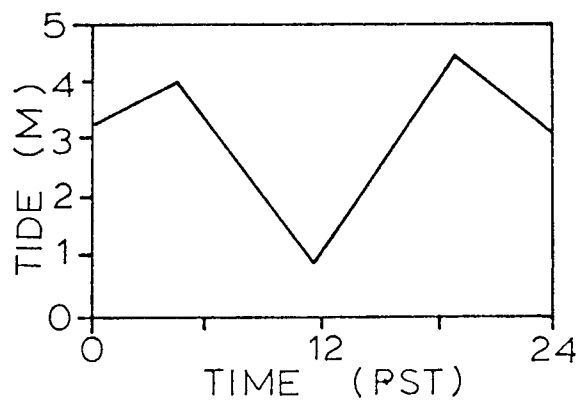
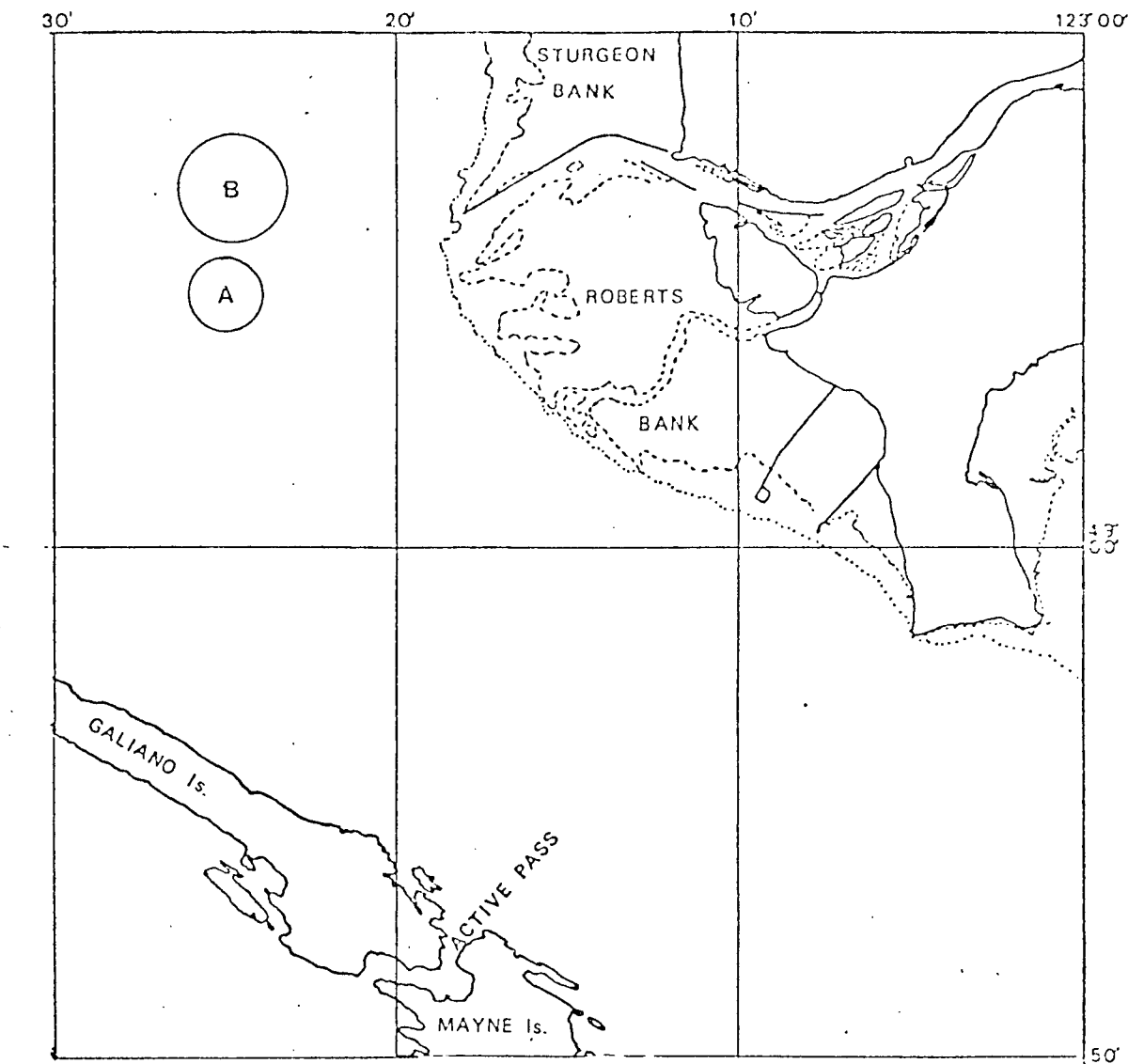


FIGURE 36. The evolution of a front, January 18, 1976.
The estimated tidal currents in the inset table are in cm/sec, positive currents are flooding.



WIND AT SAND HEADS

0100	E6
0500	E6
0900	SE1
1300	calm
1700	S8

STATION TIMES

A	0752 - 1121
B	1245 - 1425

FIGURE 37. Station positions and times, wind and tide for July 23, 1975.

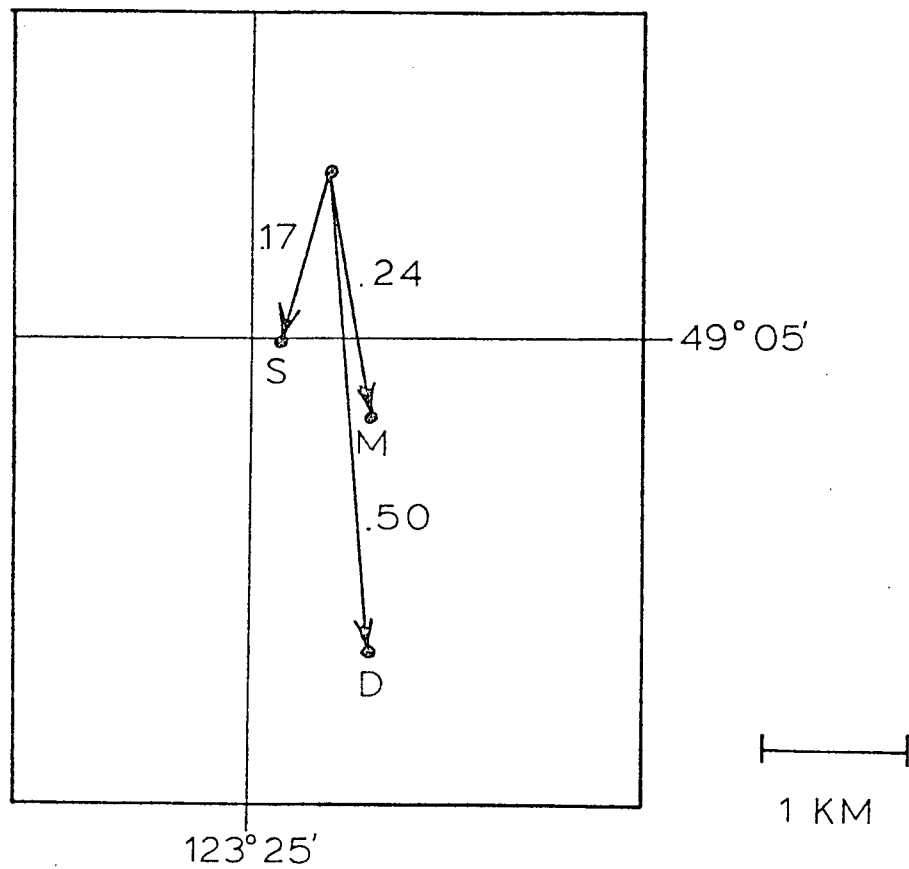


FIGURE 38a. Paths of drogues released in region A, July 23, 1975. Speeds in m/sec are indicated.

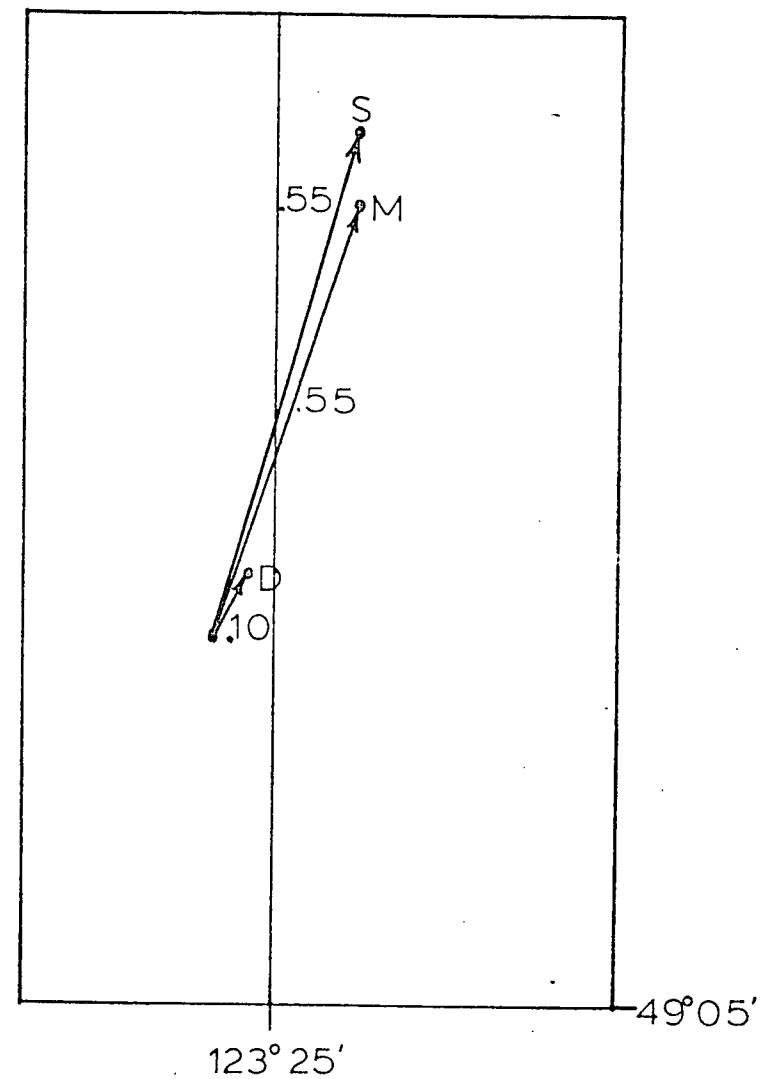


FIGURE 38b. Paths of drogues released in region B, July 23, 1975. Speeds in m/sec are indicated.

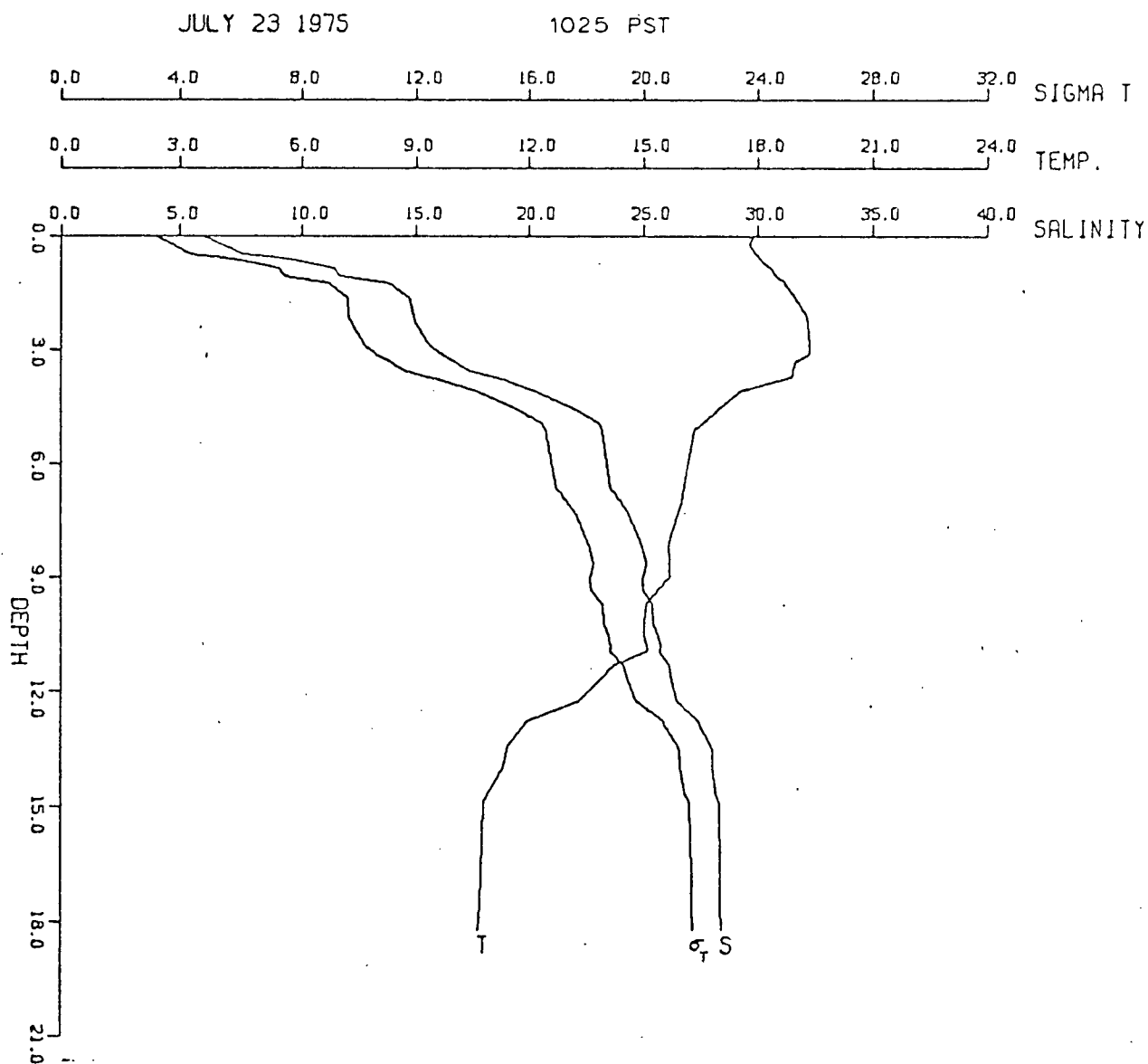


FIGURE 39. S, T, sigma t profiles in region A, 1025 PST, July 23, 1975.

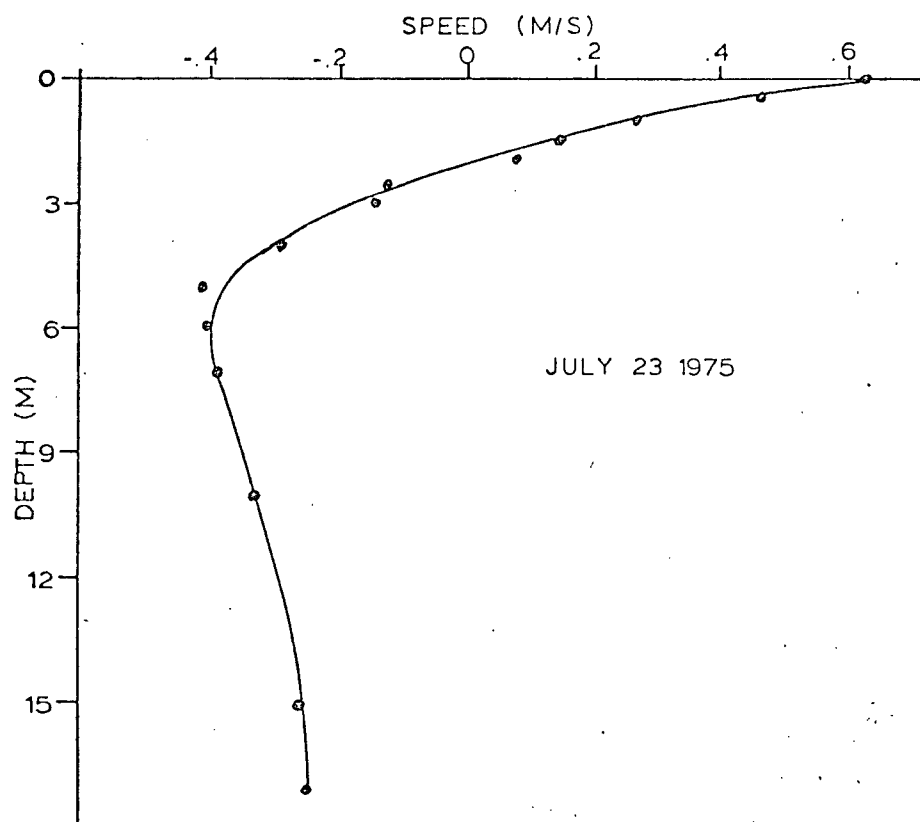
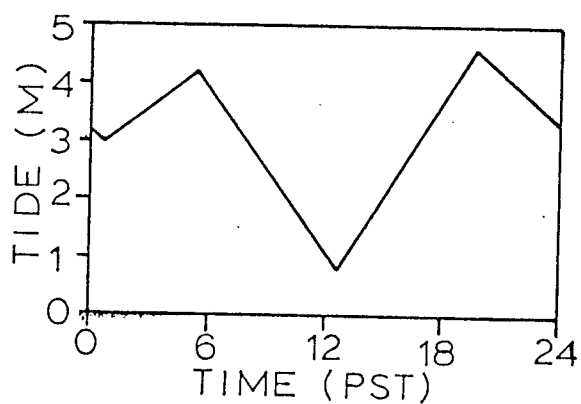
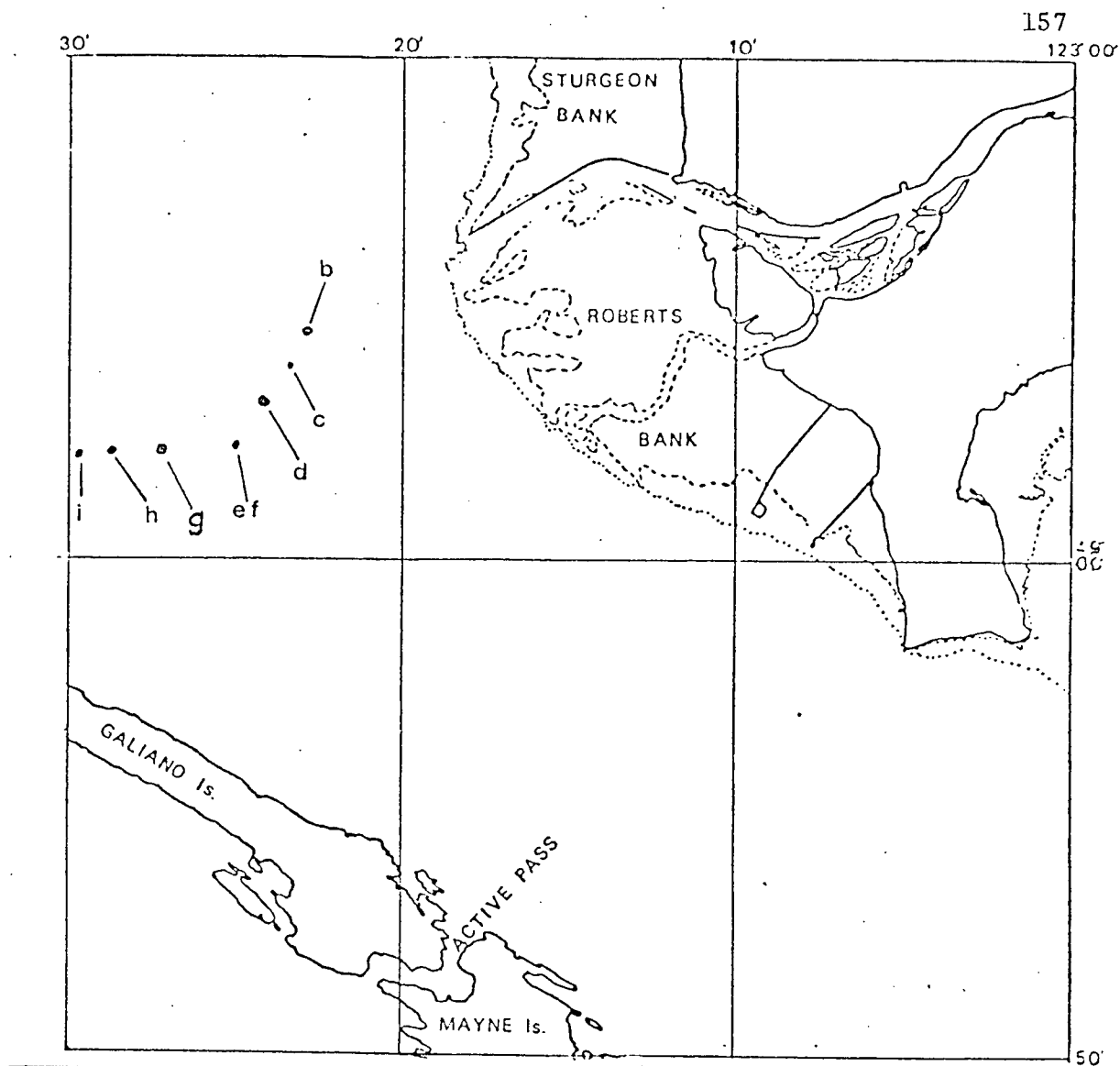


FIGURE 40. Speed profile in region A, 1015 PST to 1045 PST,
July 23, 1975.



WINDS AT SAND HEADS

0000	E10
0400	SE12
0700	SE12
0900	E12
1200	SE10
1500	S8

STATION TIMES

b	0907	f	1226
c	1020	g	1304
d	1110	h	1404
e	1222	i	1500

FIGURE 41. Station positions and times, wind and tide for July 13, 1976.

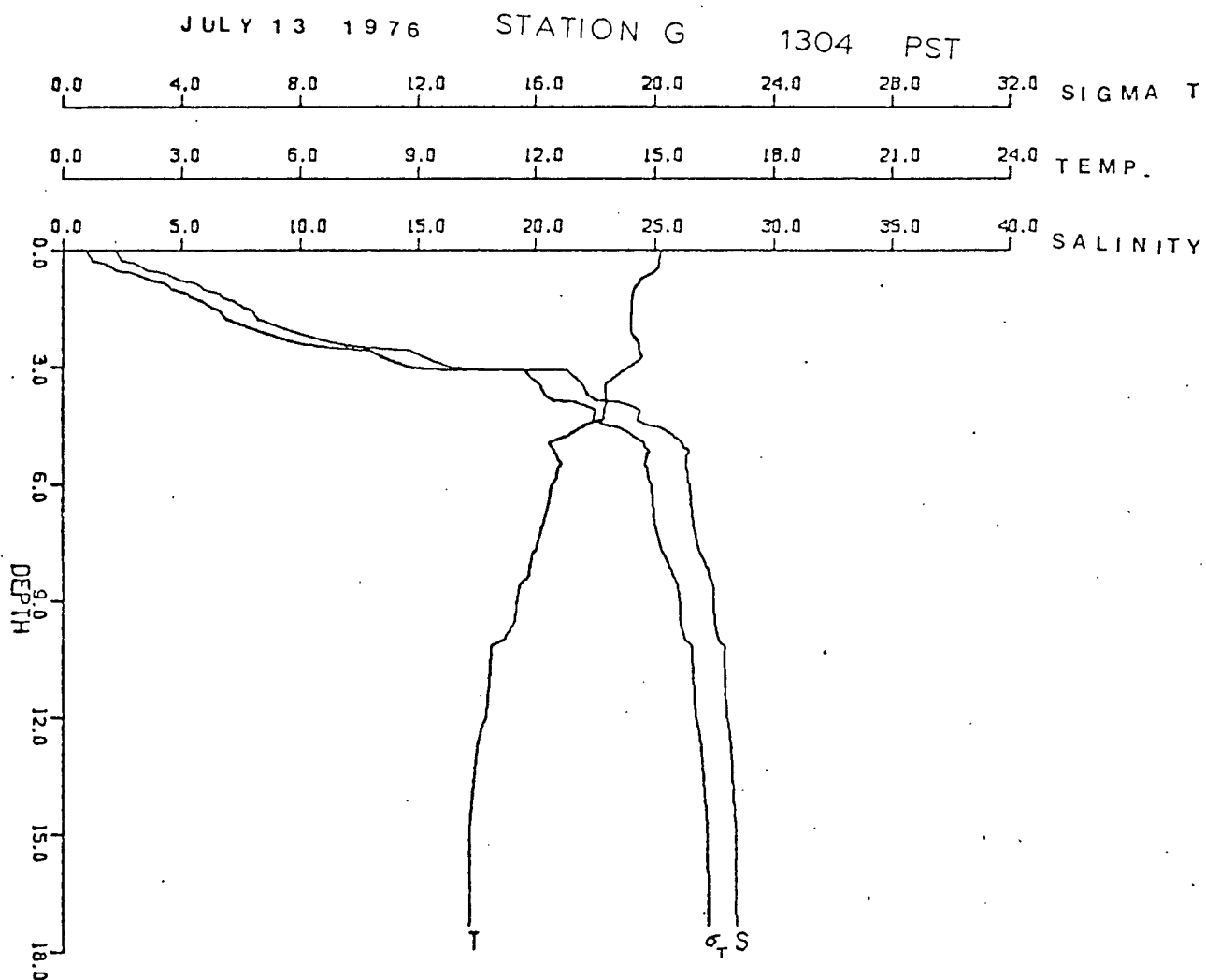


FIGURE 42. S, T, sigma t profiles at station g, 1304 PST, July 13, 1976.

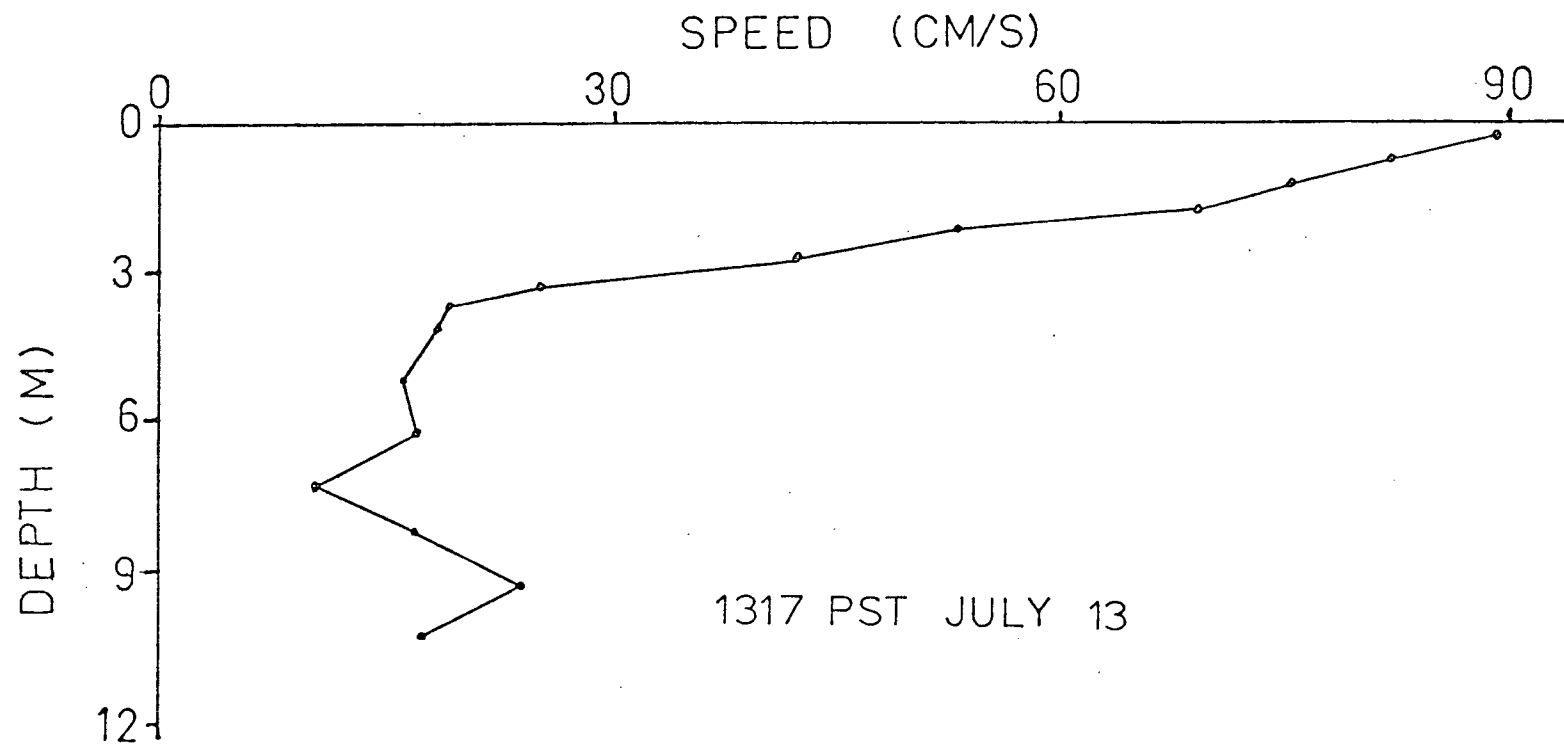


FIGURE 43. Speed profile at station g, 1317 PST, July 13, 1976.

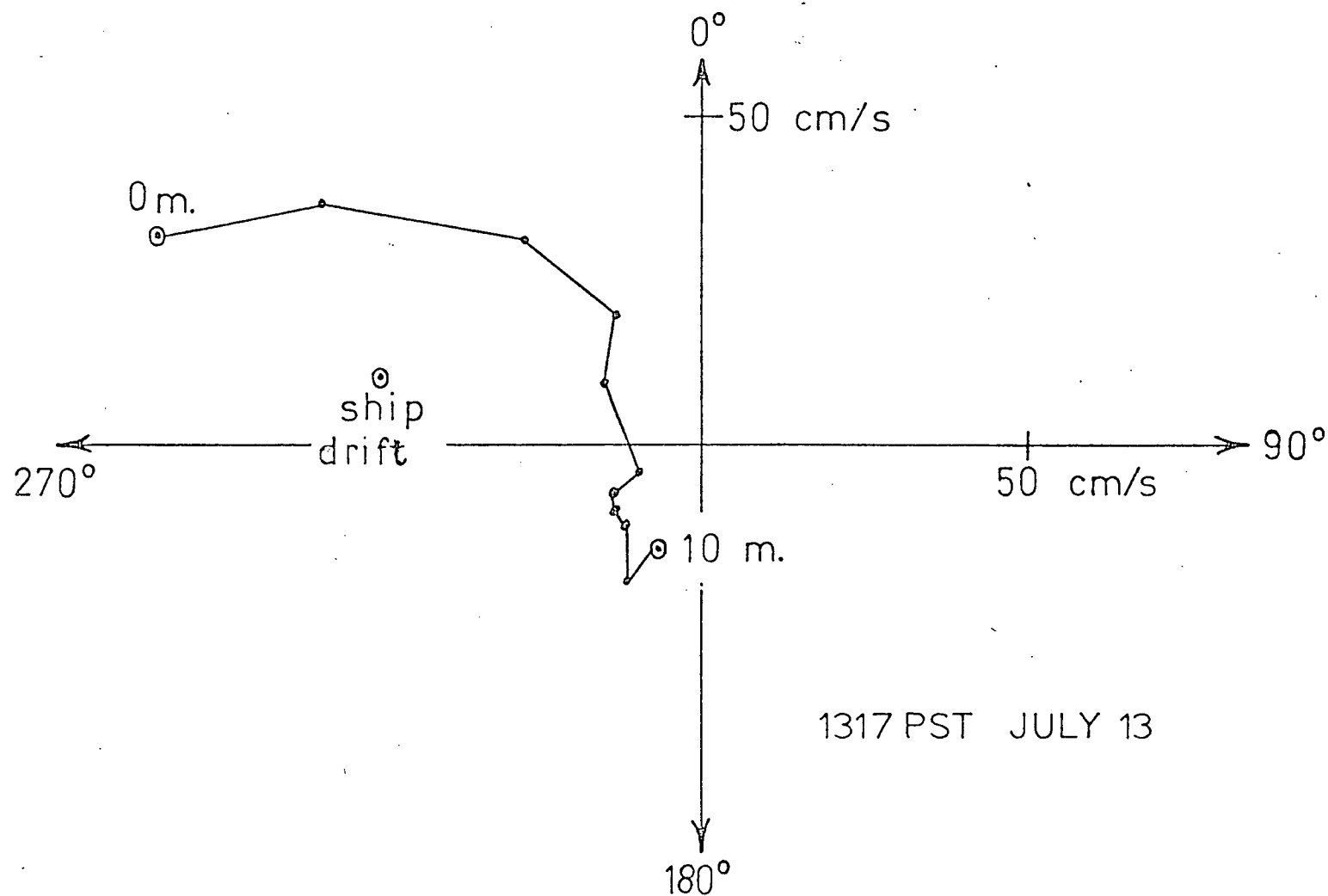


FIGURE 44. Polar plot of velocity vectors, station g, 1317 PST, July 13, 1976.

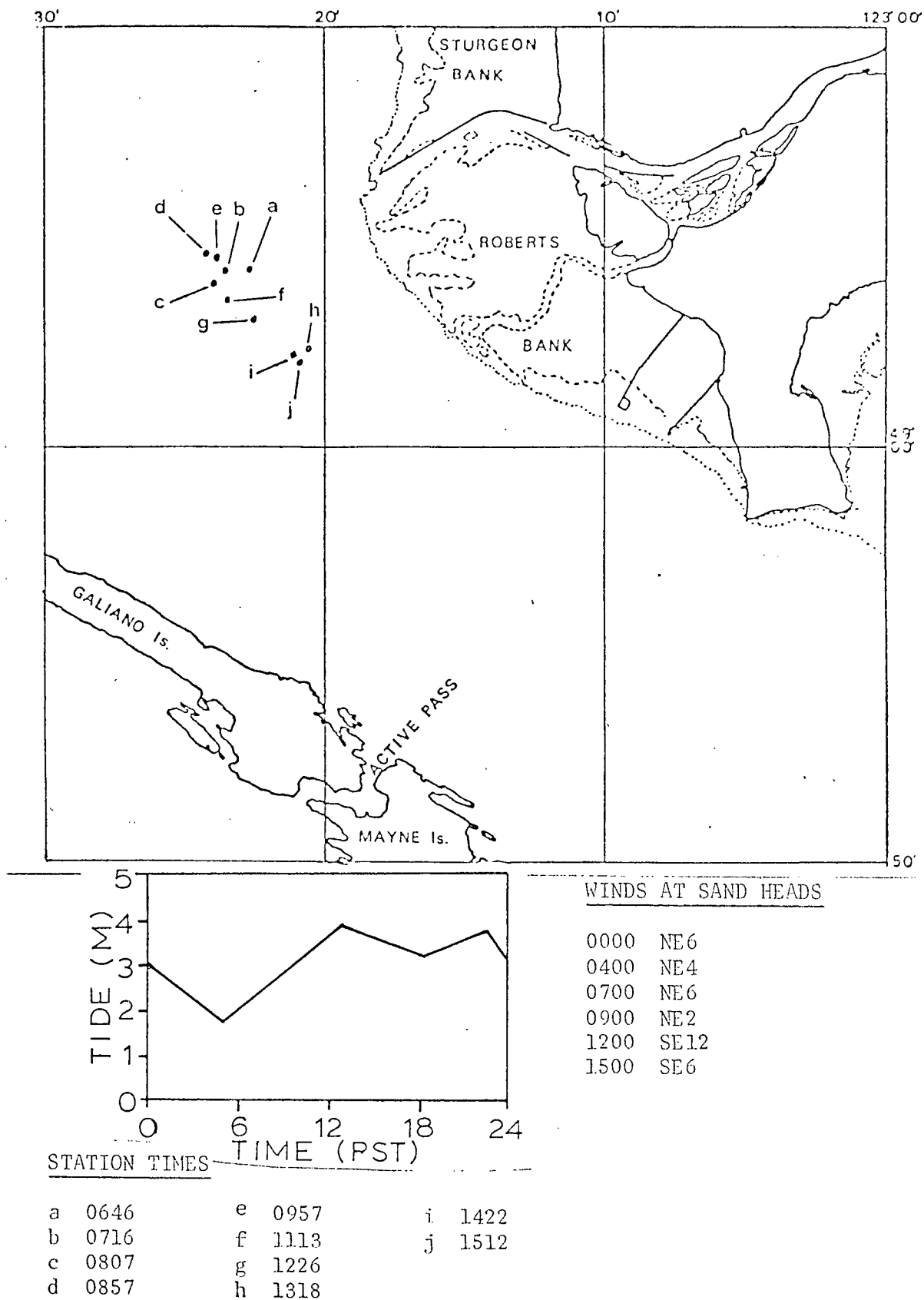


FIGURE 45. Station positions and times, wind and tide for Sept. 17, 1976.

SEPT 17 1976

STATION A 0646 PST

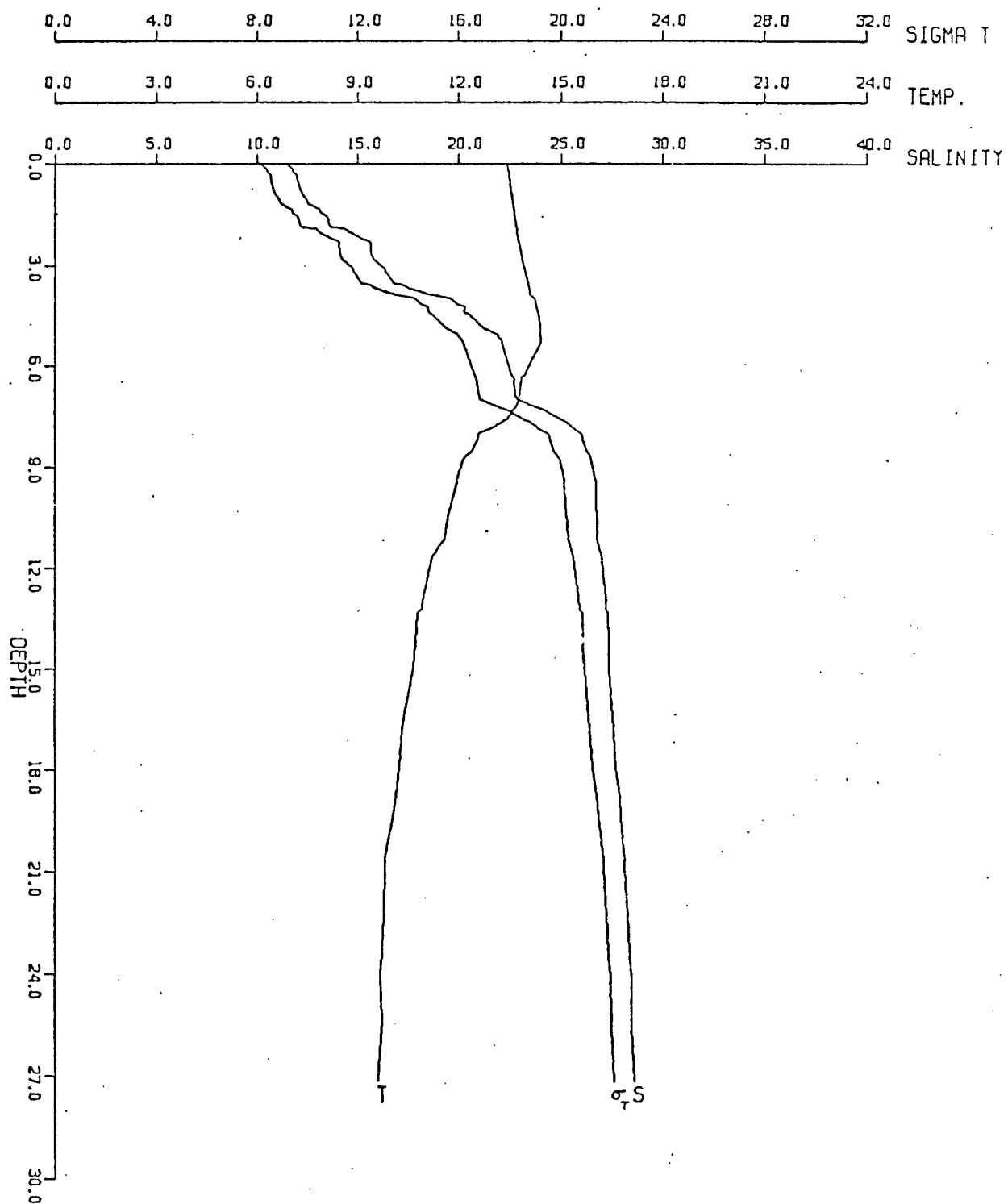


FIGURE 46. S, T, sigma t profiles at station a, 0646 PST, Sept. 17, 1976.

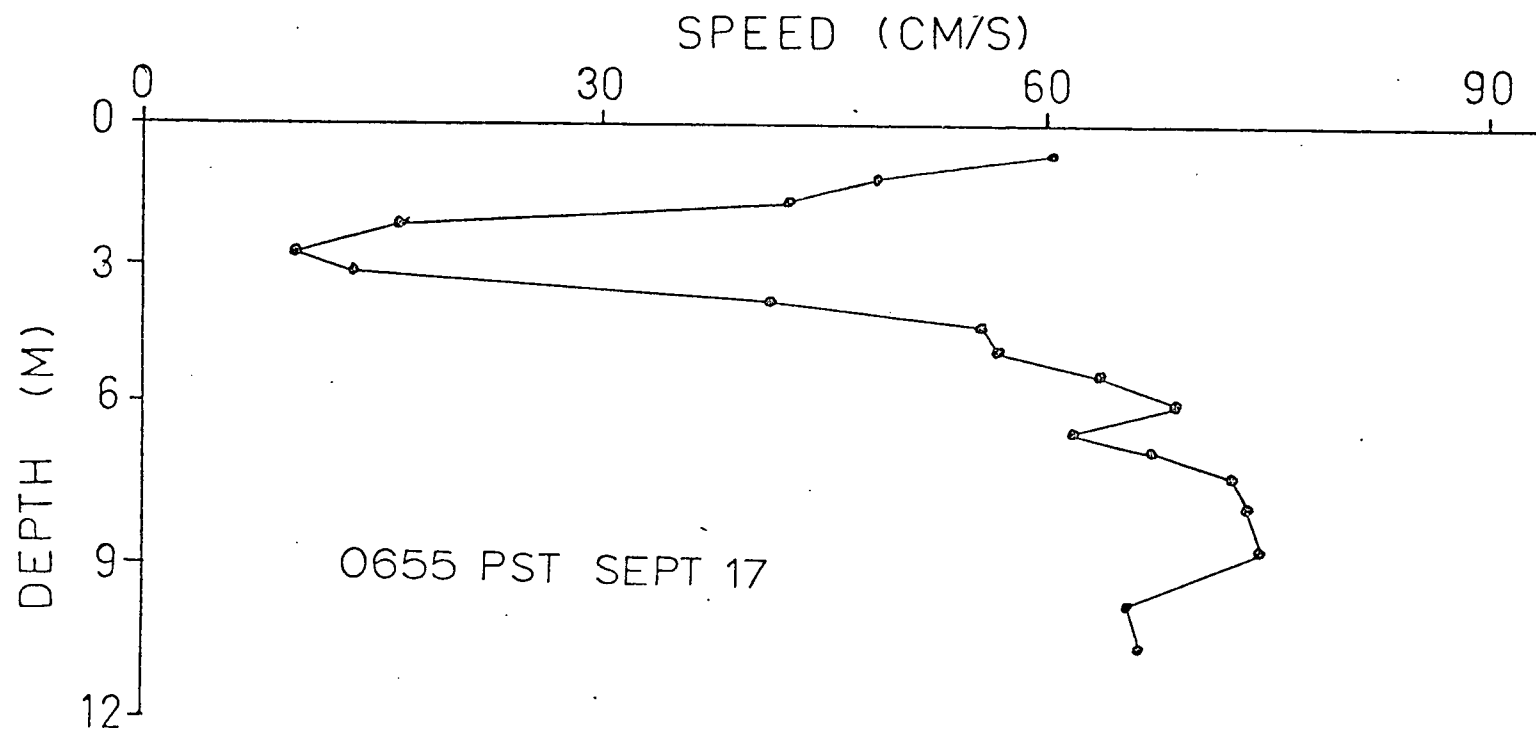


FIGURE 47. Speed profile at station a, 0655 PST, Sept. 17, 1976.

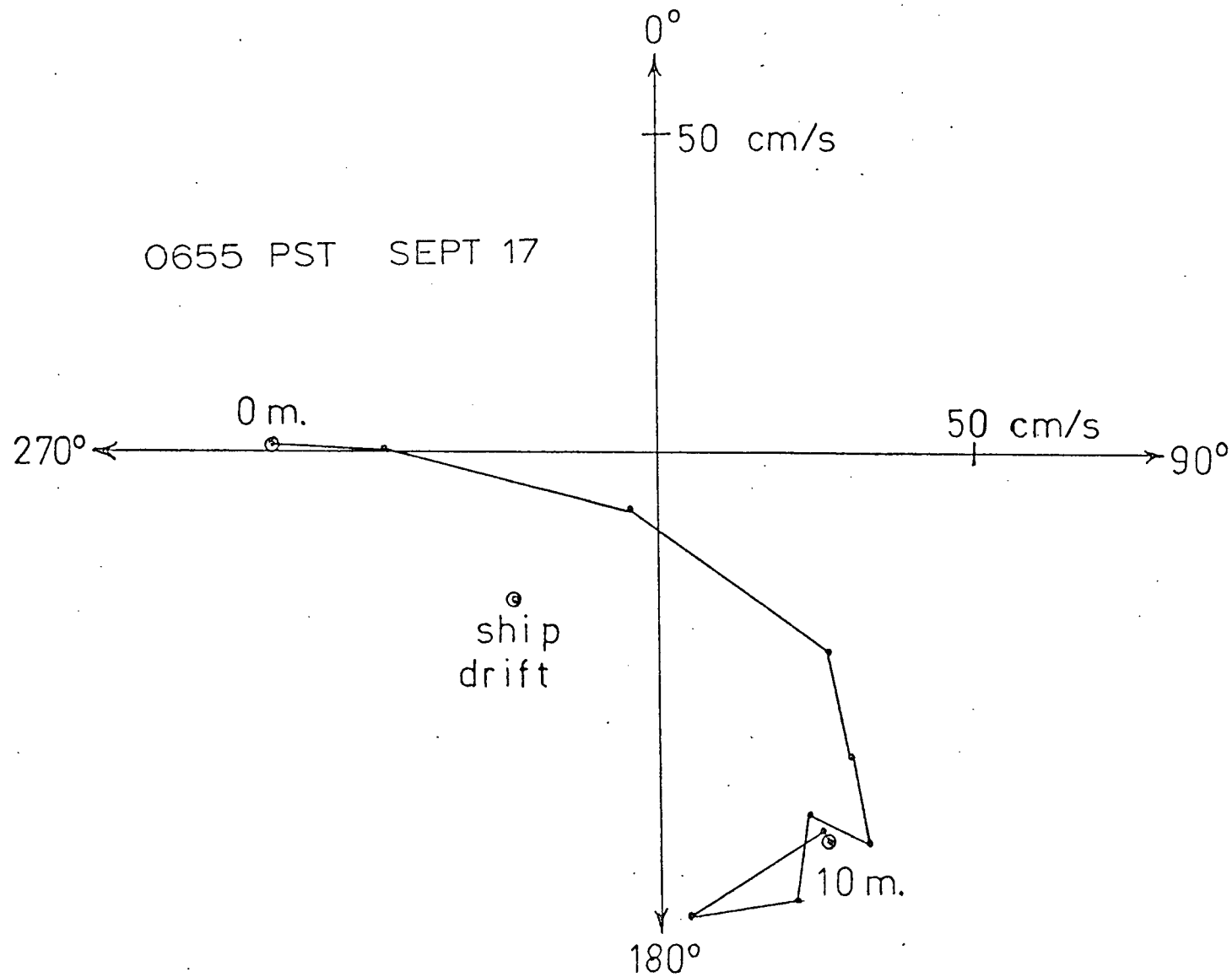


FIGURE 48. Polar plot of velocity vectors, station a, 0655 PST, Sept. 17, 1976.

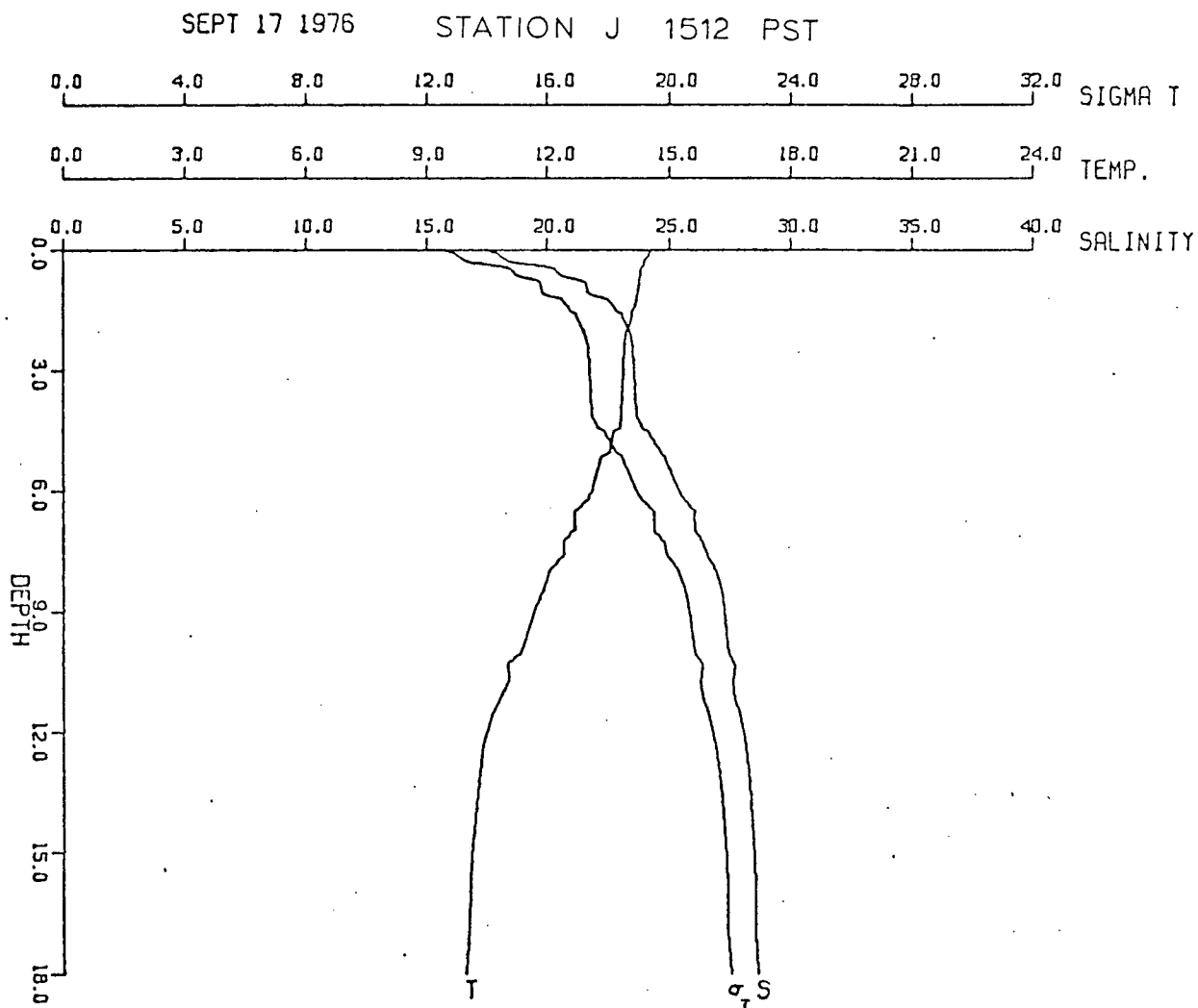


FIGURE 49. S, T, sigma t profiles at station j, 1512 PST, Sept. 17, 1976.

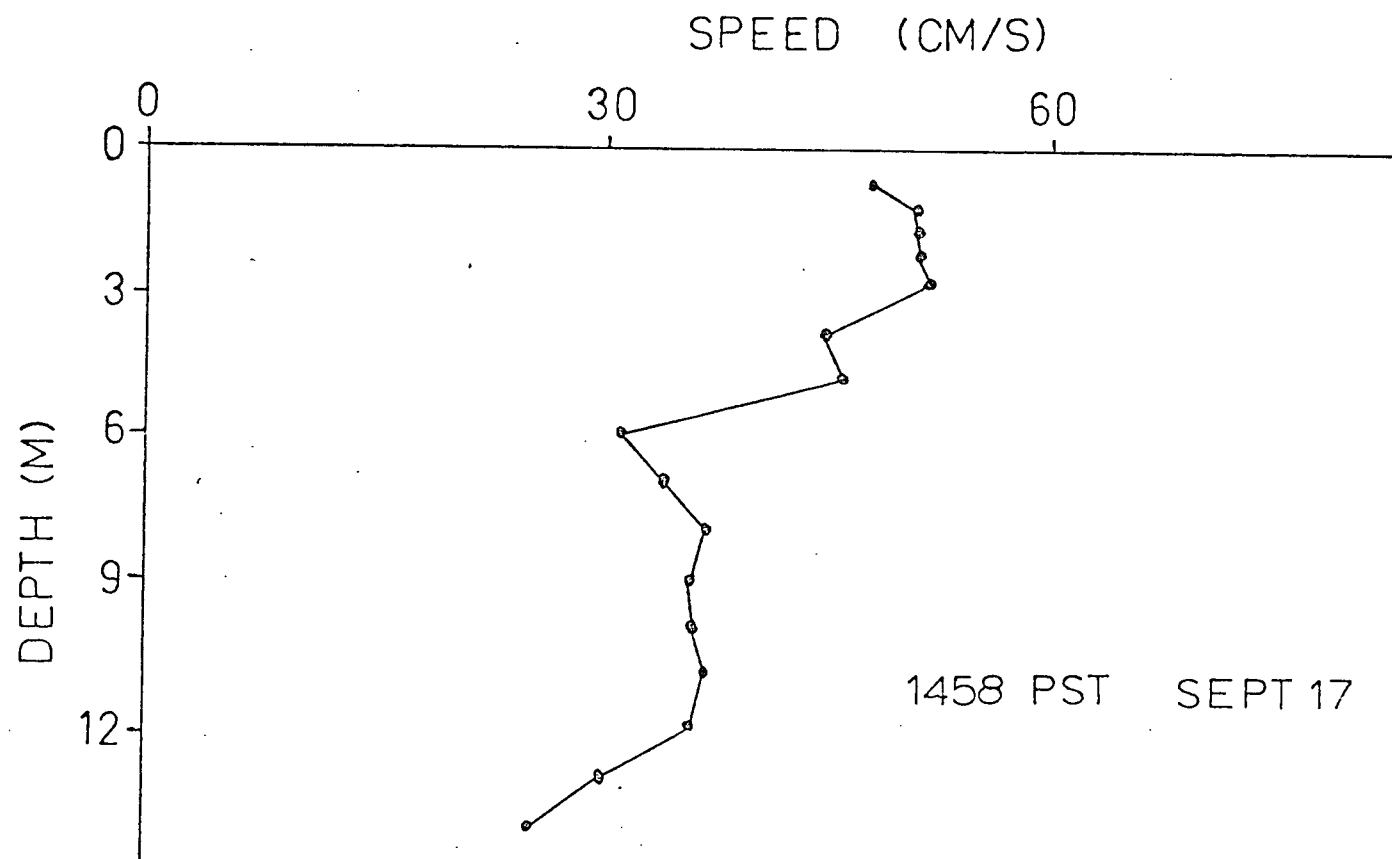


FIGURE 50. Speed profile at station j, 1458 PST, Sept 17, 1976.

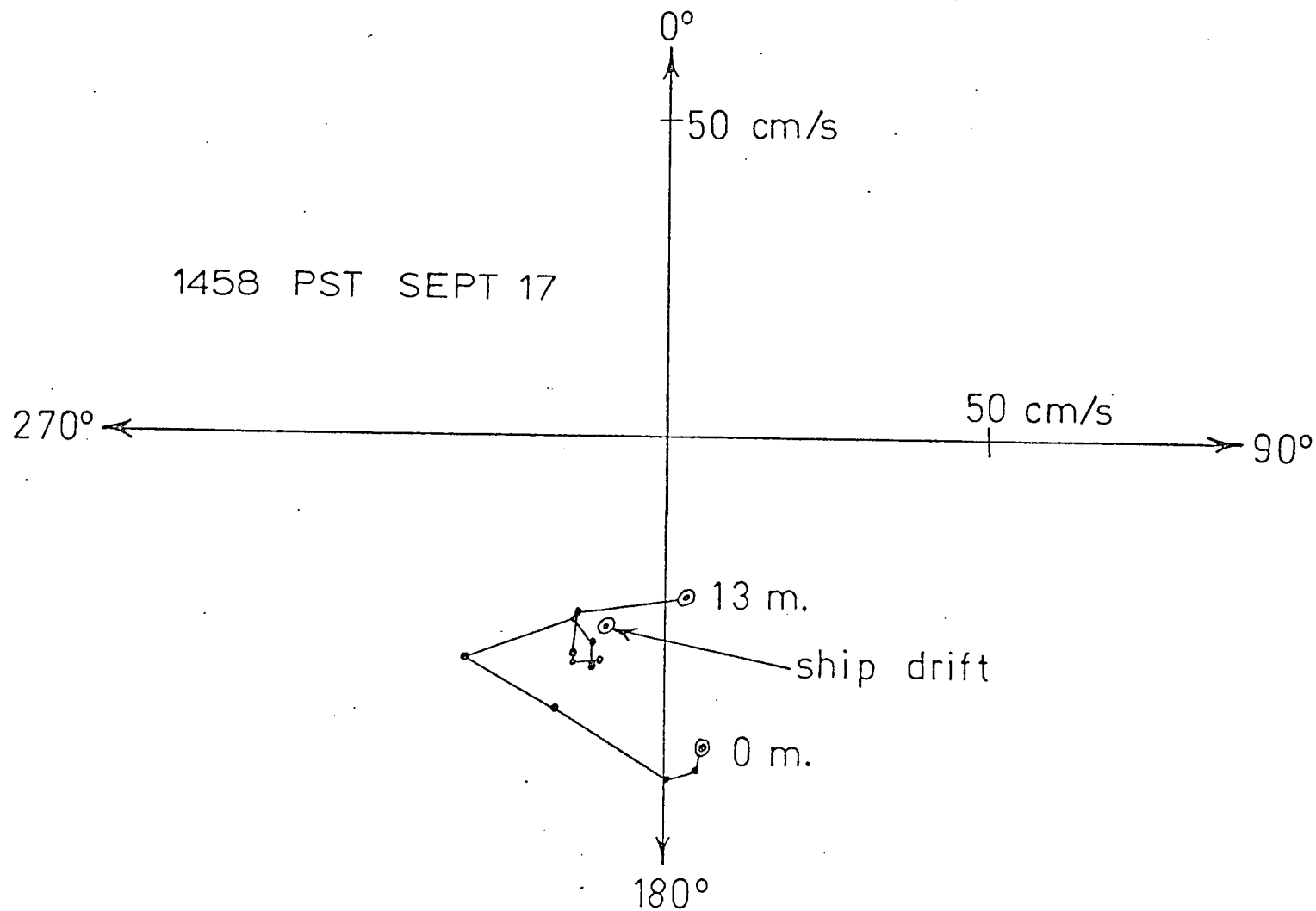


FIGURE 51. Polar plot of velocity vectors, station j, 1458 PST, Sept. 17, 1976.

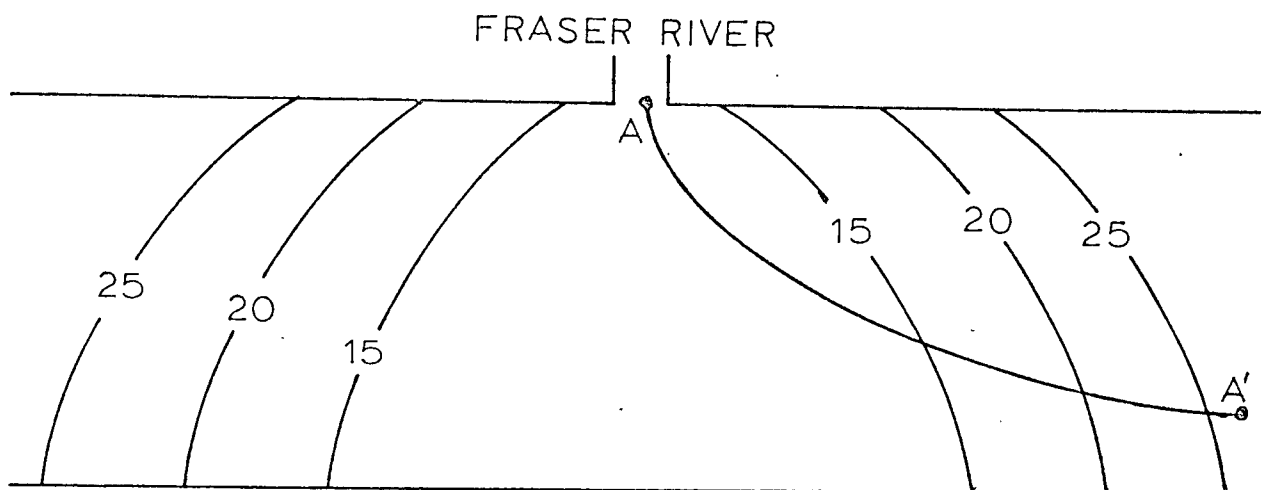


FIGURE 52. An idealized Strait of Georgia, showing contours of surface salinity (15, 20, 25 ppt). AA' is the path of a salinity section, Fig. 53.

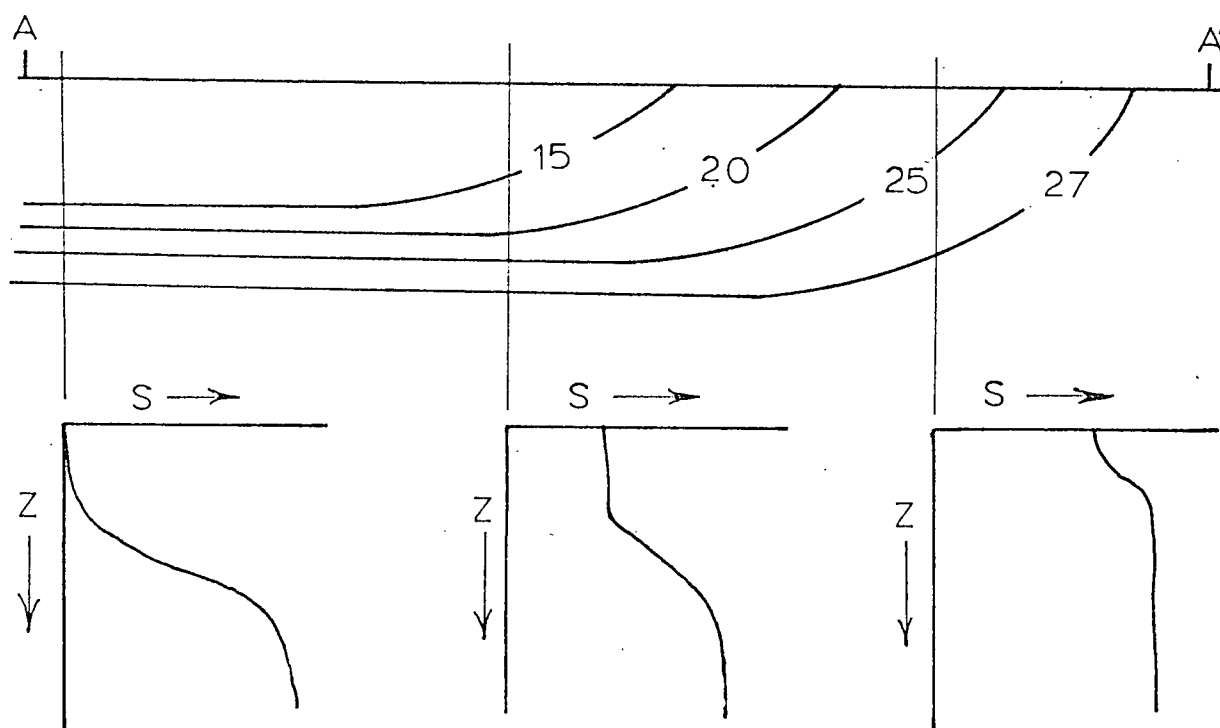


FIGURE 53. A salinity section along AA', Fig. 52, and salinity profiles at three stations along AA'.

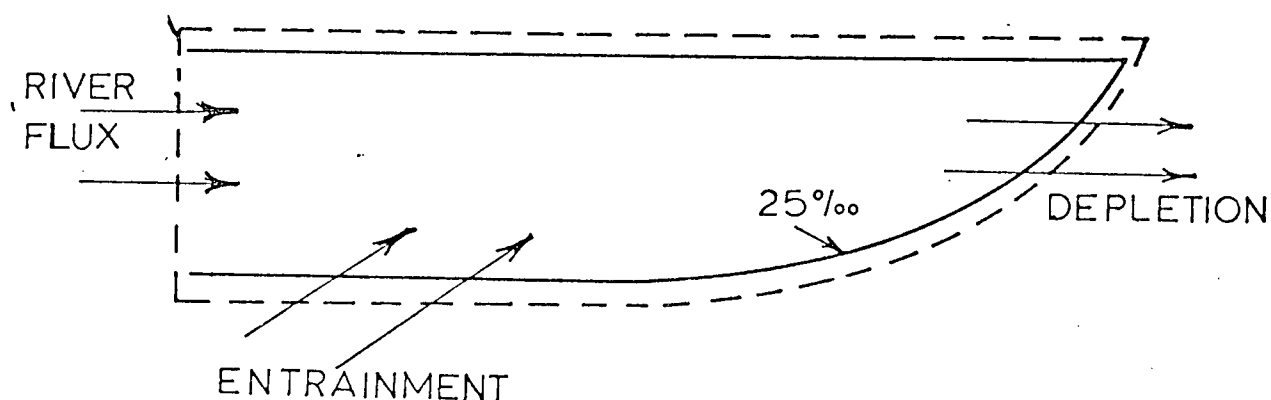


FIGURE 54. The control volume, indicated by dashed lines, surrounding the plume defined by the $S=25$ contour. The three contributions to the mass balance, river flow, entrainment, and depletion are indicated.

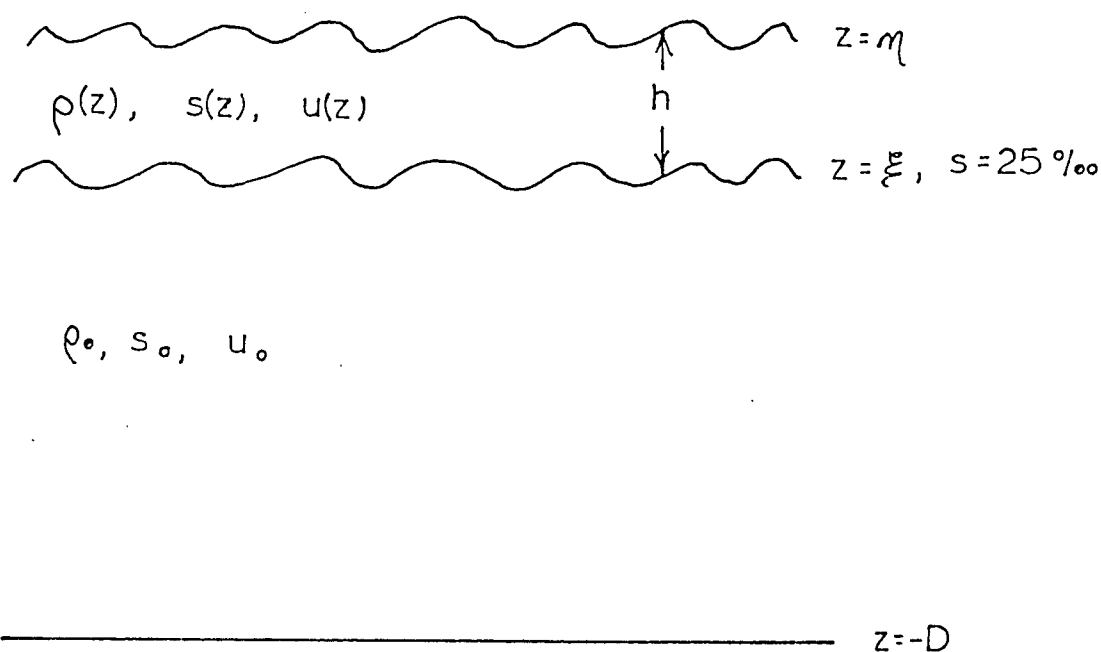


FIGURE 55. Definition sketch for the equations derived in Chapter 3.

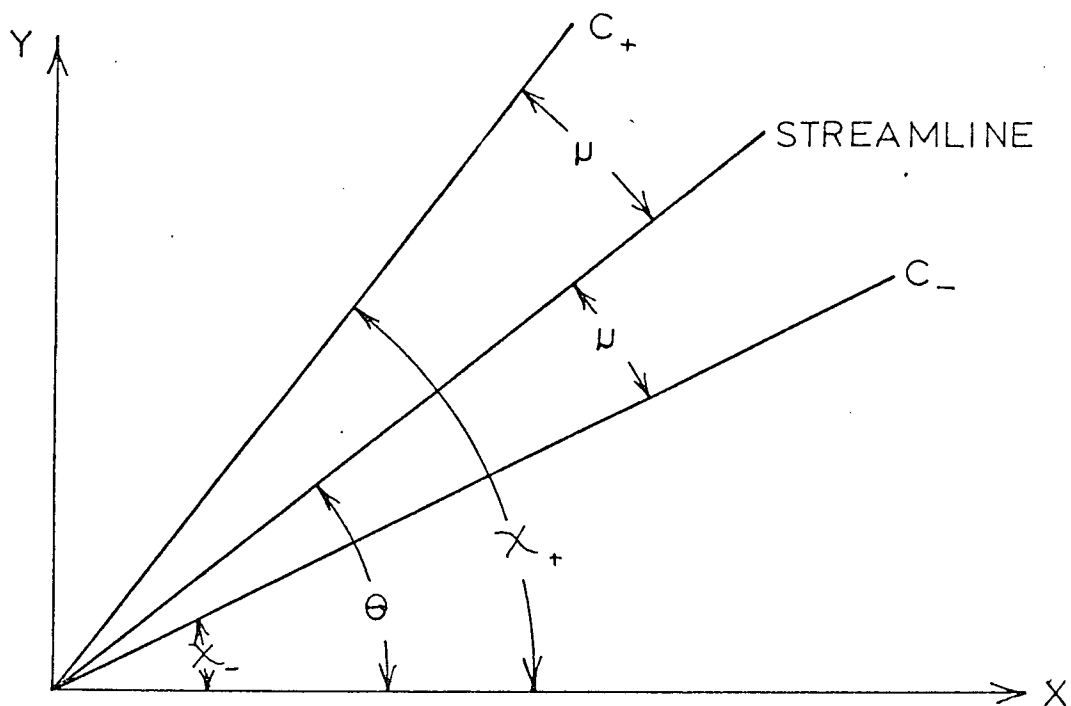


FIGURE 56a. The orientation of the two characteristics C_+ and C_- with respect to the streamline direction.

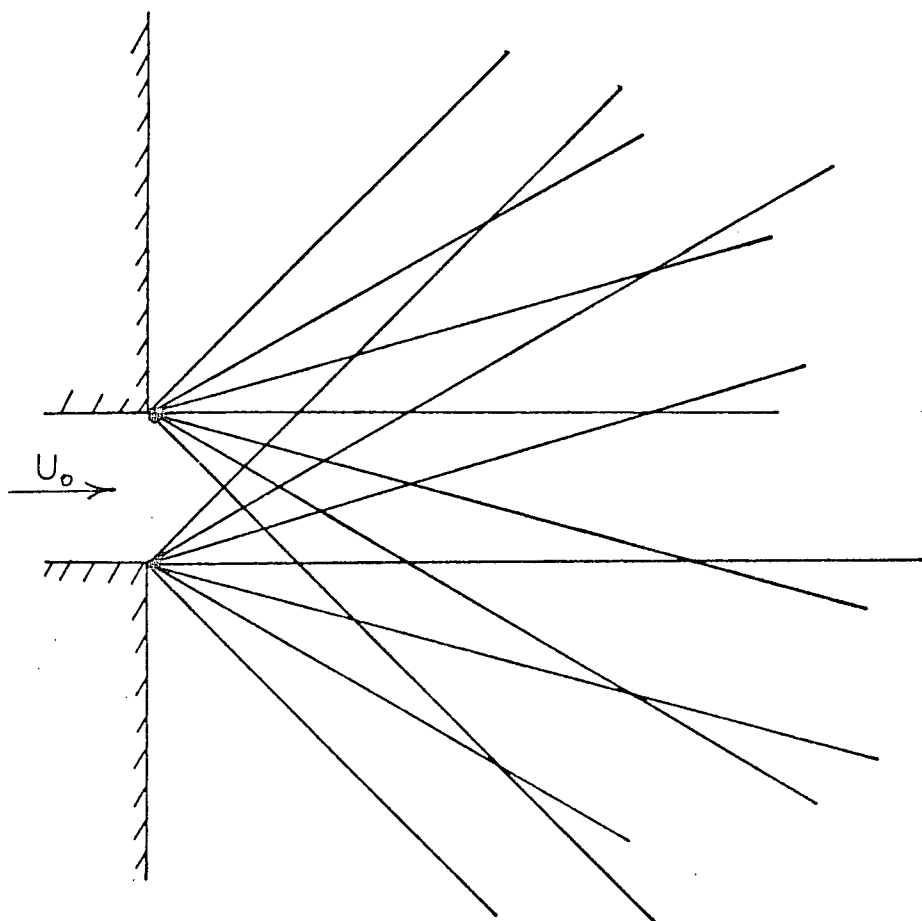


FIGURE 56b. The region of solution, filled up with intersecting characteristics.

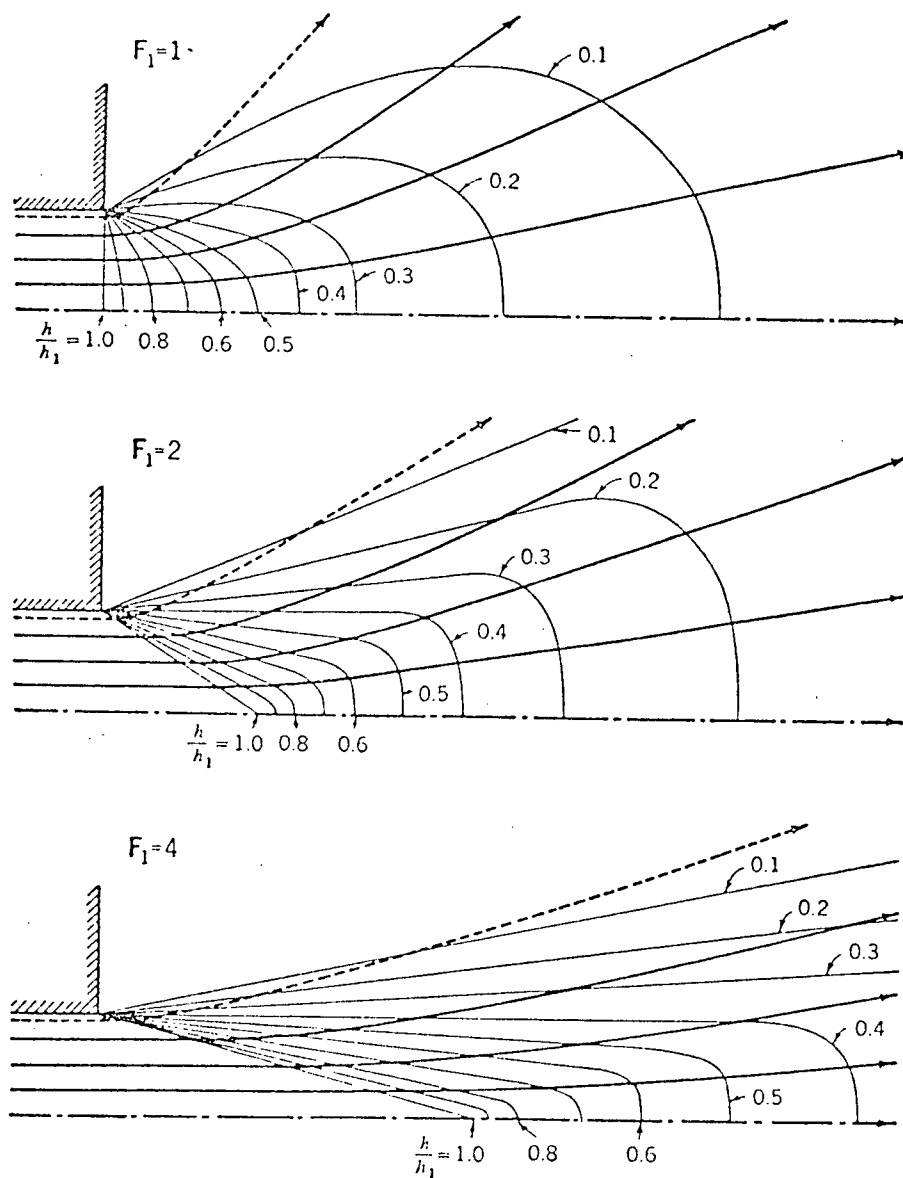


FIGURE 57. Streamlines and lines of equal thickness, from Ron   et al, 1951.

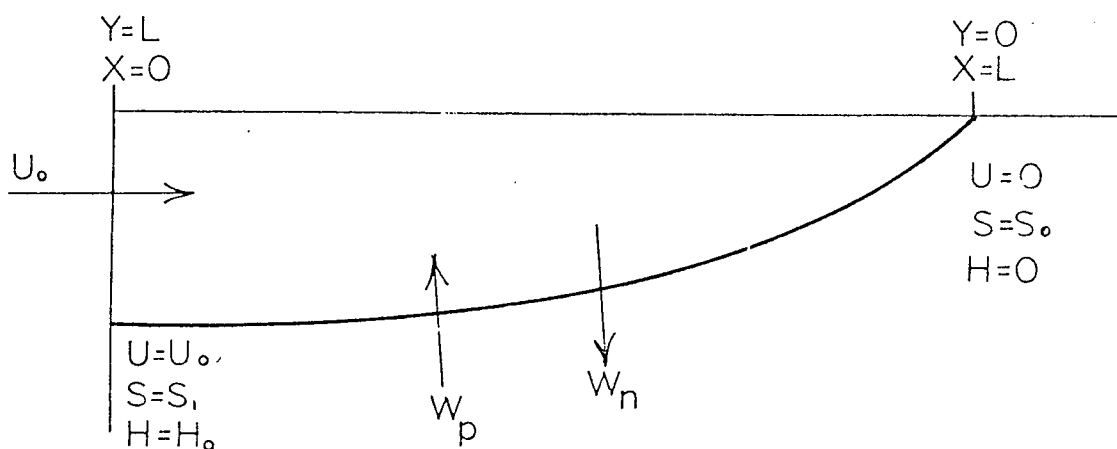


FIGURE 58a. Schematic diagram for the model of surfacing isopycnals.

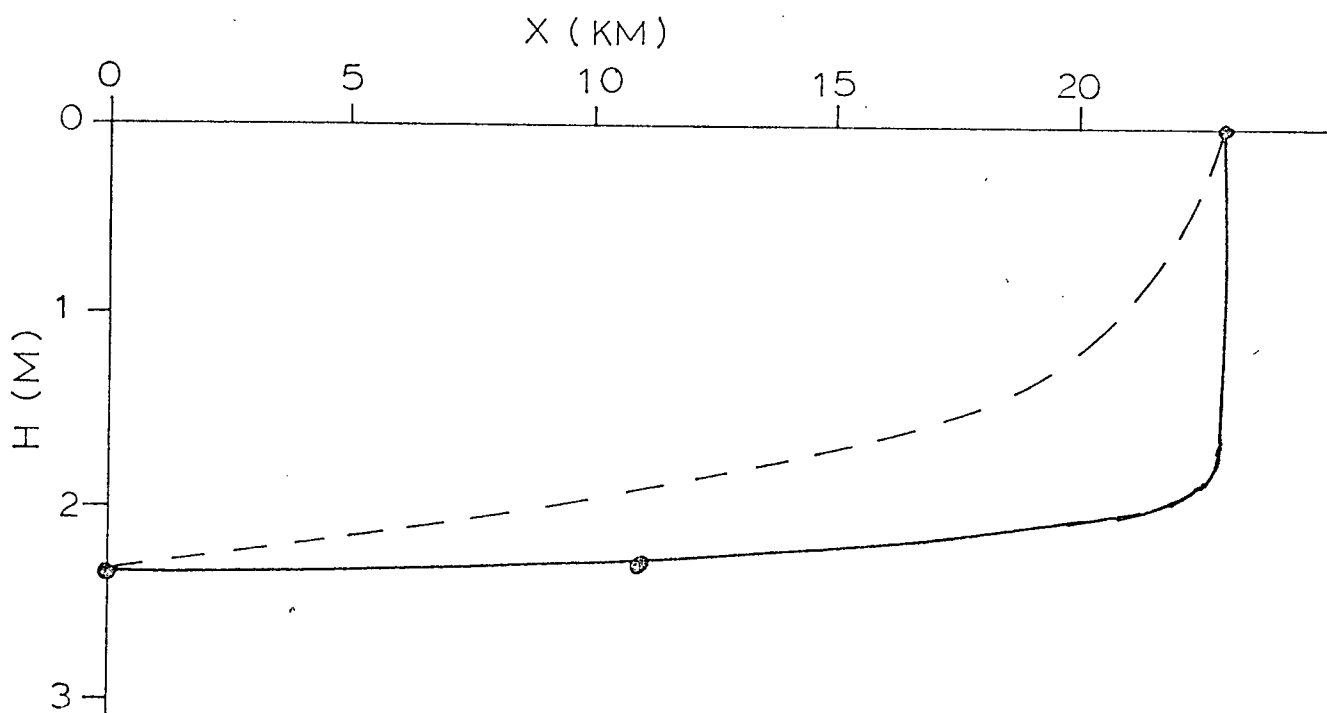


FIGURE 58b. The thickness of the upper layer, solid line, predicted by Eqn. 4.13. The dots indicate observed thicknesses, July 3, 1975. The dashed line is a plot of $h(L-x)^{1/3}$.

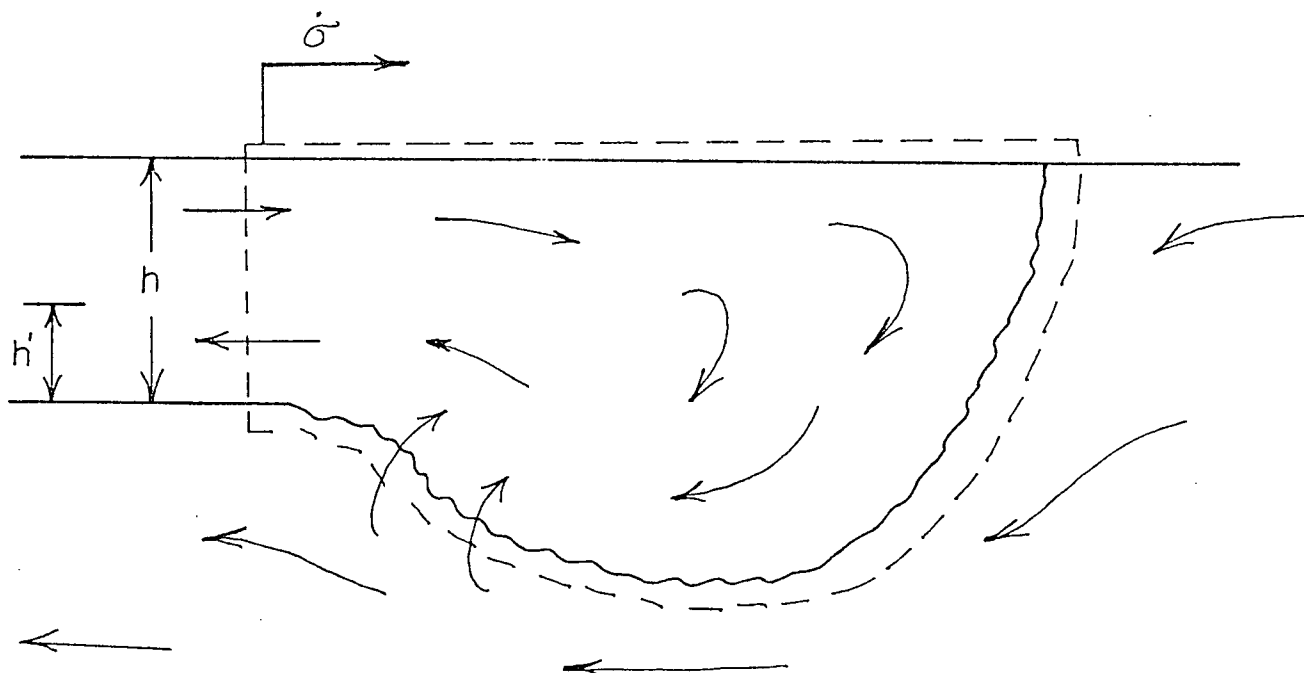


FIGURE 59a. The control volume used to obtain conditions at a strong discontinuity.

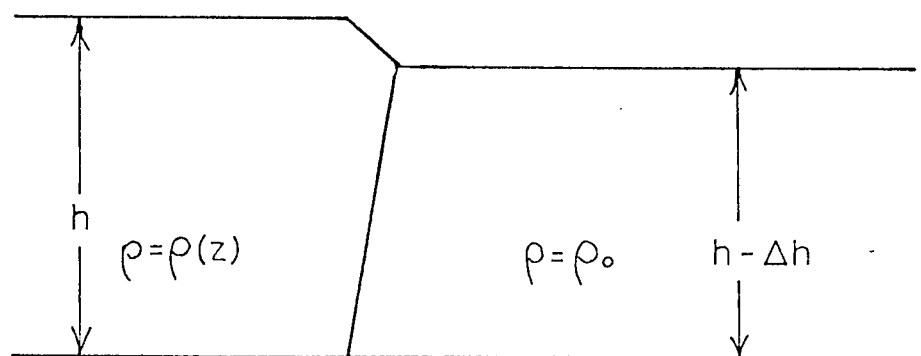


FIGURE 59b. Sketch of upper layer conditions used to obtain the integrated pressure term.

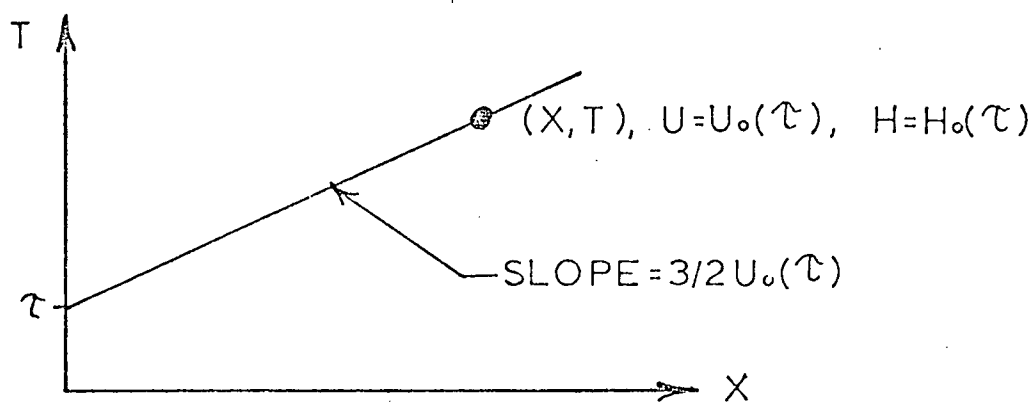


FIGURE 60a. An element of the implicit characteristic solution,
Eqn. 4.26.

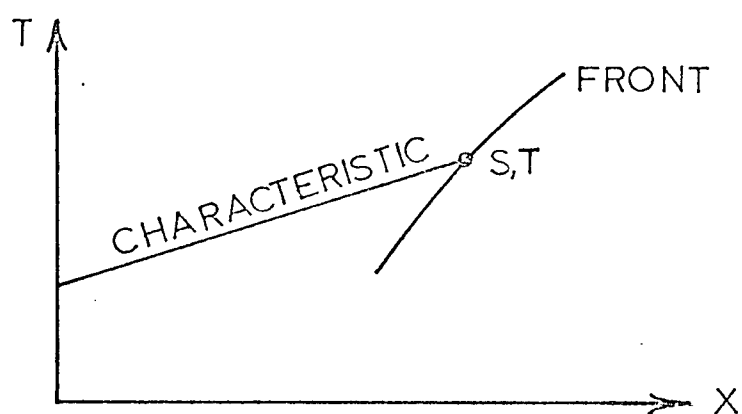


FIGURE 60b. A characteristic intersecting the front at (s, t) .

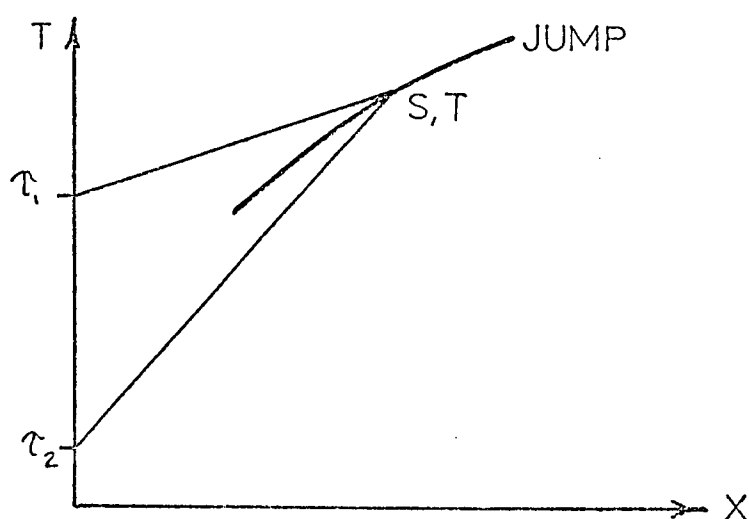


FIGURE 60c. Two characteristics intersecting at a hydraulic jump.

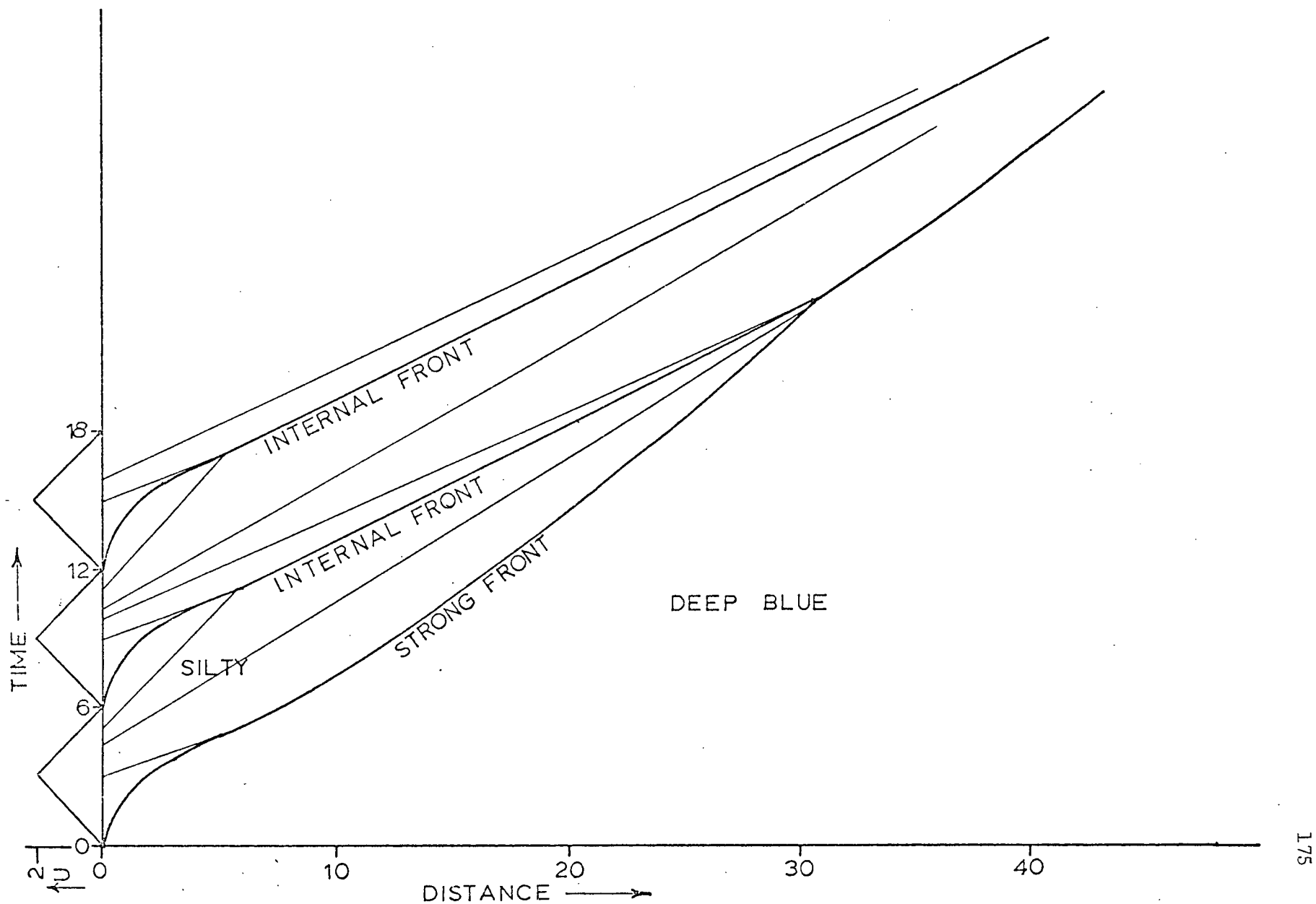


FIGURE 61. The characteristic diagram for the kinematic wave solution.

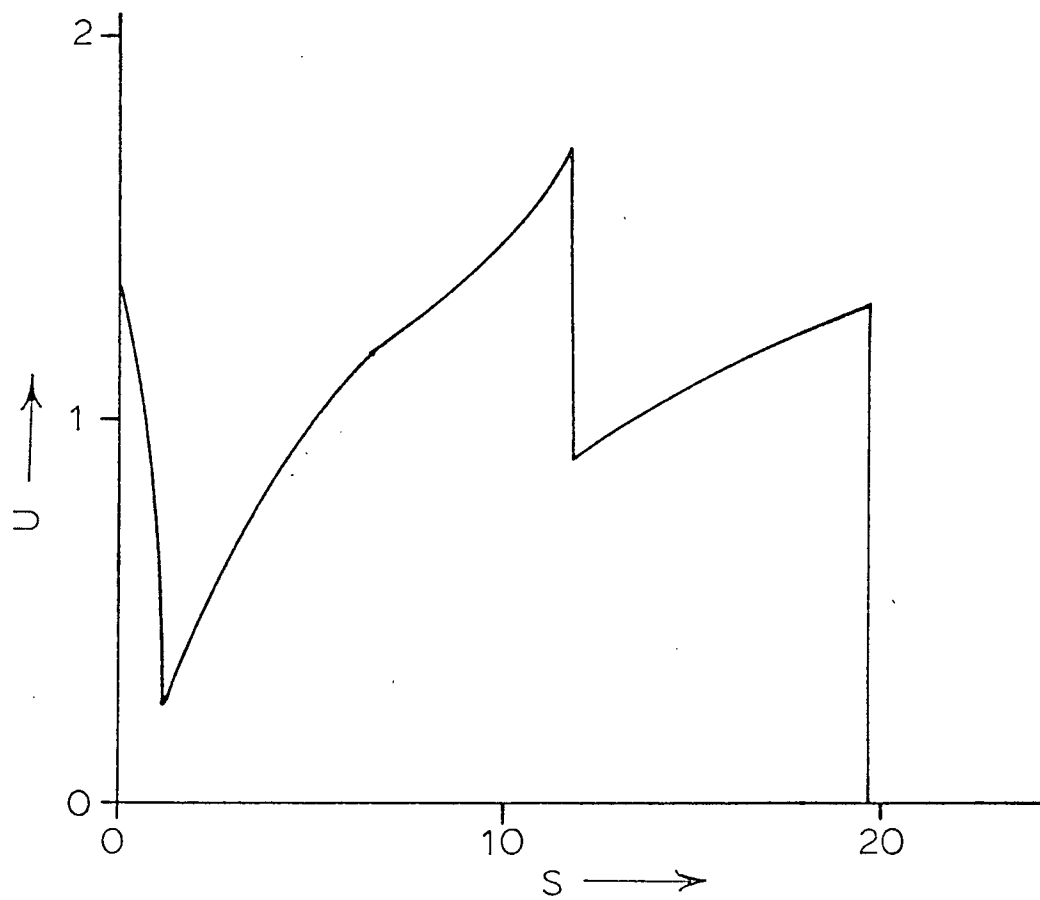


FIGURE 62. The distribution of u at $t=14$, from the kinematic wave solution.

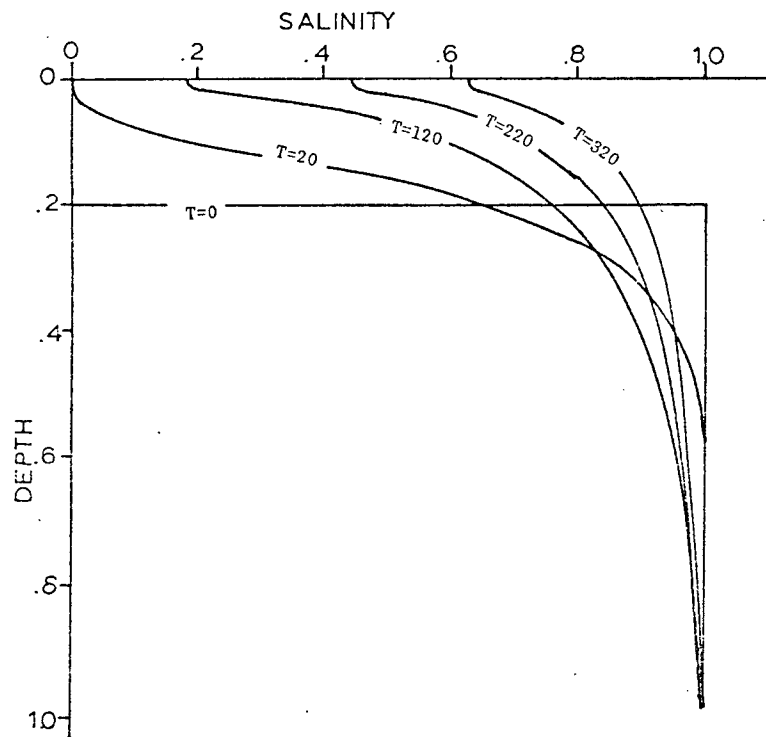


FIGURE 63a. The vertical distribution of salinity at $t=0$, $t=20\Delta t$, $120\Delta t$, $220\Delta t$, and $320\Delta t$, for $K=Z^2/(.2^2)$.

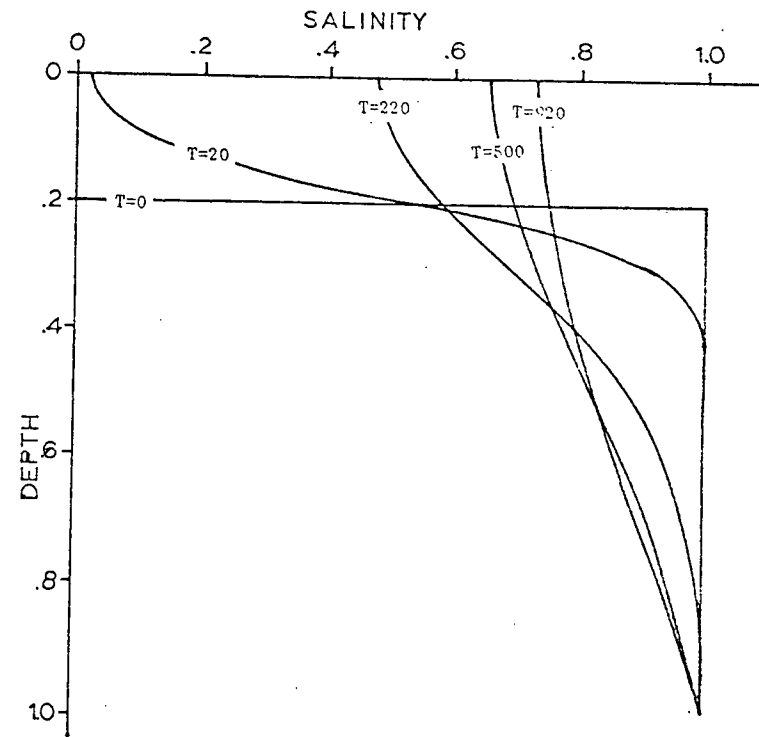


FIGURE 63b. The vertical distribution of salinity at $t=0$, $20\Delta t$, $220\Delta t$, $500\Delta t$, and $920\Delta t$, for $K=1$.

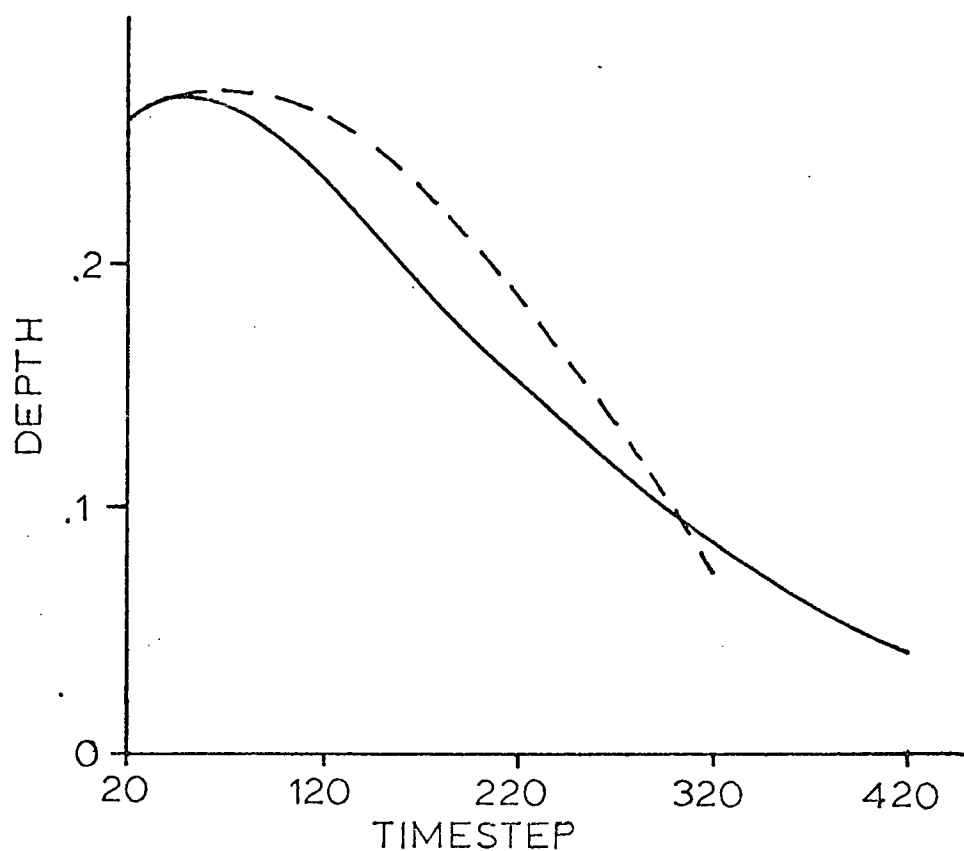


FIGURE 64a. Depth of the upper layer. The solid line is from the diffusion equation solution, the dashed line is from the discrete layer solution.

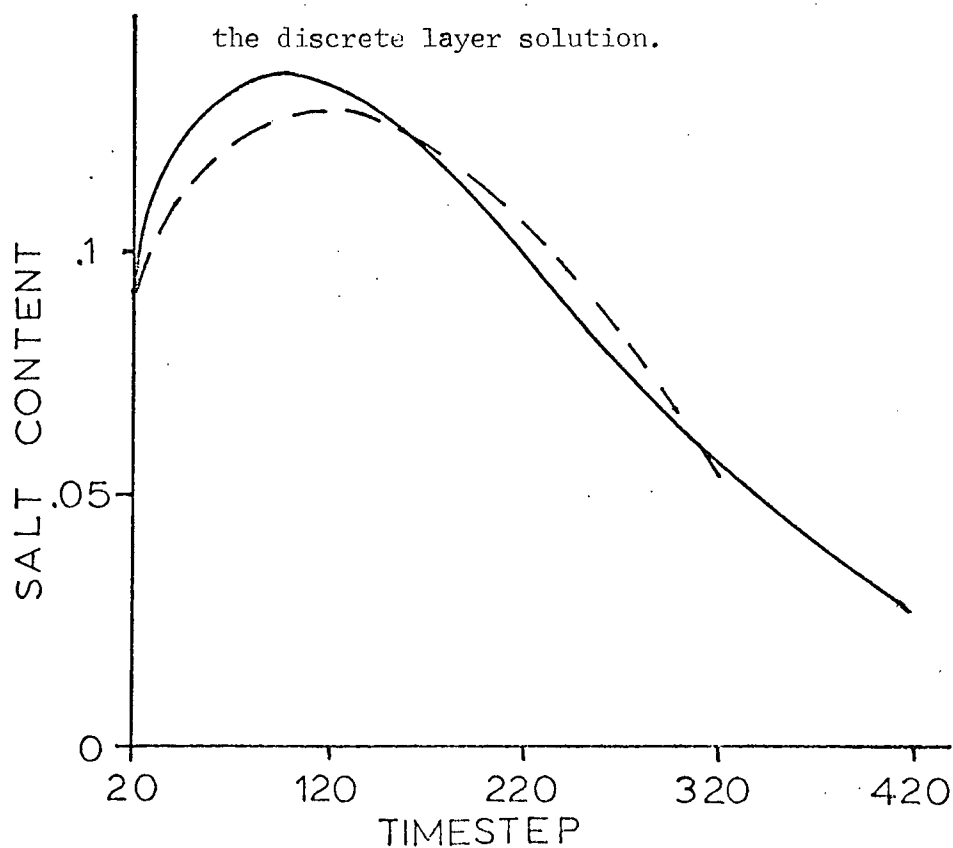


FIGURE 64b. Total salt content of the upper layer. The solid line is from the diffusion equation, the dashed from the layer solution.

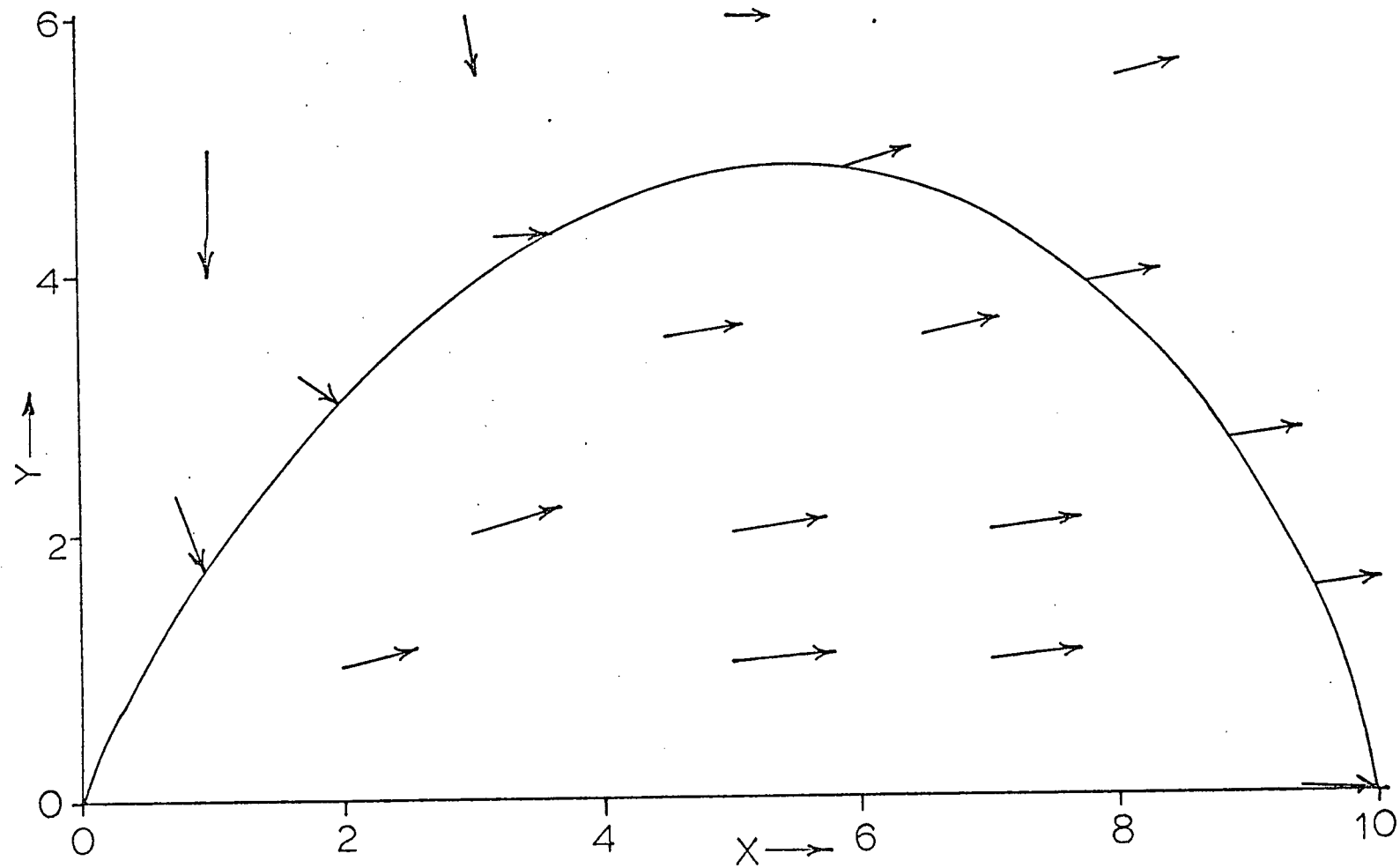


FIGURE 65. An isoconcentration curve and velocity vectors for a turbulent plane jet.

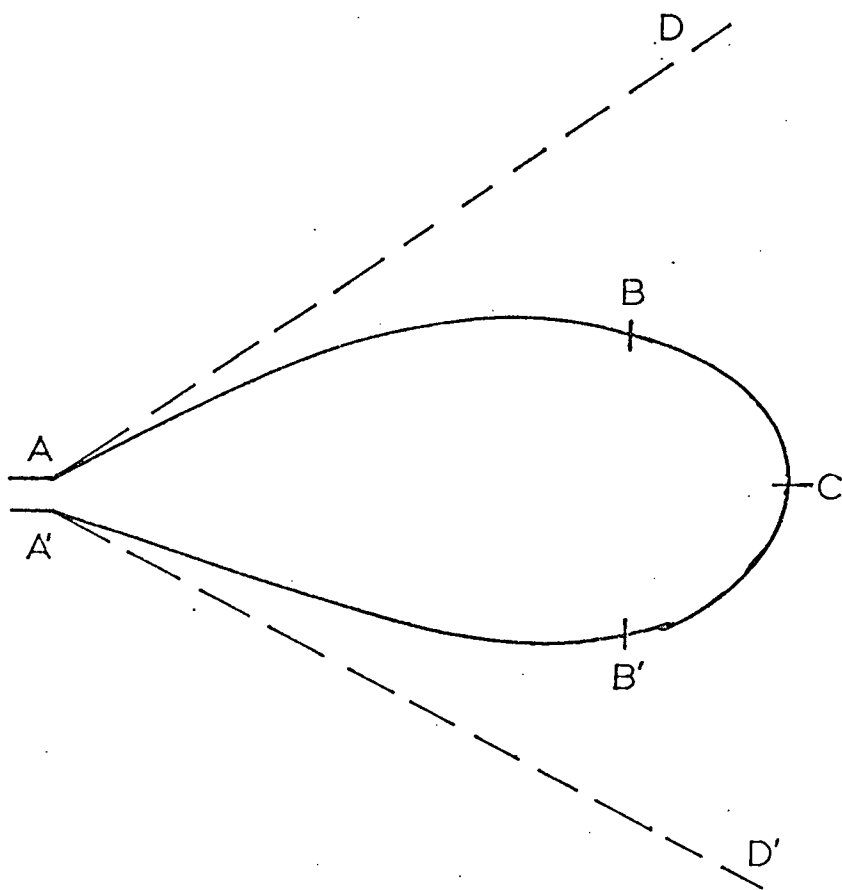


FIGURE 66a. Schematic diagram of a turbulent jet.

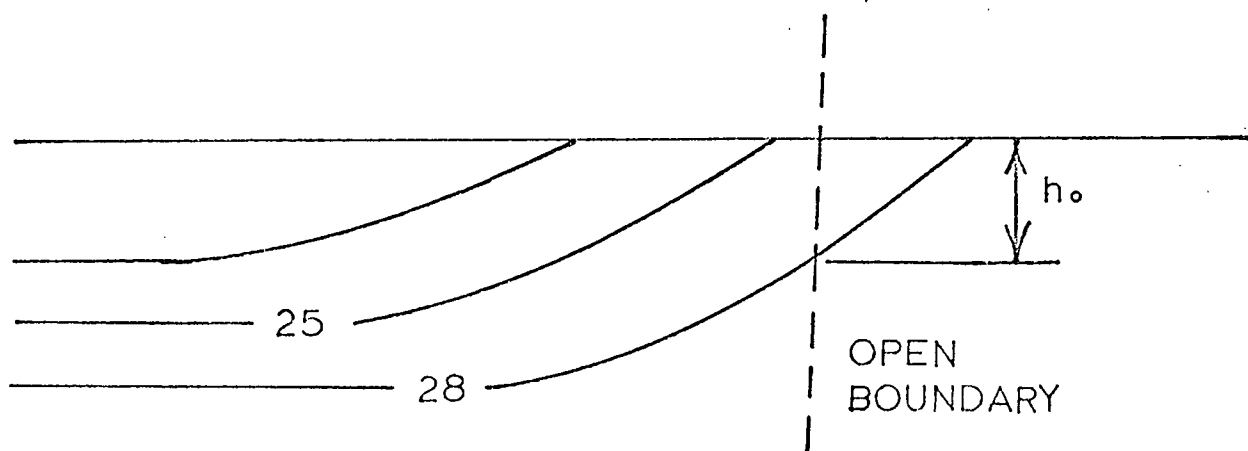


FIGURE 66b. A section through the plume, showing the effect the choice of bottom salinity has on flow through an open boundary.

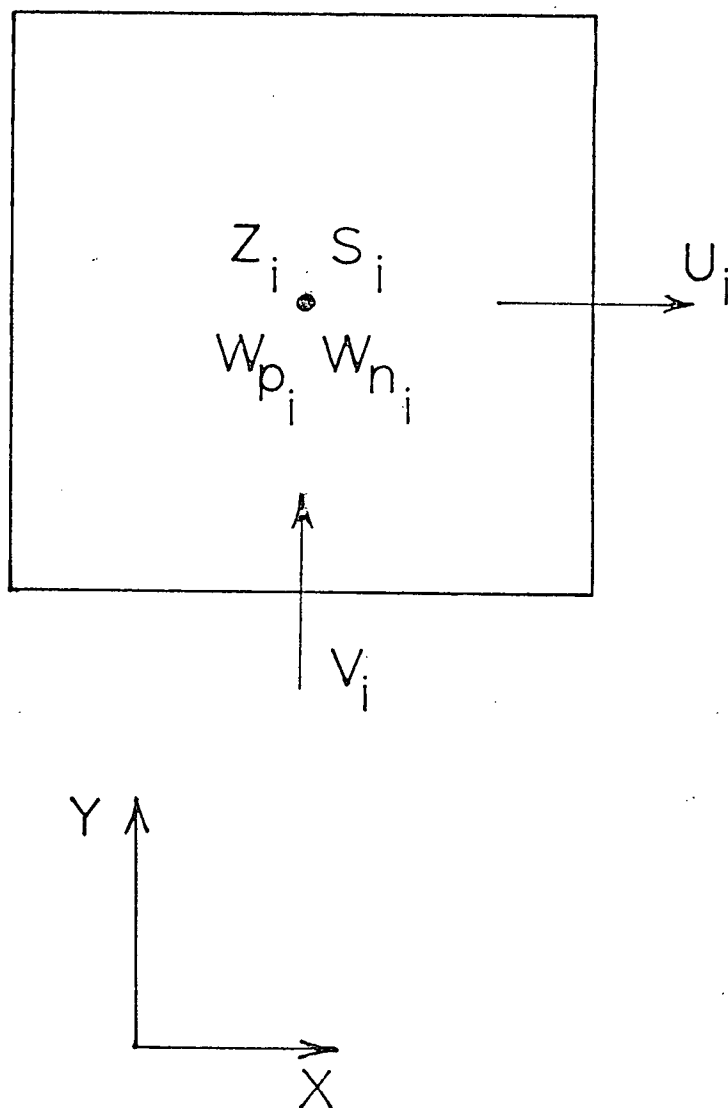
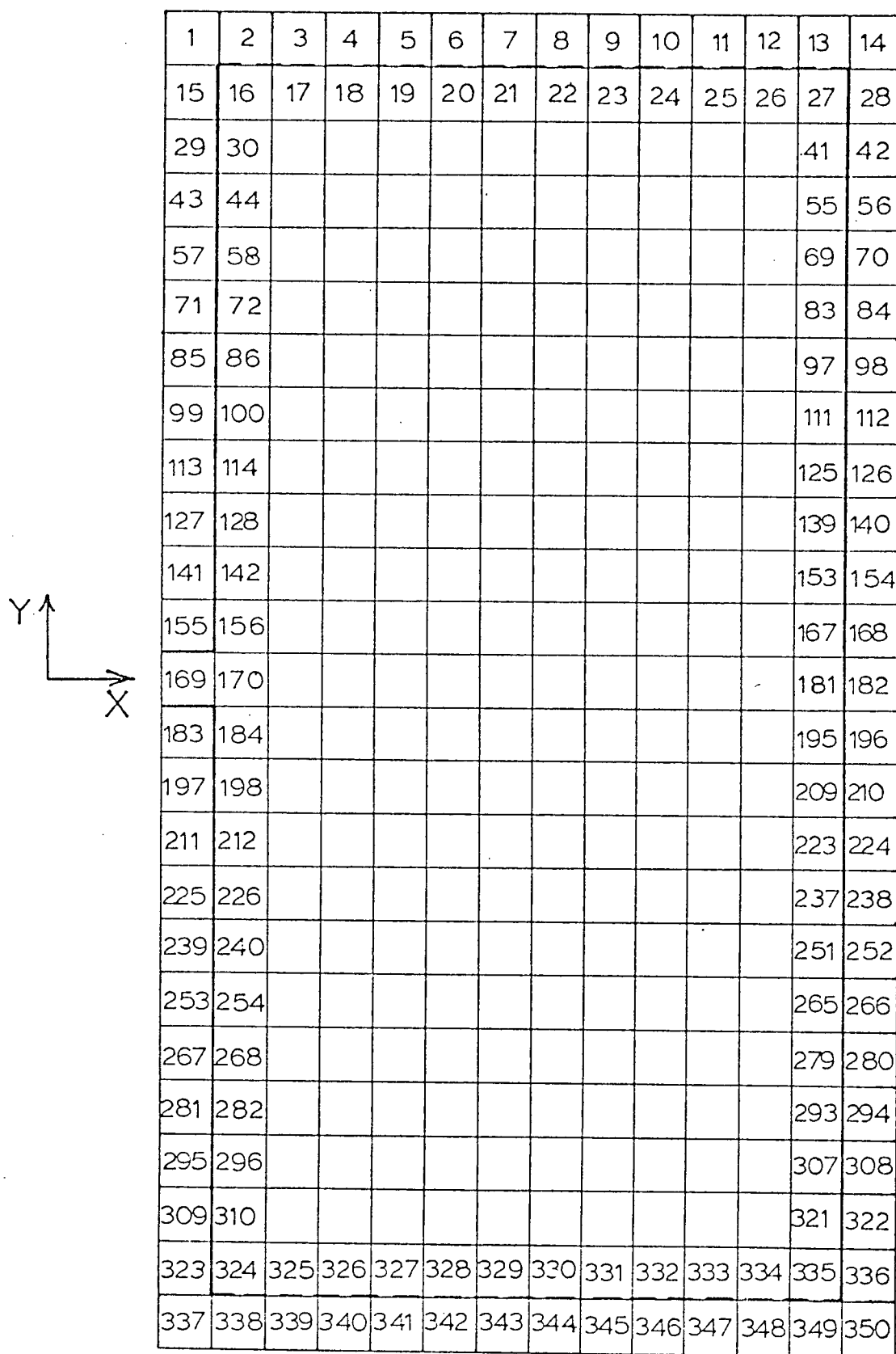


FIGURE 67. A typical computational element of the numerical grid used in this research. Z is the variable name assigned to the layer thickness, referred to as h in most equations of this thesis.



1	2	3	4	5	6	7	8	9	10	11	12	13	14
15	16	17	18	19	20	21	22	23	24	25	26	27	28
29	30											41	42
43	44											55	56
57	58											69	70
71	72											83	84
85	86											97	98
99	100											111	112
113	114											125	126
127	128											139	140
141	142											153	154
155	156											167	168
169	170											181	182
183	184											195	196
197	198											209	210
211	212											223	224
225	226											237	238
239	240											251	252
253	254											265	266
267	268											279	280
281	282											293	294
295	296											307	308
309	310											321	322
323	324	325	326	327	328	329	330	331	332	333	334	335	336
337	338	339	340	341	342	343	344	345	346	347	348	349	350

FIGURE 68. The complete grid used for the square box model. The river discharges through mesh 169. Positive values of y , (small indices), are at the southern half of the model. The solid boundaries are indicated by a thick line, the open boundaries by a heavy dashed line.

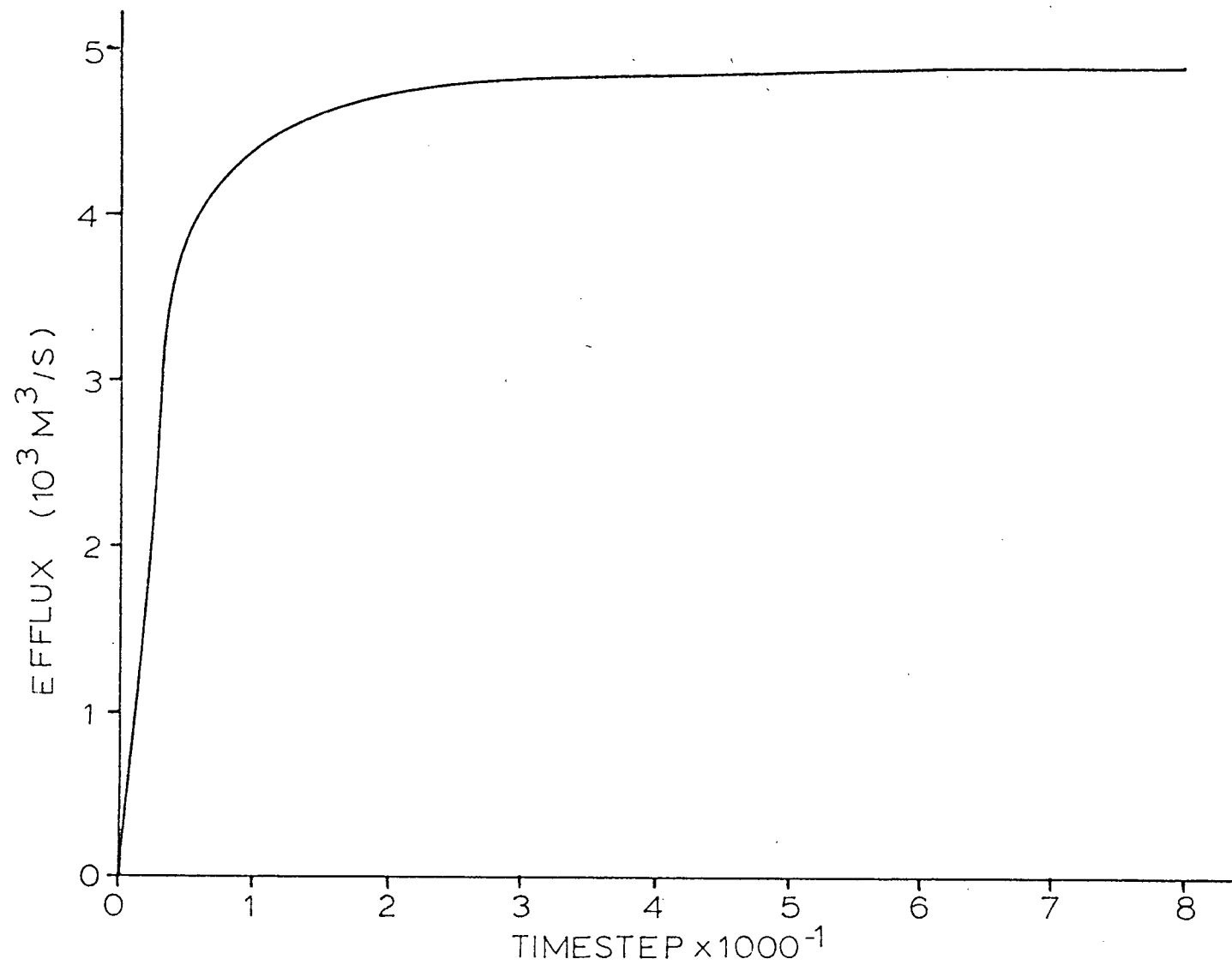


FIGURE 69. Flux out of the open ends of the linear model. 1000 timesteps are equivalent to 133.33 hours.

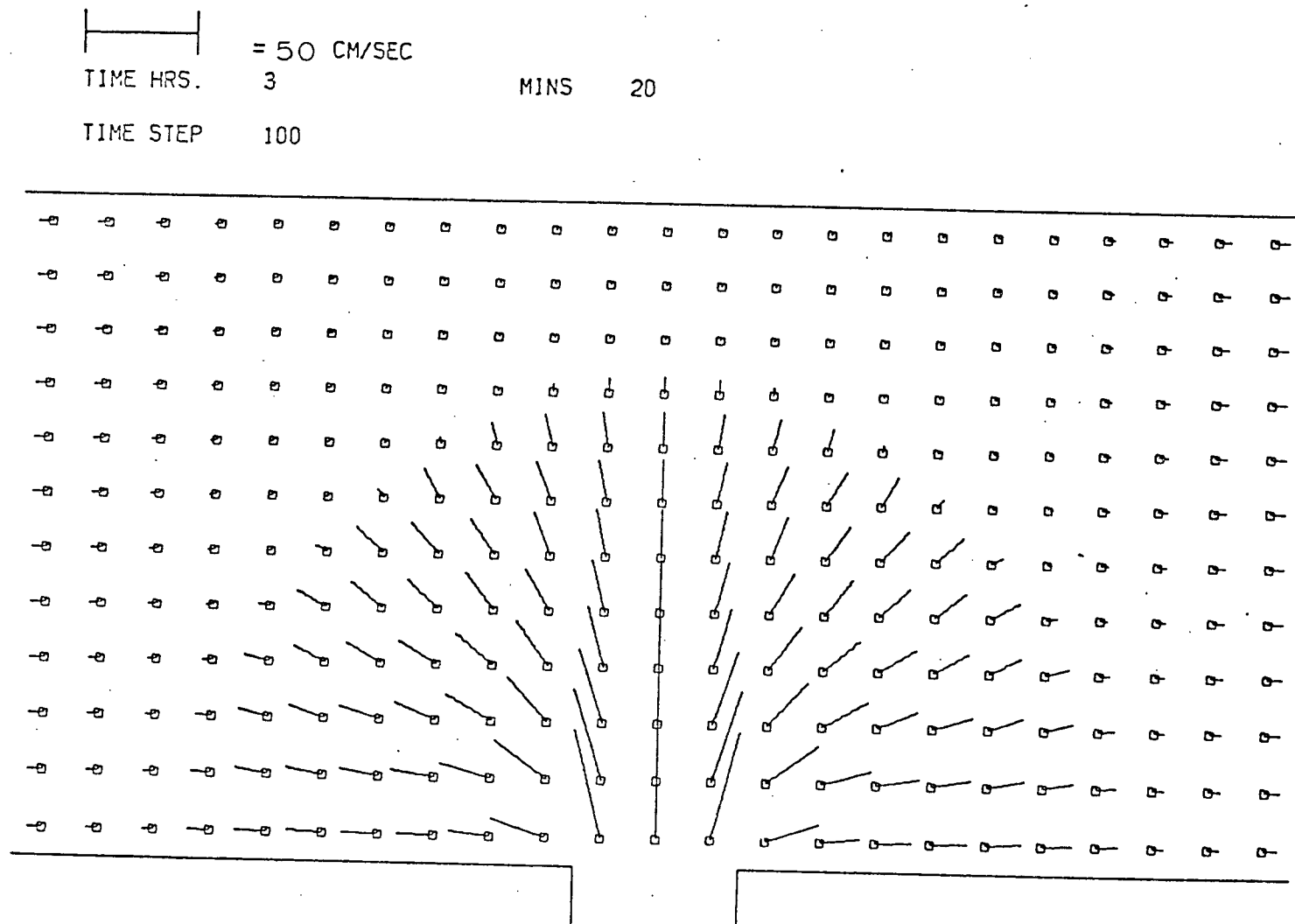
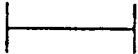


FIGURE 70. Velocity vectors after 100 timesteps of the square box model with non-linear terms. The small square represents the tail of the vector, and also is the location for which the vector represents the velocity.

 = 50 CM/SEC

TIME HRS. 16

MINS 40

TIME STEP 500

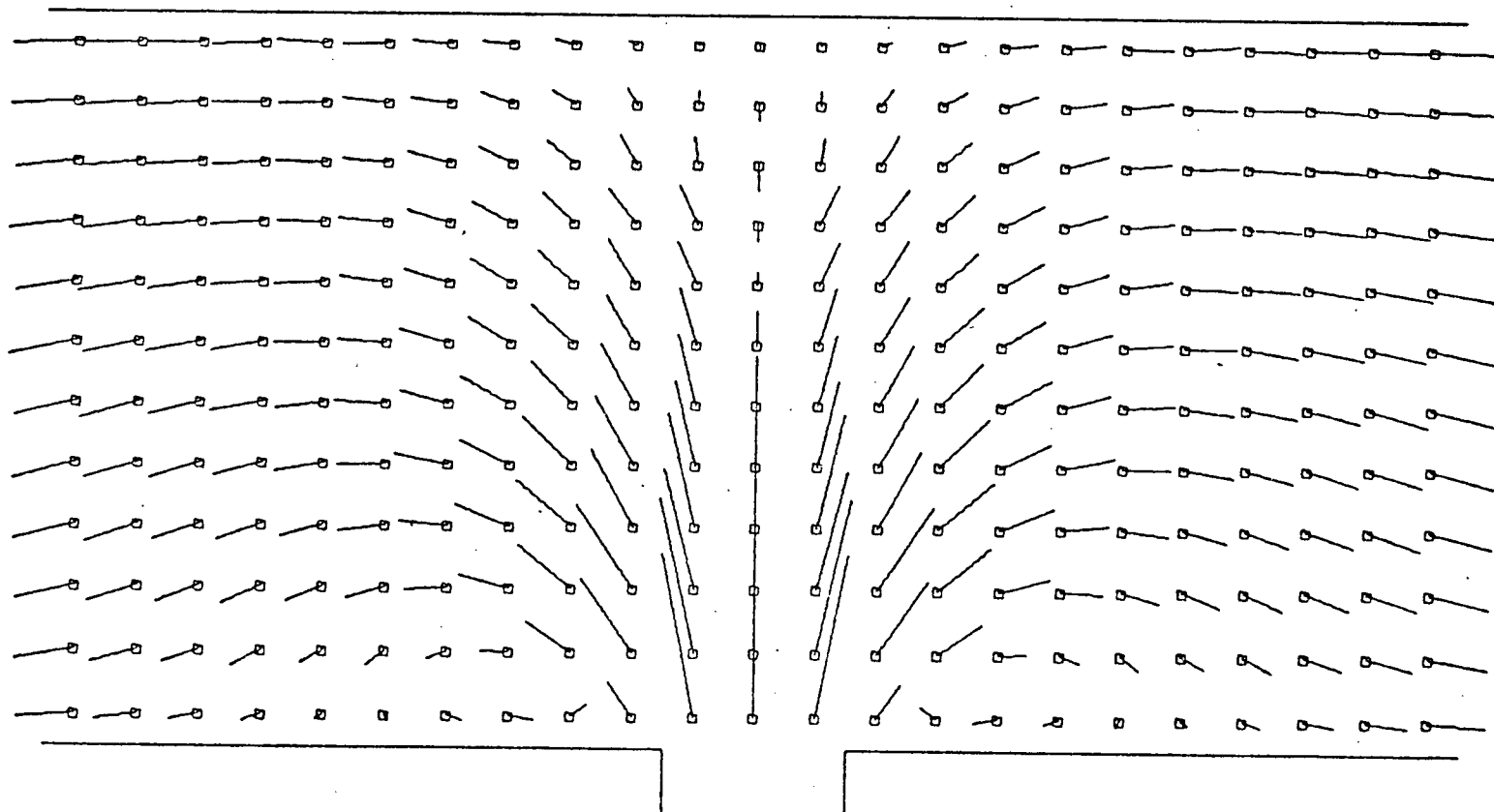


FIGURE 71. The same as Fig. 70, but at timestep 500.

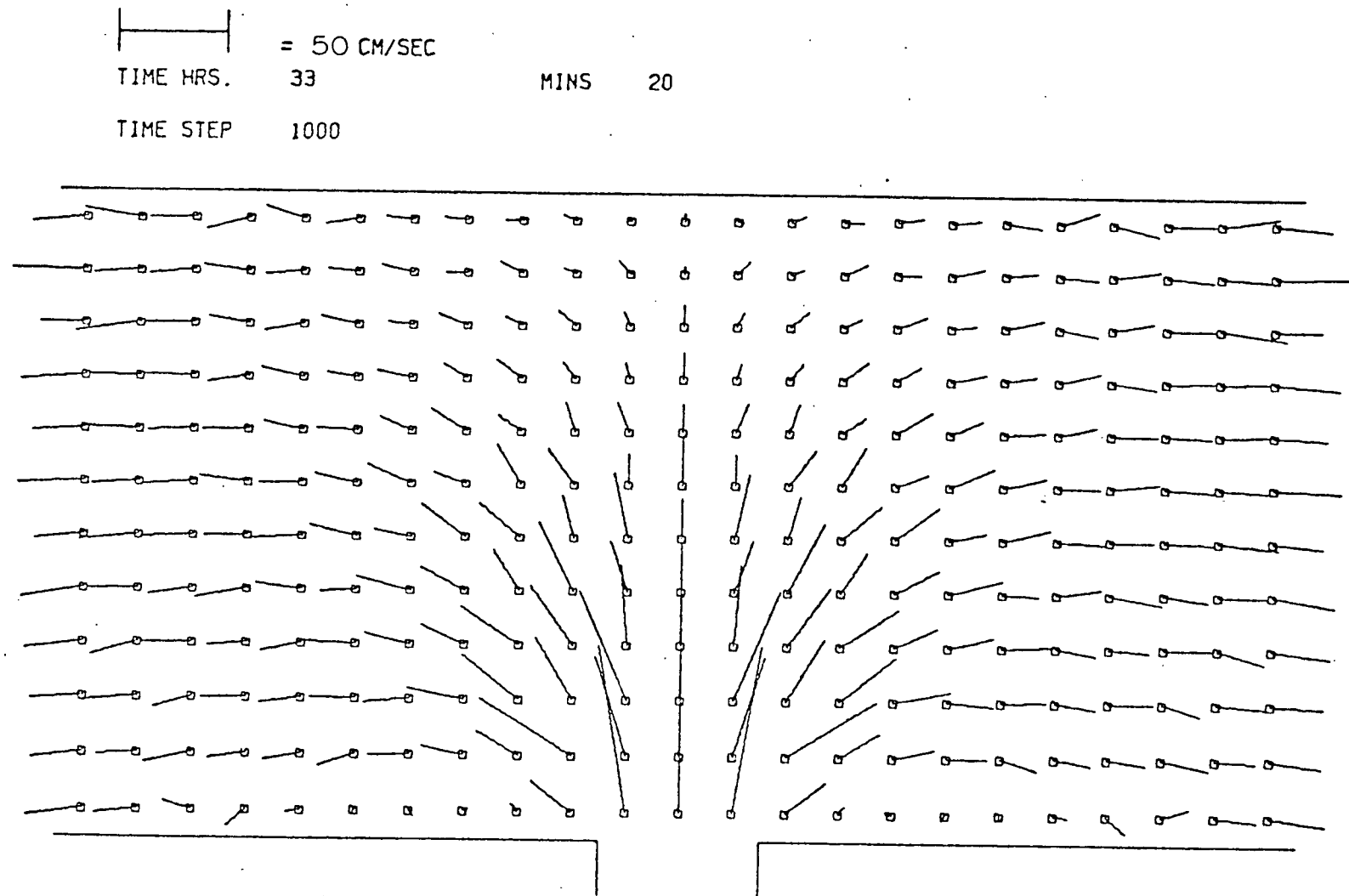


FIGURE 72. The same as Fig. 70, but at timestep 1000.

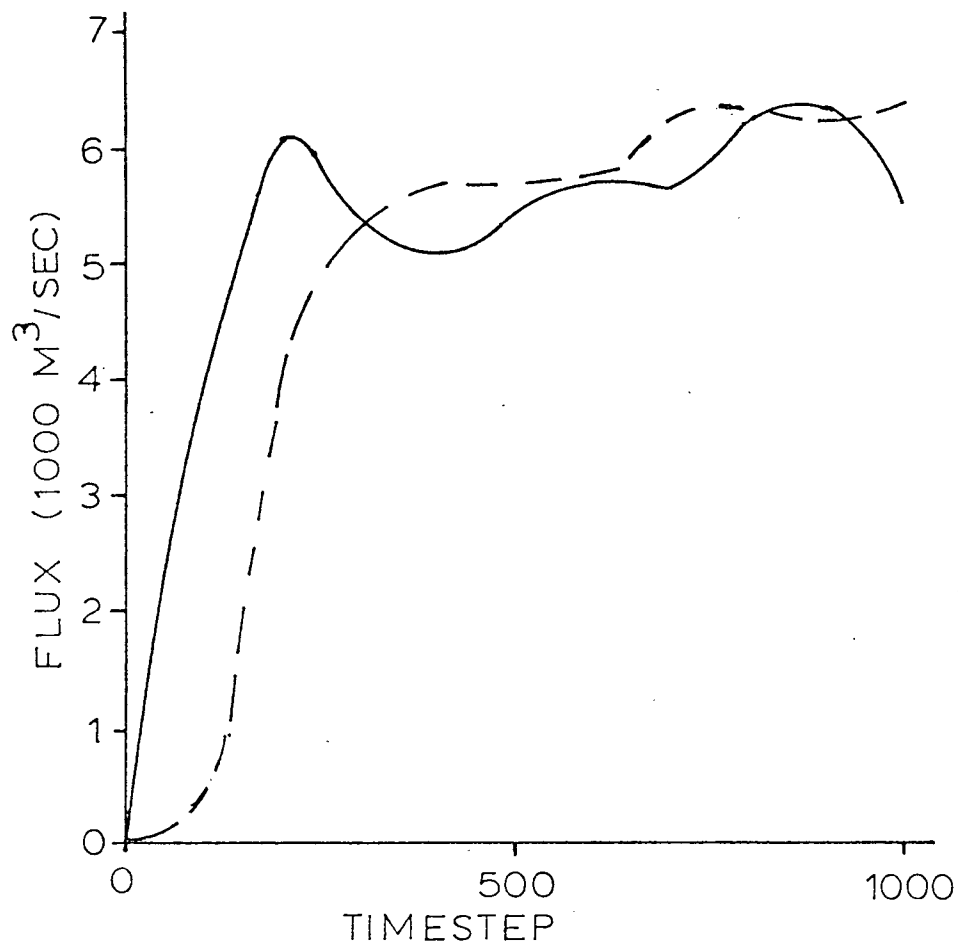


FIGURE 73a. Influx (solid line) and efflux (dashed line) for the model of Figs. 70, 71, and 72.

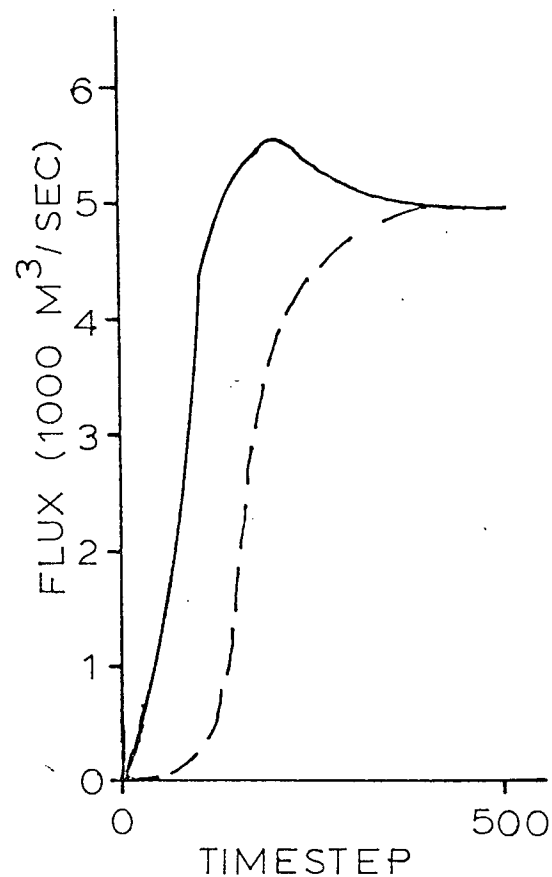


FIGURE 73b. Influx (solid line) and efflux (dashed line) for the model of Figs. 74, 75.

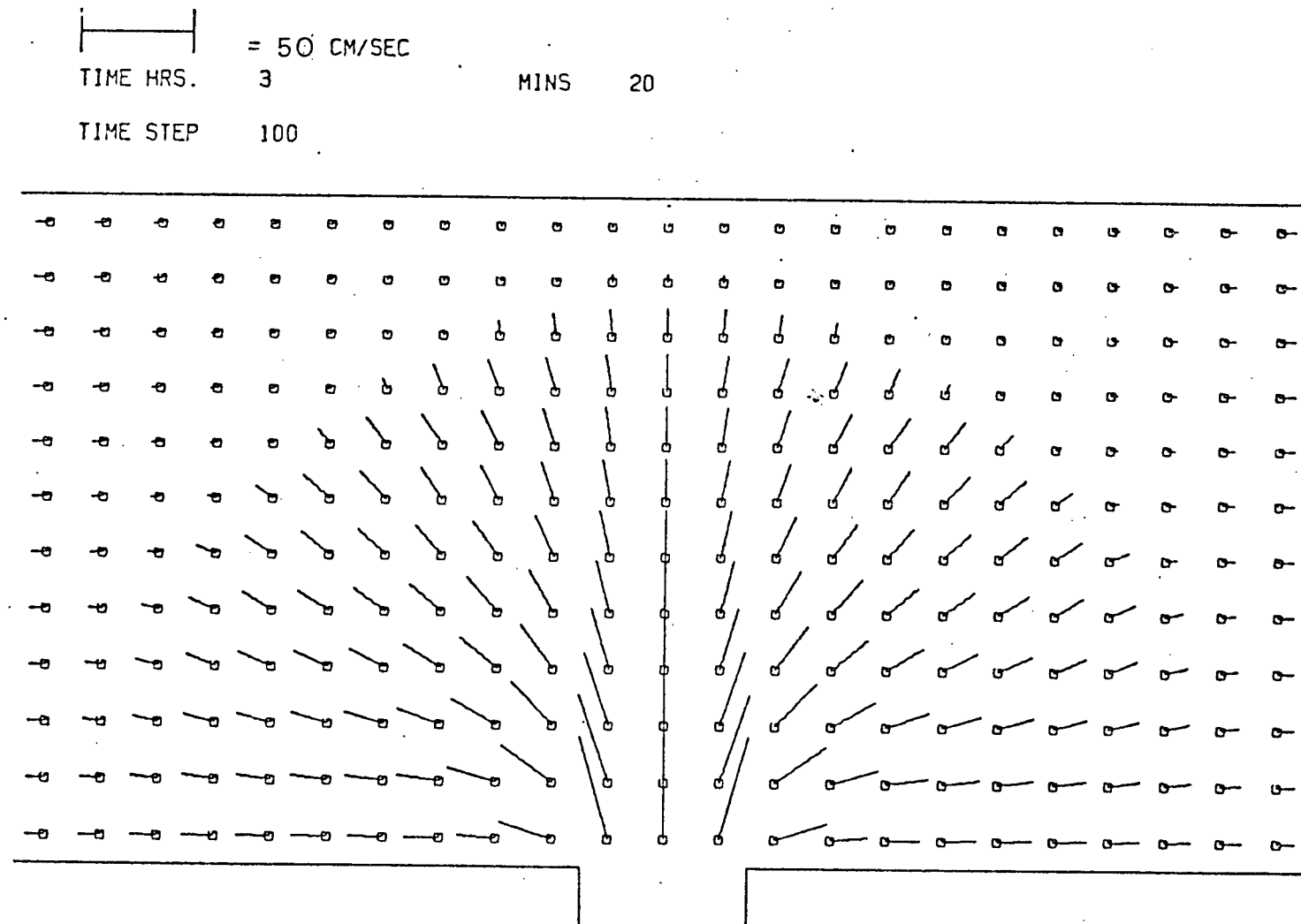


FIGURE 74. Flow field calculated in the same way as for Fig. 70, with the addition of horizontal eddy viscosity.

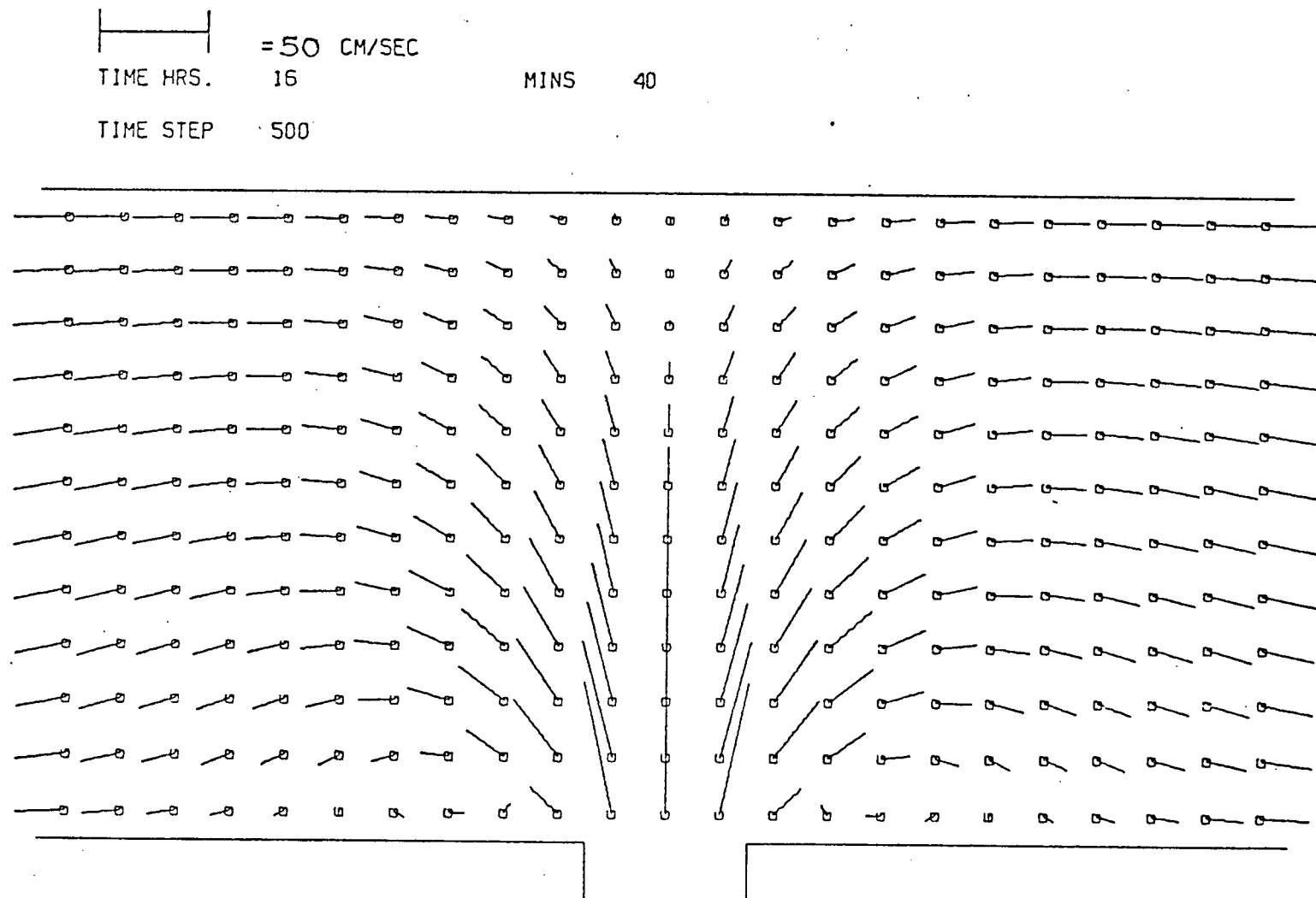


FIGURE 75. Flow field calculated in the same way as for Fig. 71, with the addition of horizontal eddy viscosity.

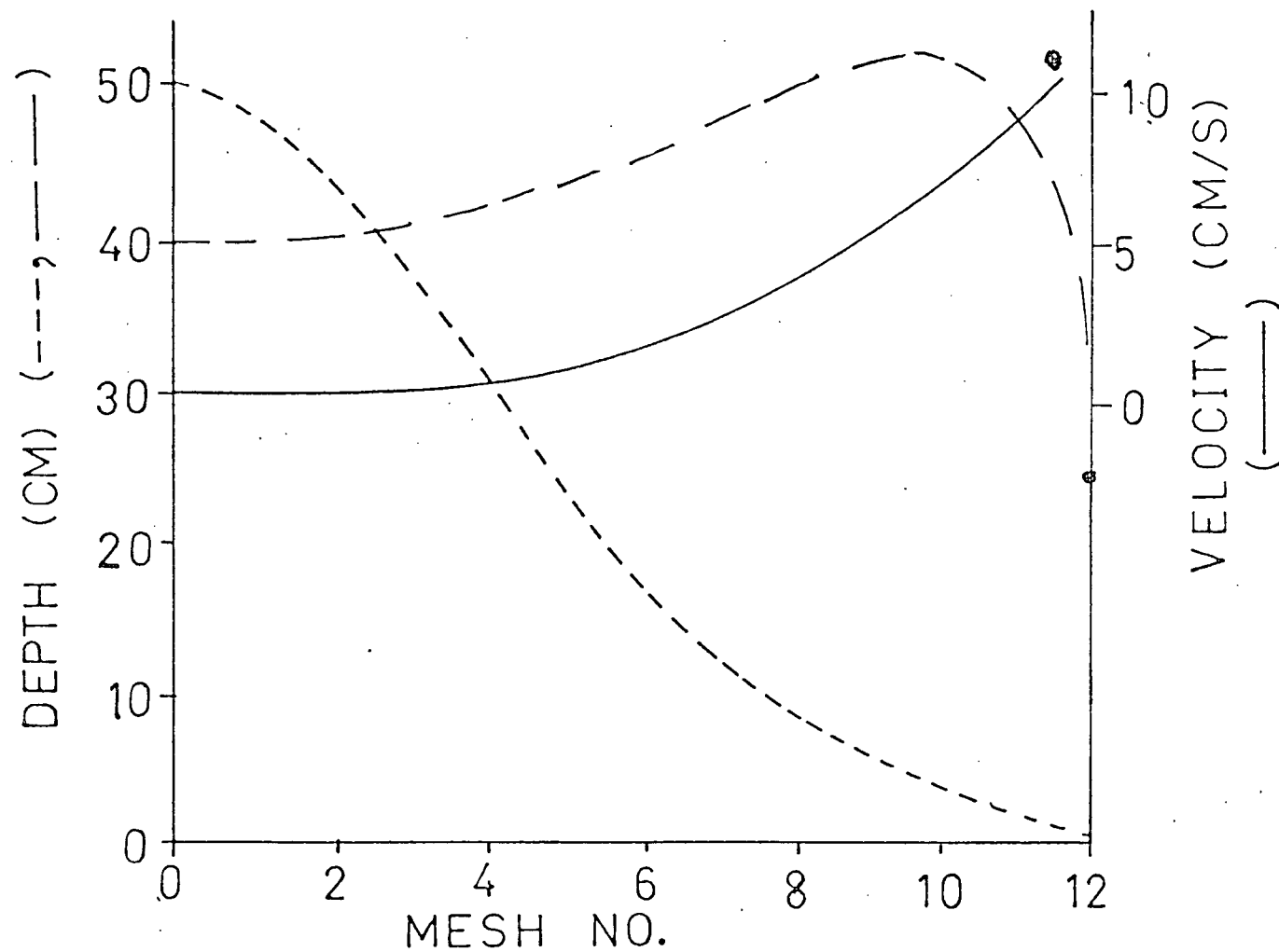


FIGURE 76. The propagation of a hump of water out of the system. the line of small dashes shows the initial distribution of thickness. The shape as the bulge passed out of the open boundary is shown by the large dashes, and the corresponding distribution of velocity by the solid line.

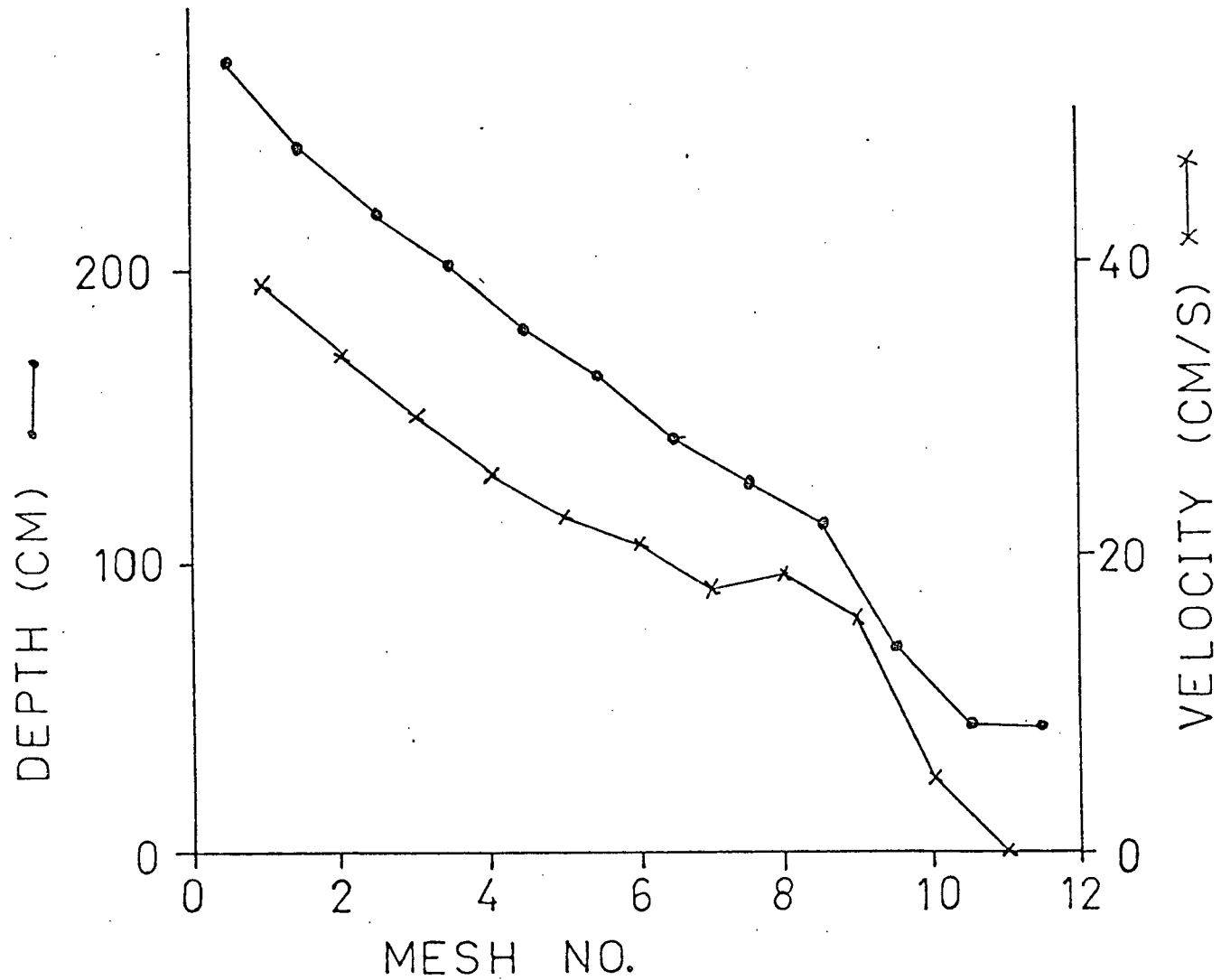


FIGURE 77. The distribution of velocity and elevation for Fig. 74, along the line from the river mouth to the opposite solid boundary.

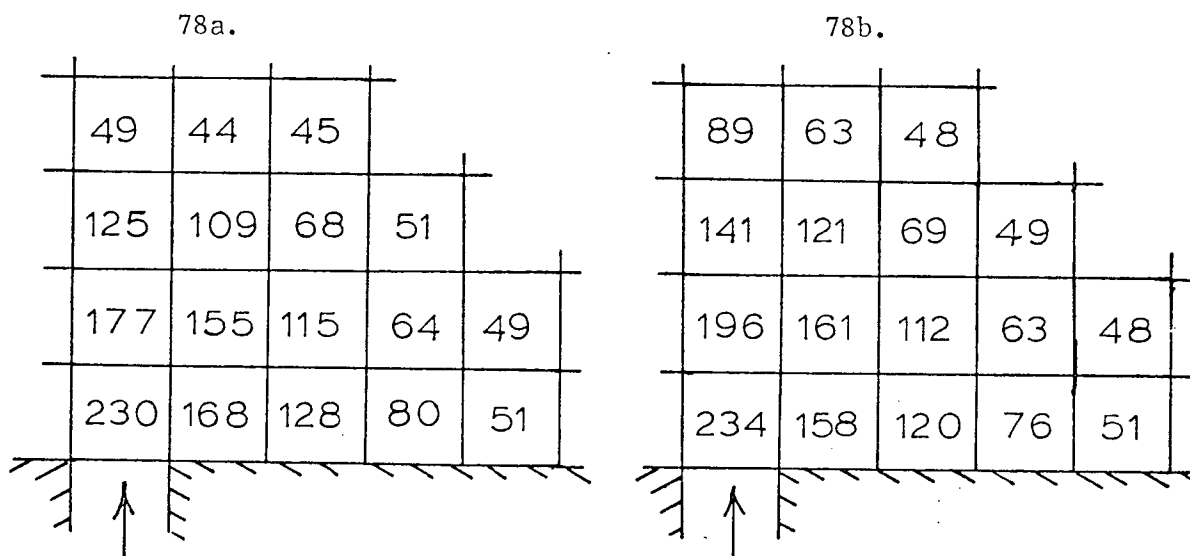


FIGURE 78a,b. Comparison of elevation fields from a .33 km grid size model, 78a, and from a 1 km grid size model, 78b.

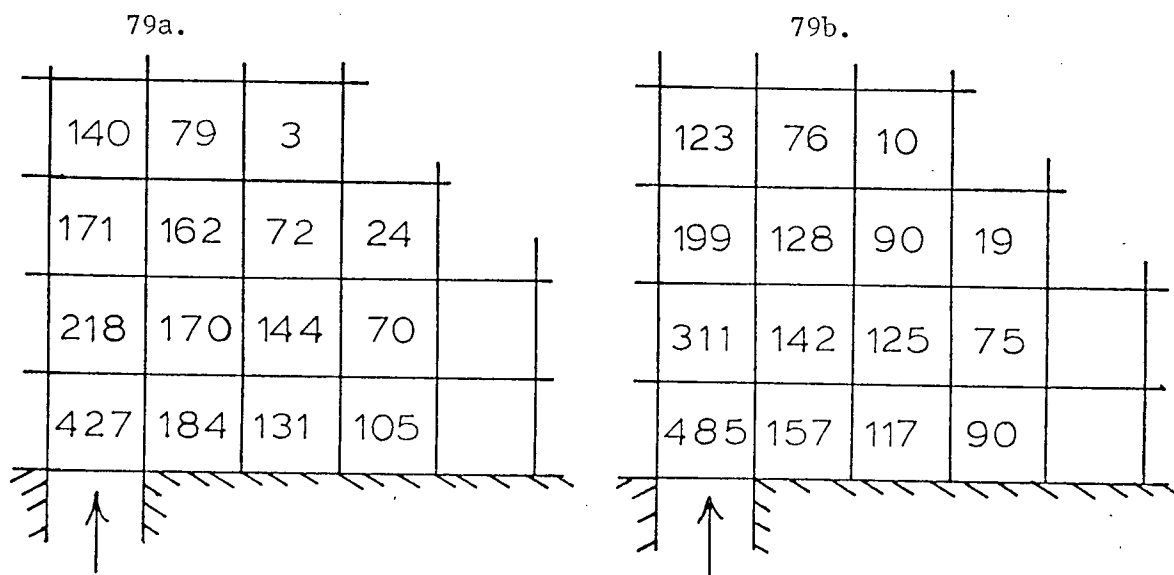
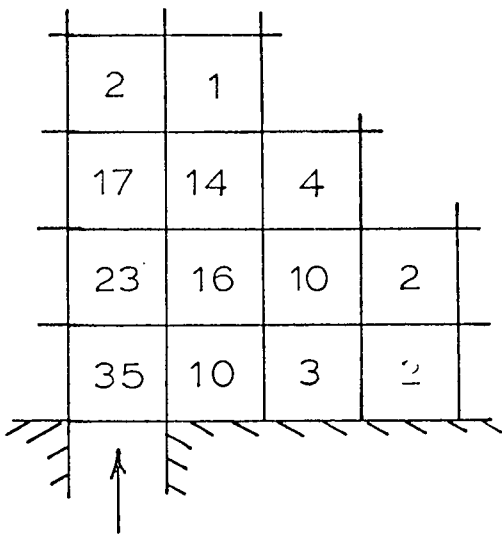


FIGURE 79a,b. Comparison of entrainment velocity from a .33 km mesh size model, 79a, and from a 1 km mesh size model, 79b.

80a.



80b.

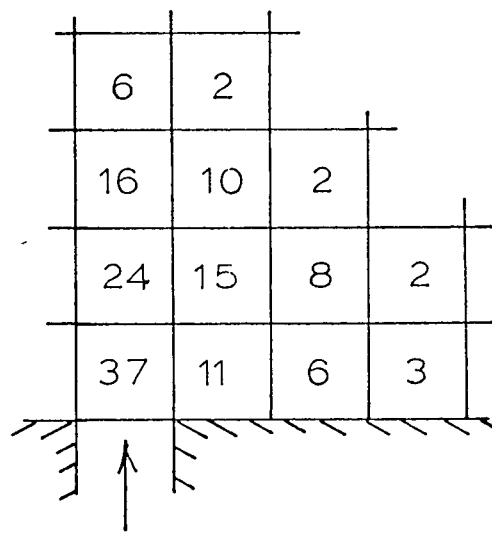
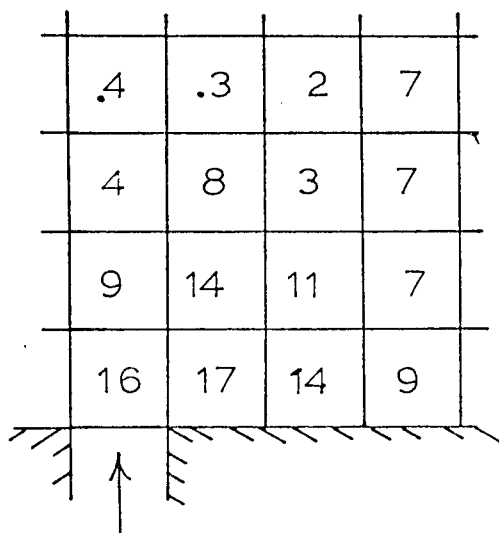


FIGURE 80a,b. Comparison of u-velocity fields from a 0.33 km mesh size model, 80a, and a 1 km mesh size model, 80b.

81a.



81b.

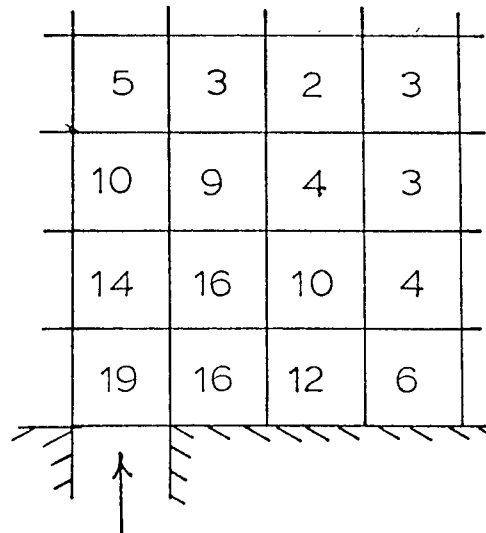


FIGURE 81a, b. Comparison of v-velocity fields from a 0.33 km mesh size model, 81a, and a 1 km mesh size model, 81b.

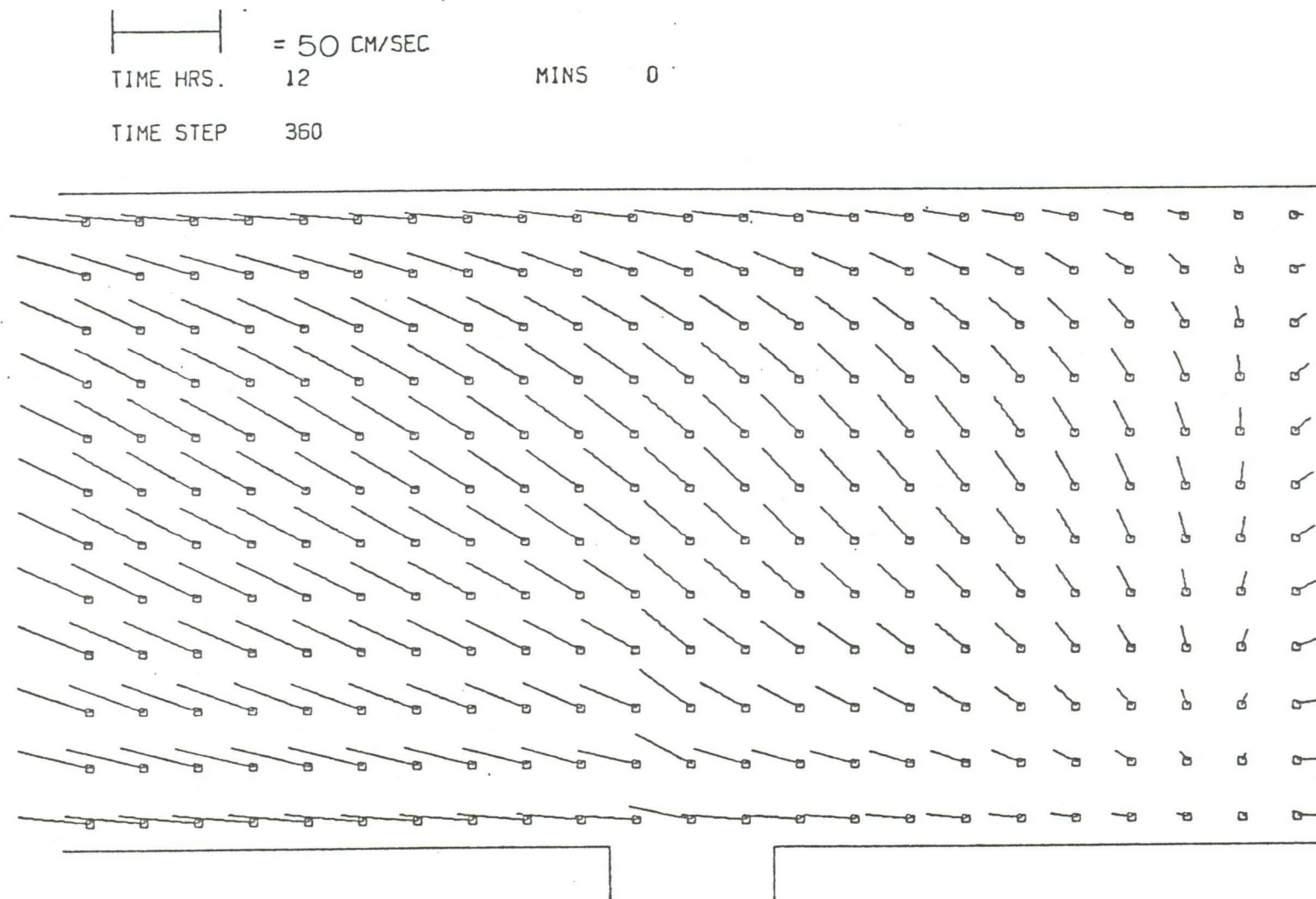


FIGURE 82. Flow field produced by a model with variable river flow, tidal streams and elevations, Coriolis force, and a constant Froude number boundary condition.

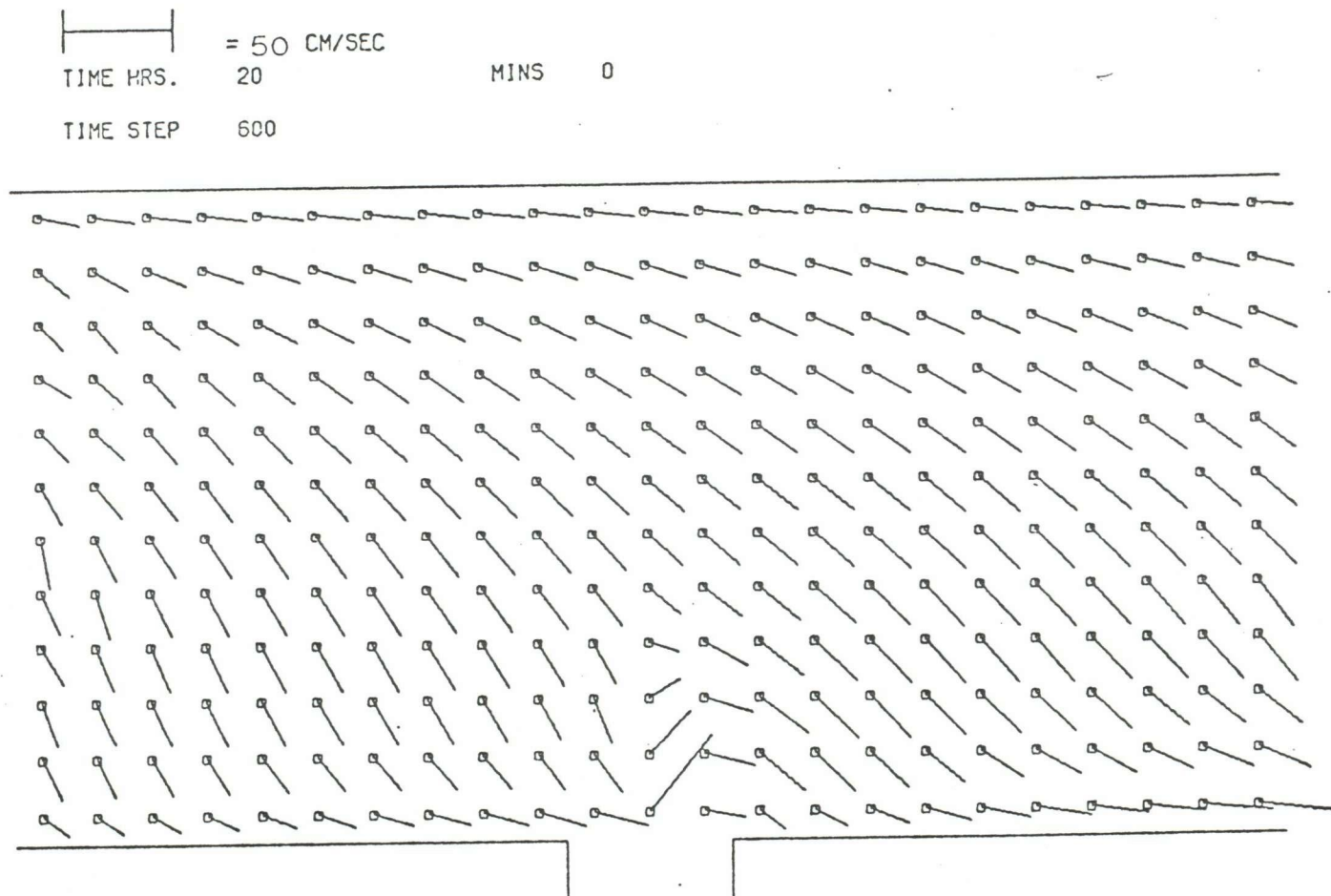


FIGURE 83. Flow field produced by a model with constant river flow, tidal elevations, Coriolis force, friction constant of 0.005, and using $\partial^2 F^2 / \partial n^2 = 0$ as a boundary condition.

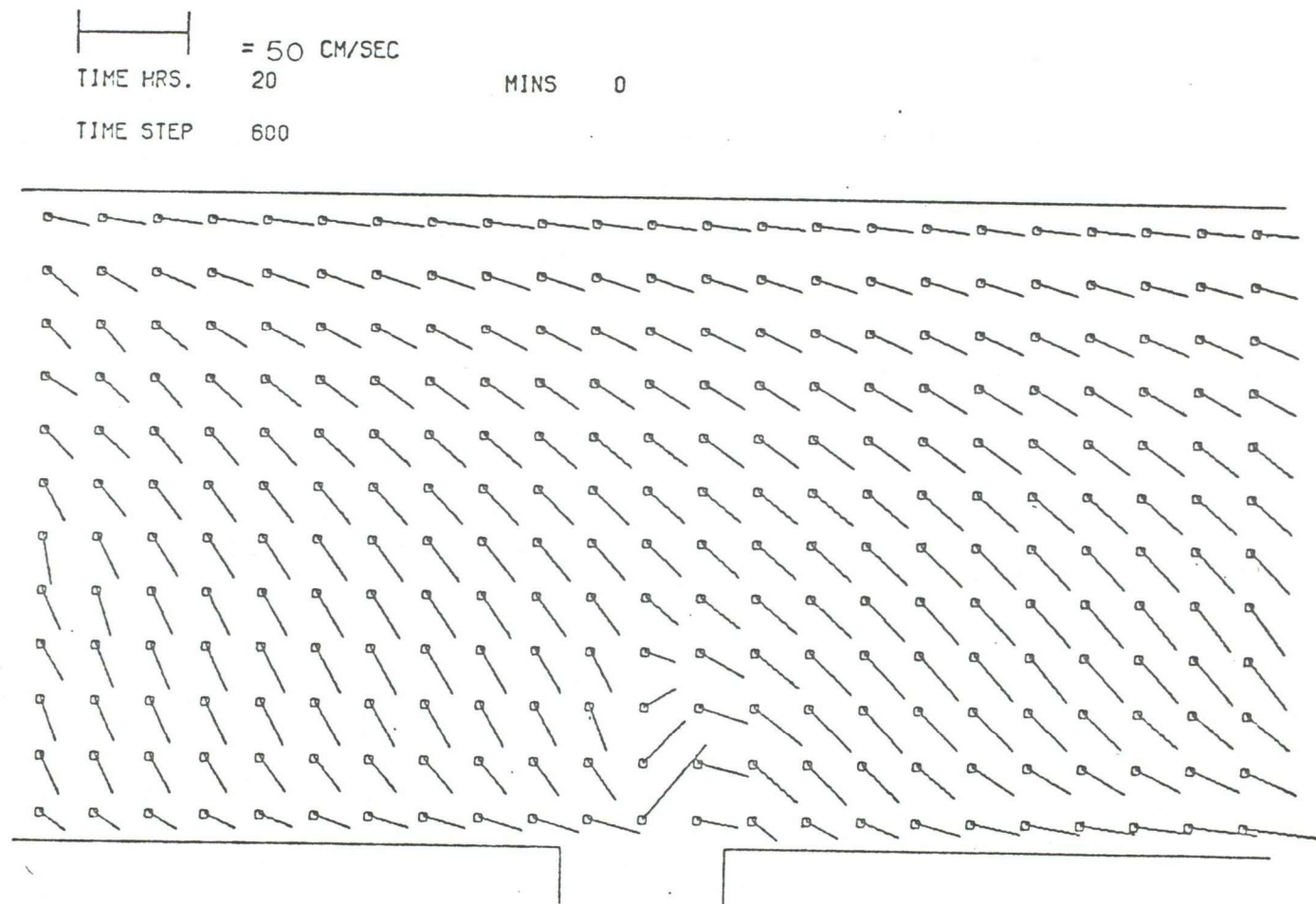


FIGURE 84. Flow field produced by a model identical to that of Fig. 83, but with a friction coefficient of 0.001.

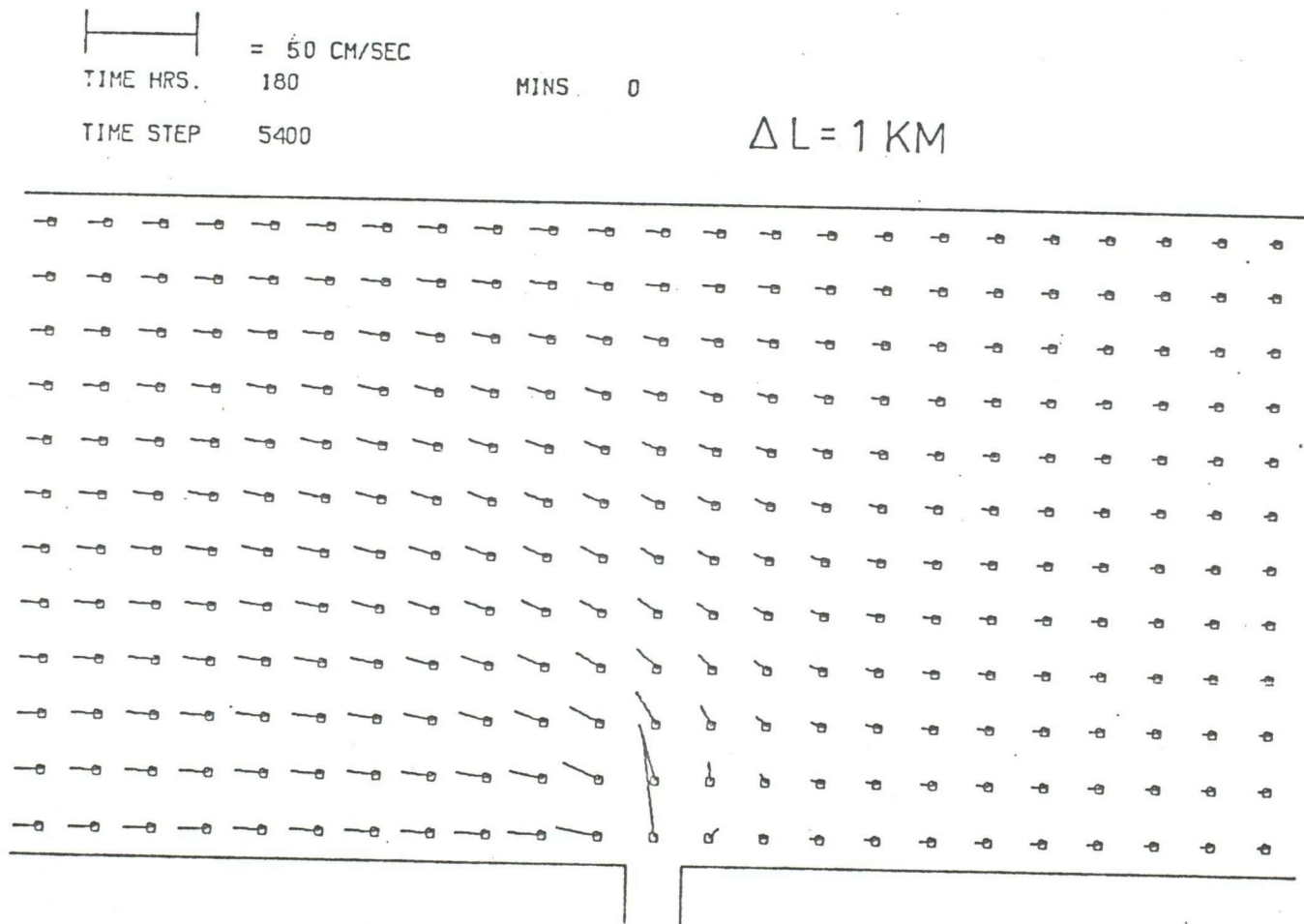


FIGURE 85. Vector velocity diagram for a model with density effects, tidal elevations, no Coriolis force, and constant river flow.

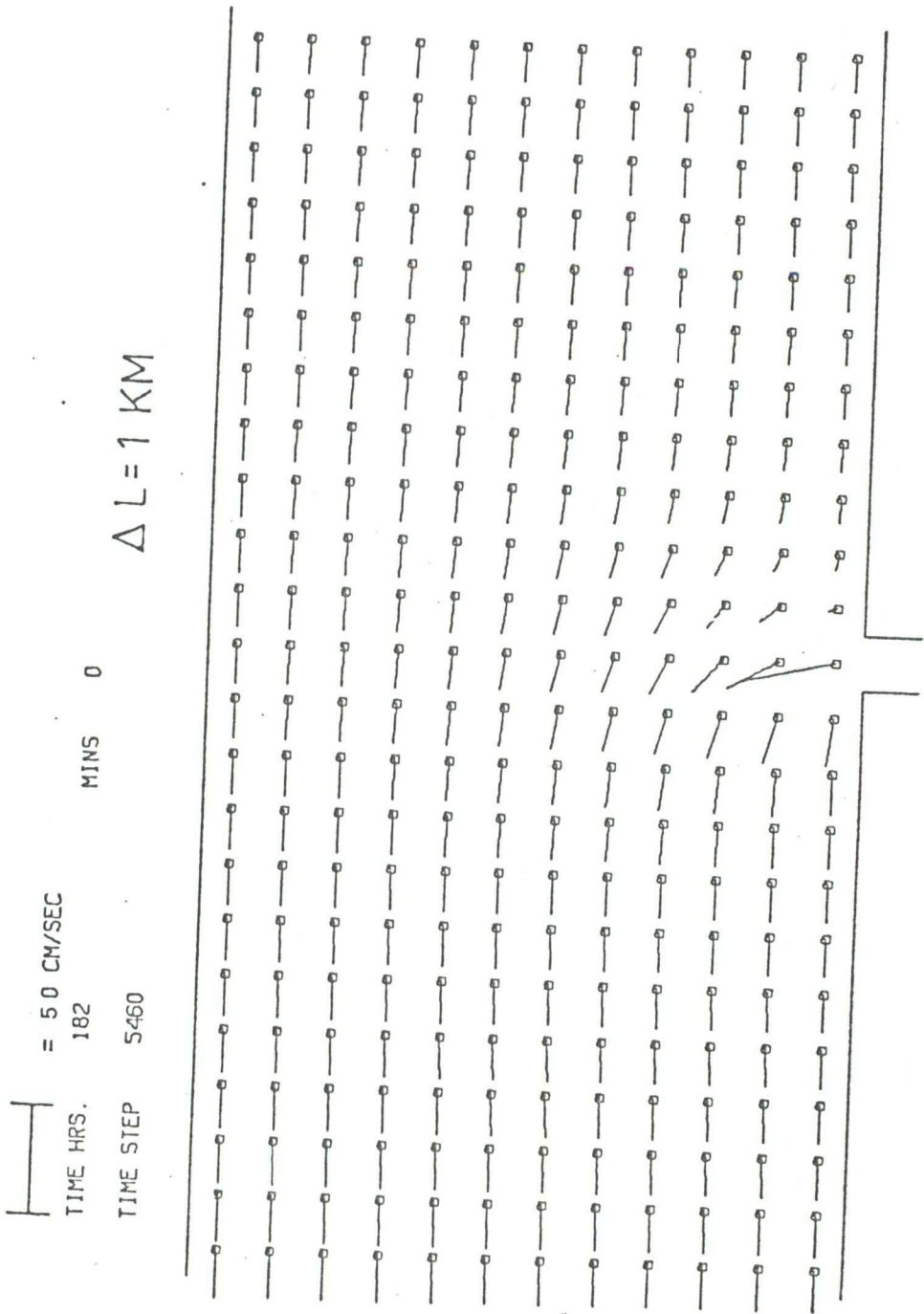


FIGURE 86. The model of Fig. 85, 2 hours later.

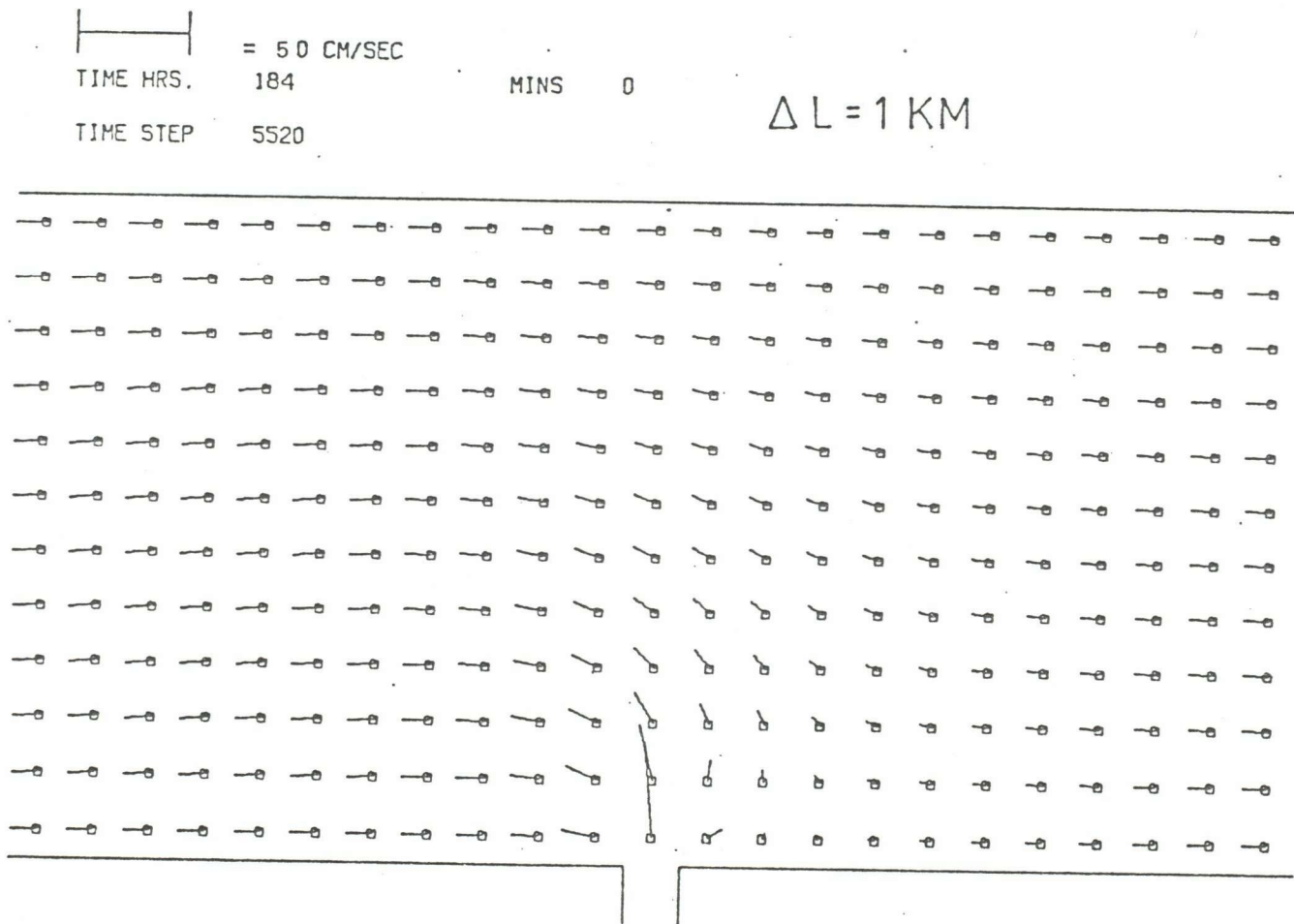



FIGURE 87. The model of figure 85, 4 hours later.


 = 5.0 CM/SEC

TIME HRS.

186

MINS

0

TIME STEP

5580

$\Delta L = 1 \text{ KM}$

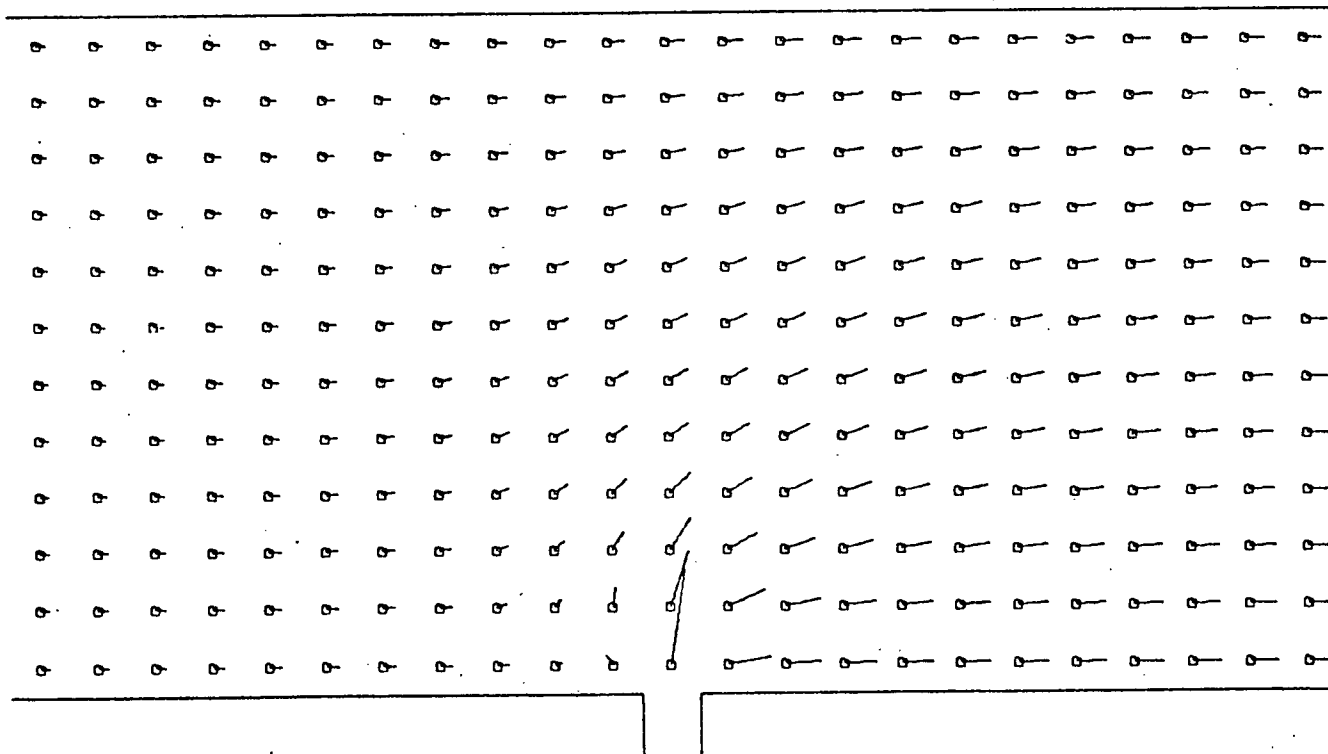


FIGURE 88. The model of Figure 85, 6 hours later.

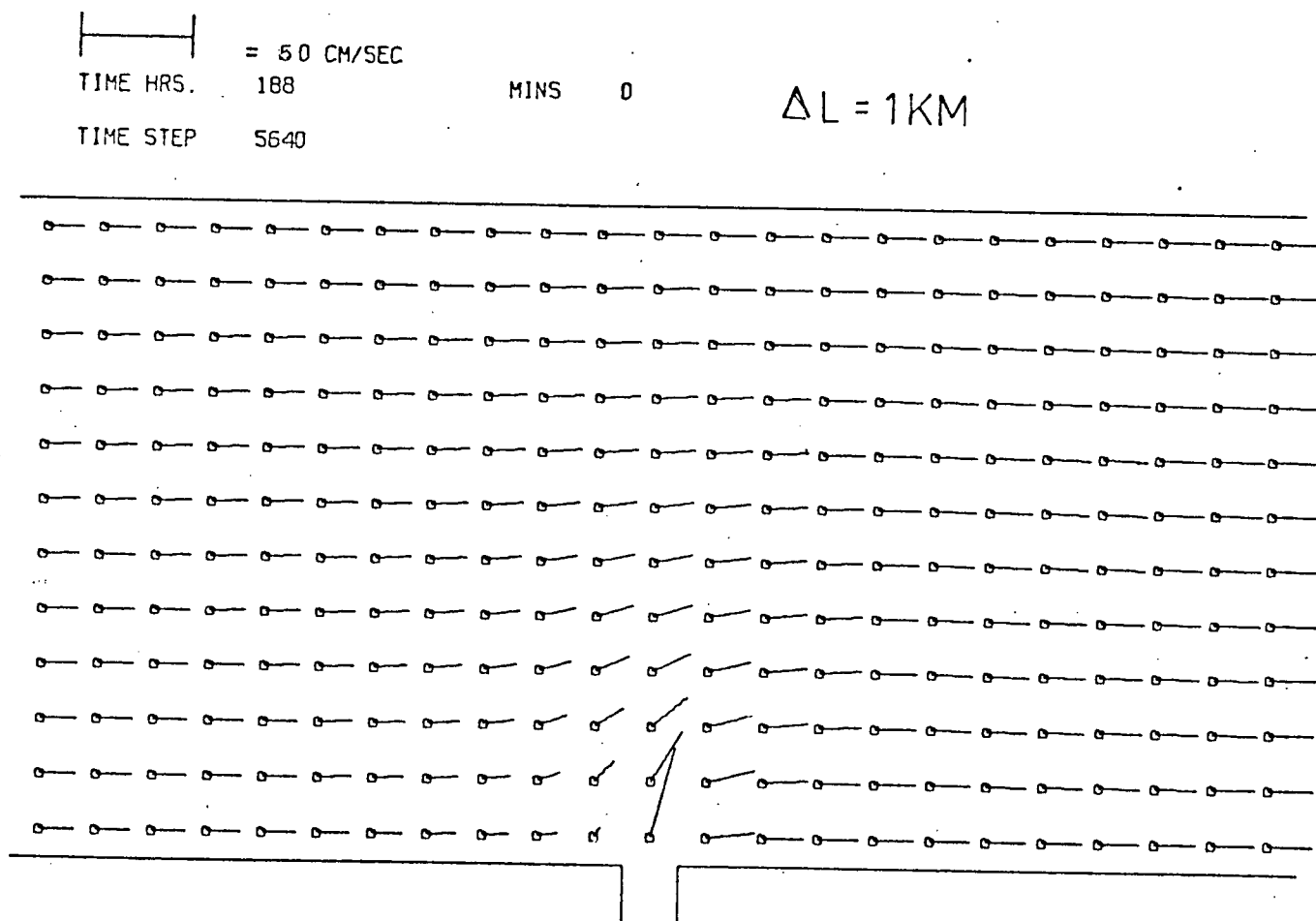


FIGURE 89. The model of Figure 85, 8 hours later.

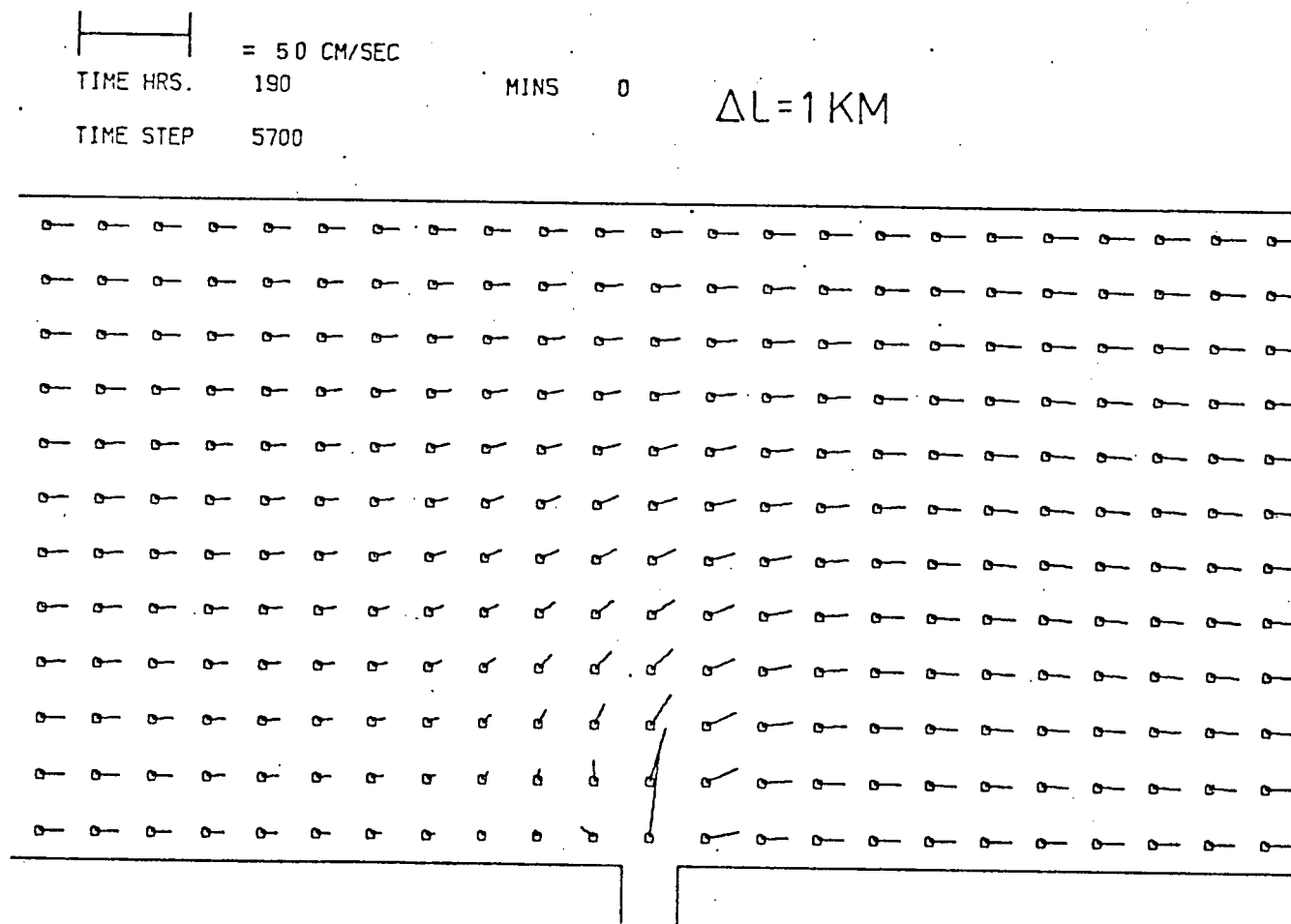


FIGURE 90. The model of Figure 85, 10 hours later.

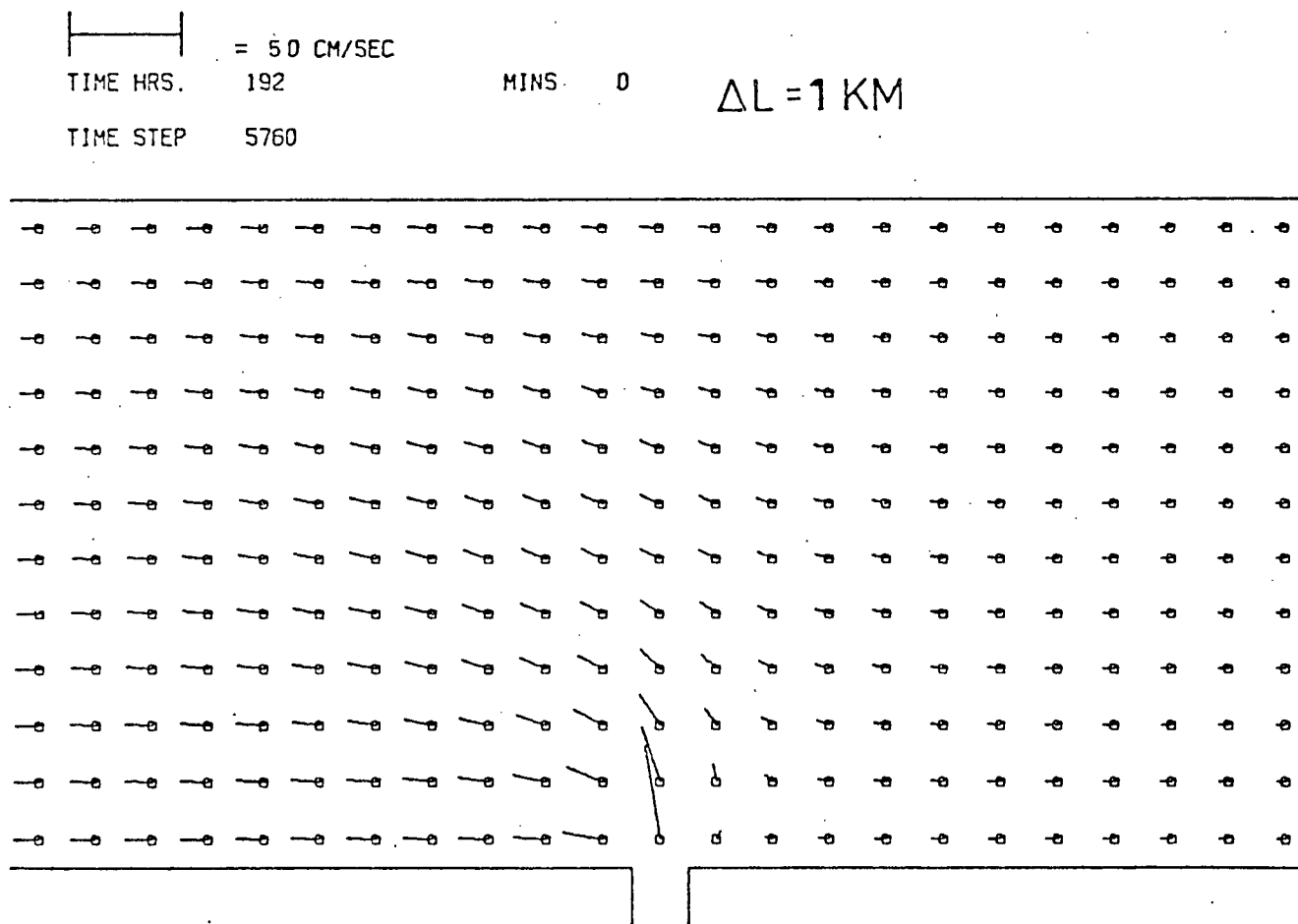


FIGURE 91. The model of Figure 85, 12 hours later.

186 HOURS

SALINITY

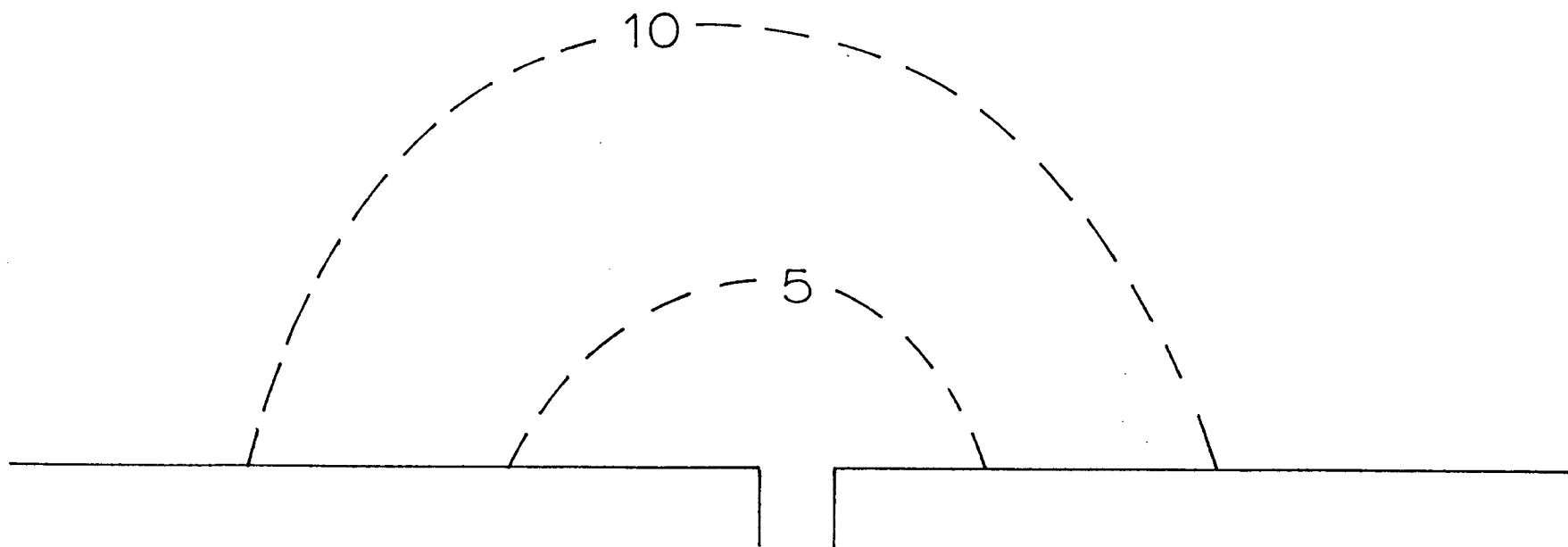


FIGURE 92. Salinity distribution at hour 186, corresponding to the flow field of Fig. 88. The 5 ppt and 10 ppt contours are shown.

192 HOURS

SALINITY

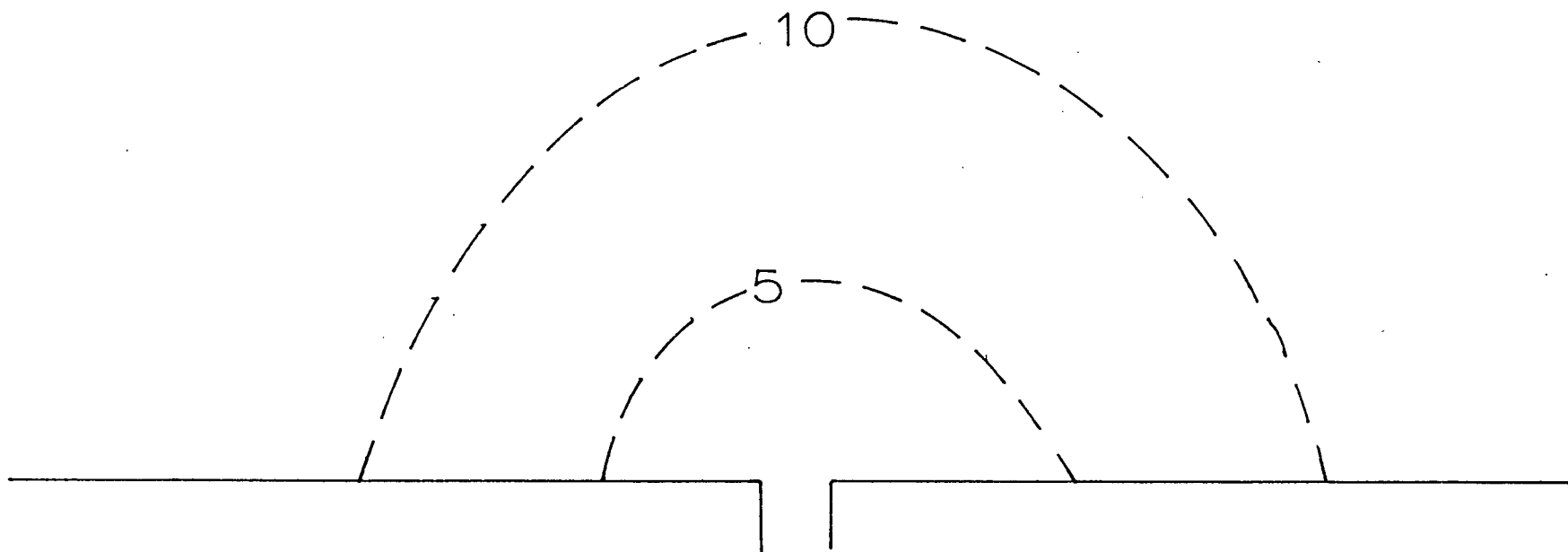


FIGURE 93. The salinity distribution at hour 192, corresponding to Fig. 91. The 5 ppt and 10 ppt contours are shown.

186 HOURS

ELEVATIONS

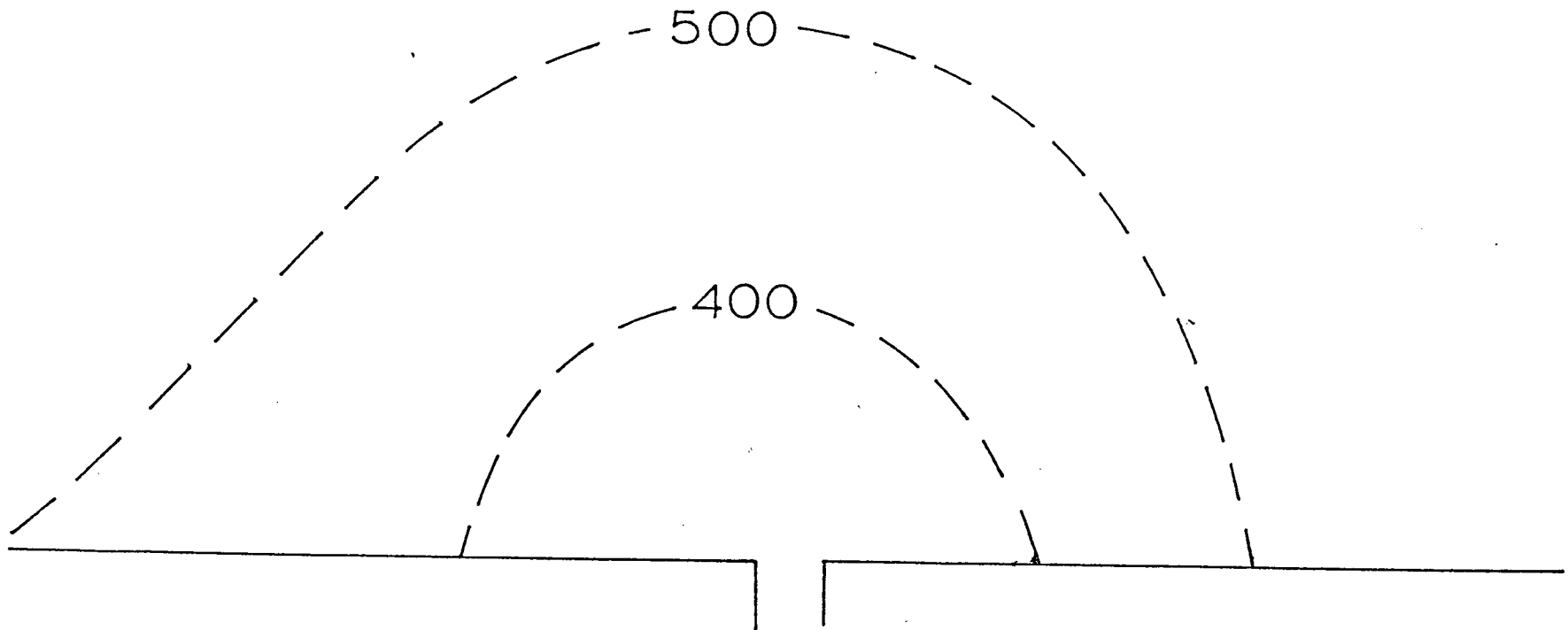


FIGURE 94. The distribution of upper layer thickness at hour 186, corresponding to Fig. 88. The 400 cm and 500 cm contours are shown.

192 HOURS

ELEVATIONS

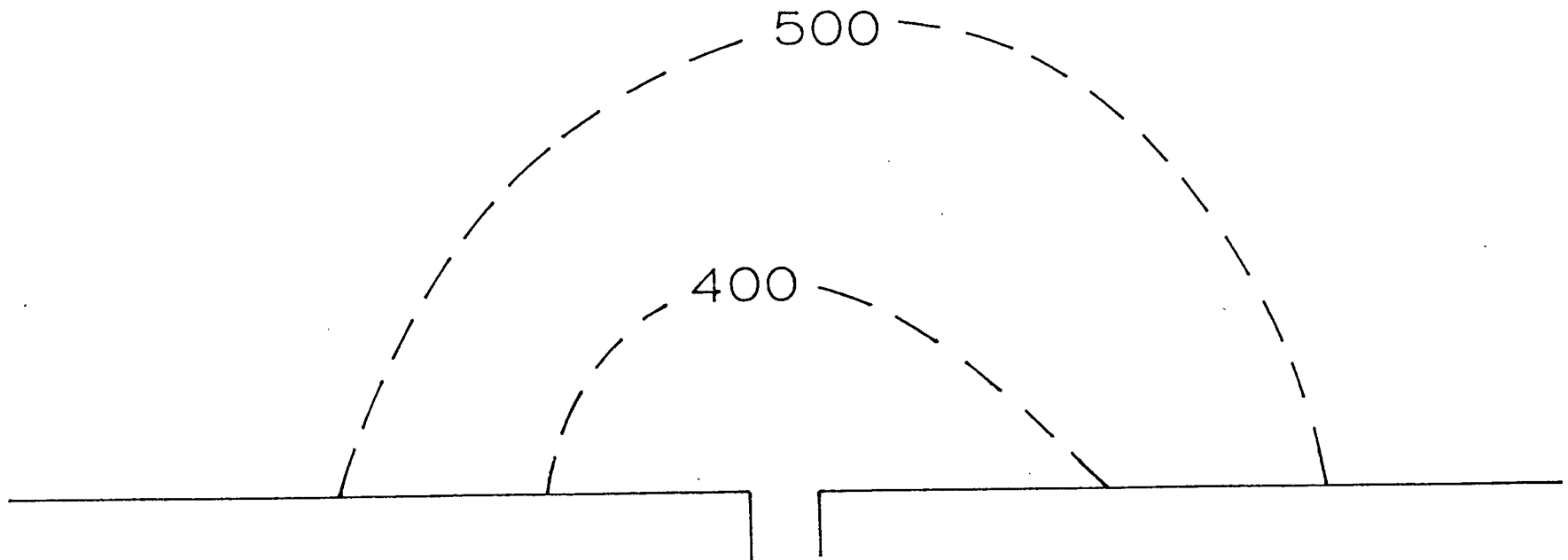


FIGURE 95. The distribution of upper layer thickness at hour 192, corresponding to Fig. 91. The 400 cm and 500 cm contours are shown.

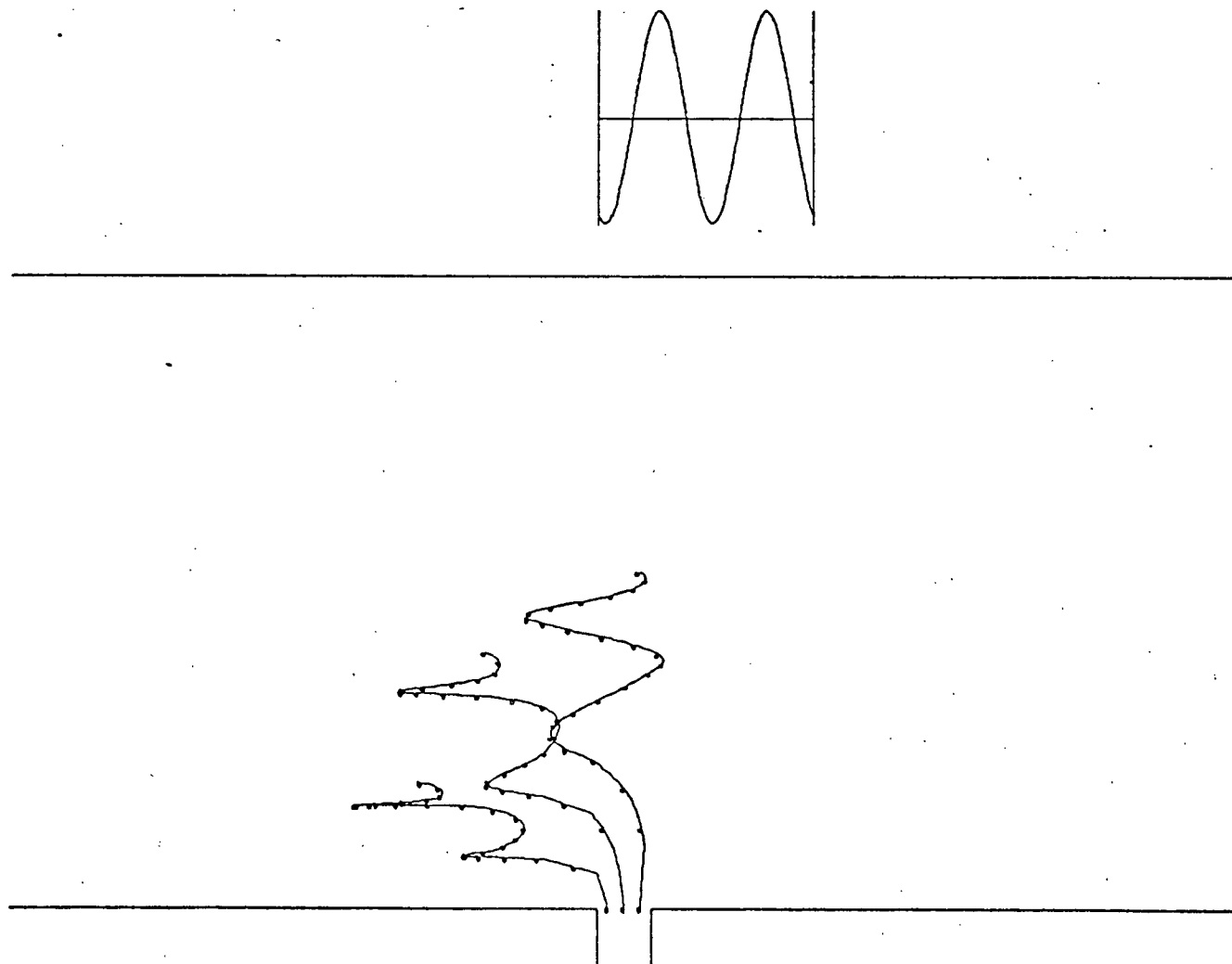


FIGURE 96. Drogue tracks produced over a 24 hour period by the flow field of Figs. 85 - 91. Dots on the tracks are separated by one hour, and the upper curve indicates the tidal elevation during the 24 hour period.

TIMESTEP 9360 TO TIMESTEP 10081

TIDAL ELEVATION AT TSAWASSEN

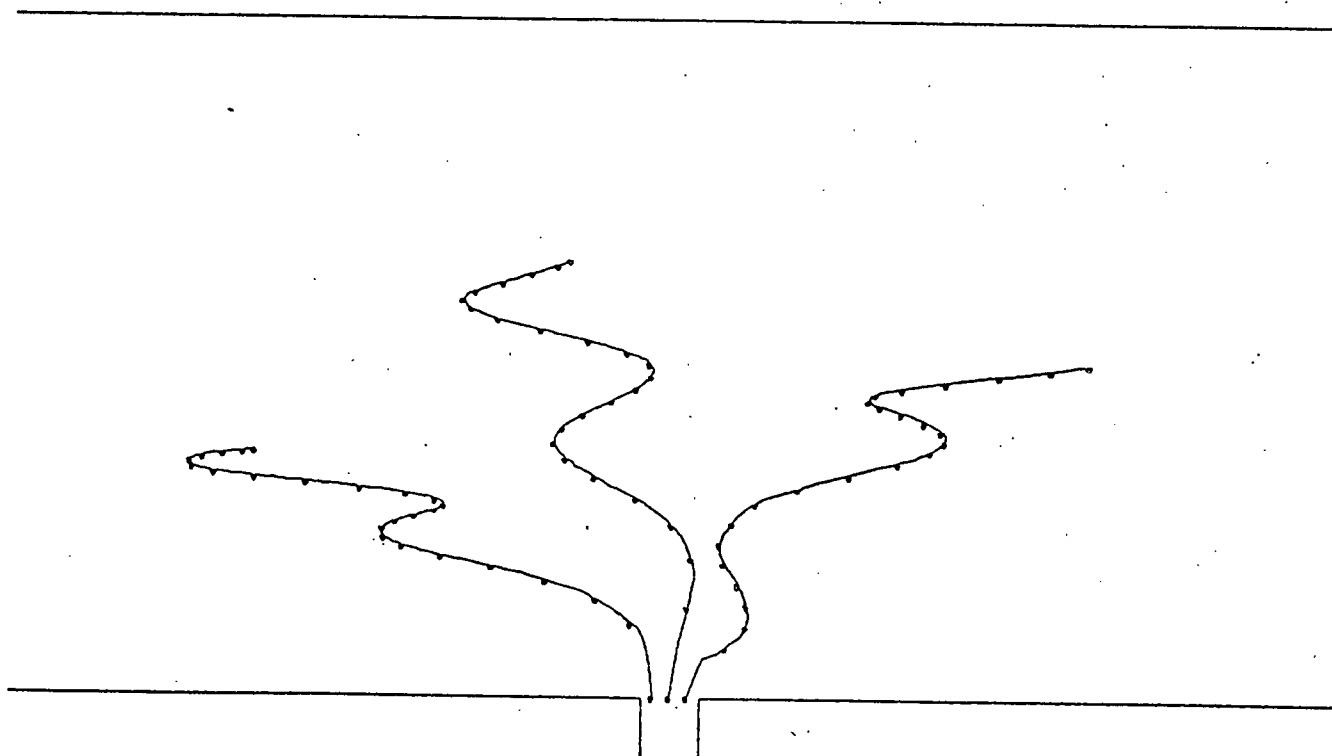
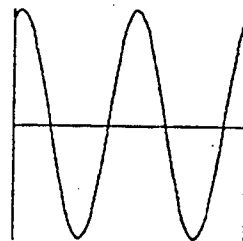


FIGURE 97. Drogue tracks produced over 24 hours by the flow field of Fig. 98, using an augmented flow at the boundaries during outflow.

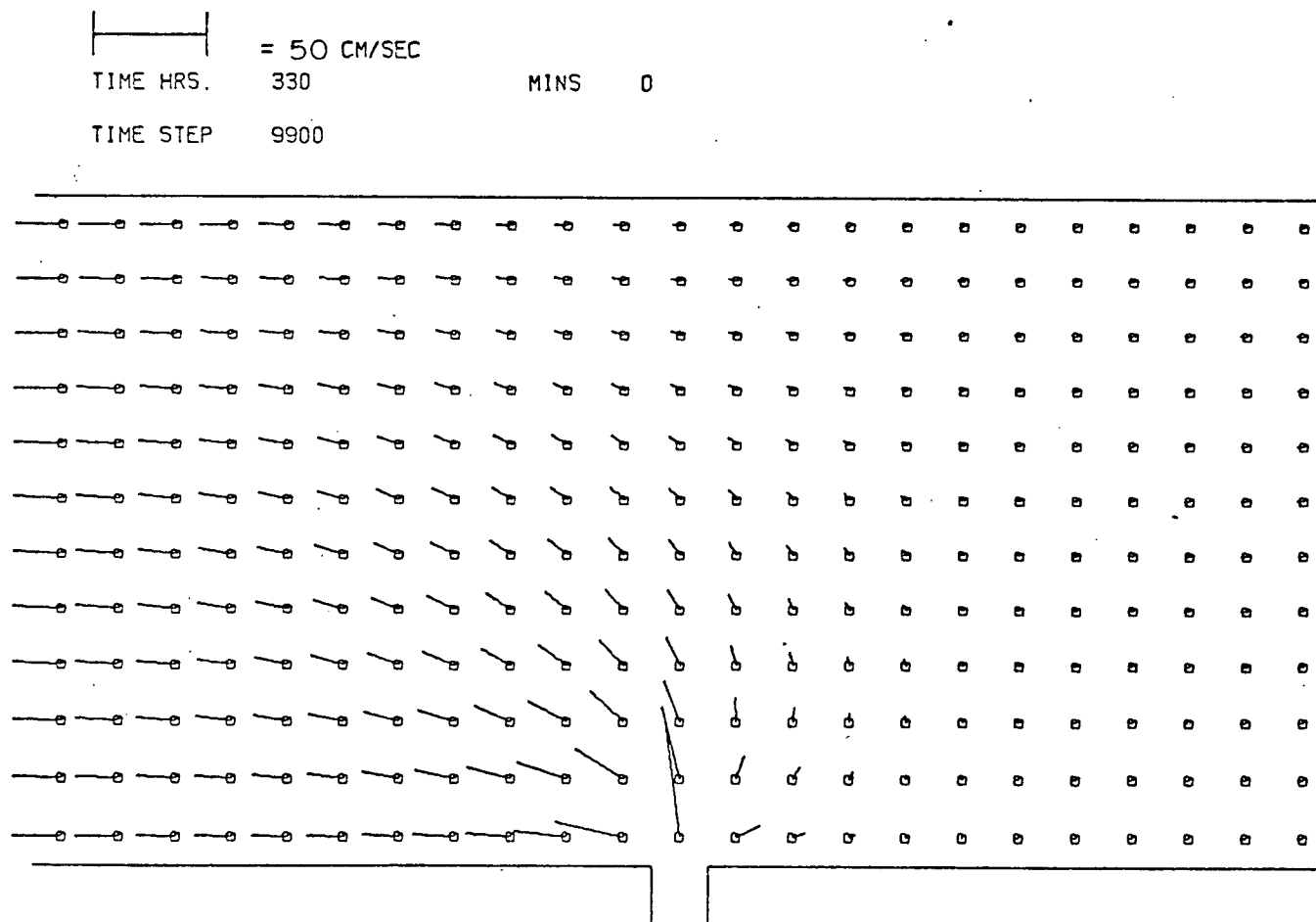


FIGURE 98. A typical velocity field produced by a model with augmented flow at the open boundaries during outflow.

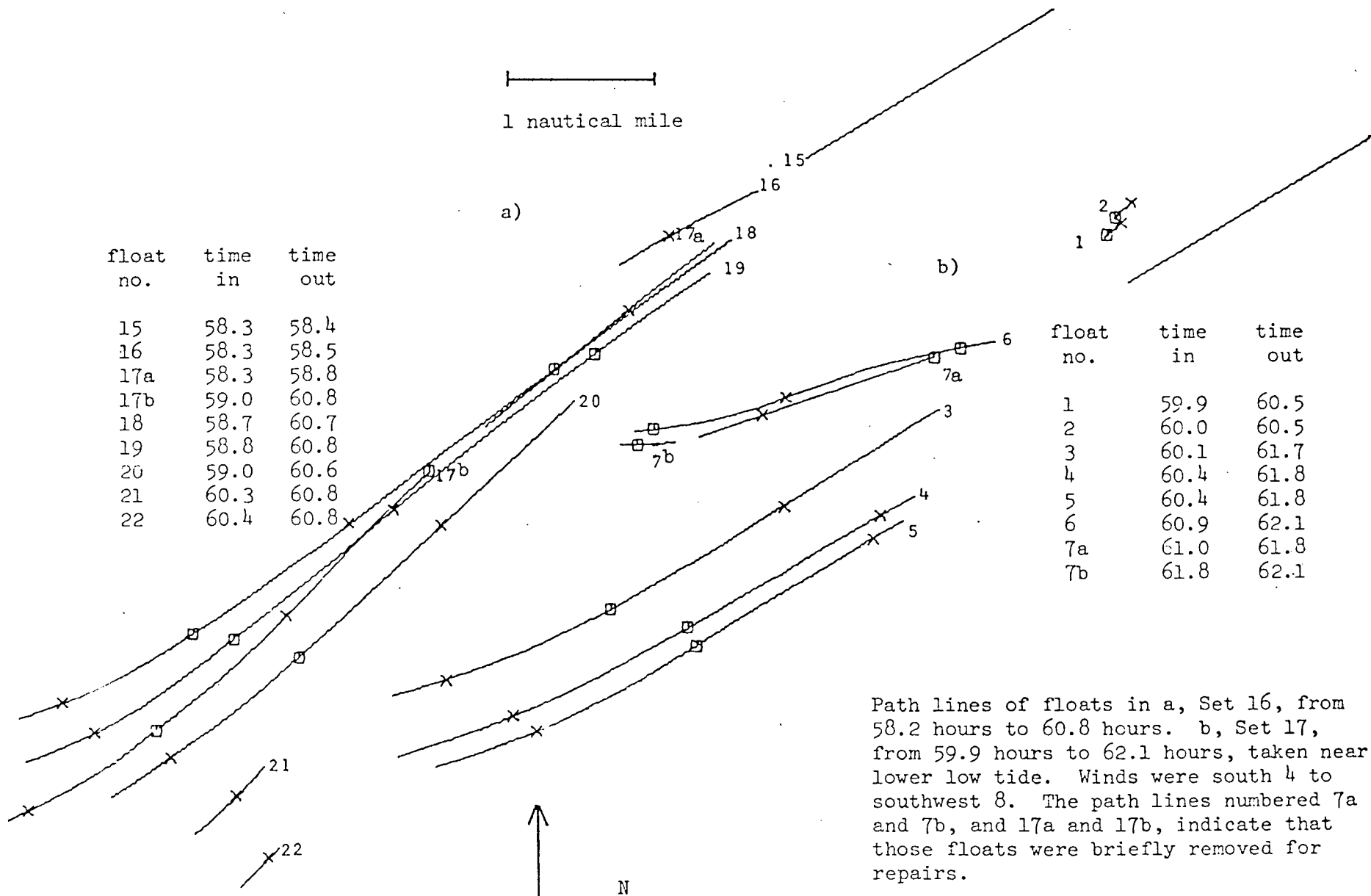


FIGURE 99. Drogue tracks for drogues released shortly before low water. (from Cordes, 1977).

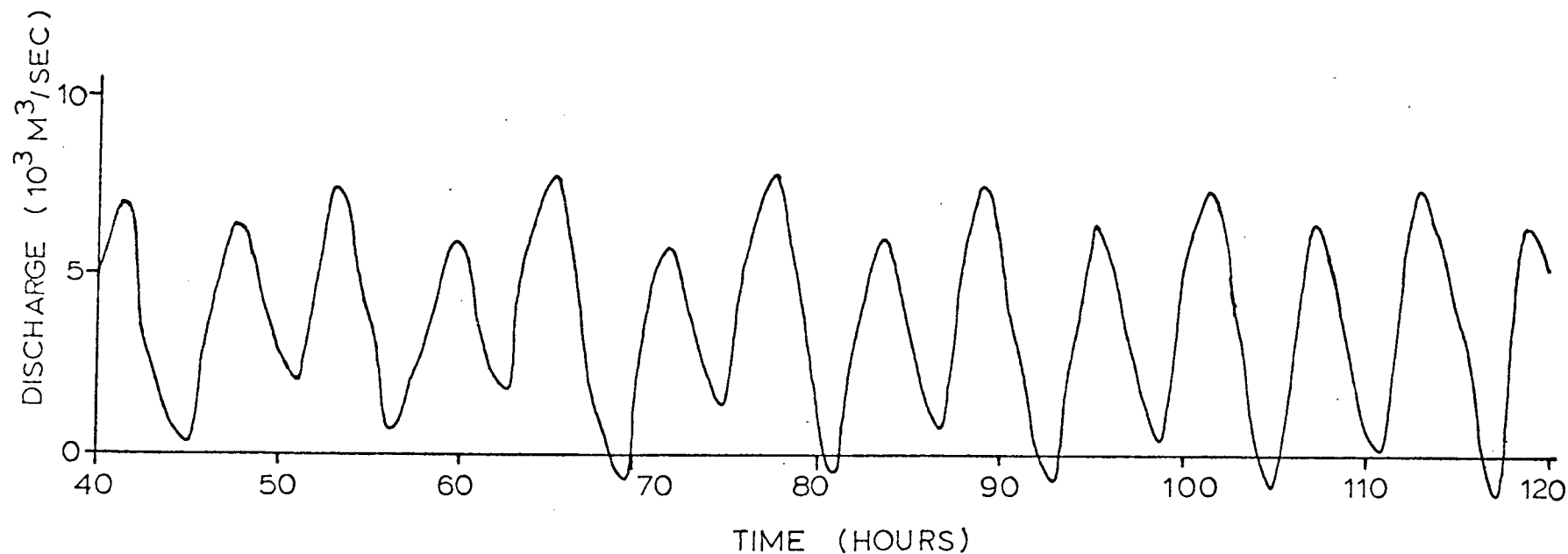


FIGURE 100. The discharge out of the open boundaries of a model with tidal elevations, variable density, constant river flow, and no Coriolis force. The river inflow was $2000 \text{ m}^3/\text{sec}$.

TIMESTEP 720 TO TIMESTEP 1441

TIDAL ELEVATION AT TSAWASSEN

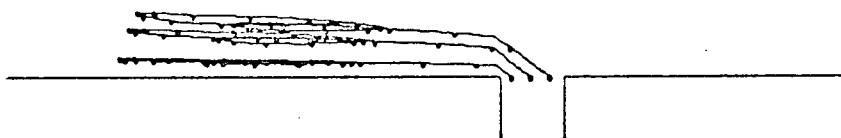
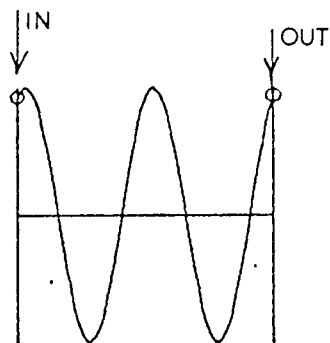


FIGURE 101. Drogue tracks produced when drogues were released at zero river flow, approaching high water.

TIMESTEP 1530 TO TIMESTEP 1981

TIDAL ELEVATION AT TSAWASSEN

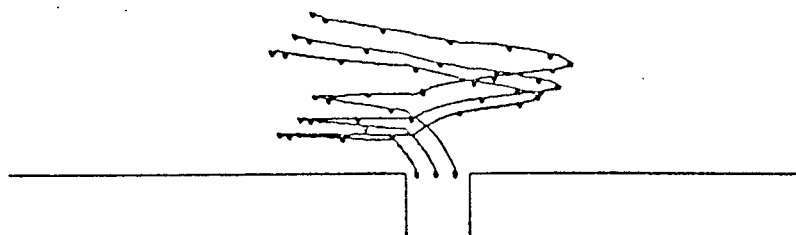
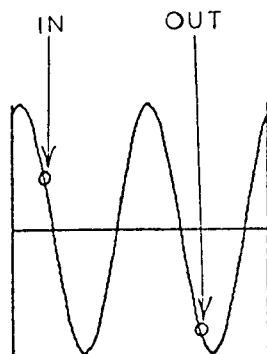


FIGURE 102. Drogue tracks produced when drogues were released at half maximum river flow, during the ebb, when river flow is increasing.

TIMESTEP 1980 TO TIMESTEP 2431

TIDAL ELEVATION AT TSAWASSEN

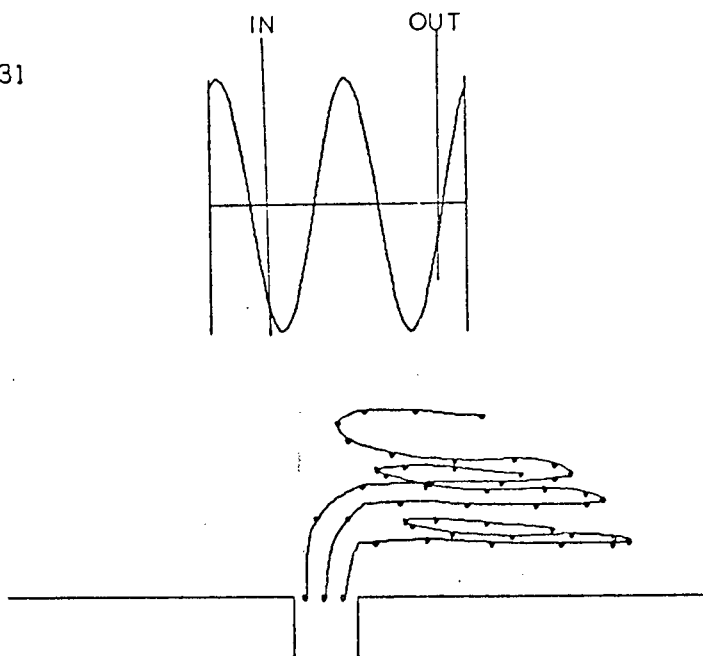


FIGURE 103. Drogue tracks produced when drogues were released at maximum river flow, near the end of the ebb.

TIMESTEP 2430 TO TIMESTEP 2881

TIDAL ELEVATION AT TSAWASSEN

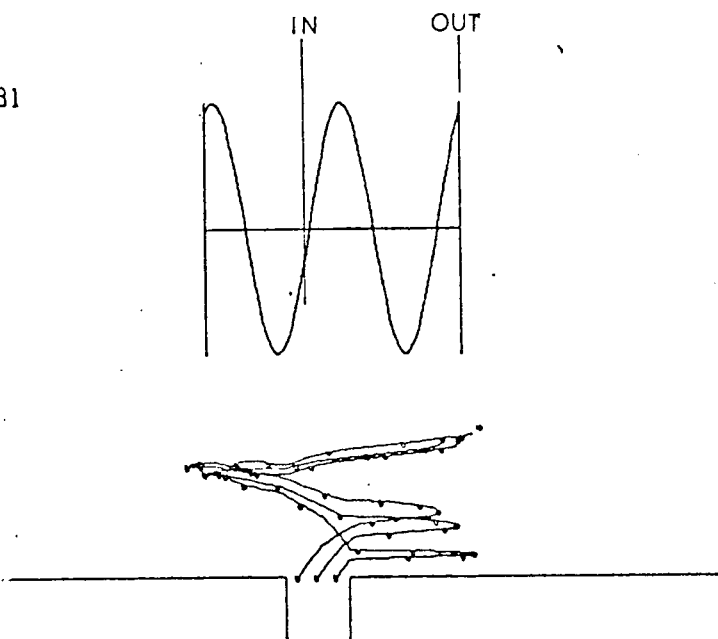


FIGURE 104. Drogue tracks produced when drogues were released at half maximum river flow during the flood stage of the tide.

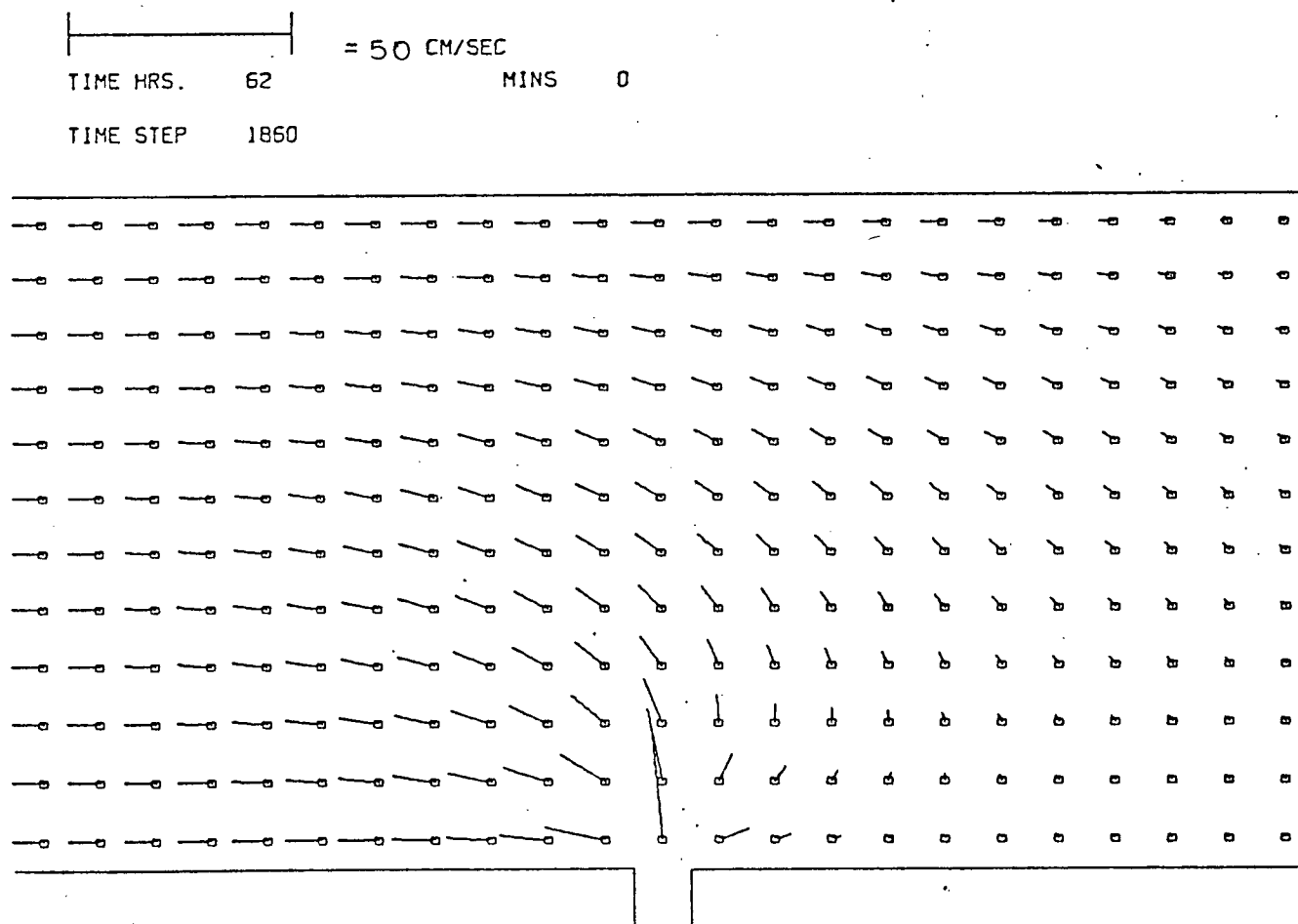


FIGURE 195. Velocity field produced by a model with depletion. Other terms are the same as those which produced Fig. 86, except salinity is 20 % on inflow.

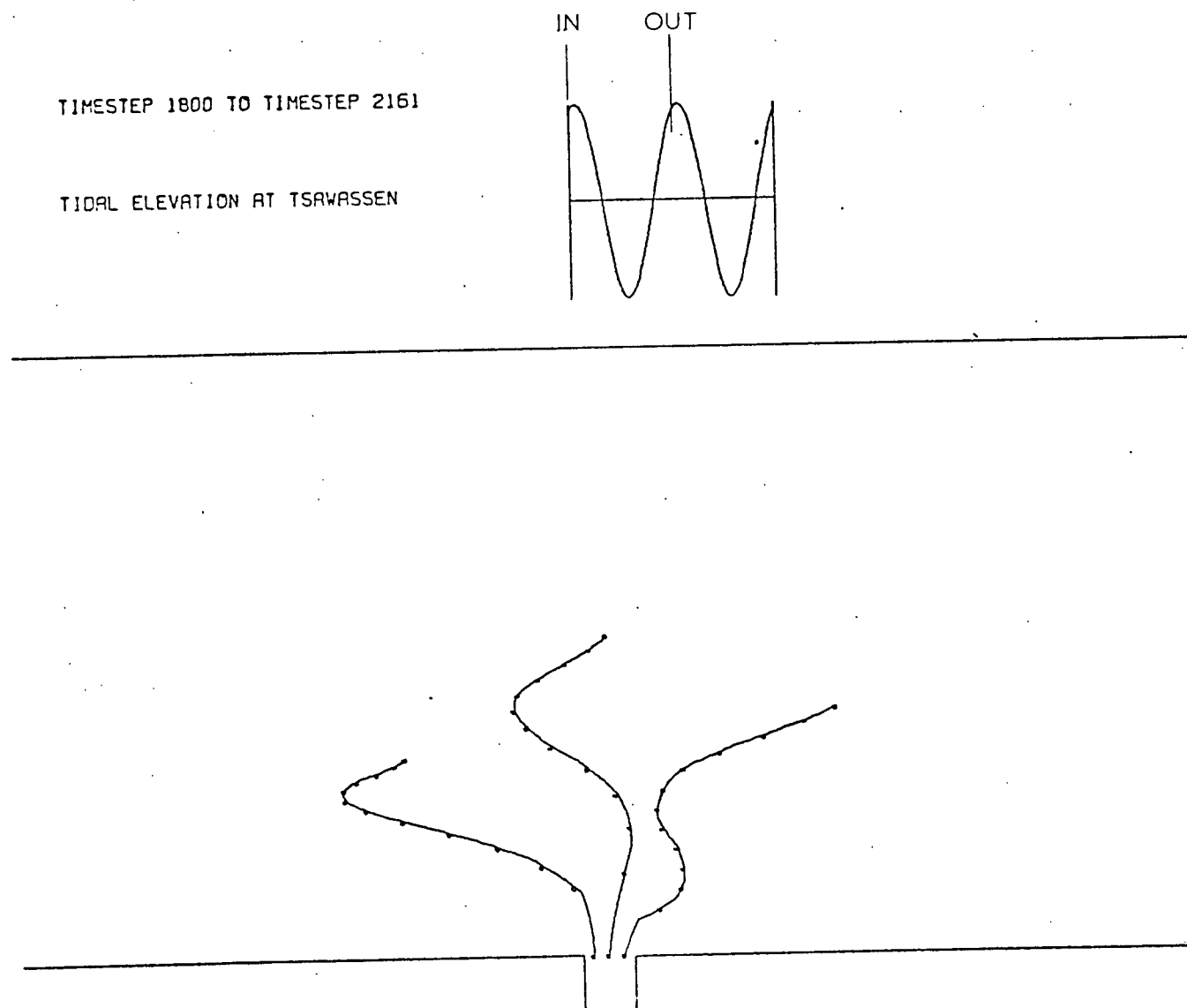


FIGURE 106. Drogue tracks produced over 12 hours by the model which produced the flow field of Fig. 105.

66 HOURS

ELEVATIONS

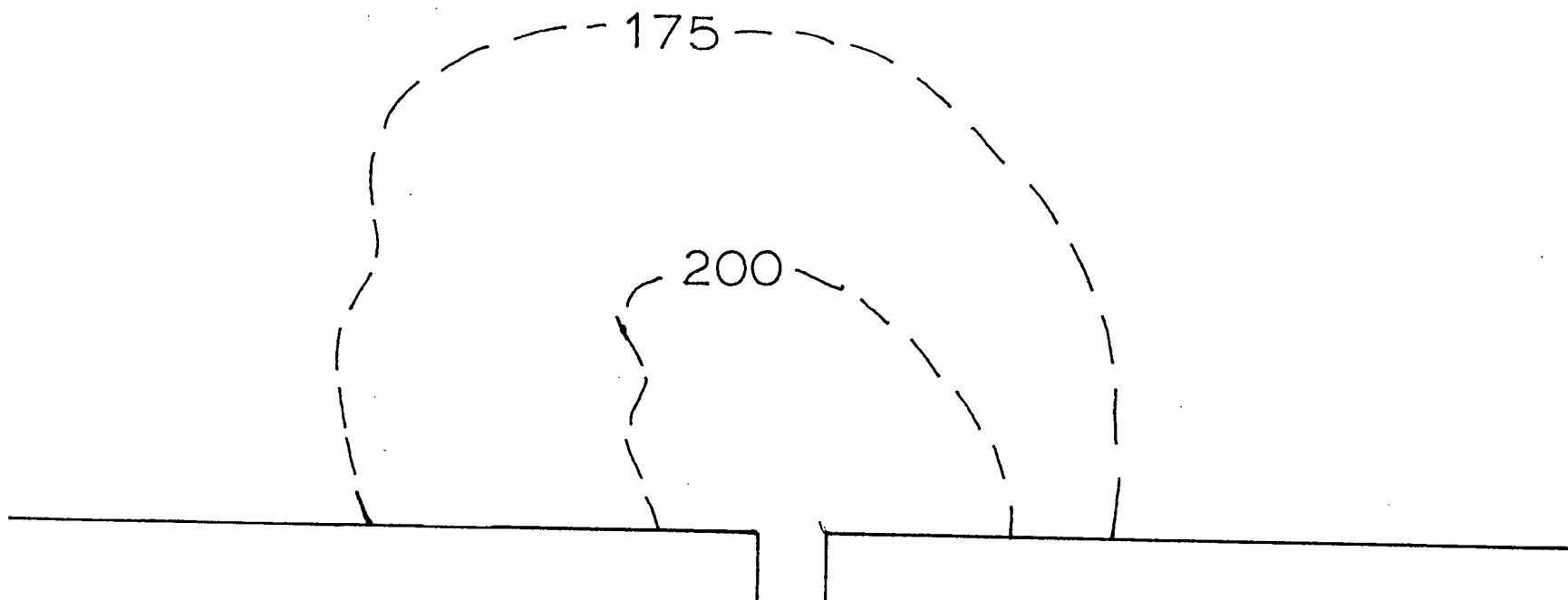


FIGURE 107. Elevation field produced by the model with depletion at 66 hours, at the same tidal phase as Fig. 94. The 175 cm and 200 cm contours are shown.

72 HOURS

ELEVATIONS

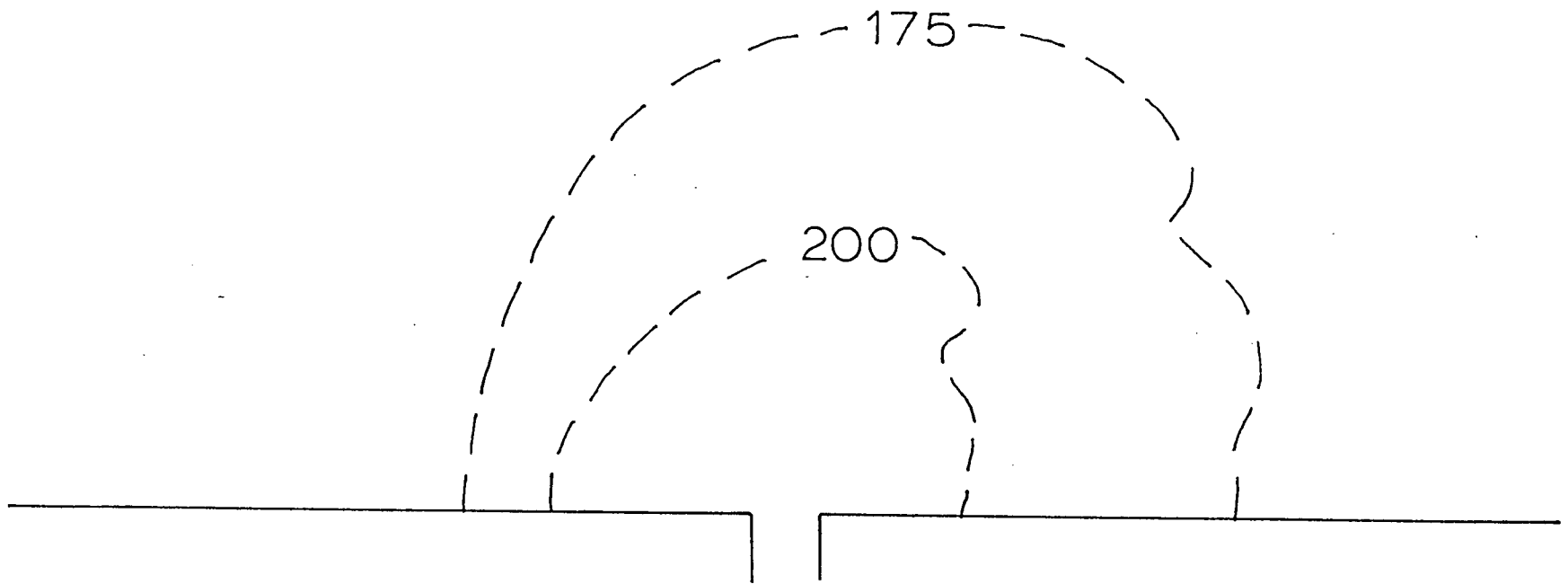


FIGURE 108. Elevation field at 72 hours, produced by the model with depletion. The tidal phase is the same as in Fig. 95. The 175 cm and 200 cm contours are shown.

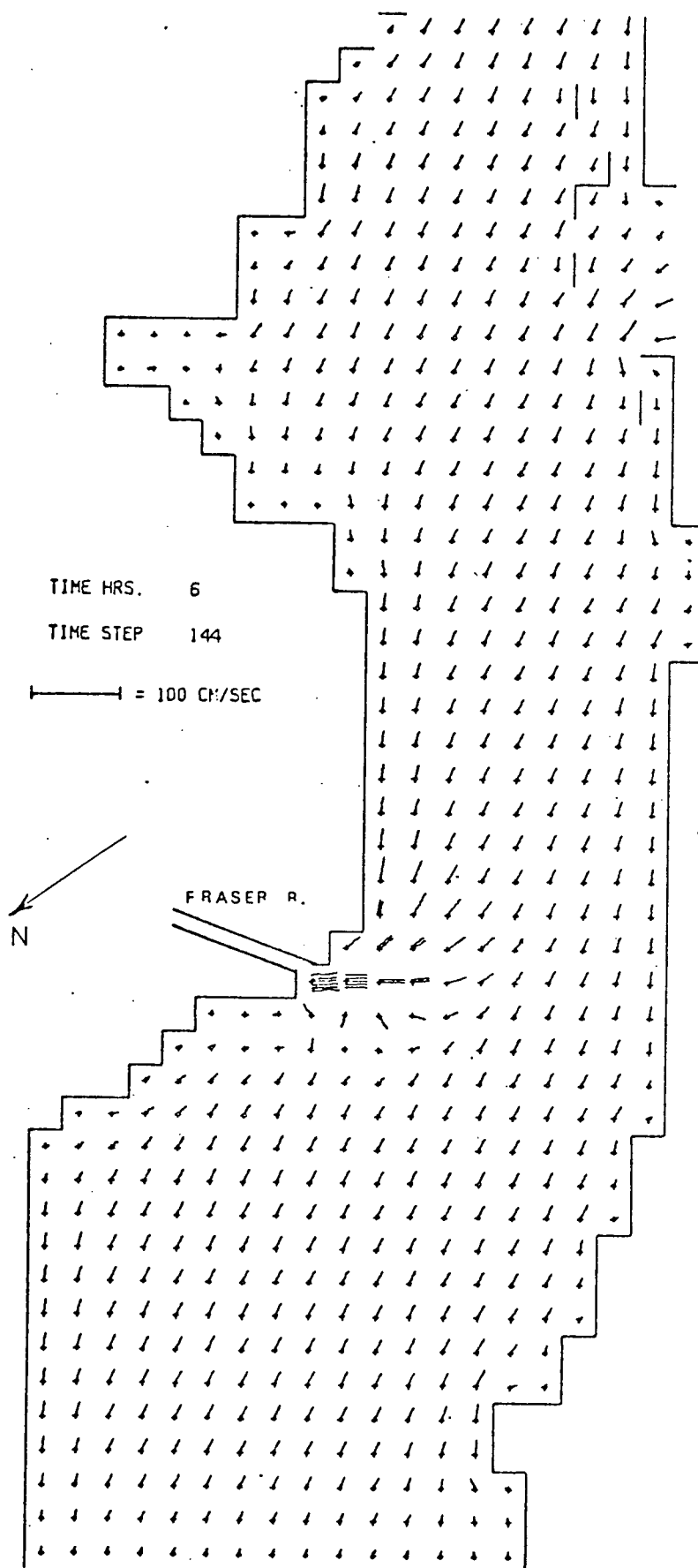


FIGURE 109. Velocity field produced by the first real geometry model, at time of maximum river flow.

END OF EBB

8 HOURS

200 CM, 300 CM
CONTOURS

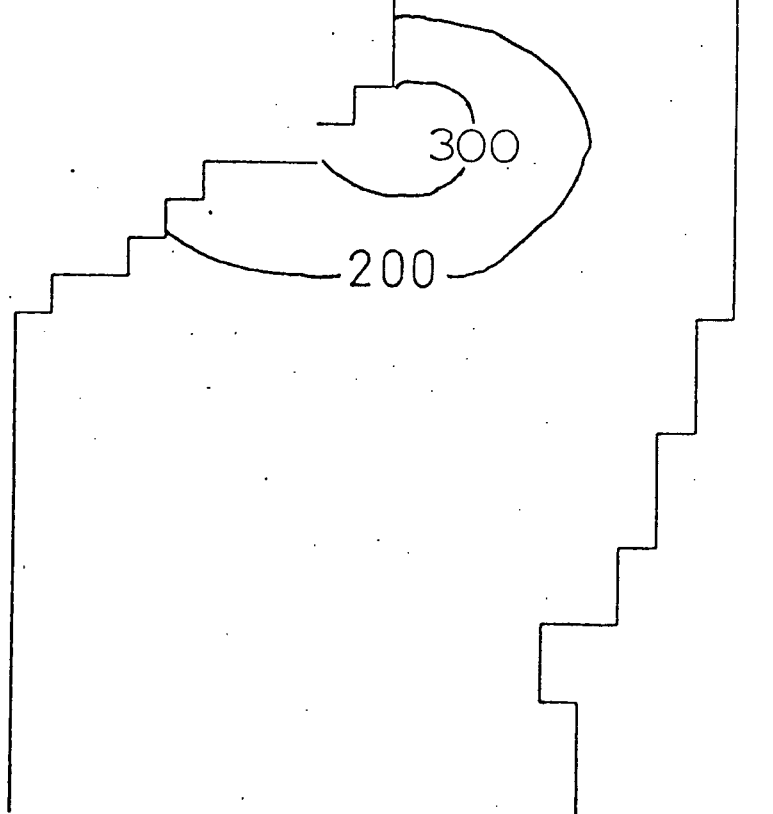


FIGURE 110. Distribution of upper layer thickness at the end of the ebb.

END OF FLOOD

14 HOURS

200 CM, 250 CM
CONTOURS

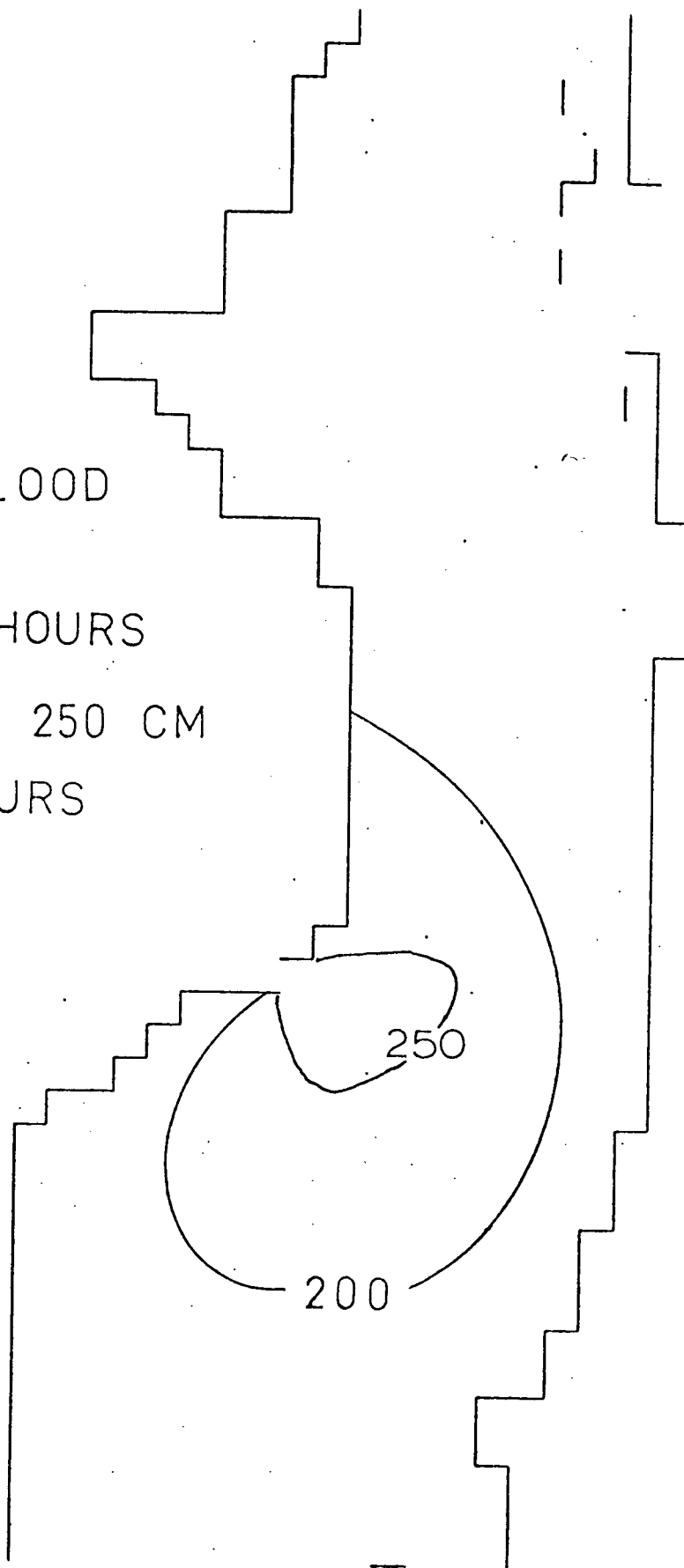


FIGURE 111. Distribution of upper layer thickness at the end of the flood.

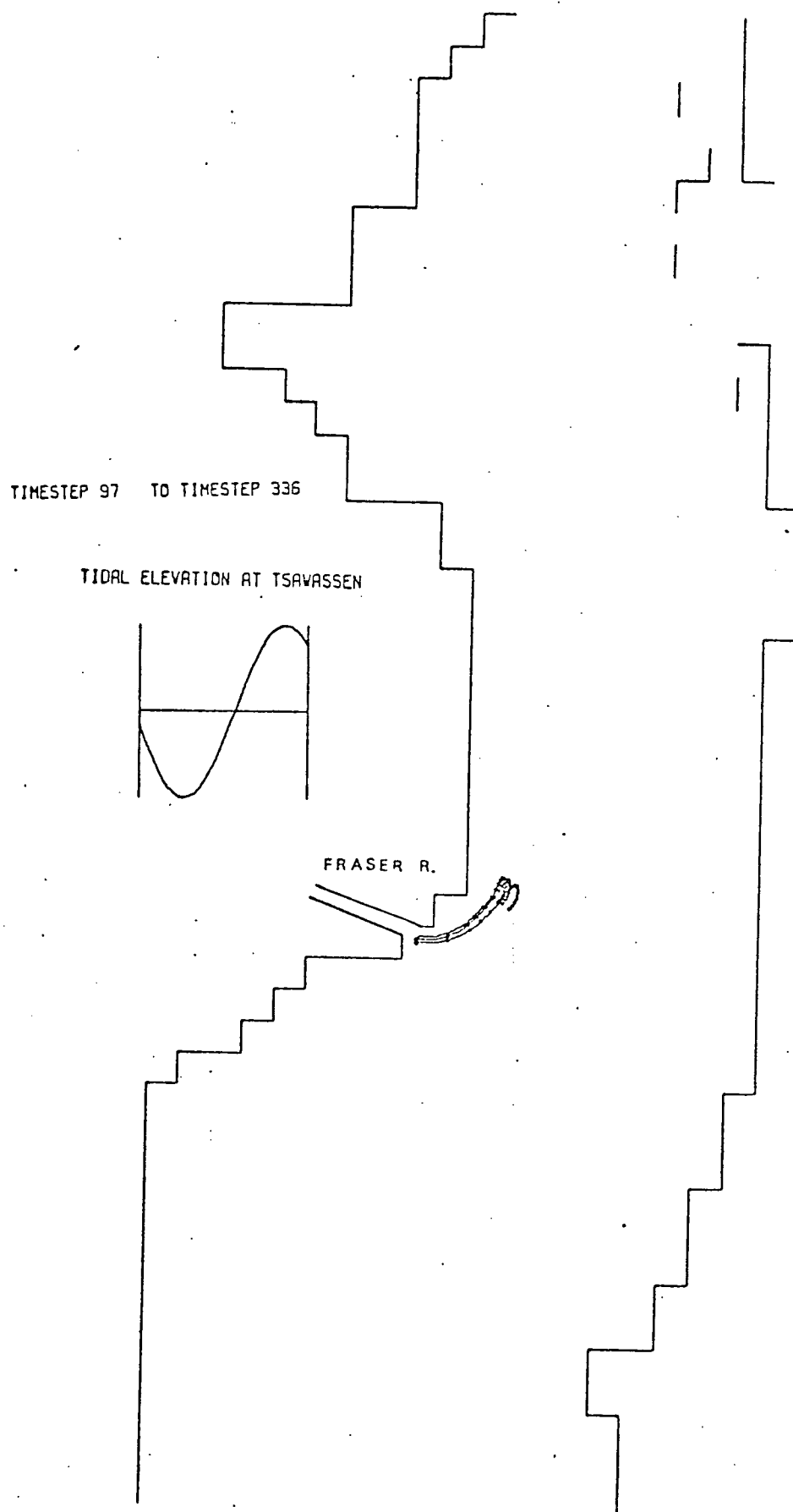


FIGURE 112. Drogue tracks produced over 12 hours by drogues released at maximum river flow.

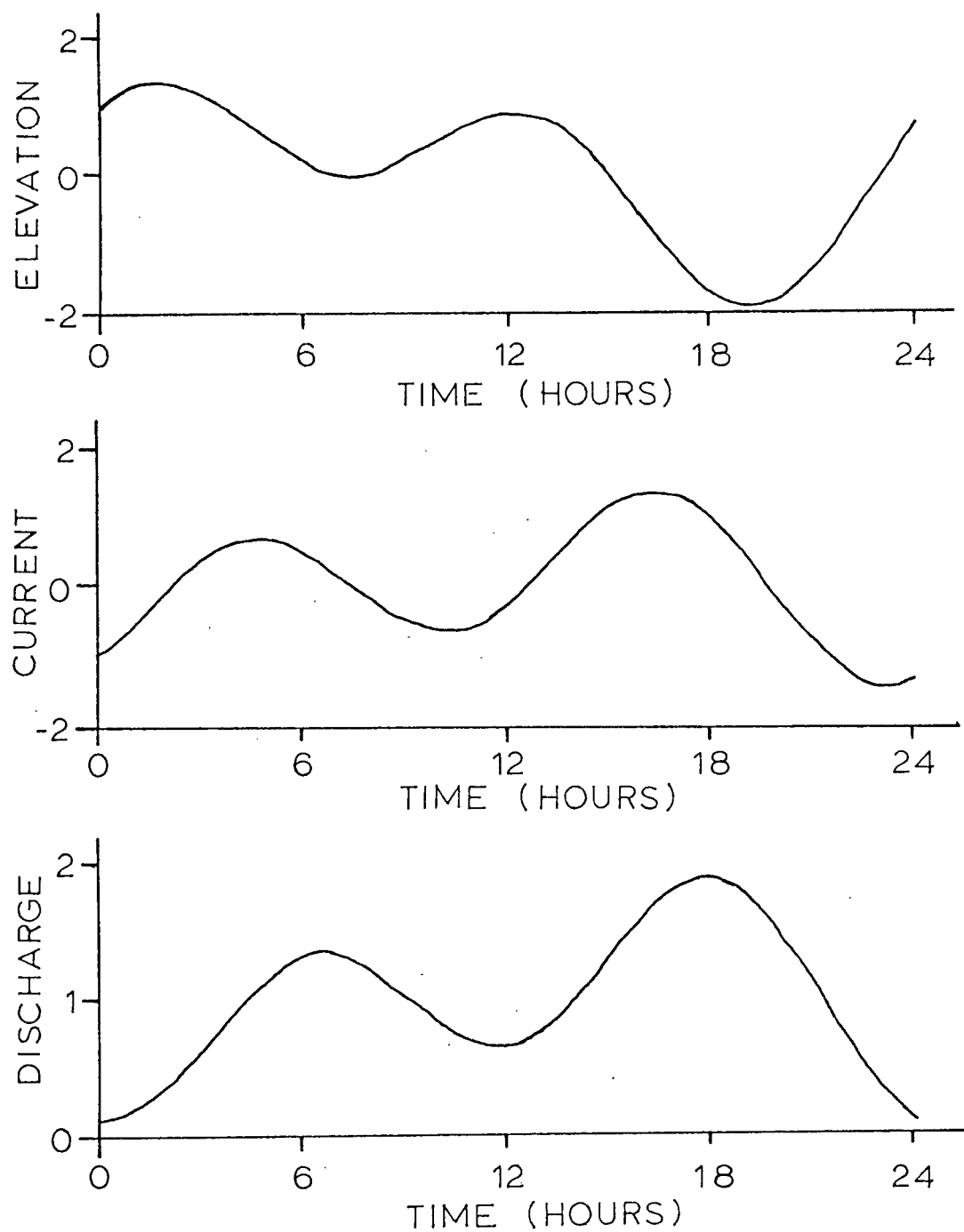


FIGURE 113. Normalized elevations, currents, and river discharge used in the second version of the real geometry model.

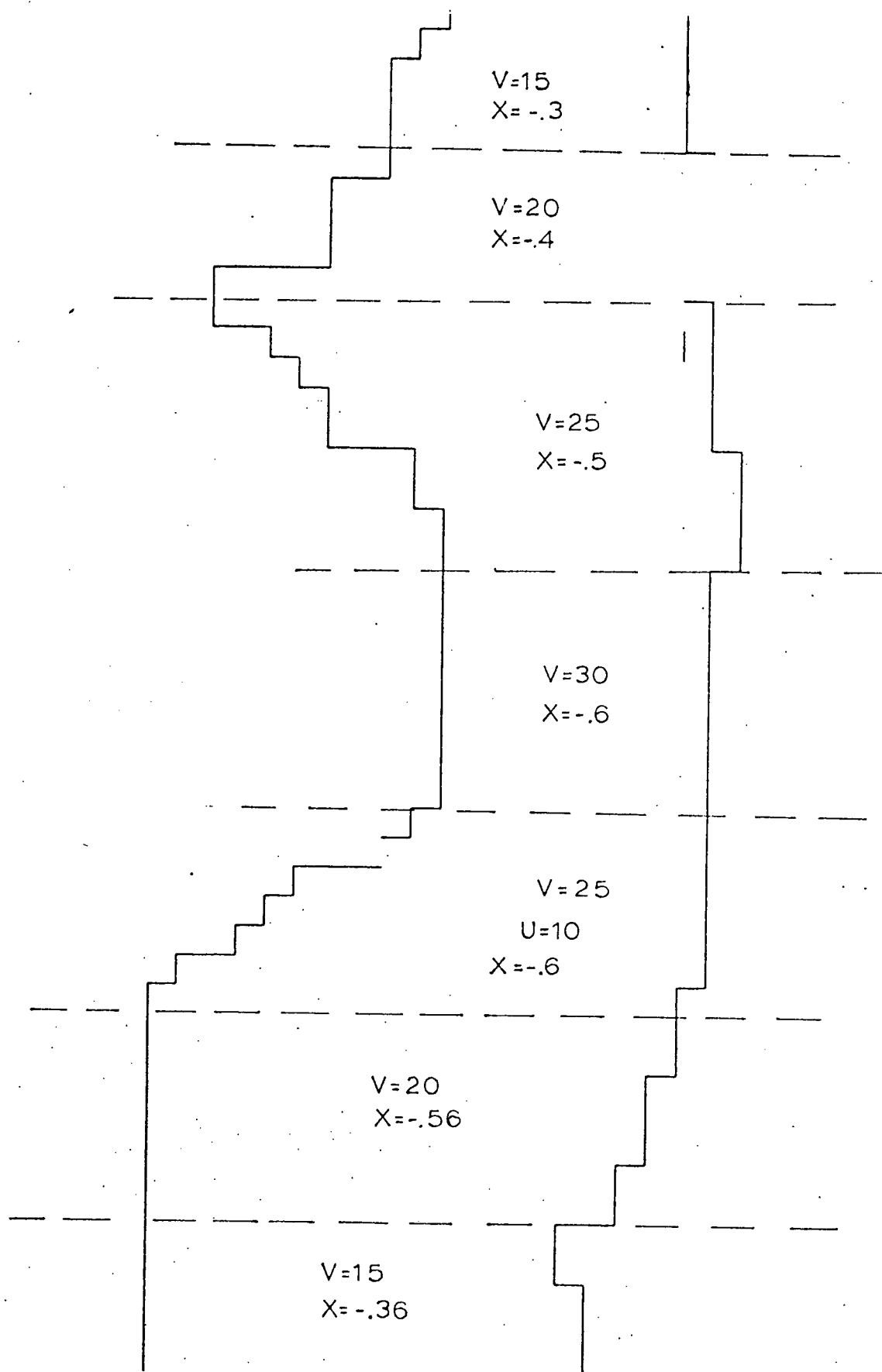


FIGURE 114. Distribution of velocities and surface slopes (cm/2km) used in the second version of the real geometry model.

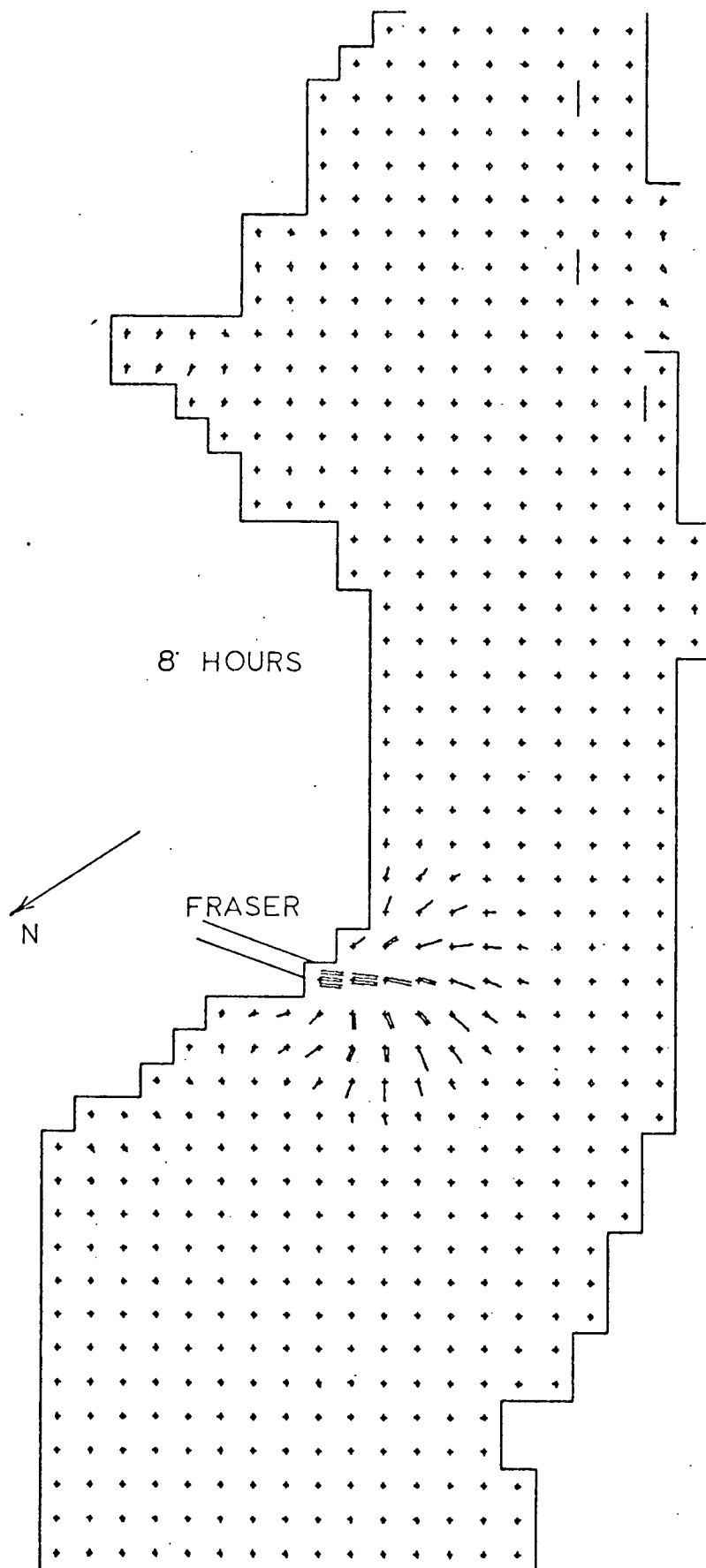


FIGURE 115. Velocity field of the model with more realistic tidal forcing, at 8 hours.

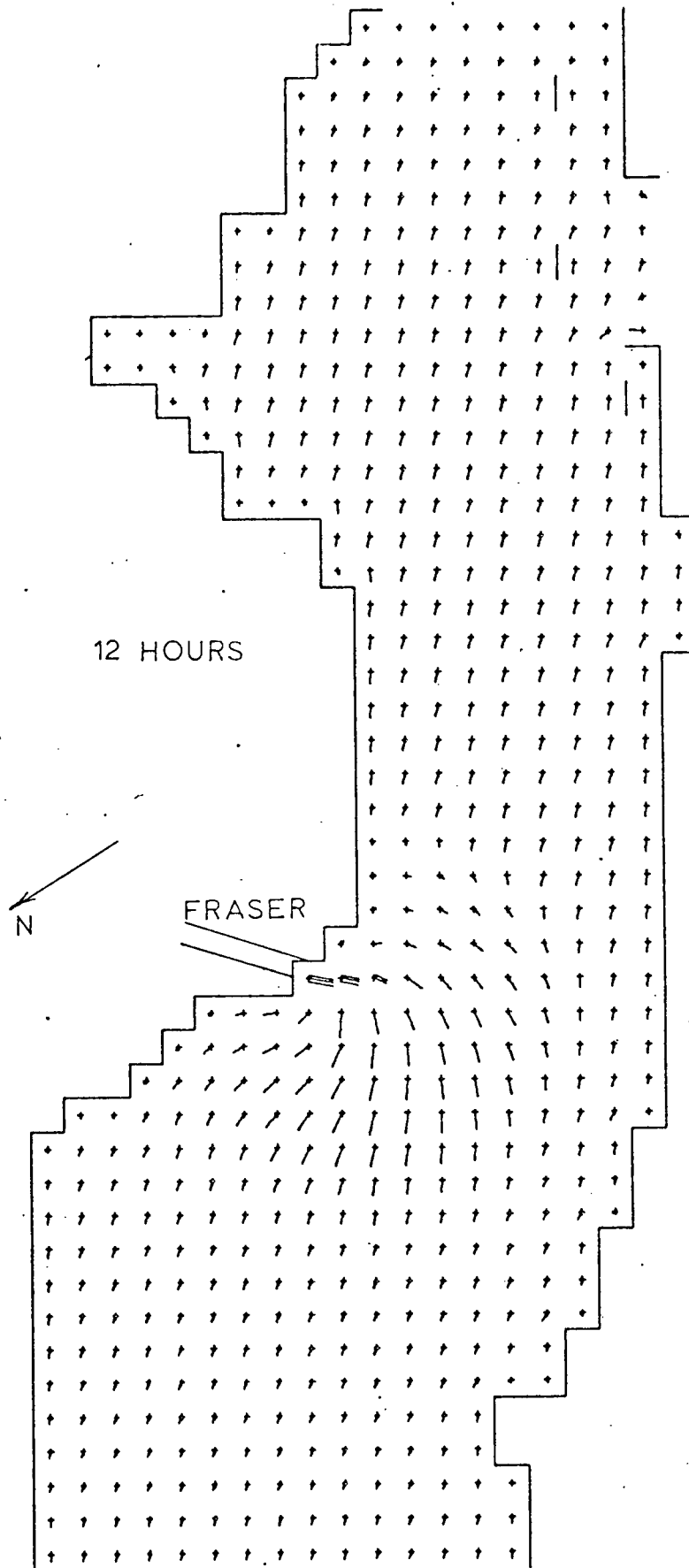


FIGURE 116. Velocity field produced by the model of Figure 115, 4 hours later.

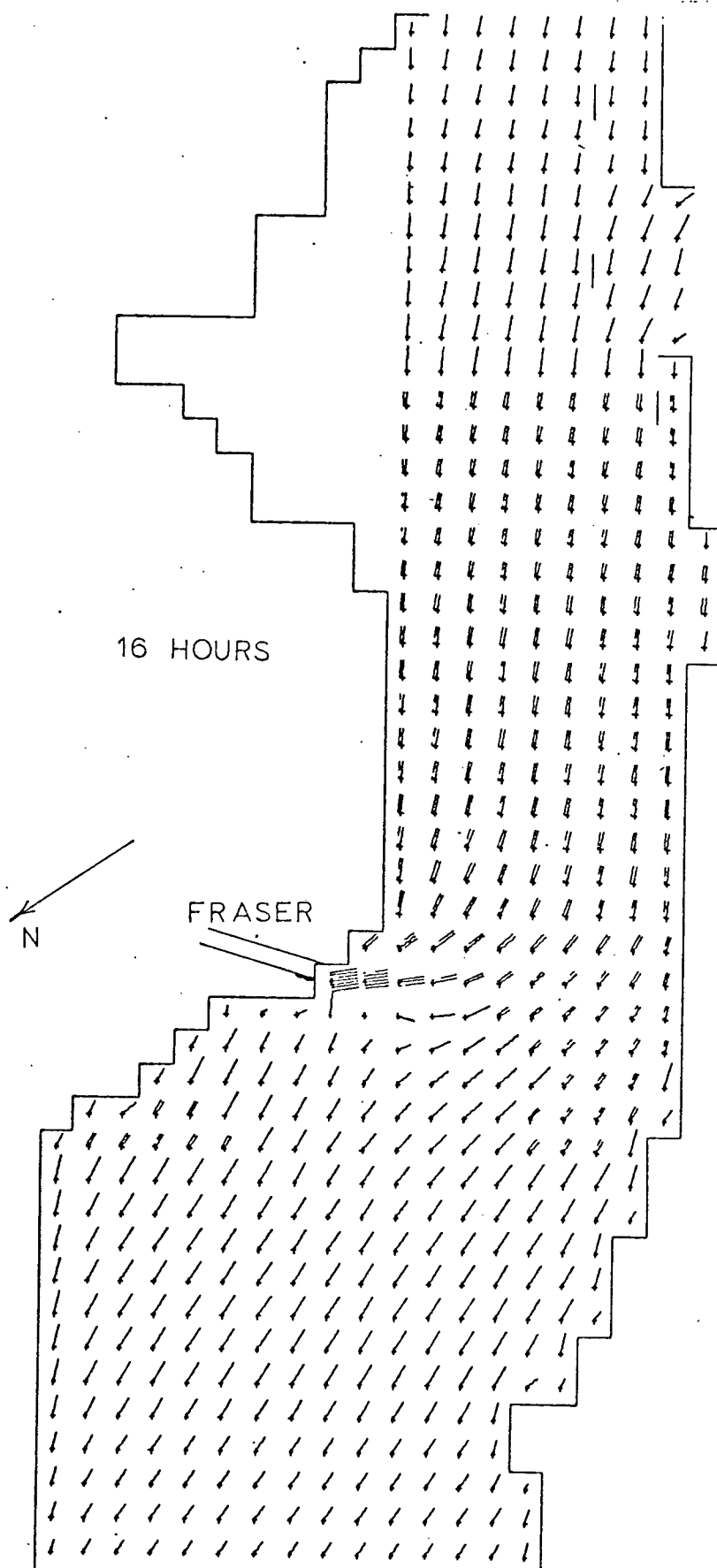


FIGURE 117. Velocity field produced by the model of Fig. 115, 8 hours later.

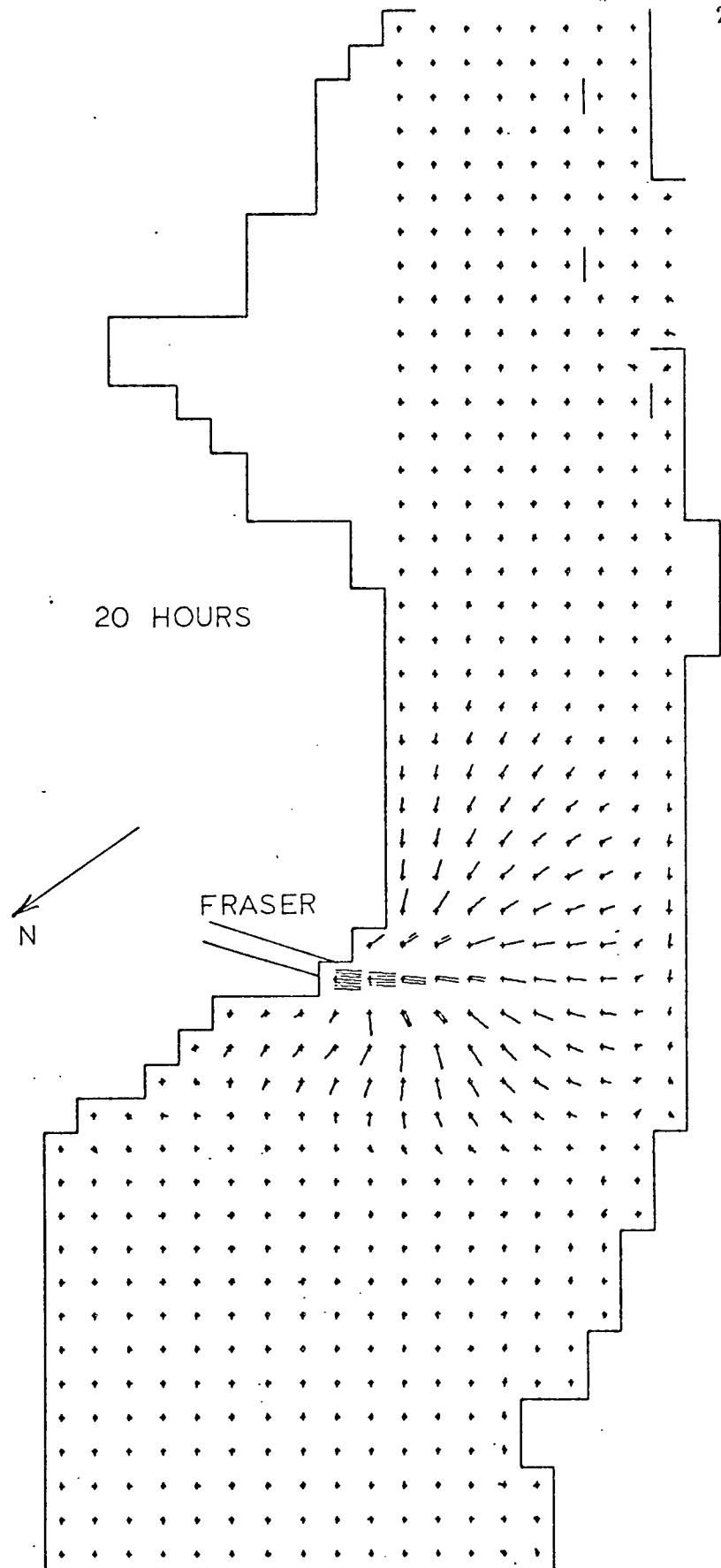


FIGURE 118. Velocity field produced by the model of Fig. 115, 12 hours later.

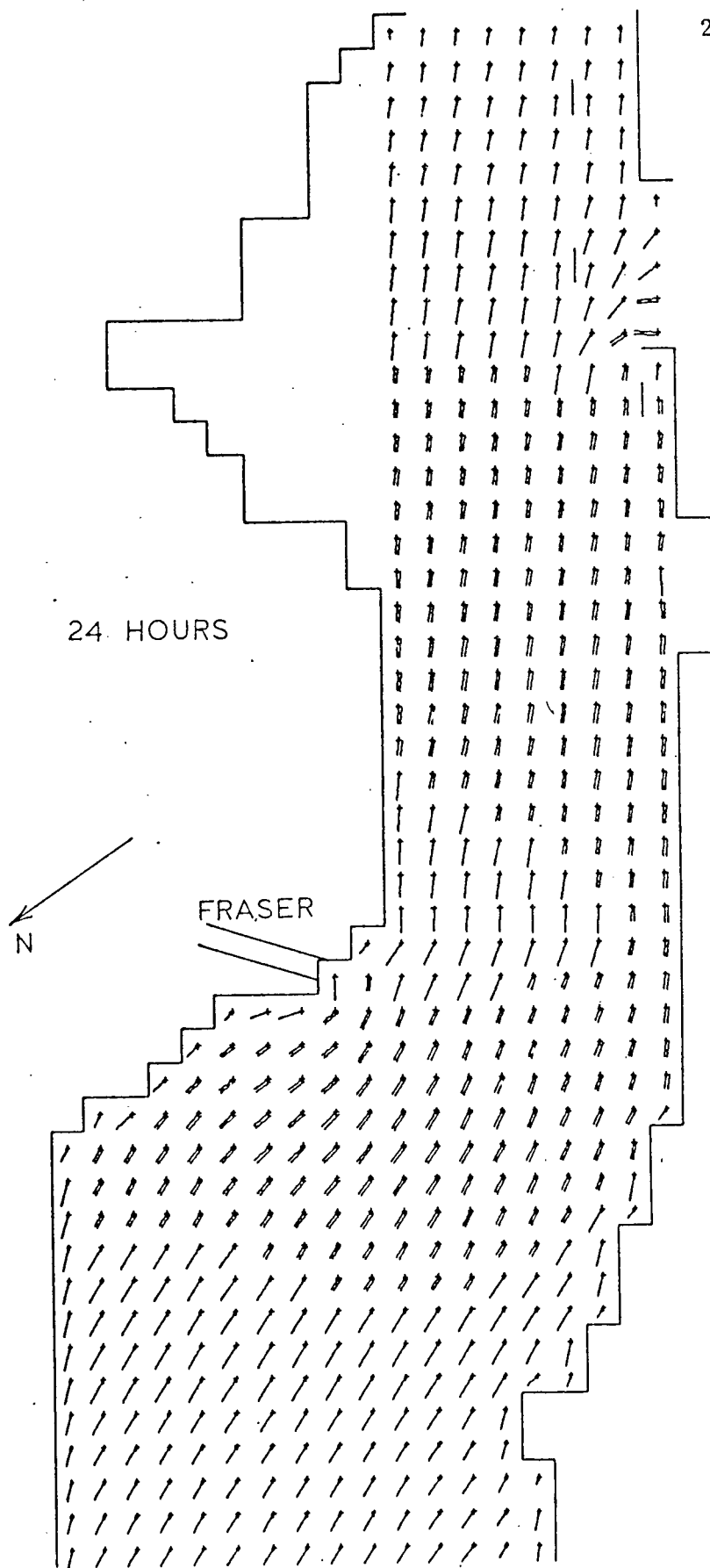


FIGURE 119. Velocity field produced by the model of Fig. 115, 16 hours later.

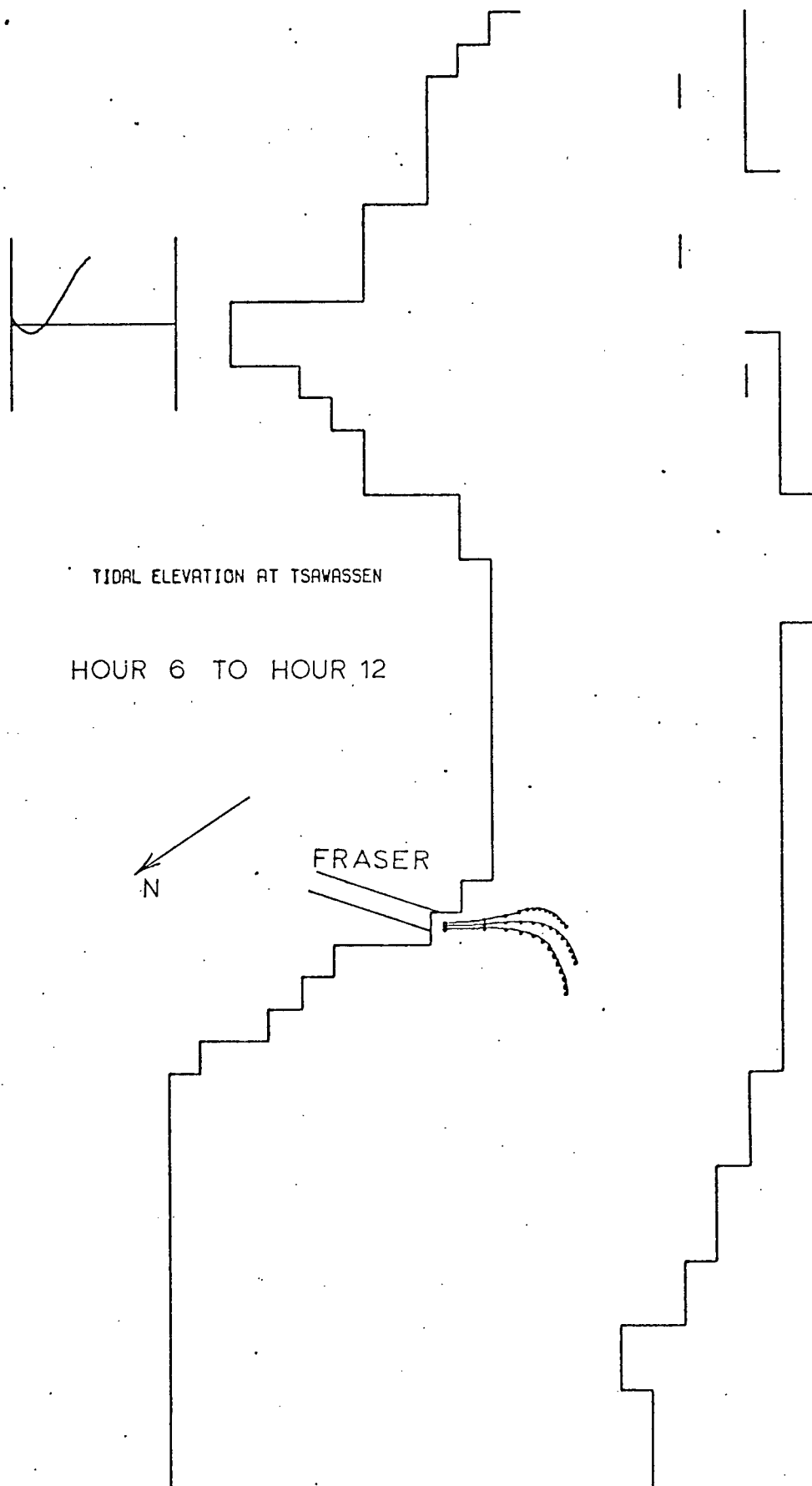


FIGURE 120. Tracks produced by drogues released at hour 6, approximately high low water.

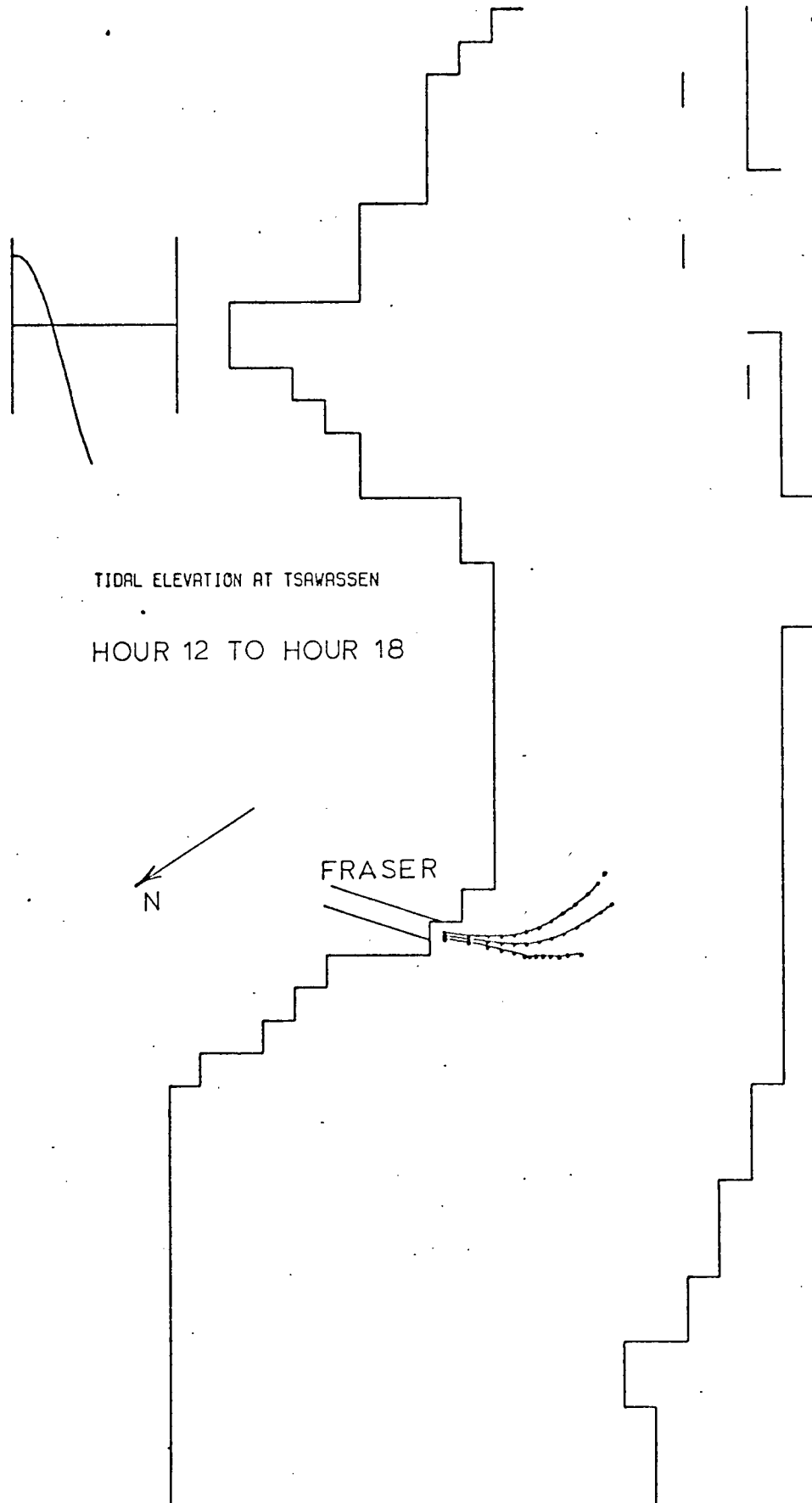


FIGURE 121. Tracks produced by drogues released at hour 12, low high water.

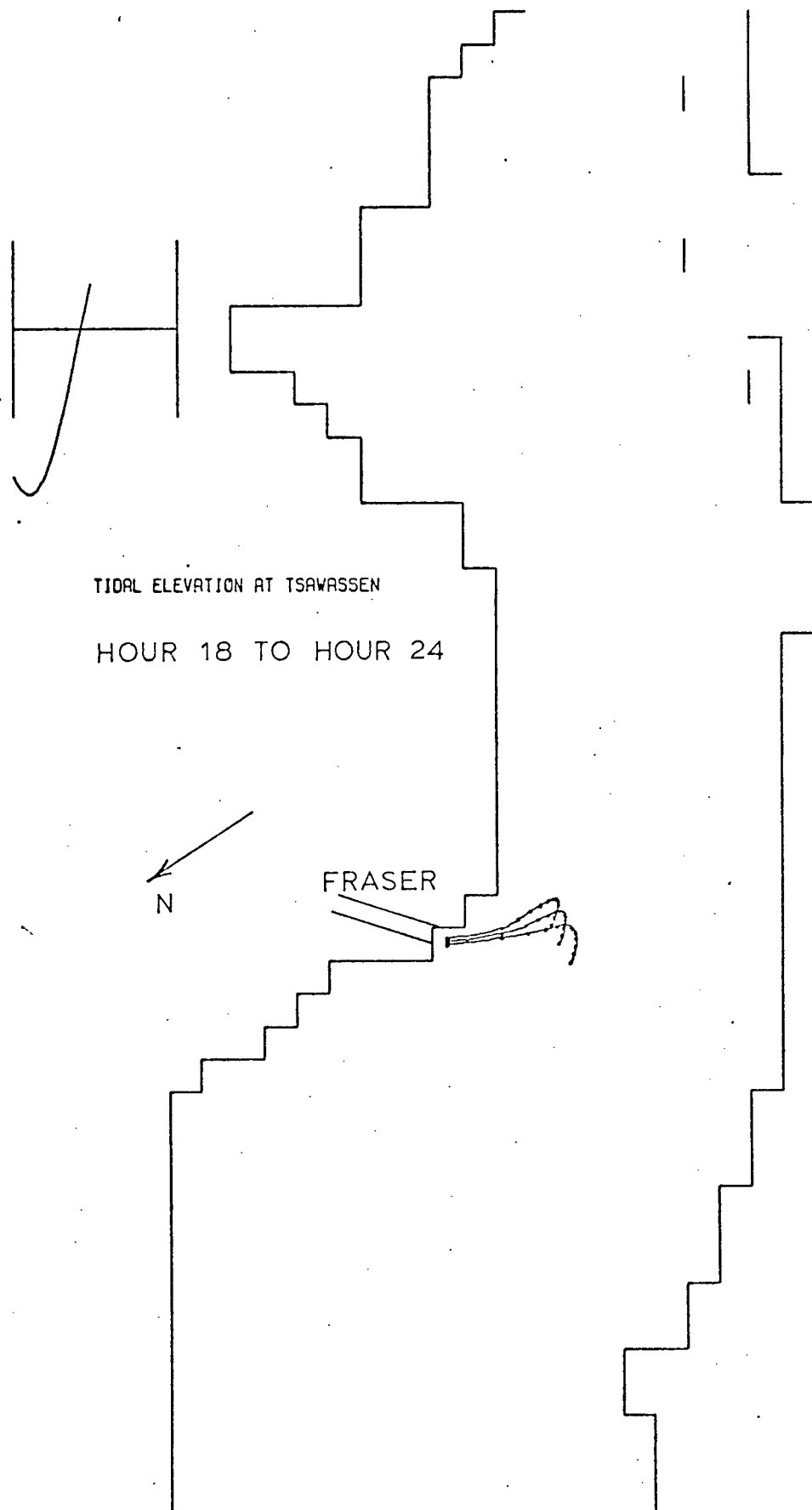


FIGURE 122. Tracks produced by drogues released at 18 hours, at maximum river discharge, near low low water.

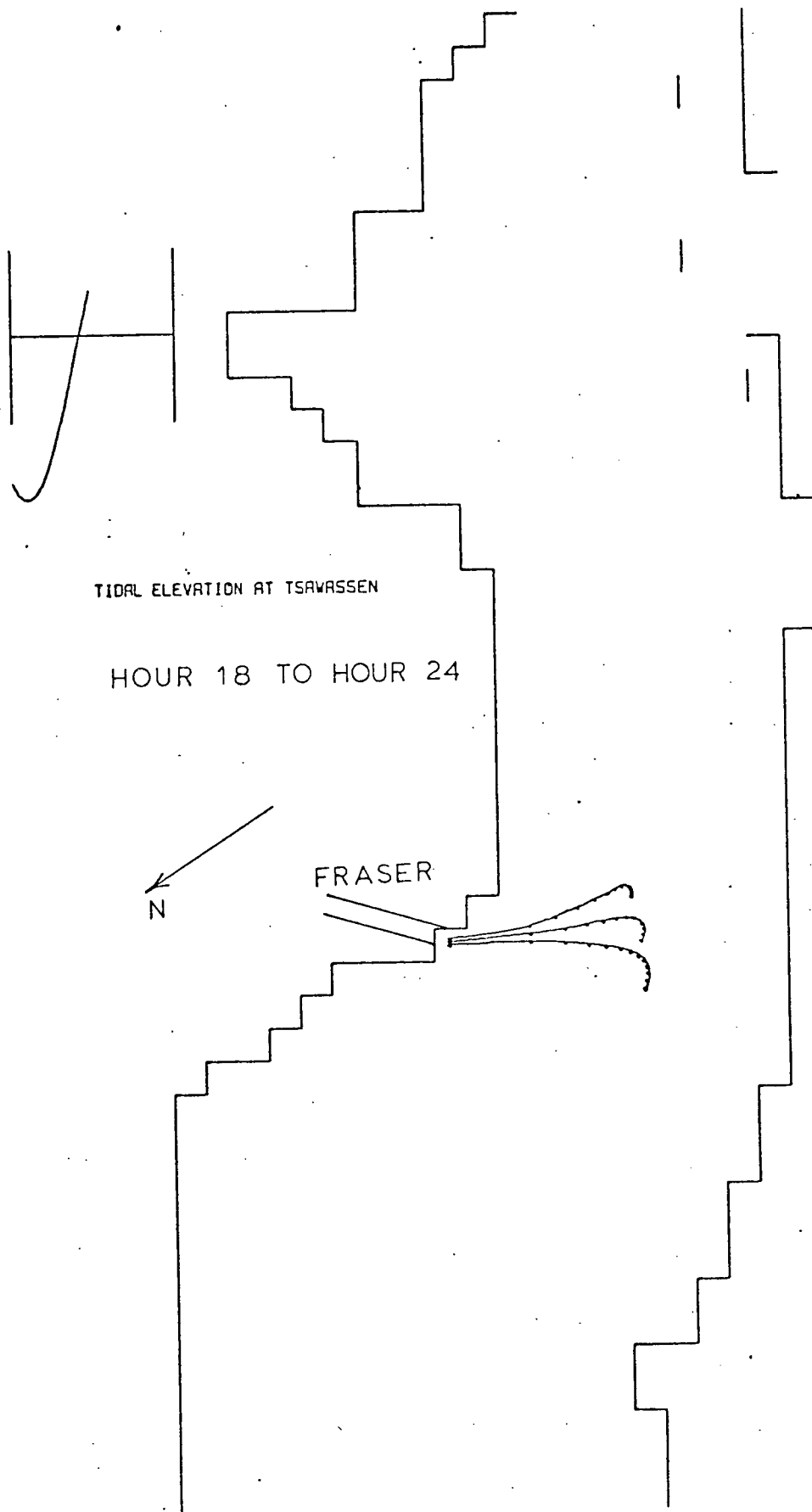


FIGURE 123. Tracks produced by drogues travelling in the same flow field as those in Fig. 122, but with a correction for vertical shear in calculating the drogue velocity.

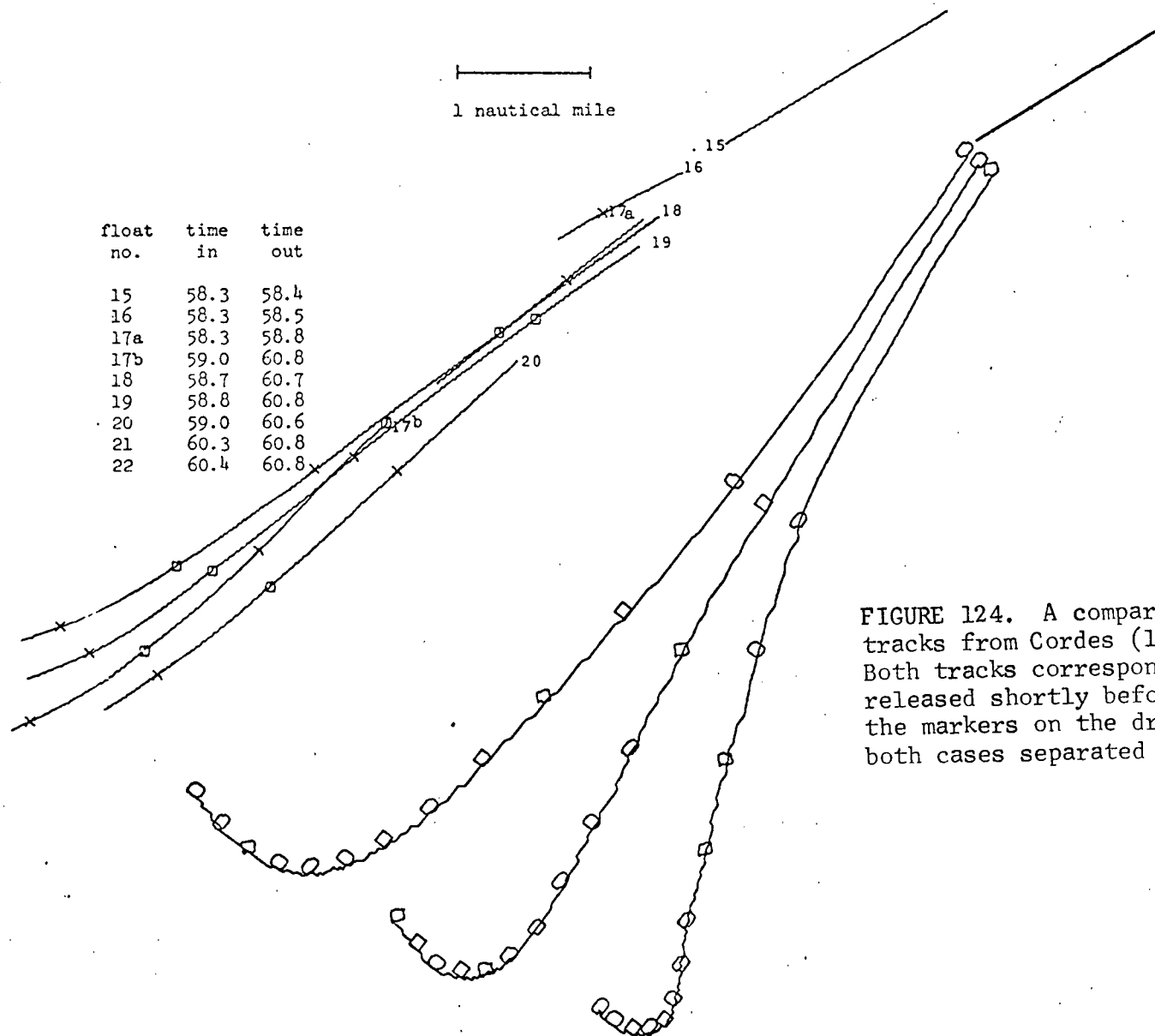


FIGURE 124. A comparison of drogue tracks from Cordes (1977), and this model. Both tracks correspond to drogues being released shortly before low water, and the markers on the drogue tracks are in both cases separated by one half hour.

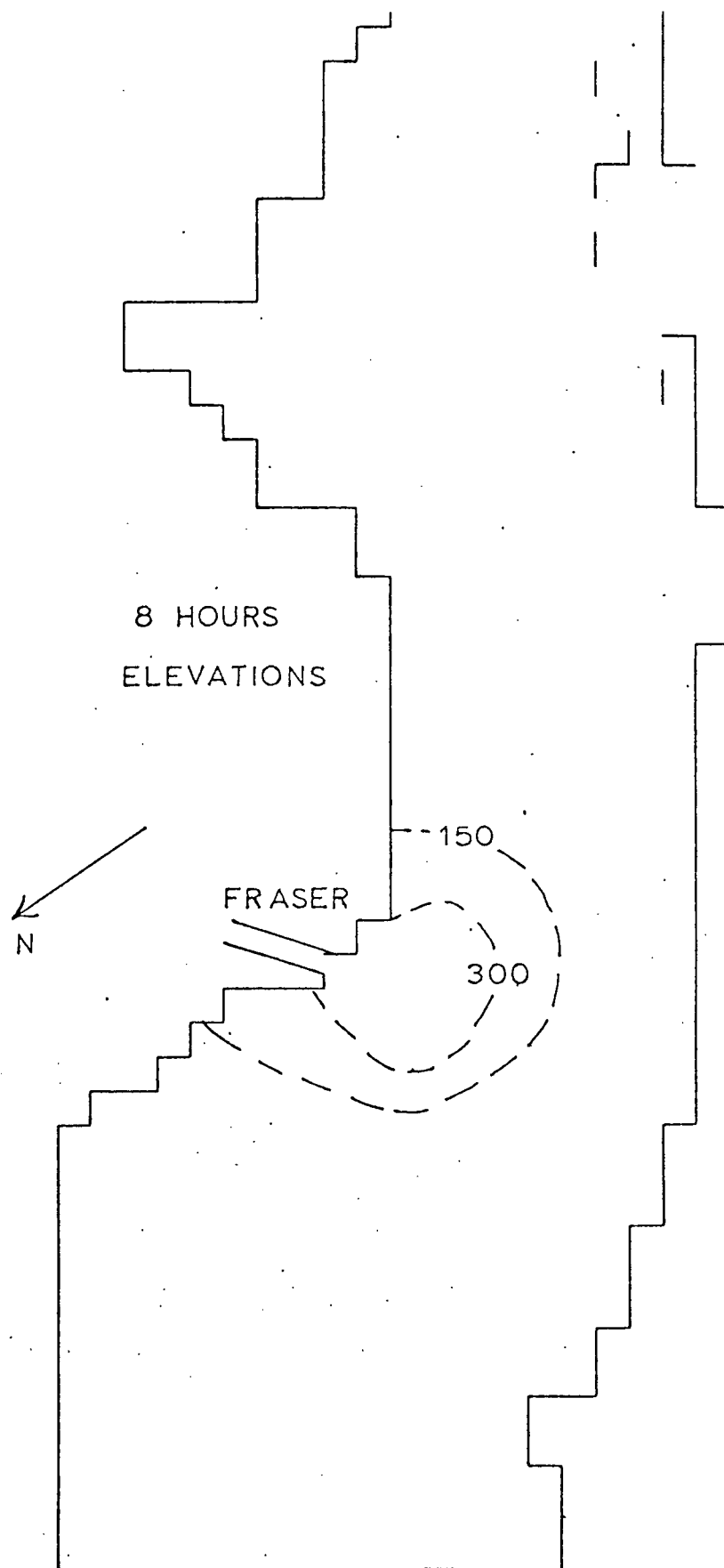


FIGURE 125. Distribution of upper layer thickness at hour 8.

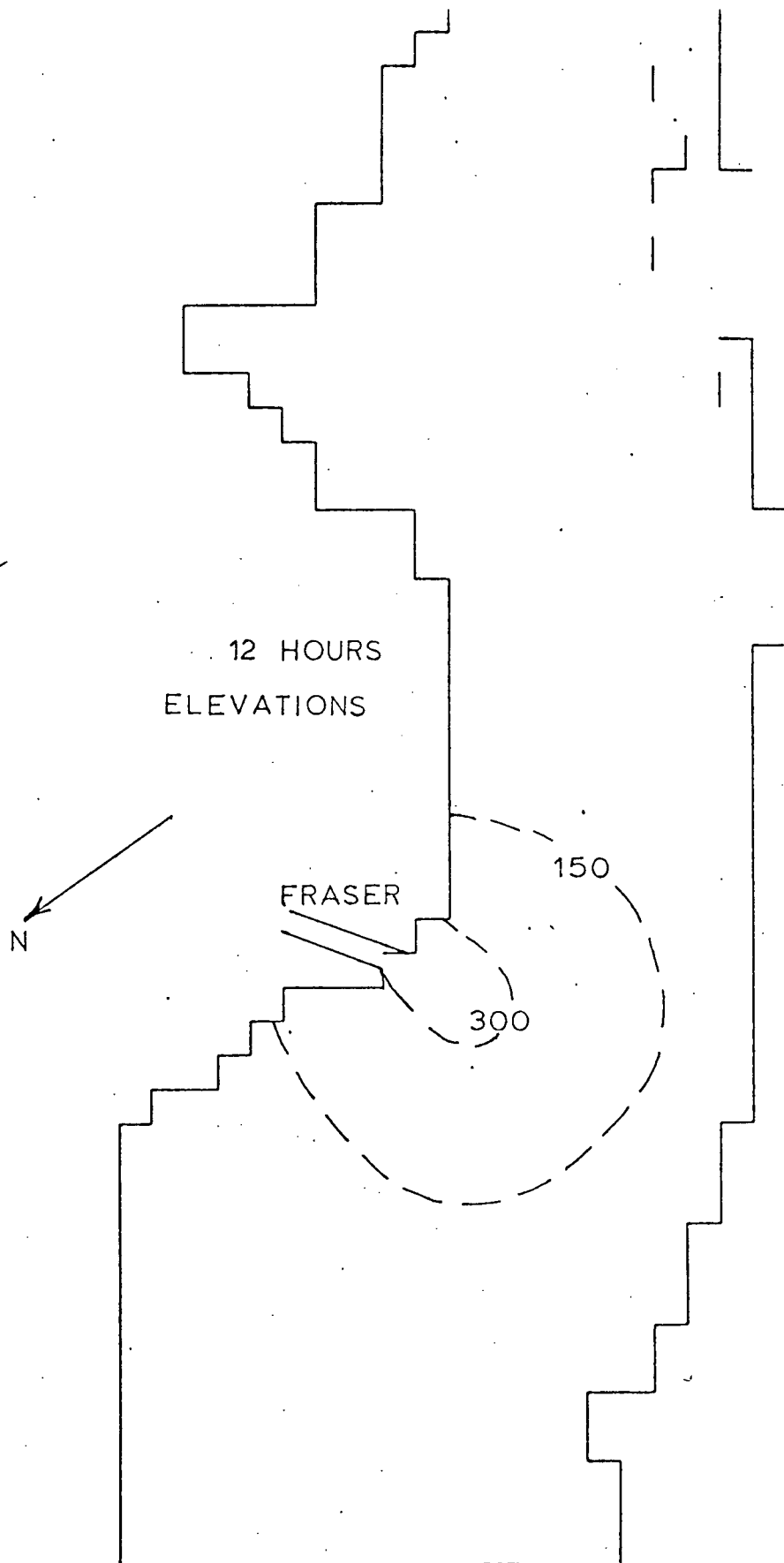


FIGURE 126. Distribution of upper layer thickness at hour 12.

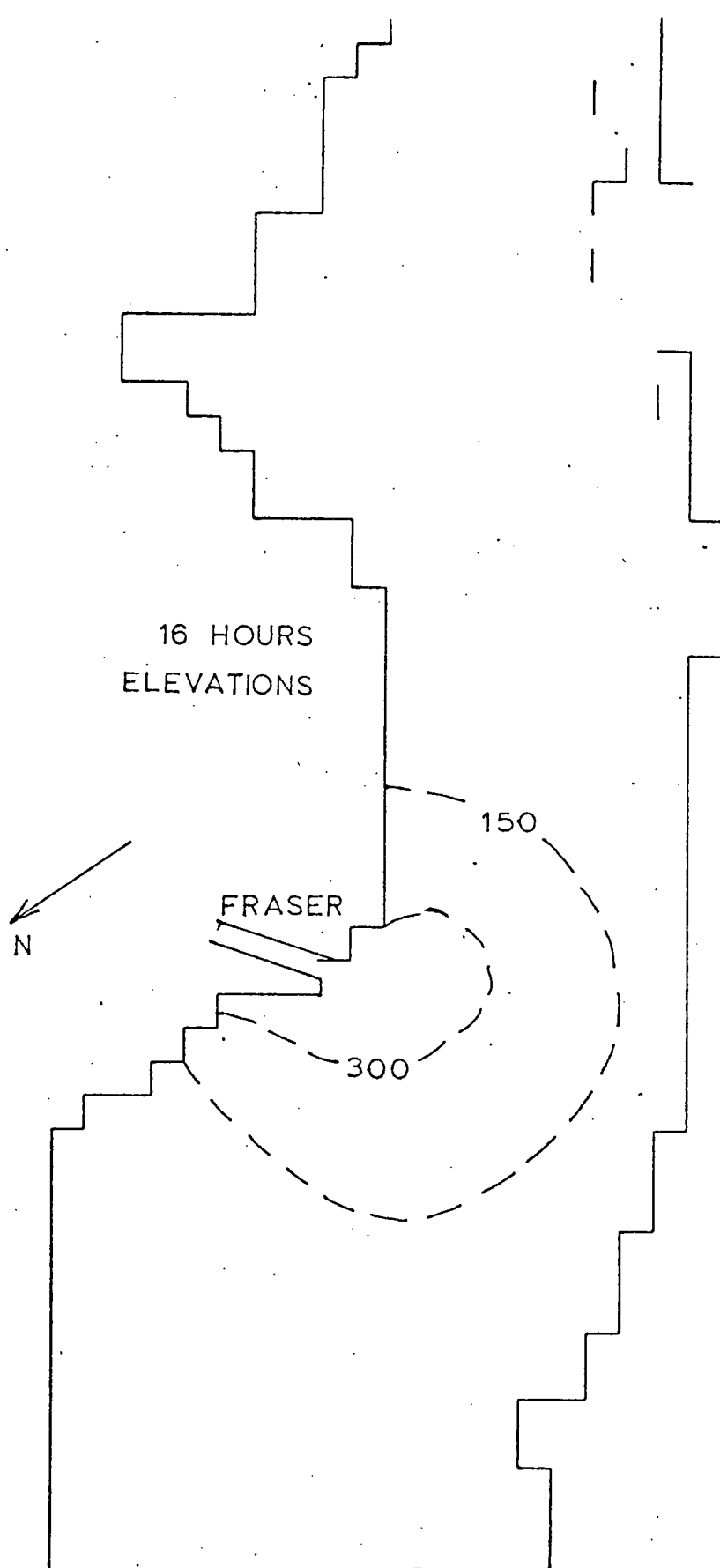


FIGURE 127. Distribution of upper layer thickness at hour 16.

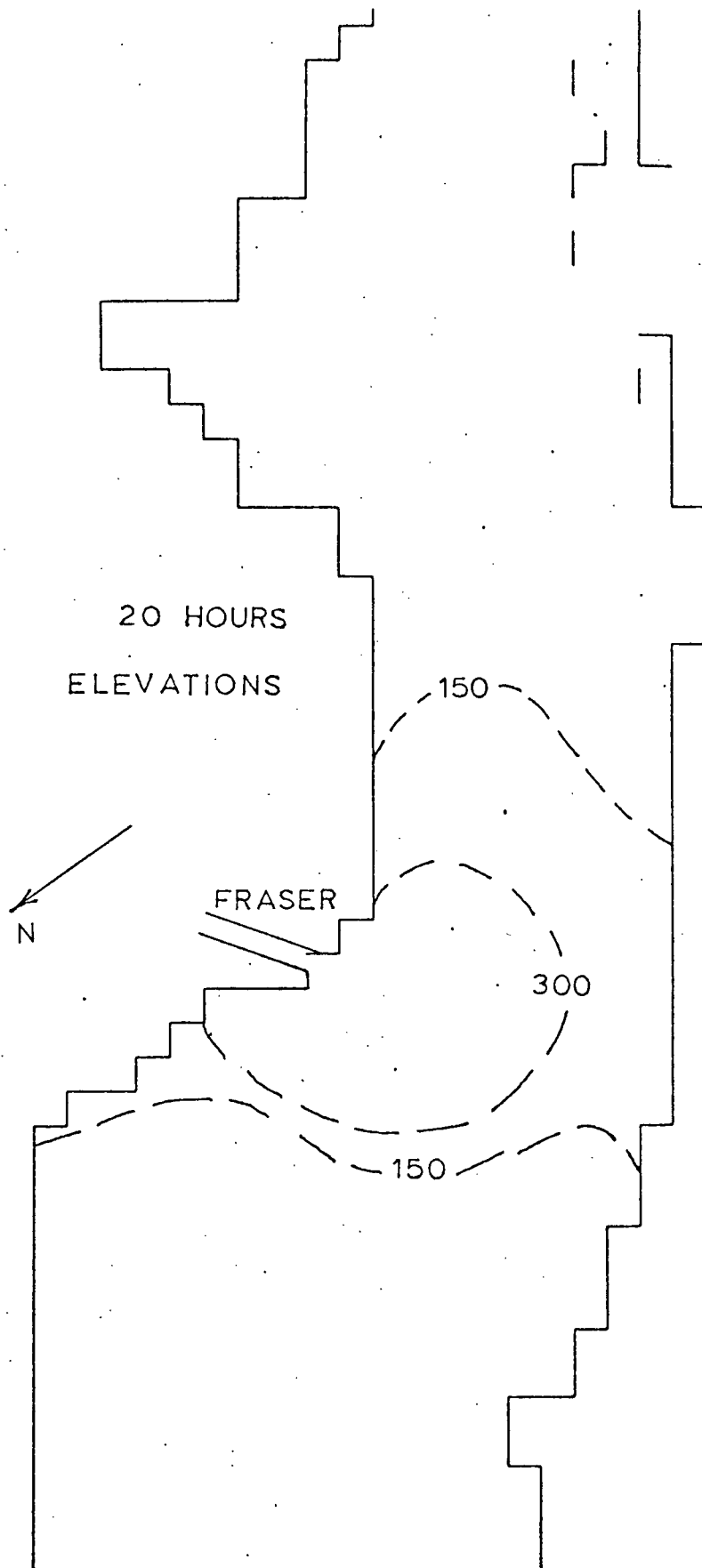


FIGURE 128. Distribution of upper layer thickness at hour 20.

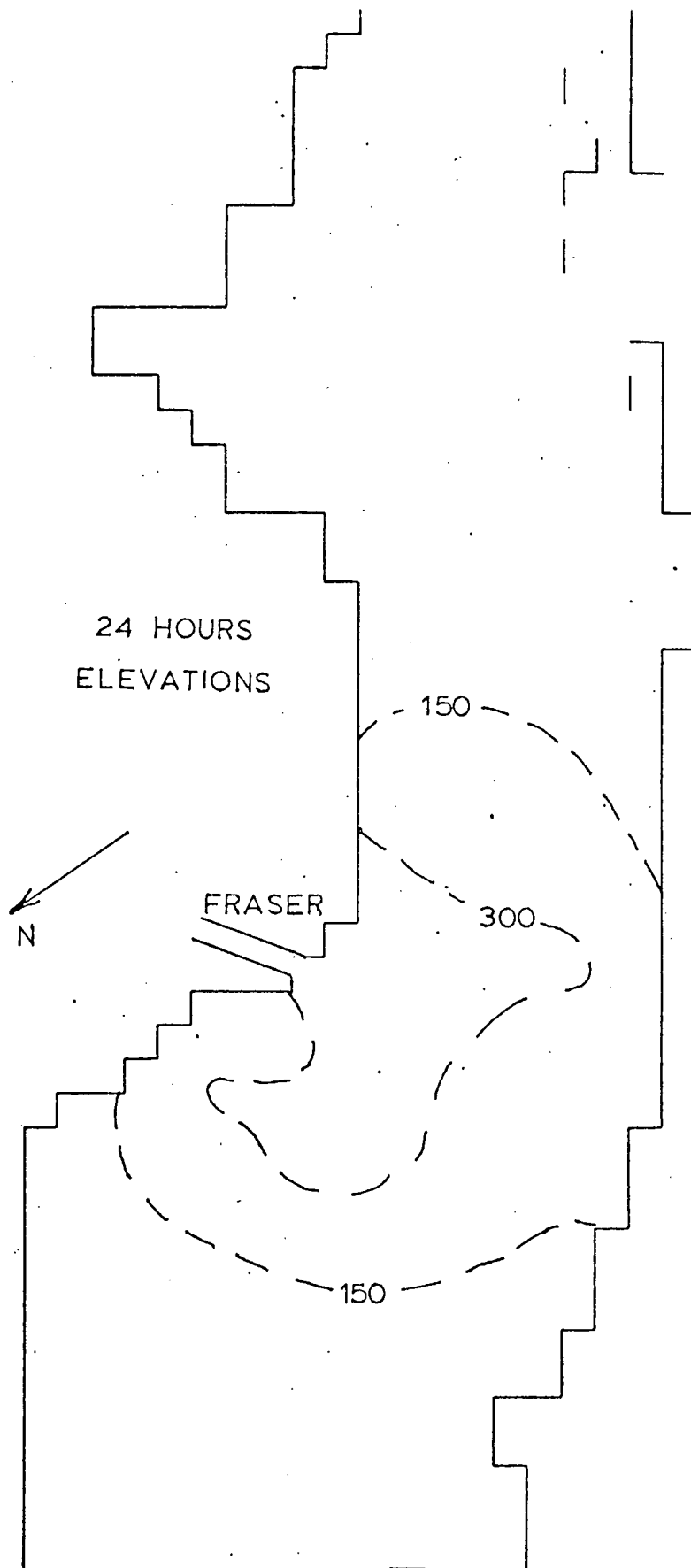


FIGURE 129. Distribution of upper layer thickness at hour 24.

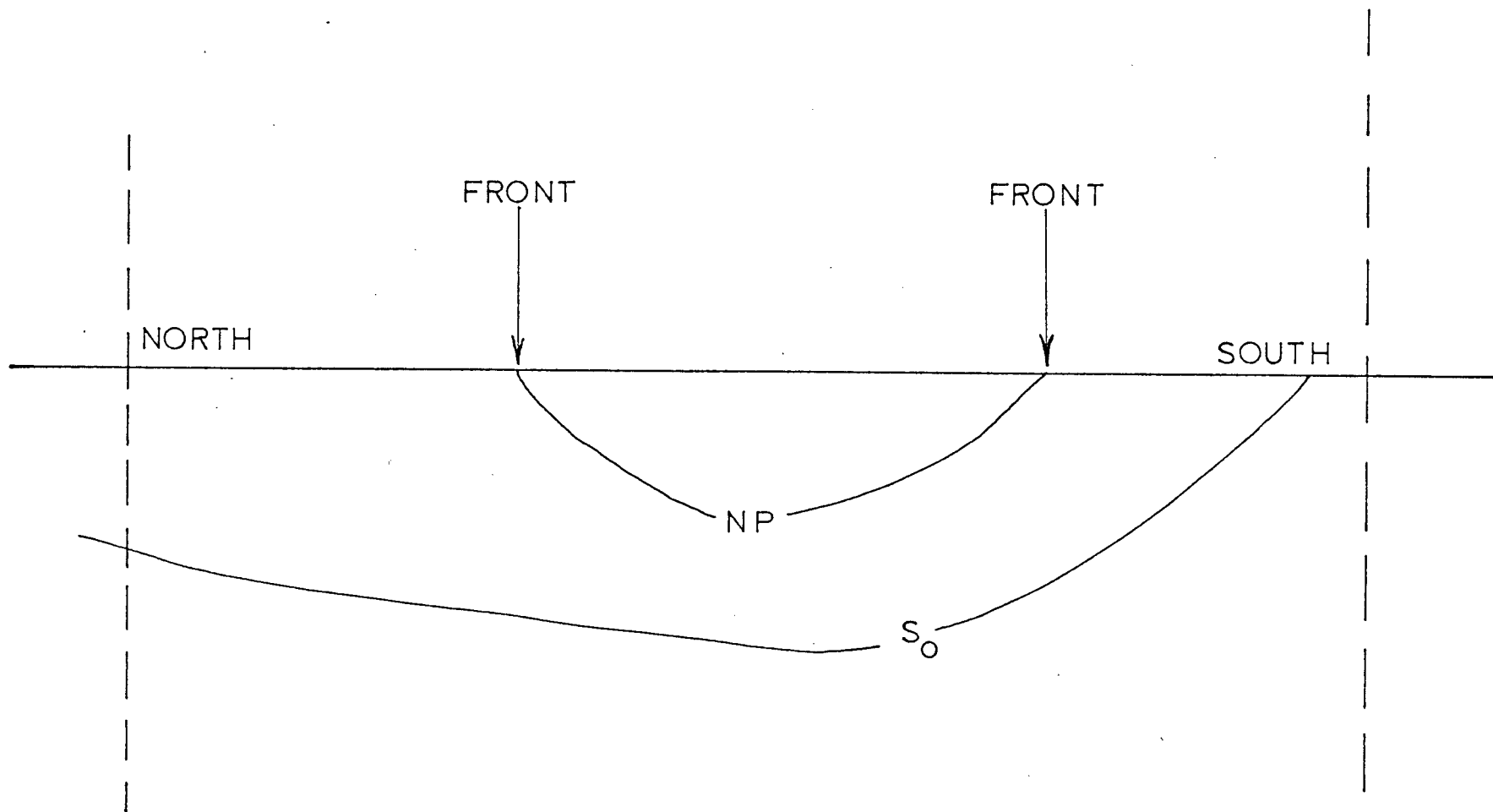


FIGURE 130. Schematic diagram of a possible extension of the upper layer model to 2 layers.

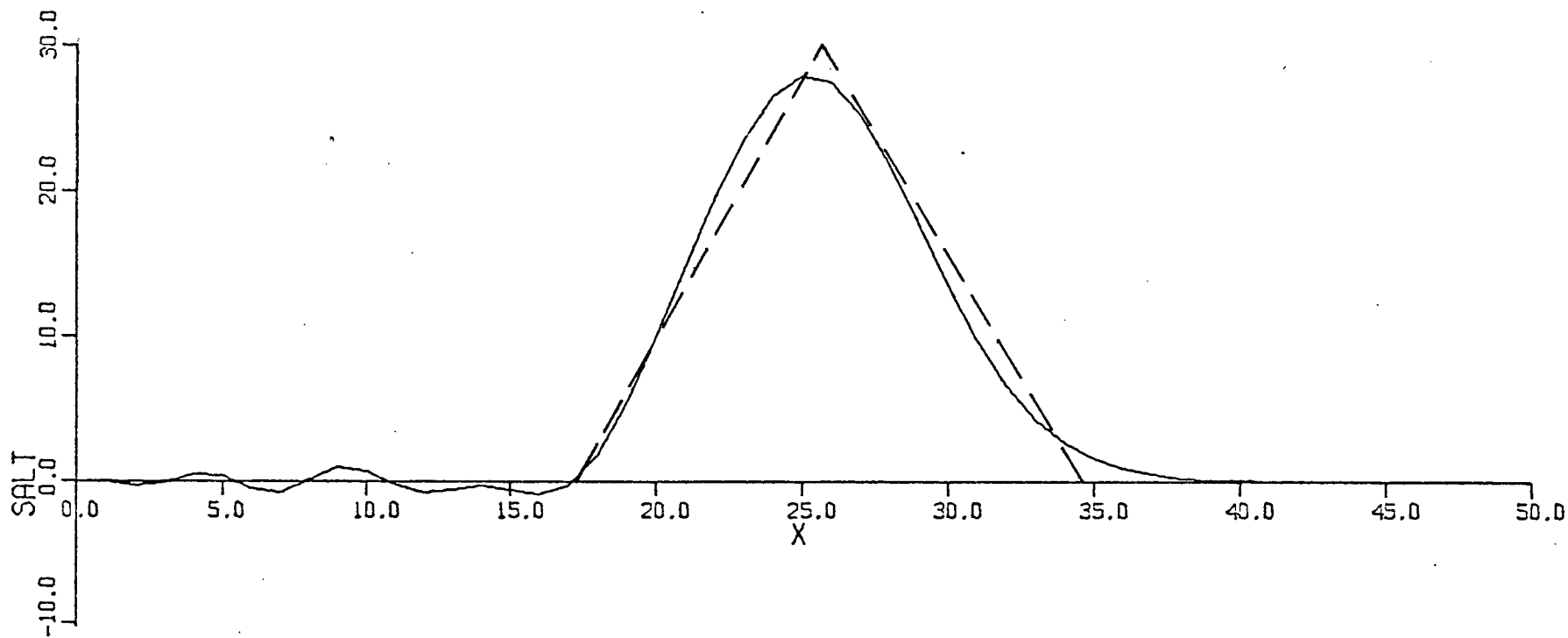


FIGURE 131. The distribution of salt as calculated by a first order scheme. The dashed line is the exact solution.

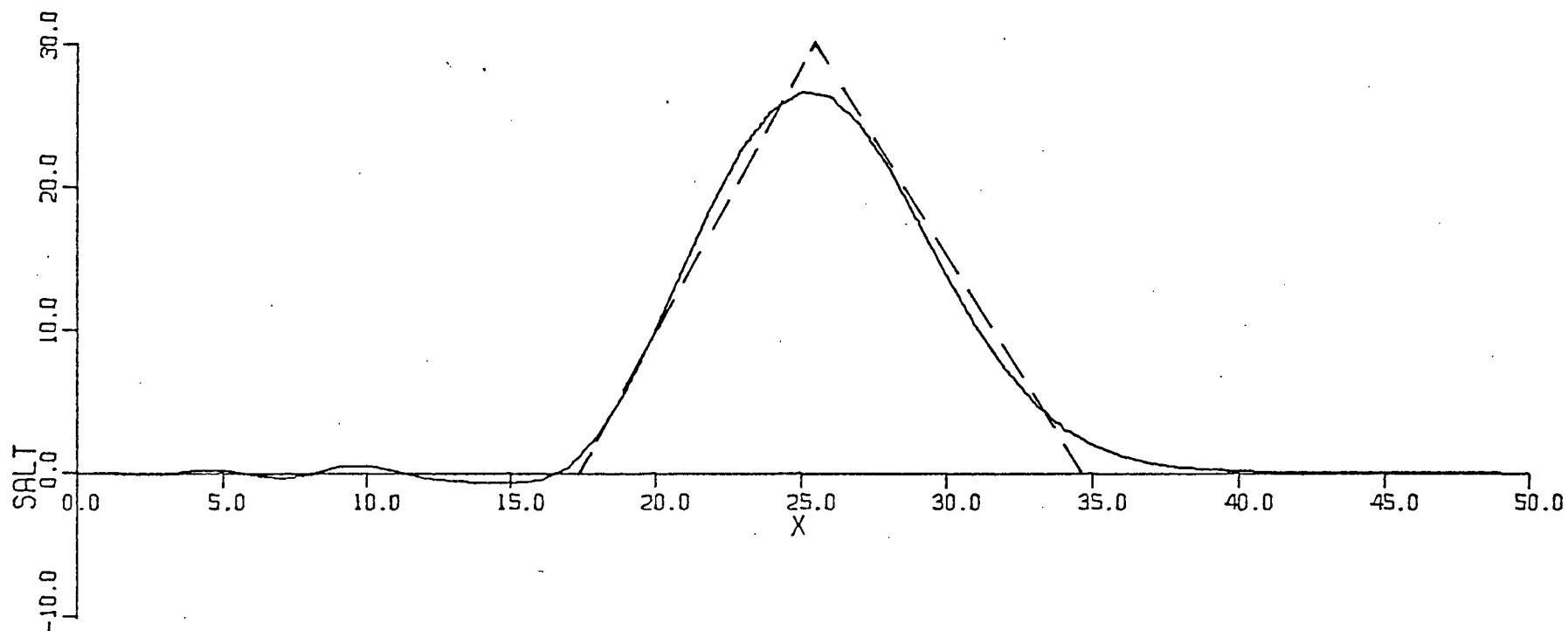


FIGURE 132. The distribution of salt as calculated by a second order scheme. The exact solution is shown by the dashed line.